



Analysis of personalized mechano-bio-faithful radio-cephalic arteriovenous Fistula

Yang Yang

► To cite this version:

Yang Yang. Analysis of personalized mechano-bio-faithful radio-cephalic arteriovenous Fistula. Biomechanics [physics.med-ph]. Université de Lyon, 2021. English. NNT : 2021LYSEI067 . tel-03625310

HAL Id: tel-03625310

<https://theses.hal.science/tel-03625310>

Submitted on 30 Mar 2022

HAL is a multi-disciplinary open access archive for the deposit and dissemination of scientific research documents, whether they are published or not. The documents may come from teaching and research institutions in France or abroad, or from public or private research centers.

L'archive ouverte pluridisciplinaire **HAL**, est destinée au dépôt et à la diffusion de documents scientifiques de niveau recherche, publiés ou non, émanant des établissements d'enseignement et de recherche français ou étrangers, des laboratoires publics ou privés.



N° d'ordre NNT : 2021LYSEI067

THESE DE DOCTORAT DE L'UNIVERSITE DE LYON

opérée au sein de
l'INSA Lyon

Ecole Doctorale N°ED162

Mécanique, Énergétique, Génie Civil et Acoustique (MEGA)

Spécialité/discipline de doctorat :
Biomécanique

Soutenue publiquement le 19/10/2021, par :
YANG Yang

Analysis of Personalized Mechano-Bio-faithful Radio-Cephalic Arteriovenous Fistula

Devant le jury composé de :

Philippe VEZIN	Directeur de Recherche	Université Gustave Eiffel	Rapporteur
Shengzhang WANG	Associate Professor	Fudan University	Rapporteur
Pascale KULISA	Chargée de Recherche CNRS	Ecole Centrale de Lyon	Examinatrice
Patrick LERMUSIAUX	Professeur des Universités/PH	Hospices Civils de Lyon	Examinateur
Hassan ZAHOUANI	Professeur des Universités	ENI Saint-Étienne	Examinateur
Benyebka BOU-SAÏD	Professeur des Universités	INSA Lyon	Directeur de thèse
Nellie DELLA SCHIAVA	PH en Chirurgie Vasculaire	Hospices Civils de Lyon	Invité
Serge SIMOËNS	Directeur de Recherche CNRS	Ecole Centrale de Lyon	Invité
Mahmound EL HAJEM	Maître de Conférences H.D.R	INSA Lyon	Invité

Département FEDORA – INSA Lyon - Ecoles Doctorales

SIGLE	ECOLE DOCTORALE	NOM ET COORDONNEES DU RESPONSABLE
CHIMIE	<u>CHIMIE DE LYON</u> https://www.edchimie-lyon.fr Sec. : Renée EL MELHEM Bât. Blaise PASCAL, 3e étage secretariat@edchimie-lyon.fr	M. Stéphane DANIELE C2P2-CPE LYON-UMR 5265 Bâtiment F308, BP 2077 43 Boulevard du 11 novembre 1918 69616 Villeurbanne directeur@edchimie-lyon.fr
E.E.A.	<u>ÉLECTRONIQUE, ÉLECTROTECHNIQUE, AUTOMATIQUE</u> https://edeea.universite-lyon.fr Sec. : Stéphanie CAUVIN Bâtiment Direction INSA Lyon Tél : 04.72.43.71.70 secretariat.edeea@insa-lyon.fr	M. Philippe DELACHARTRE INSA LYON Laboratoire CREATIS Bâtiment Blaise Pascal, 7 avenue Jean Capelle 69621 Villeurbanne CEDEX Tél : 04.72.43.88.63 philippe.delachartre@insa-lyon.fr
E2M2	<u>ÉVOLUTION, ÉCOSYSTÈME, MICROBIOLOGIE, MODÉLISATION</u> http://e2m2.universite-lyon.fr Sec. : Sylvie ROBERJOT Bât. Atrium, UCB Lyon 1 Tél : 04.72.44.83.62 secretariat.e2m2@univ-lyon1.fr	M. Philippe NORMAND Université Claude Bernard Lyon 1 UMR 5557 Lab. d'Ecologie Microbienne Bâtiment Mendel 43, boulevard du 11 Novembre 1918 69 622 Villeurbanne CEDEX philippe.normand@univ-lyon1.fr
EDISS	<u>INTERDISCIPLINAIRE SCIENCES-SANTÉ</u> http://ediss.universite-lyon.fr Sec. : Sylvie ROBERJOT Bât. Atrium, UCB Lyon 1 Tél : 04.72.44.83.62 secretariat.ediss@univ-lyon1.fr	Mme Sylvie RICARD-BLUM Institut de Chimie et Biochimie Moléculaires et Supramoléculaires (ICBMS) - UMR 5246 CNRS - Université Lyon 1 Bâtiment Raulin - 2ème étage Nord 43 Boulevard du 11 novembre 1918 69622 Villeurbanne Cedex Tél : +33(0)4 72 44 82 32 sylvie.ricard-blum@univ-lyon1.fr
INFOMATHS	<u>INFORMATIQUE ET MATHÉMATIQUES</u> http://edinfomaths.universite-lyon.fr Sec. : Renée EL MELHEM Bât. Blaise PASCAL, 3e étage Tél : 04.72.43.80.46 infomaths@univ-lyon1.fr	M. Hamamache KHEDDOUCI Université Claude Bernard Lyon 1 Bât. Nautibus 43, Boulevard du 11 novembre 1918 69 622 Villeurbanne Cedex France Tél : 04.72.44.83.69 hamamache.kheddouci@univ-lyon1.fr
Matériaux	<u>MATÉRIAUX DE LYON</u> http://ed34.universite-lyon.fr Sec. : Yann DE ORDENANA Tél : 04.72.18.62.44 yann.de-ordenana@ec-lyon.fr	M. Stéphane BENAYOUN Ecole Centrale de Lyon Laboratoire LTDS 36 avenue Guy de Collongue 69134 Ecully CEDEX Tél : 04.72.18.64.37 stephane.benayoun@ec-lyon.fr
MEGA	<u>MÉCANIQUE, ÉNERGÉTIQUE, GÉNIE CIVIL, ACOUSTIQUE</u> http://edmega.universite-lyon.fr Sec. : Stéphanie CAUVIN Tél : 04.72.43.71.70 Bâtiment Direction INSA Lyon mega@insa-lyon.fr	M. Jocelyn BONJOUR INSA Lyon Laboratoire CETHIL Bâtiment Sadi-Carnot 9, rue de la Physique 69621 Villeurbanne CEDEX jocelyn.bonjour@insa-lyon.fr
ScSo	<u>ScSo*</u> https://edsciencessociales.universite-lyon.fr Sec. : Mélina FAVETON INSA : J.Y. TOUSSAINT Tél : 04.78.69.77.79 melina.faveton@univ-lyon2.fr	M. Christian MONTES Université Lumière Lyon 2 86 Rue Pasteur 69365 Lyon CEDEX 07 christian.montes@univ-lyon2.fr

*ScSo : Histoire, Géographie, Aménagement, Urbanisme, Archéologie, Science politique, Sociologie, Anthropologie

Résumé général

Avec le développement de la science et les progrès de la technologie médicale, l'espérance de vie moyenne s'est allongée. Dans le même temps, comme de plus en plus de femmes reçoivent une éducation et travaillent, le taux de fécondité diminue également d'année en année. Par conséquent, le vieillissement de la population est une tendance inévitable dans le monde. L'augmentation du nombre de personnes âgées, en plus d'avoir un impact sur la main-d'œuvre, entraînera également une lourde charge financière pour le gouvernement et les entreprises en termes d'assurance médicale. Elle est particulièrement importante en termes de dépenses médicales et de soins pour les maladies chroniques. L'une des maladies chroniques les plus connues, l'insuffisance rénale chronique (IRC), est confrontée à de graves difficultés de traitement. D'après la situation générale dans le monde, ce défi se manifeste principalement dans la prévention et le traitement de la maladie rénale chronique, avec les "trois points forts" que sont la prévalence élevée, le taux élevé de maladies cardiovasculaires combinées et la mortalité élevée, ainsi que la faible sensibilisation, les faibles taux de prévention et de traitement et la faible connaissance des maladies cardiovasculaires combinées, les "trois points faibles". Compte tenu de l'augmentation actuelle de l'incidence de l'insuffisance rénale chronique (IRC) dans le monde et du manque général de connaissances sur la prévention et le traitement de cette maladie, la Société internationale de néphrologie (ISN) et la Fédération internationale des fondations du rein (IFKF) ont proposé conjointement que le deuxième jeudi du mois de mars soit désigné comme Journée mondiale du rein à partir de 2006, afin de sensibiliser le public à l'IRC et aux maladies cardiovasculaires associées, et d'attirer l'attention sur les besoins mondiaux urgents en matière de détection précoce et de prévention de l'IRC.

Selon les estimations de l'ISN et de l'IFKF, les patients atteints d'IRC représentent un dixième de la population mondiale, soit plus de 500 millions de personnes, et la plupart d'entre eux n'ont pas bénéficié d'un diagnostic et d'un traitement en temps utile. La conséquence de la non-détection des patients atteints d'IRC est la perte de la fonction rénale, qui conduit à l'insuffisance rénale et à la nécessité d'une dialyse ou d'une transplantation. Bien que la dialyse et la transplantation puissent sauver la vie des patients et améliorer leurs qualités de vie, leurs familles et la société doivent supporter d'énormes dépenses médicales, indépendamment de la dialyse ou de la transplantation rénale. Aux États-Unis, le coût annuel de chaque patient en dialyse est de 65 000 dollars, et le coût annuel d'une transplantation rénale est de 40 000 dollars. Les coûts élevés de la dialyse proviennent principalement du maintien de la fonction de la fistule et de la réparation secondaire de la fistule dysfonctionnelle. L'objectif de recherche de ce projet de doctorat est d'aider les patients à augmenter le taux de maturité postopératoire de la fistule artérioveineuse radio-céphalique (FAVRC), l'accès vasculaire préféré dans la fistule, et de prolonger sa durée de vie afin de réduire les douleurs physiques et mentales et les charges économiques causées par le dysfonctionnement de la fistule.

Nous avons présenté de manière détaillée le contexte du sujet dans le premier chapitre. Nous

avons expliqué les méthodes de traitement standard des patients atteints d'insuffisance rénale terminale (IRT), présenté les types d'accès vasculaire couramment utilisés en dialyse et comparé leurs avantages et inconvénients. Nous avons ensuite présenté les méthodes cliniques couramment utilisées pour l'examen des fistules. En même temps, nous avons brièvement présenté la structure du sang et de la paroi vasculaire des artères et des veines utilisées pour la fistule. Nous avons analysé la norme de maturité de la FVA et la stimulation mécanique requise pour la maturité. Enfin, nous avons résumé les raisons de l'immaturité et du dysfonctionnement de la fistule artérioveineuse radio-céphalique (FAVRC).

Nous avons d'abord présenté les cinq paramètres géométriques (PGs) du FAVRC et les méthodes de création des modèles FAVRC utilisés dans notre recherche. Inspirés par la loi de Murry, nous avons optimisé les configurations FAVRC en réduisant la perte d'énergie dans le FAVRC, augmentant ainsi le taux de maturité. Nous avons créé un modèle théorique pour calculer le taux de perte d'énergie dans le FAVRC. Les résultats de la simulation ont été utilisés pour vérifier les résultats théoriques. Grâce à ce modèle théorique, nous avons analysé la relation entre la perte d'énergie dans le FAVRC et ses cinq PG. L'étude a révélé que l'artère radiale et la veine céphalique avec un grand diamètre et une courte distance devraient être sélectionnées, et qu'un grand angle d'anastomose devrait être utilisé pour la conception de l'anastomose afin de réduire la perte d'énergie dans le FAVRC. Parallèlement, l'analyse séparée de chaque paramètre géométrique révèle que le diamètre de la veine céphalique a l'impact le plus significatif sur la perte d'énergie dans le FAVRC, suivi de l'angle d'anastomose et de la distance du vaisseau, et que l'impact le plus négligeable est le diamètre de l'artère radiale et le diamètre de l'anastomose.

Ensuite, nous avons étudié la relation entre les distributions des contraintes de cisaillement de la paroi et l'angle anastomotique dans la FAVRC. Dans l'opération d'anastomose du FAVRC, les chirurgiens doivent concevoir le diamètre et l'angle de l'anastomose. Dans la recherche sur la perte d'énergie du FAVRC, il a été constaté que l'influence de l'angle anastomotique sur la perte d'énergie était beaucoup plus significative que le diamètre anastomotique. On peut donc en déduire que l'angle d'anastomose influence grandement la distribution hémodynamique dans le FAVRC. Nous avons donc créé cinq angles différents (30° , 45° , 60° , 75° et 90°) dans une fourchette de 0° à 90° . En effectuant des simulations CFD sur ces modèles, nous avons sélectionné l'angle optimal en comparant les distributions des contraintes de cisaillement de la paroi dans les modèles FAVRC avec différents angles. Nos analyses de l'angle anastomotique ont été réalisées dans deux ensembles de modèles. Le modèle non mature a simulé le FAVRC juste après l'anastomose, qui présentait les vaisseaux avec des flux sanguins normaux et des formes originales (les vaisseaux sanguins n'ont pas été remodelés). Le modèle mature simule l'état du flux sanguin dans le FAVRC mature, qui illustre le FAVRC qui répond aux exigences de la dialyse. Nous avons analysé les distributions de trois indicateurs (time-averaged wall shear stress (TAWSS), oscillatory shear index (OSI) et relative residence time (RRT)) pour déterminer les emplacements de la contrainte de cisaillement de paroi faible et oscillante, ainsi que leurs valeurs minimales et les zones de distribution à différents angles. En observant les comportements hémodynamiques (champs de vitesse, lignes de courant), les causes des contraintes de cisaillement faibles et oscillantes ont été analysées. Grâce à ces recherches, nous sommes parvenus aux conclusions suivantes :

- Peu importe les modèles non matures ou matures, le modèle à 30° reçoit les moindres stimulations de contraintes de cisaillement de paroi faibles et oscillantes, et les modèles à grand angle souffrent des plus grandes stimulations de contraintes de cisaillement de paroi faibles et oscillantes. Par conséquent, nous recommandons aux chirurgiens de choisir un angle anastomotique inférieur ou égal à 30° pour le FAVRC.
- Bien que les distributions hémodynamiques dans les modèles non matures et matures soient différentes, la tendance à l'évolution entre les distributions de la contrainte de cisaillement de la paroi et l'angle anastomotique est la même. Par conséquent, le modèle non mature peut pré-simuler le FAVRC pour aider le chirurgien à concevoir une fistule préopératoire plus raisonnable.
- Grâce à la comparaison des deux groupes de modèles, nous avons analysé les endroits propices à la sténose dans le FAVRC et la tendance du développement de la sténose pendant la maturation du FAVRC sous différents angles anastomotiques.

Finalement, nous avons fusionné les résultats précédents pour créer un modèle préopératoire personnalisé mécano-bio-fidèle du FAVRC (modèle PerMeBio du FAVRC). L'objectif de ce modèle est d'optimiser le FAVRC d'un point de vue mécanique et biologique pour aider le chirurgien à juger si les vaisseaux sanguins du patient peuvent être utilisés pour le FAVRC et créer un FAVRC adapté aux différents patients en fonction des paramètres de leurs vaisseaux sanguins. Nous avons utilisé ce modèle pour analyser cinq cas cliniques et avons d'abord vérifié son opérabilité.

L'optimisation de l'anastomose de la FAV est un sujet brûlant dans le domaine de la recherche biomécanique. La plupart des recherches sur les configurations d'anastomose FAV se sont concentrées sur le choix du diamètre des vaisseaux et des angles d'anastomose. Notre recherche a créé un nouveau modèle PerMeBio du FAVRC sous une nouvelle perspective (analyse de la perte d'énergie) qui peut être combiné avec les résultats de simulations numériques pour aider les chirurgiens à affiner leur diagnostic pour le choix des vaisseaux dans toute la mesure du possible tout en réduisant le risque de complications.

Contents

List of Figures	10
List of Tables	14
1 Medical Context and Problem Position	15
1.1 Background	16
1.2 Vascular access types	17
1.2.1 Central venous catheter	17
1.2.2 Arteriovenous VA	17
1.2.3 Clinical VA selections	18
1.3 Vascular examination	19
1.3.1 Vascular imaging methods	19
1.3.2 Doppler ultrasound examination	20
1.4 Characteristics of blood vessels used for fistulas	21
1.4.1 Blood flow	21
1.4.1.1 Blood components	21
1.4.1.2 Mechanical properties of blood flow	22
1.4.2 Histology of the vessel wall	24
1.5 AVF Maturation	26
1.5.1 AVF establishment and mature	26
1.5.2 Effects of hemodynamic flow in AVF maturation	28
1.6 AVF failure	30
1.6.1 Effects of disturbed flow	30
1.6.2 Early failure	32
1.6.2.1 Vein outward remodeling failure	32
1.6.2.2 Neointimal Hyperplasia	33
1.6.2.3 Early thrombosis	34
1.6.3 Late failure in the mature AVF	34
1.7 Research strategies	35
1.7.1 Current researches and limitations	36
1.7.2 Objectives and outlines	37
2 A theoretical model to optimize the RCAVF configuration	39
2.1 Introduction	40
2.2 RCAVF geometric parameters	40
2.3 Theoretical analysis	41
2.3.0.1 Energy loss rate in bending cephalic vein (B segment)	42
2.3.0.2 Energy loss rate at anastomosis	43
2.3.0.3 Total energy loss rate in RCAVF	45

2.4	Numerical models for RCAVF energy loss model verification	46
2.4.1	RCAVF 3D virtual model creation	46
2.4.2	Model validation	47
2.5	Results analysis	49
2.5.1	Theoretical model compared to numerical simulation	49
2.5.2	Relationship between energy loss rate and GPs	50
2.6	Discussions and conclusions	58
3	Numerical simulation to optimize the RCAVF configuration	59
3.1	Introduction	61
3.2	RCAVF physical modeling	62
3.2.1	Blood mechanical properties	62
3.2.2	Numerical model definitions	63
3.2.2.1	Computational fluid dynamics numerical models	63
3.2.2.2	Fluid-structure coupling numerical model	64
3.2.3	Mechanical properties of RCAVF walls tissue	65
3.3	Computational fluid dynamics simulation	67
3.3.1	The governing equations for fluid dynamics	67
3.3.2	Fluid domain discretization	70
3.3.3	Boundary condition	73
3.3.3.1	Flow rates measured by DUS images	75
3.3.3.2	Inlet velocity profile creations	76
3.3.4	Fluid simulation with Foam-extend	77
3.4	Fluid-structure interaction simulation	79
3.4.1	Fluid-structure coupling equations	79
3.4.1.1	fluid domain	79
3.4.1.2	Solid domain	81
3.4.2	Solid domain discretization	81
3.4.3	Boundary conditions	82
3.4.4	Fluid-structure interaction simulation in Foam-extend	82
3.5	Result analysis	84
3.5.1	Analytical indicators used in the result analysis	84
3.5.1.1	Hemodynamic analysis	84
3.5.1.2	Wall shear stress distributions	85
3.5.2	Comparison between Newtonian and non-Newtonian fluids	86
3.5.3	Comparison between CFD and FSI non-mature RCAVF models	89
3.5.4	RCAVF mature model verified by clinical imaging measurement	94
3.5.5	Analyzing the results of non-mature models	96
3.5.5.1	Hemodynamic flow in non-mature models	96
3.5.5.2	Wall shear stress distributions in non-mature models	99
3.5.6	Analyzing the results of mature models	104
3.5.6.1	Hemodynamic flow in mature models	104
3.5.6.2	Influence of distal artery inlet blood flow on recirculating region in mature models	107

3.5.6.3	Wall shear stress distributions in mature models	111
3.5.7	Discussions and Conclusions	116
4	Personalized mechano-bio-faithful RCAVF preoperative model	120
4.1	Introduction	121
4.2	Critical energy loss rate (CEL)	121
4.2.1	CEL definition	121
4.2.2	CEL to help for RCAVF anastomosis design	122
4.3	Personalized mechano-bio-faithful RCAVF preoperative model (PerMeBio-RCAVF model)	124
4.4	Clinical cases analyses	127
4.4.1	Clinical data acquisition	127
4.4.2	Clinical cases analyzed by PerMeBio-RCAVF model	129
4.5	Discussions and conclusions	132
5	Conclusions and perspectives	134
5.1	Conclusions	134
5.2	Perspectives	136
A	Matlab code of the Poiseuille flow adapted to a circular face	138
B	Setting up the numerical models with rigid walls in Foam-extend	140
C	Setting up the numerical models with fluid-structure coupling in Foam-extend	150
C.1	Fluid	150
C.2	Solid	152
	Bibliography	163

List of Figures

1.1	Flowchart of ESRD treatment options	16
1.2	central venous catheter (CVC)	17
1.3	arteriovenous graft (AVG)	17
1.4	AVF blood vessel anatomy	18
1.5	Doppler ultrasonography (The images were generated by Philips Affiniti 70 G. Images (a)-(c) are provided by Hospices civils de Lyon (HCL))	19
1.6	Digital subtraction angiography of the left forearm [1].	20
1.7	Postoperative observation of RCAVF using DUS	21
1.8	Composition of blood [2]	22
1.9	(a) Colorized scanning electron microscope (SEM) of normal erythrocytes with each side concave. X3000. (b) Diagram of an erythrocyte giving the cell's dimensions [2]	23
1.10	(a) In small vessels red blood cells also often stack up in aggregates called rouleaux. X250 [2]. (b) Red blood cell aggregates termed rouleaux, which can form linear or branched structures. The number of red blood cells in a rouleaux can vary from 2 to approximately 50. Red blood cells in the microcirculation typically traverse through capillaries within rouleaux structures [3]	23
1.11	(a) Blood and plasma shear stress according to the shear rate (b) Shape of the blood non-Newtonian viscosity curve as a function of the shear rate [4].	24
1.12	(a) Mean pressure in cardiovascular system[5](ART.: arterioles; CAP.: capillaries; VEN.: venules) (b) Structures of artery and vein (c) Average lumen diameters and wall thickness of vessels	24
1.13	Microscopic anatomy of arterial and venous walls [6]	25
1.14	Cross-section of human vessel	26
1.15	AVF creation (DV/DA: the distal vein/artery near the hand; PV/PA: the proximal artery near the heart; $Q_v/Q_a/Q_{da}/Q_{pa}$: blood flow in the vein/artery/DA/PA)	27
1.16	Fistula anastomosis surgery (a) Radial artery and cephalic vein before suture (b) Fistula anastomosis just after surgery (Intraoperative images, Hospices civils de Lyon)	27
1.17	Successful AVF maturation	28
1.18	Hemodynamic force load on endothelial cell surface (illustration adapted from servier medical art)	29
1.19	hemodynamic conditions and structural responses[7]	29
1.20	Disturbed flow in AVF	31
1.21	Morphological changes induced in a confluent EC mono-layer by exposure to disturbed flow[8]	31
1.22	AVF early failure	32
1.23	Neointimal hyperplasia ((a) and (b) adapted from servier medical art; (c) adapted from [9])	33
1.24	Early thrombosis ((a) adapted from servier medical art; (b) adapted from [10])	34

2.1	RCAVF geometric parameters	41
2.2	Blood flow in bending cephalic vein	42
2.3	Blood flow at anastomosis	43
2.4	3D simplified diagram of the anastomosis operation (Top is the original CV artery before being stretched (middle) to be linked to the RA (bottom))	44
2.5	Top view, 3D view, and front view of cephalic vein (CV) after stretching	45
2.6	RCAVF vascular segments	46
2.7	RCAVF 3D virtual model creation ($\theta=90^\circ$)	46
2.8	RCAVF simulation model	48
2.9	Comparison of numerical results and analytical results in 25 models	51
2.10	The relationship between energy loss rate (E_{avf}) and radial artery diameter (D_{ra})	53
2.11	The relationship between energy loss rate (E_{avf}) and radial artery diameter (D_{cv})	54
2.12	The relationship between energy loss rate (E_{avf}) and radial artery diameter (h)	55
2.13	The relationship between energy loss rate (E_{avf}) and radial artery diameter (D_a)	56
2.14	The relationship between energy loss (E_{avf}) and anastomotic angle (θ)	57
3.1	RCAVF numerical simulation process	61
3.2	Non-mature vs. mature models with θ equals 30°	64
3.3	RCAVF 3D virtual model with vessel wall ($\theta=90^\circ$)	65
3.4	The stress-strain relations of biological material and linearly elastic or Hookean material [11]	66
3.5	Bar graphs showing E_{inc} for the three groups (ESRD: end-stage renal disease; CT: normotensive control subjects; HT: patients with essential hypertension). [12]	66
3.6	The nine components of the stress tensor on a differential fluid volume [3] (for conserve angular momentum, only six tensors are independent)	68
3.7	The surface forces acting on a differential surface element expressed in terms of the stress tensor[13] (bold font represents vector)	69
3.8	Structural mesh and unstructured mesh	71
3.9	Mesh cell types	71
3.10	RCAVF blood fluid mesh by STAR-CCM+ 12.06.011 with $\theta = 90^\circ$ (250 977 cells)	72
3.11	Comparison of the WSS distribution of different mesh sizes at systole	73
3.12	RCAVF boundary conditions	74
3.13	(a) The flowrate waveform at the proximal radial artery inlet of non-mature models; (b) The flowrate waveform at the proximal radial artery inlet of mature models	75
3.14	Flow rates at distal radial artery inlet of two DUS imaging measurements (provided by Hospices civils de Lyon)	76
3.15	Hydrodynamic entry length in a circular pipe [14]	76
3.16	Separate the boundary points and inner points	77
3.17	Velocity profiles at proximal radial artery inlet	78
3.18	One-dimensional example of Lagrangian, Eulerian and ALE mesh and particle motion [15]	80
3.19	RCAVF FSI mesh by STAR-CCM+ 12.06.011 with $\theta = 90^\circ$ (144 504 cells in vessel wall)	81
3.20	FSI boundary conditions	82

3.21	Monolithic method	83
3.22	Partitioned method	83
3.23	Resolution process for a fluid-structure interaction problem with weak coupling and strong coupling using the partitioned method	84
3.24	Viscosity curves of Newtonian and non-Newtonian (Carreau model)	87
3.25	Definition of Carreau model parameters in Foam-extend	87
3.26	Comparison of velocity fields in different cross-sections of RCAVF during systole between Newtonian model and non-Newtonian model ($\theta = 90^\circ$)	87
3.27	The streamlines during systole in Newtonian and non-Newtonian models	88
3.28	Comparisons of WSS indicators between Newtonian model and non-Newtonian model ($\theta = 90^\circ$)	88
3.29	Displacement of the outer wall in non-mature model with $\theta = 90^\circ$ (Gray transparent blood vessels represent the blood vessel wall without deformation)	90
3.30	Displacement of a point at the bending venous segment during the third cardiac cycle	90
3.31	Comparison of velocity fields at systole and end-diastole between FSI and CFD models ($\theta = 90^\circ$)	91
3.32	Velocity profiles during systole in FSI and CFD models ($\theta = 90^\circ$)	92
3.33	The comparison of the mean velocity over the cross sections between FSI and CFD models ($\theta = 90^\circ$)	92
3.34	WSS indicators in FSI model	94
3.35	Comparison between the numerical result of RCAVF virtuel model and DUS measurement	95
3.36	Velocity fields in non-mature models	97
3.37	Streamlines in non-mature models ($\theta = 30^\circ$ and $\theta = 90^\circ$)	98
3.38	The cause of recirculating eddy [16]	99
3.39	WSS distributions in non-mature models at systole and end-diastole (each set of figures shows respectively the left, main and right views of RCAVF)	100
3.40	TAWSS distributions in non-mature models	101
3.41	OSI distributions in non-mature models	103
3.42	RRT distributions in non-mature models	103
3.43	Velocity fields in mature models	105
3.44	Streamlines in mature models with small anastomotic angles ($\theta = 30^\circ, 45^\circ$)	106
3.45	Streamlines in mature models with larger anastomotic angles ($\theta = 60^\circ, 75^\circ, 90^\circ$)	106
3.46	Streamlines of eddies in small- θ models	107
3.47	Streamlines of eddies in large- θ models	108
3.48	Streamlines in mature model with low flow rate from DA inlet ($\theta = 60^\circ$)	108
3.49	Streamlines of eddies in mature model with low flow rate from DA inlet ($\theta = 60^\circ$)	108
3.50	WSS distributions in mature models with different flow rates at DA inlet ($\theta = 60^\circ$)	109
3.51	TAWSS, OSI and RRT distributions in mature models with different flow rates at DA inlet ($\theta = 60^\circ$)	110
3.52	WSS distributions in mature models	111
3.53	TAWSS distributions in mature models	112
3.54	OSI distributions in mature models	114

3.55	The distributions of RRT higher than 1 in mature models	115
3.56	The classifications of stenosis-prone locations in RCAVF (a) The stenosis-prone locations in non-mature RCAVF (b) The stenosis-prone locations in non-mature RCAVF when θ is less than or equals 30° (c) The stenosis-prone locations in mature RCAVF when θ is around 45° (d) The stenosis-prone locations in mature RCAVF when θ is larger than or equals 60°	117
3.57	The three specific sites of stenosis in mature RCAVF identified by a clinical study [17]	118
4.1	The relationship between E_{avf} and θ regarding the critical energy loss	123
4.2	Personalized mechano-bio-faithful RCAVF preoperative model (PerMeBio-RCAVF model)	125
4.3	Clinical information for 5 ESRD patients using RCAVF for dialysis (data provided by Hospices civils de Lyon)	128
4.4	The analysis of energy loss rate for patient No.1	130
4.5	The analysis of energy loss rate for patient No.2	131
4.6	The analysis of energy loss rate for patient No.4	132
5.1	TRAIFAV (Traitement des fistule artério-veineuses) project	136

List of Tables

2.1	The research ranges of 5 GPs	47
2.2	Geometric parameters of 25 RCAVF 3D models	48
2.3	Relative difference between numerical results and analytical results	49
3.1	Re ranges in the numerical models	63
3.2	Geometric parameters in CFD models	64
3.3	The specific form of each symbol in the general governing equation	70
3.4	Mesh details for mesh convergence analysis	73
3.5	Mesh convergence analysis	74
3.6	Parameters of Carreau model [18]	86
3.7	Flow properties comparisons between Newtonian and non-Newtonian models	89
3.8	Comparison of cross-section areas at systole between FSI and CFD models ($\theta = 90^\circ$)	93
3.9	Comparison of WSS indicators between FSI and CFD models ($\theta = 90^\circ$)	93
3.10	The GPs in a patient-specific RCAVF mature model	95
3.11	LTAWSS in non-mature models	102
3.12	OSI in non-mature models	102
3.13	RRT in non-mature models	104
3.14	The LTAWSS in mature models	113
3.15	RRT in mature models	116
4.1	Definition of CEL	122
4.2	Recommended level for anastomosis design	122

Medical Context and Problem Position

This chapter describes the background of end-stage renal disease (ESRD), the vessel access (VA) types used in hemodialysis for ESRD treatment, the preoperative preparation for AVF anastomosis, the method of intraoperative anastomosis, and the maturity of postoperative AVF. This Ph.D. project focuses on the research of the preferred vascular access RCAVF, therefore, in the second half of this chapter, the causes of RCAVF dysfunction are introduced. Finally, the limitations of the current research and the research goals of this topic are discussed.

Contents

1.1	Background	16
1.2	Vascular access types	17
1.2.1	Central venous catheter	17
1.2.2	Arteriovenous VA	17
1.2.3	Clinical VA selections	18
1.3	Vascular examination	19
1.3.1	Vascular imaging methods	19
1.3.2	Doppler ultrasound examination	20
1.4	Characteristics of blood vessels used for fistulas	21
1.4.1	Blood flow	21
1.4.1.1	Blood components	21
1.4.1.2	Mechanical properties of blood flow	22
1.4.2	Histology of the vessel wall	24
1.5	AVF Maturation	26
1.5.1	AVF establishment and mature	26
1.5.2	Effects of hemodynamic flow in AVF maturation	28
1.6	AVF failure	30
1.6.1	Effects of disturbed flow	30
1.6.2	Early failure	32
1.6.2.1	Vein outward remodeling failure	32
1.6.2.2	Neointimal Hyperplasia	33
1.6.2.3	Early thrombosis	34
1.6.3	Late failure in the mature AVF	34
1.7	Research strategies	35
1.7.1	Current researches and limitations	36
1.7.2	Objectives and outlines	37

1.1 Background

Chronic kidney disease (CKD) is one of the world's major chronic diseases, with a high incidence and great harm. End-stage renal disease (ESRD), also known as the late stage of kidney disease, is when CKD develops to the late stage. CKD will gradually impair renal function, and the kidney will be severely damaged at the end stage, which cannot meet the needs of the human body. Under normal conditions, the kidneys can filter the metabolic waste and excess fluid in the blood, and these extra things will be excreted from the body with urine. Once the kidney loses its filtering function, excess fluid, electrolytes, and waste accumulate in the human body, endangering human health and even life. If it develops into ESRD, medical intervention is needed to be taken into consideration to maintain life.

According to the 2018 Clinical Practice Guidelines of the European Society for Vascular Surgery (ESVS) [19], ESRD treatments (fig.1.1) are divided into three categories: kidney transplantation, peritoneal dialysis, and hemodialysis through a vascular access (VA).

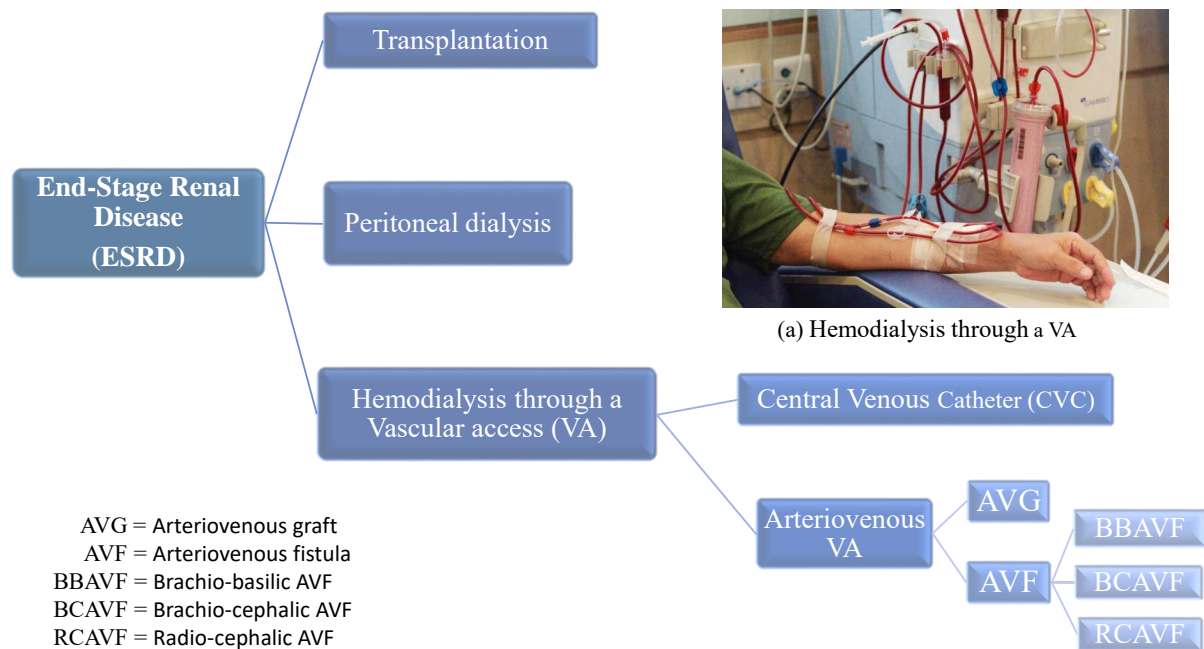


Figure 1.1: Flowchart of ESRD treatment options

For ESRD patients, timely and effective dialysis treatment (fig.1.1(a)) is the best and the most comment way to maintain their lives which can be achieved by two methods: central venous catheter (CVC) and arteriovenous VA. Most patients need to undergo dialysis treatment three times a week, each for about 4 hours. People who choose to dialysis at home may need to dialysis more frequently, 4-7 times a week, and each time is relatively short. The quality is related to the duration of dialysis and depends on the patient's vascular system's reliability. Dialysis VA must be reliable, uncomplicated access that can introduce and return blood well and quickly. Therefore, a

superficial, easy-to-puncture, and high-flow blood vessel is the key to ensuring these requirements. The superficial veins in the human body are easy to puncture whereas have a low flow. While the arteries have a large flow, however, the locations are deep and are not easy to stab repeatedly. For these reasons, it is necessary to connect the artery and the superficial vein to build a VA that meets dialysis requirements.

1.2 Vascular access types

1.2.1 Central venous catheter

Central venous catheter (CVC) places a catheter in a large vein for temporary or long-term hemodialysis (shown in fig.1.2). Usually, it preferably inserted into the superior vena cava [20]. CVC does not have a mature period and can be used at any time to instantly correct metabolic disorders for patients with acute renal failure quickly. It is a VA choice when urgent or emergency dialysis is requested or when arteriovenous VA becomes dysfunctional. However, its disadvantages are also very prominent, such as high infection rate, high thrombosis rate, long dialysis time, inappropriate use, waste of venous resources, etc. Therefore, it is not recommended as a standard dialysis method for ESRD patients.

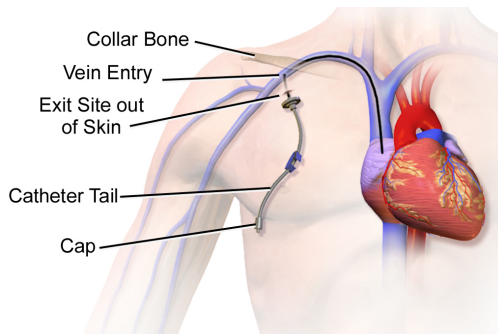


Figure 1.2: central venous catheter (CVC)

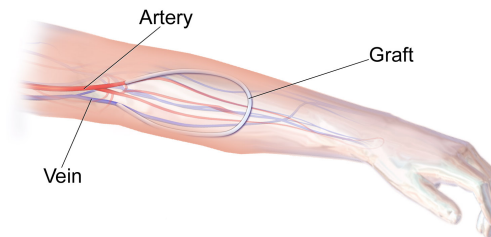


Figure 1.3: arteriovenous graft (AVG)

1.2.2 Arteriovenous VA

Arteriovenous VA's creation allows the blood flow in the artery to bypass the capillary's distal resistance and flow directly into the vein from a parallel, fixed, low-resistance return vessel to the heart. Due to the decrease of vascular resistance, the arterial blood flow increases gradually, thereby forming a VA that meets the requirements of dialysis[21]. Arteriovenous VA can be divided into heterologous VA and autologous VA. Heterologous VA is called arteriovenous graft (AVG), which uses a graft to establish a VA that satisfies the standards of hemodialysis. Autologous VA uses the patient's native blood vessels, which is called arteriovenous fistula (AVF).

- Arteriovenous graft (AVG)

AVG access is usually made of synthetic polymer or bioprosthesis, which connects the artery

and the vein with a conduit. It can be constructed as a straight graft or a looped graft (fig.1.3) and be situated on the upper arm or the forearm.

- *Arteriovenous fistula (AVF)*

AVF uses native vessels and is developed to fit with patient anatomic and physiologic characteristics. Briefly, it can be divided into two types according to its anastomotic position (fig.1.4):

- (a) Wrist AVF: Radio—Cephalic arteriovenous fistula (RCAVF)(fig.1.4(b));
- (b) Elbow AVF: Brachio—Cephalic arteriovenous fistula (BCAVF)(fig.1.4(c)),
Brachio—Basilic arteriovenous fistula (BBAVF)(fig.1.4(d)).

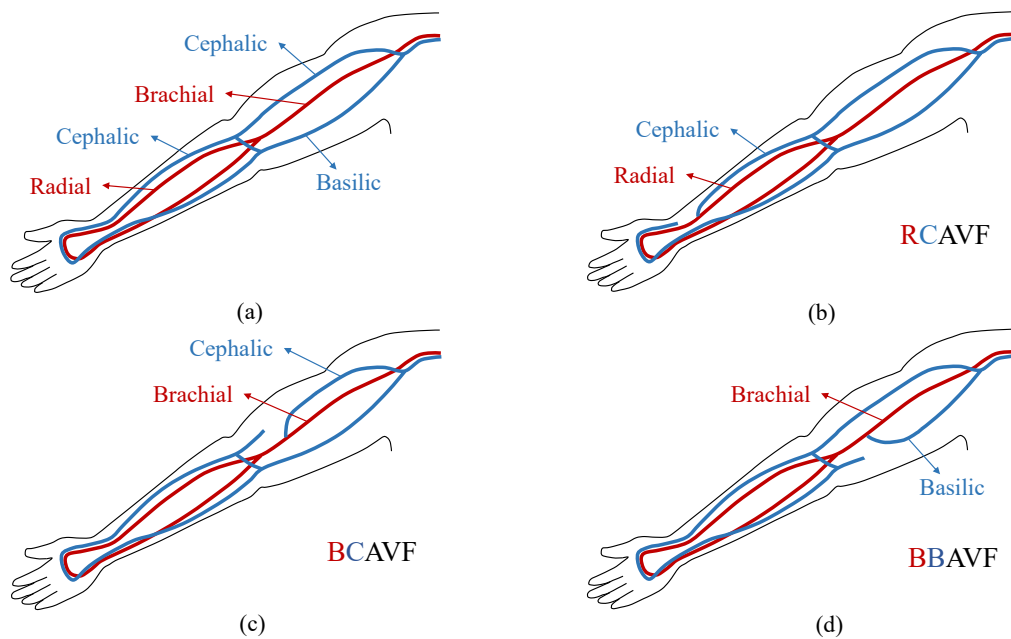


Figure 1.4: AVF blood vessel anatomy

1.2.3 Clinical VA selections

The VA determination needs to be combined with ESRD patient's specific conditions, such as gender, age, blood vessel anatomical variance, comorbidities (such as diabetes, hypertension, ischemic heart disease, etc). In most cases, native AVF is the preferred VA strongly recommended by practice guidelines (such as kidney disease outcomes quality initiative (KDOQI) clinical practice guideline for vascular[22]). It has the advantages of longer survival patency, fewer complications, and lower risk of infection, which make it have lower morbidity and mortality and could reduce patient's financial burden. The average AVF's service life is usually 3-10 years. 78% of French dialysis patients choose to use native AVF. In Europe, the Percentage of using AVF is generally similar, varying between 70 and 85% for dialysis (data provided by Hospices Civils de Lyon). If the ESRD patient is not a suitable AVF candidate (such as thin vessels, vein stenosis, vessel lesions, etc), the AVG can be considered as the second VA option. AVG is easier to operate and construct,

whereas, its average service life is only 1-4 years. The intervention rate to keep VA patency is 3-10 times higher with AVG than AVF[20]. As for CVC, because of its higher risk of mortality, fatal infection, and cardiovascular events than arteriovenous VA [23], it is the final choice for ESRD patients. In the common situation, CVC will not take into consideration until AVF or AVG fails. Nonetheless, in some particular cases, such as acute renal failure, acute transplant rejection or other complications requiring dialysis, CVC can instantly correct metabolic disorders.

The European Society for Vascular Surgery (ESVS) [19] recommends that the AVF selection strategy is: upper body first, then lower body; distal vessels first, then proximal vessels; non-dominant side first, then dominant side. Compared with wrist AVF, elbow AVFs (BBAVF, BCAVF) make the arm's appearance looks better after anastomosis, however, there are more postoperative complications: swelling of the arm, vascular stenosis, and a higher probability of high-flow. When fistula successfully matured, RCAVF can function for years with minimal complications, revisions, and hospital admissions. It is apt to create and retains more proximal veins than other VA. For these reasons, RCAVF at the level of wrist (fig.1.4(b)) is the first choice of native AVF[19] and it is also our main research object VA. However, with the low blood flow at the forearm, RCAVF can easily cause an early failure, which causes RCAVF to have higher requirements for blood vessels' choice and the anastomosis design.

1.3 Vascular examination

1.3.1 Vascular imaging methods

Vascular imaging plays a significant role in the selection of VA and post-operative observation. The usual imaging methods include Doppler ultrasound (DUS), Digital subtraction angiography (DSA), Computed tomography angiography (CTA), and Magnetic resonance angiography (MRA) [19].

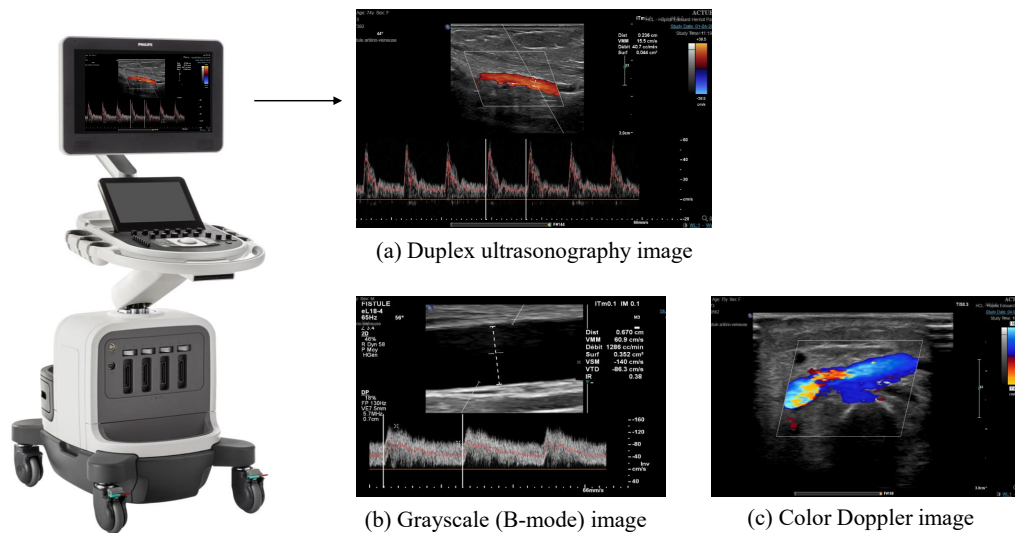


Figure 1.5: Doppler ultrasonography (The images were generated by Philips Affiniti 70 G. Images (a)-(c) are provided by Hospices civils de Lyon (HCL))

DUS (fig.1.5) can safely and non-invasively assess the anatomy and function of blood vessels. Therefore, it is currently the standard of practice for preoperative vessel mapping for access planning [24]. Using DUS to evaluate the vascular diameter, wall characteristics, and hemodynamic behavior can increase the fistula maturity rate. Although conventional angiography is still the gold standard for evaluating central veins, it provides limited information. It can incur adverse effects on patients due to its invasiveness and the use of contrasts [24]. The iodinated contrast agent used by DSA (fig.1.6) can cause further deterioration of residual renal function [19]. MRA can accurately detect upper extremity arterial and venous stenosis and occlusion before surgery [25]. However, contrast-enhanced magnetic resonance angiography (CE-MRA) is not recommended because the use of gadolinium may cause nephrogenic systemic fibrosis, especially in CKD patients [26]. CTA requires the use of iodinated contrast media and radiation. It is recommended when no equivalent technology is available [19].

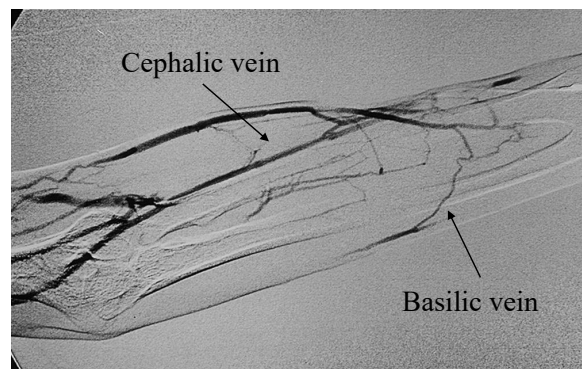


Figure 1.6: Digital subtraction angiography of the left forearm [1].

1.3.2 Doppler ultrasound examination

Doppler ultrasonography images (fig.1.5(a)) are generally used Color Doppler images (fig.1.5(c)) combined with gray-scale (B-mode) images (fig.1.5(b)) to display, allowing for simultaneous visualization of the anatomy of the area. Brightness-mode ultrasound is referred to as B-mode ultrasound. It refers to using an ultrasonic probe to transmit ultrasonic waves to an object, record the echo, and process the echo to form a gray-scale image to reflect the internal structure of the object. Doctors often use it to observe the anatomy of blood vessels, analyze the geometry of the vessel wall and find the location of stenosis. Color Doppler ultrasound is more helpful to assess the state of blood vessels and the cardiac circulatory system. The computer converts the received data into colors, making it easier for doctors to see the speed and blood direction. Objects moving towards the detector (sensor) are red, while objects far away from the detector are blue. The flow speed is expressed in red or blue, with lighter colors indicating higher speeds and darker colors indicating lower speeds.

DUS plays an essential role in selecting VA and provides critical information for AVF creation, such as the diameter of blood vessels and whether there are lesions. In a randomized trial, a primary failure rate of 25% without pre-operative DUS was observed compared to a failure rate of 6%

with DUS [27]. DUS is a cost-effective technique for evaluating VA maturation, surveillance, and complications at the same time. For patients using RCAVF, doctors will evaluate the performance of their fistula in the following ways:

1. Measure the brachial artery blood flow at the upper arm (fig.1.7), where the blood flow is approximately equal to the fistula blood flow at the vein outlet. Through this measurement, it can be judged whether the fistula is mature.
2. Check the vessel condition from the brachial artery to the anastomosis, focusing on observing the vessel shape near the anastomosis. Determine whether there is stenosis by measuring the blood velocity and the vessel diameter at the narrow part.

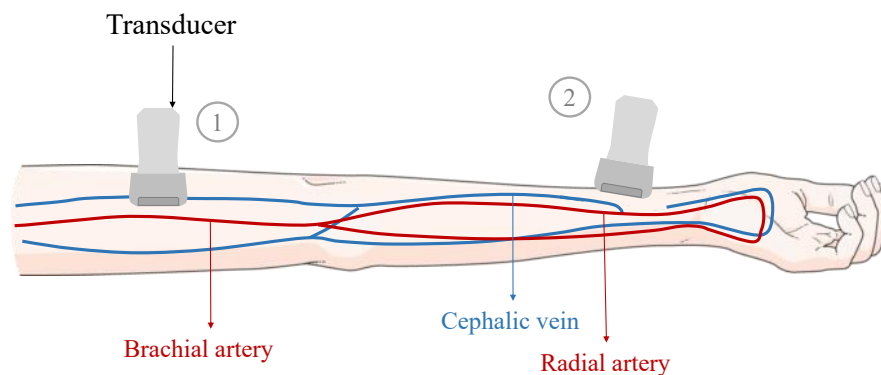


Figure 1.7: Postoperative observation of RCAVF using DUS

1.4 Characteristics of blood vessels used for fistulas

1.4.1 Blood flow

1.4.1.1 Blood components

Blood is a sticky fluid that flows in a regular unidirectional movement within the closed circulatory system. It accounts for approximately 8% of body weight [28]. Propelled mainly by rhythmic contractions of the heart, about five liters of blood in an average adult moves unidirectionally within the closed circulatory system. Blood is used to transport gases, nutrients, waste products, processed and regulatory molecules, etc. It can help regular the pH and osmosis of the human body and maintain body temperature.

Blood is made up of two parts: plasma and blood cells (formed elements). It is a specialized connective tissue in which cells are suspended in fluid extracellular material called plasma. The so-called formed elements circulating in the plasma are erythrocytes (red blood cells), leukocytes (white blood cells) and platelets [2]. With the separation of blood (fig.1.8), it can be divided by three layer:

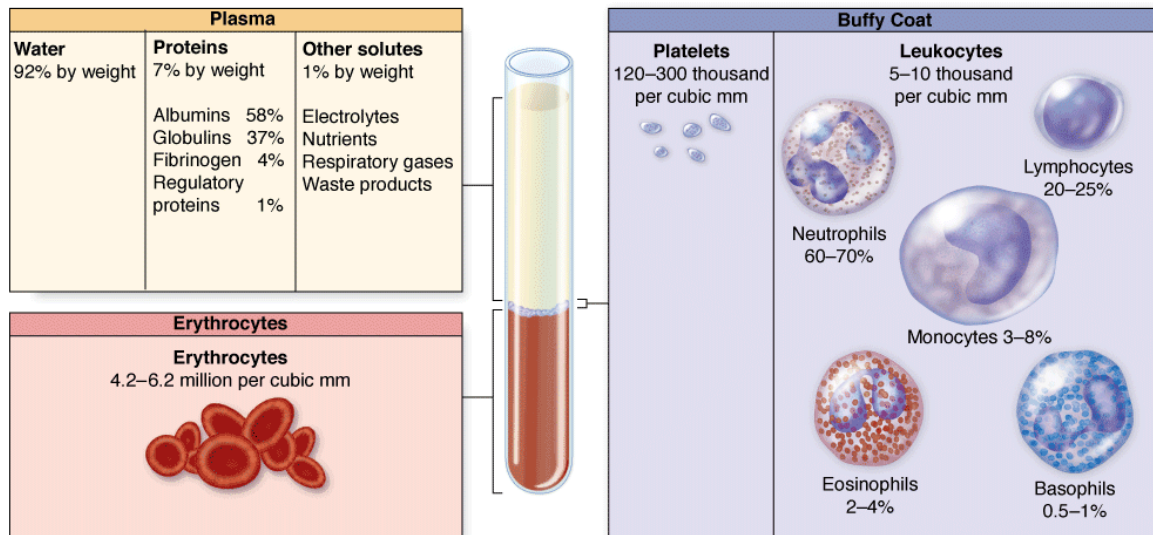


Figure 1.8: Composition of blood [2]

- *The top layer*

The top layer is plasma, a pale yellow fluid, mainly composed of water (92% by weight). It also contains dissolved proteins and other solutes. Normally, plasma constitutes 55% of blood flow volume [3].

- *The middle layer*

The middle layer is the buffy coat (fig.1.8), it composed of platelets and leukocytes, and only accounts for 1% of blood flow volume. Leukocytes protect us against microorganisms and remove dead cells and debris. Platelets promote blood clotting and help repair minor tears or leaks in the walls of blood vessels, preventing loss of blood [2].

- *The bottom layer*

The bottom layer is erythrocytes (fig.1.8), which are also called red blood cells (RBCs). The volume percentage of RBCs is hematocrit. It normally constitutes 45% of blood flow volume and 95% of formed elements [3]. RBCs are flexible biconcave disks (fig.1.9(a)). They are approximately $7.5 \mu\text{m}$ in diameter (fig.1.9(b)). Compared to the human body, it is very small, but its diameter is about the same level as some capillaries.

1.4.1.2 Mechanical properties of blood flow

The blood mechanical properties should be studied by considering a fluid containing a suspension of particles. Plasma, which consists mostly of water, behaves as a Newtonian fluid [29] (the shear stress is proportional to the shear rate and the viscosity is the constant of proportionality) (fig.1.11(a)). However, the RBCs are small semisolid particles. They increase the blood viscosity and make the whole blood has complex mechanical properties which become particularly significant when the

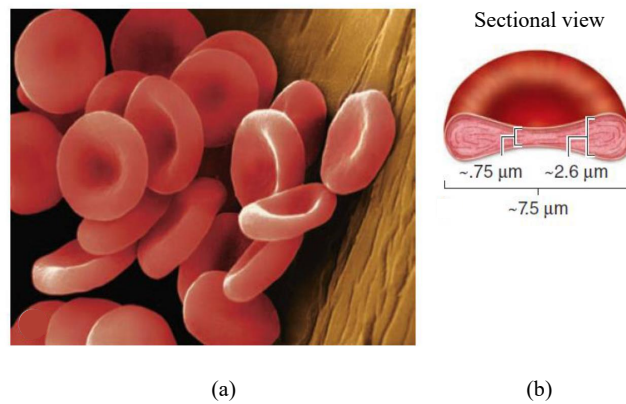


Figure 1.9: (a) Colorized scanning electron microscope (SEM) of normal erythrocytes with each side concave. X3000. (b) Diagram of an erythrocyte giving the cell's dimensions [2]

particles size is much larger, or at least comparable, with the lumen size (fig.1.10). For this reason, general blood has higher viscosity (shear thinning viscosity) than plasma (fig.1.11(a)), and when the hematocrit rises, the viscosity of the suspension increases and the non-Newtonian behaviour of blood becomes more relevant, in particular at very low shear rates [30]. In this condition, the erythrocytes have the ability to form a primary aggregate structure of rod shaped stacks of individual cells called rouleaux (fig.1.10), that align to each other and form a secondary structure consisting of branched three-dimensional (3D) aggregates [31] (fig.1.11(b)). Therefore, the non-Newtonian characteristics of blood happens more evident in small size vessels (less than 1 mm) [30]. However, in most parts of the arterial system, blood flow is Newtonian in normal physiological conditions [30].

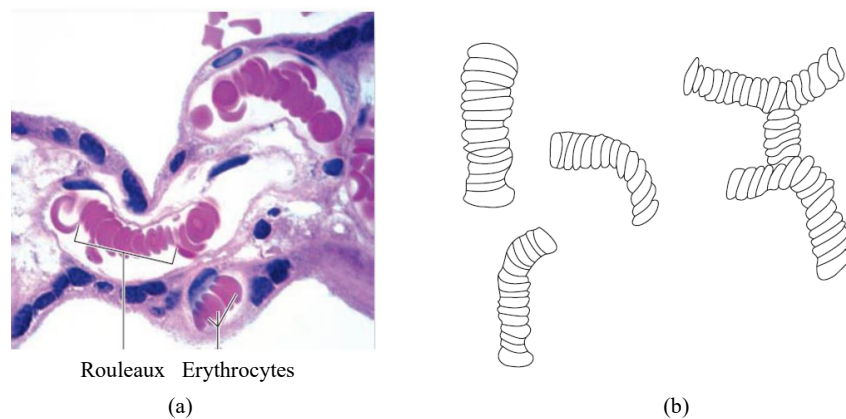


Figure 1.10: (a) In small vessels red blood cells also often stack up in aggregates called rouleaux. X250 [2]. (b) Red blood cell aggregates termed rouleaux, which can form linear or branched structures. The number of red blood cells in a rouleaux can vary from 2 to approximately 50. Red blood cells in the microcirculation typically traverse through capillaries within rouleaux structures [3]

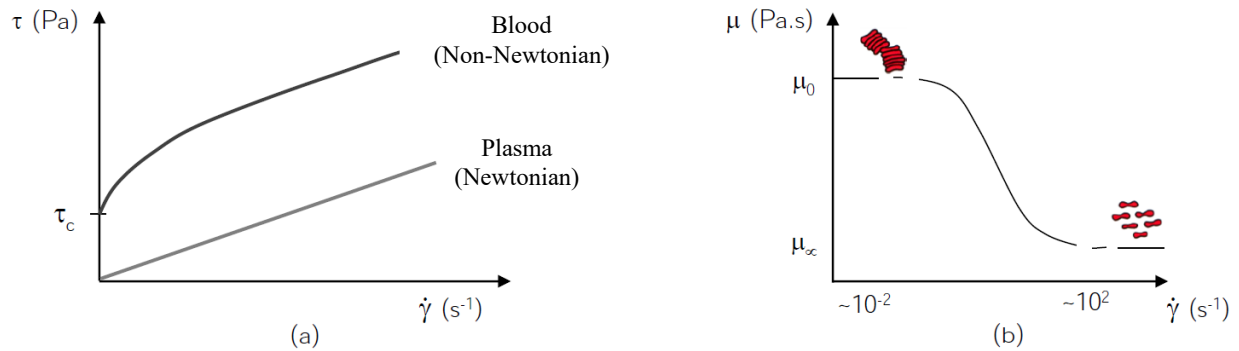


Figure 1.11: (a) Blood and plasma shear stress according to the shear rate (b) Shape of the blood non-Newtonian viscosity curve as a function of the shear rate [4].

1.4.2 Histology of the vessel wall

The mean pressure changing in the cardiovascular system illustrated in fig.1.12(a). The lumen diameters and wall thickness of arteries and veins are different due to the changing pressure [32] (fig.1.12(c)). In average, the human vein is with 5mm diameter and 0.5mm thickness compared with the artery in 4mm diameter and 1mm thickness [33]. Under high pressure, the arteries and small arterioles have thick wall and they are circular in profile (fig.1.12(b)). Once the blood gets into the capillary bed and beyond, the pressure becomes low. In the veins, the lumens collapse down (fig.1.12(b)) and open up and transmits the blood forward when it is needed to return it back to the heart. The venous lumen is usually larger relative to the wall thickness (fig.1.12(c)).

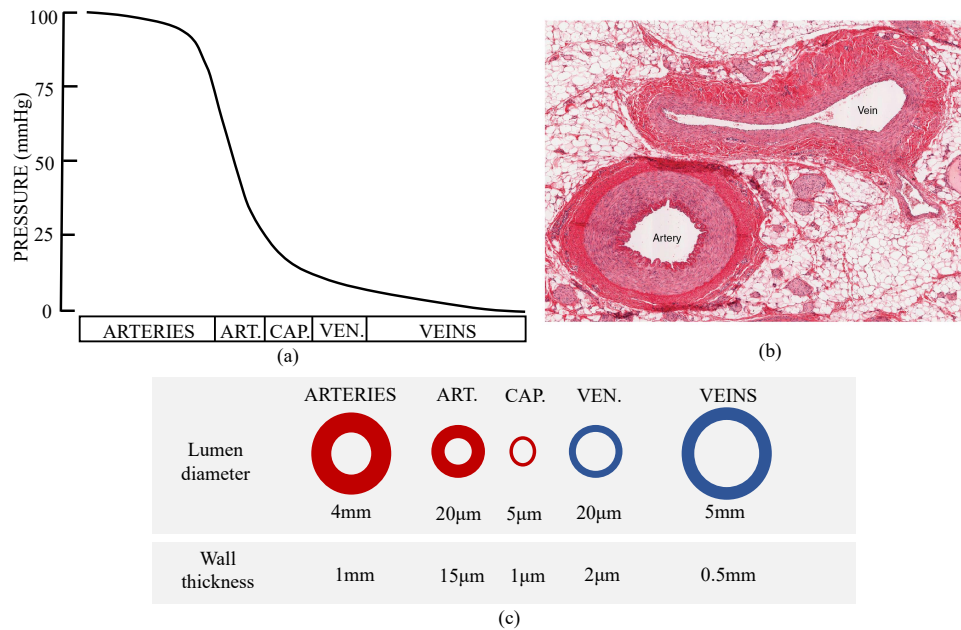


Figure 1.12: (a) Mean pressure in cardiovascular system[5](ART.: arterioles; CAP.: capillaries; VEN.: venules) (b) Structures of artery and vein (c) Average lumen diameters and wall thickness of vessels

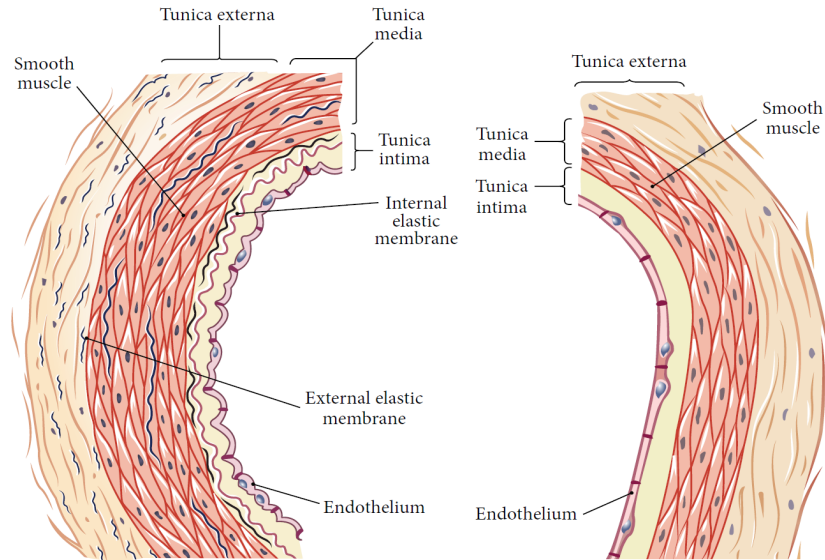


Figure 1.13: Microscopic anatomy of arterial and venous walls [6]

The blood vessel wall normally is composed of three layers (fig.1.13):

- *Tunica intima*

Tunica intima is made up of the single layers of endothelium, sub-endothelium and internal elastic membrane (it usually exists inside the large arteries). The endothelium is made up of numerous endothelial cells (ECs) which is directly in contact with the blood. The ECs have a number of functions including the absorption of nutrients and oxygen from the blood and disposal of waste into the blood.

- *Tunica media*

Tunica media is the middle region which consists of smooth muscle, collagen, and minimal amounts of elastic tissues (collagen). The smooth muscle tissue is regulated by the nerve fibers of the autonomic nervous system which make this layer contractile and can significantly change to control the lumen dimension. The collagen strengthens the blood vessel. And the elastic tissue allows some aspect of recoil or stretching. this layer plays an essential role in blood flow and blood pressure.

- *Tunica externa*

Tunica externa is the outside layer of vessel wall, it is also called tunica adventitia. It consists of connective tissue (collagen fibers). It is an important layer to strengthen the whole blood vessel. Therefore, the vessel does not rupture under the blood pressure. In the meantime, it blend the vessel with surrounding tissues. Hence from the junction between this layer and surrounding connective tissues is often hard to find. From the cross-sections of artery and vein (fig.1.14) it is difficult to find a clear vessel boundary.

From the microscopic anatomy of arterial and venous walls (fig.1.13), they both have three layers, however, to follow the different vessel functions, the ratio of the thickness of three layers varies between different blood vessels. In order to transport blood in a high-pressure environment, arteries

must have strong muscle walls. The cross-section of a human vessels (fig.1.12(b)) is stained to show that arterial tunics media is thicker than venous. The arteries invest in additional smooth muscle tissue, and have the thickest tunica media of any blood vessel. Therefore, they are able to expand and recoil with every heartbeat. The veins carry blood in a low-pressure environment. The requirements for the strength of the vessel wall are relatively small. Sometimes they are merely storing blood and then return the blood to the heart. Therefore, compared with arteries, veins have thinner walls and relatively larger lumens.

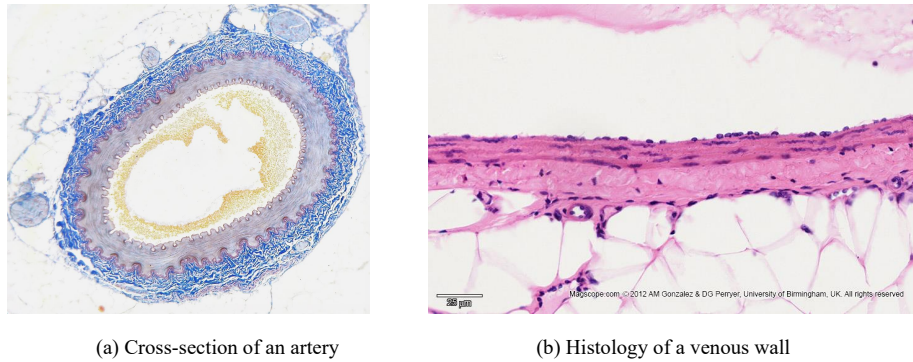


Figure 1.14: Cross-section of human vessel

1.5 AVF Maturation

1.5.1 AVF establishment and mature

After the surgeon completes the patient's physical assessment, based on observing the blood vessels with the help of medical images (fig.1.5), the patient's personal anastomosis plan will be formulated by surgeon's own surgery experiences. In this preoperative plan, the type and the location of AVF need to be chosen (forearm RCAVF (fig.1.4(b)) is usually preferred), and the fistula configuration needs to be designed. During the operation, the vein is cut along a pre-designed anastomosis angle, and the distal vein DV needs to be ligated (fig.1.15(b)). Simultaneously, the artery is cut along the axial direction with the planned diameter, and finally, the vein and the artery are sutured to form the AVF vascular access (fig.1.15(c)). Figure 1.16 (given by Hospices Civils de Lyon) shows the actual surgical anastomosis process of a patient using RCAVF.

The average blood flow Q_a of the radial artery is usually less than 25ml/min in the resting state [21]. After the RCAVF creation, the blood flow Q_{pa} in the proximal artery PA will bypass the distal resistance generated by the capillaries and flow directly into the vein through the anastomosis. Due to the anastomosis establishment, the blood flow Q_{da} in the distal artery DA will change the direction during the fistula maturation and flow into the vein together with Q_{pa} (fig.1.15(c)). After the anastomosis, the arterial flowrate will continue to increase. To adapt to the high flow and the high blood pressure, the vein has to remodeling and augmenting the wall thickness to protect the vein. Therefore, the vein becomes arterialized (fig.1.17). Due to the substantial increase in blood flow, the arteries will also produce this change at the same time. This process of vein and artery

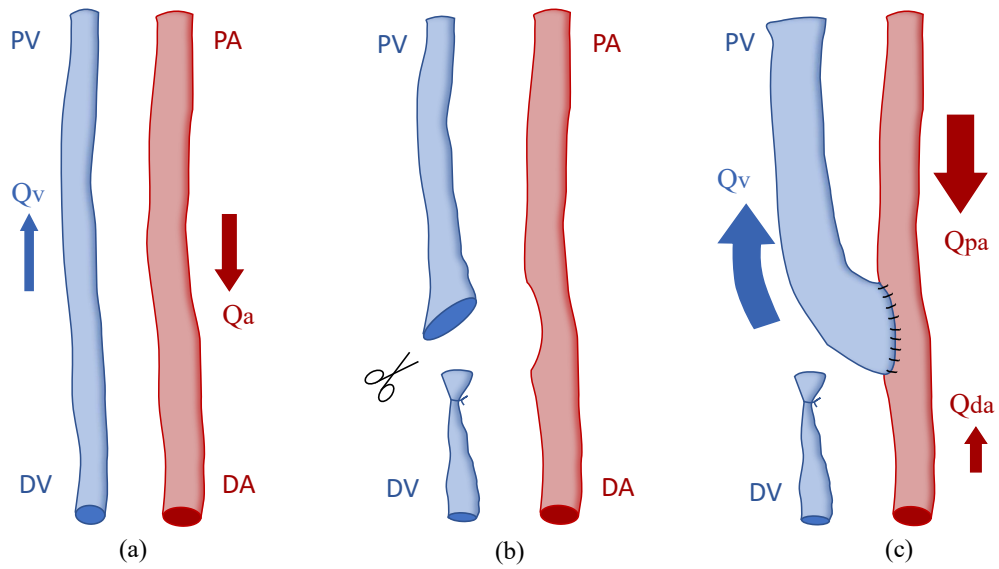


Figure 1.15: AVF creation (DV/DA: the distal vein/artery near the hand; PV/PA: the proximal artery near the heart; $Q_v/Q_a/Q_{da}/Q_{pa}$: blood flow in the vein/artery/DA/PA)

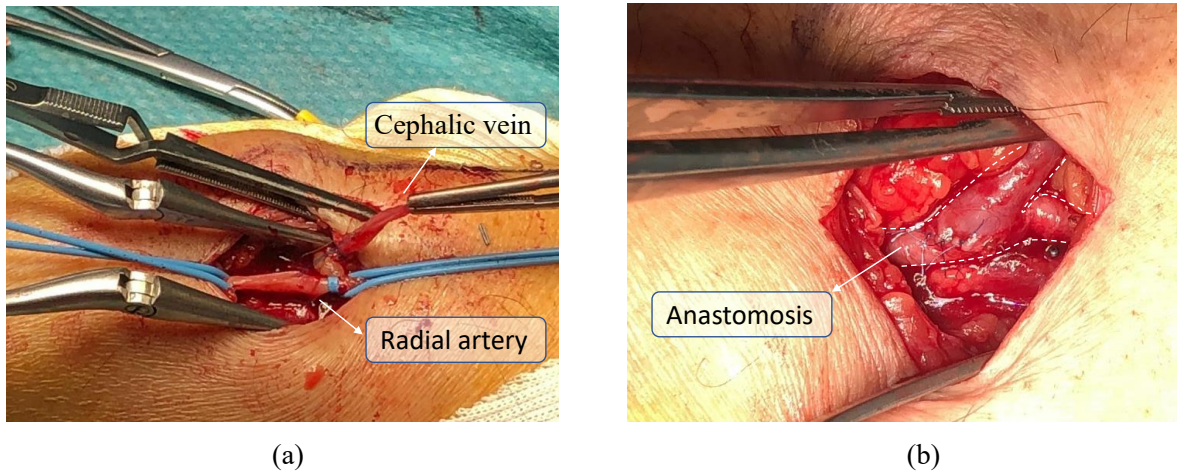


Figure 1.16: Fistula anastomosis surgery (a) Radial artery and cephalic vein before suture (b) Fistula anastomosis just after surgery (Intraoperative images, Hospices civils de Lyon)

changes is called fistula maturation. After one week, the blood flowrate in AVF will increase to about 540 ml/min and will reach 600-1200 ml/min around one month in a well-developed fistula at the end [20].

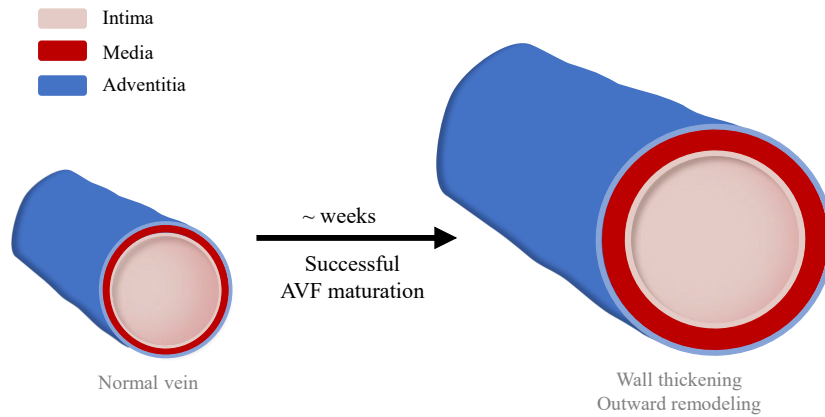


Figure 1.17: Successful AVF maturation

The 2019 Kidney Disease Outcomes Quality Initiative (KDOQI) clinical practice guideline for vascular access propose [22]: a mature fistula must have all of the following characteristics, which can be referred to as the 6s rule: blood flow need to be greater than 600 ml/min to support dialysis; Mature fistula diameter needs to be greater than 6 mm with precise edges, and the location is convenient for repeated puncture; depth of fistula is about 0.6 cm (ideally, 0.5 to 1.0 cm from the skin surface).

1.5.2 Effects of hemodynamic flow in AVF maturation

Hemodynamic flow plays a fundamental and essential roles in regulating vascular remodeling. With the AVF establishment, the hemodynamic forces generated by the briskly increasing blood flow produce continuous mechanical stimulations to the vessel wall. These stimulations include the friction force (high wall shear stress τ_h) between the high-speed blood flow and the vessel wall and the high hemodynamic pressure which increases the transmural pressure to the vessel wall (circumferential stress σ_θ and axial stress σ_z)(fig.1.18). At the macro level, blood flow regulates the diameter of blood vessels through changes in wall shear stress (τ_h), while high blood pressure regulates the thickness of vessel walls through its influence on wall tension (σ_θ, σ_z)(fig.1.19).

In the human body, the magnitude of the shear force in the venous system is from 1 to 6 dyn/cm^2 (0.1 to 0.6 Pa), and it is between 10 and 70 dyn/cm^2 (1 to 7 Pa) in the arterial system [8]. With the creation of AVF, the friction force acting parallel to the vascular surface will be much higher than the average level. The vessels respond to the presence of high wall shear stress by expanding outwards [34]. Research has shown that increased blood pressure also affects the dimensions and characteristics of blood vessel walls [34]. The high blood pressure increases the transmural pressure with the high flow appearance, causing the blood vessel wall to be stimulated

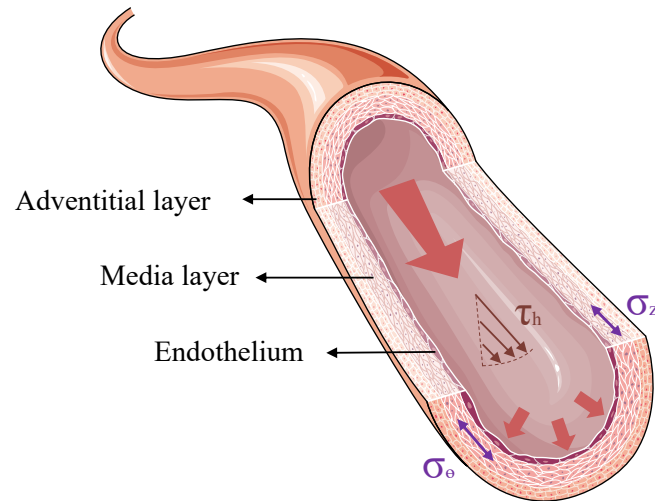


Figure 1.18: Hemodynamic force load on endothelial cell surface (illustration adapted from servier medical art)

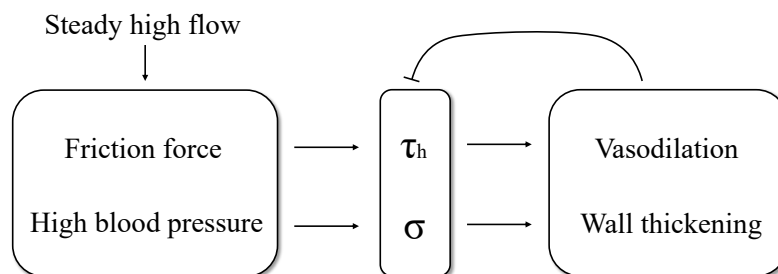


Figure 1.19: hemodynamic conditions and structural responses[7]

by circumferential and axial stress [35]. In order to restore the peripheral wall stress to a normal value, one of the specific biomechanical manifestations of vessel wall adaptation in response to high pressure is thickening [35]. Therefore, steady high flow plays an essential role in vascular remodeling.

Those mechanical forces act directly on the endothelial cells (ECs) of blood vessels. ECs are located at the boundary surface between the blood and vessel wall and are the blood vessel wall's primary sensors and regulation tissues. After sensing those forces, ECs remodel blood vessels by releasing chemotactic and inflammatory mediators, thereby maintaining the balance of the vascular environment [34]. Under normal physiological conditions, hemodynamics will produce positive stimulation to ECs, which protects blood vessels from normal working. After AVF is produced, the high flow will lead to the up-regulation of endothelial nitric oxide synthase (eNOS), promoting the synthesis of a large amount of nitric oxide (NO). NO is an effective vasodilator and signaling molecule with anti-inflammatory and anti-platelet properties, which leads to the relaxation of vascular smooth muscle cells (VSMCs), thereby causing acute vascular remodeling [34].

1.6 AVF failure

For ESRD patients who require dialysis, native AVF is the preferred VA [22]. Although it is recommended as the leading VA, AVF still has many drawbacks. Approximately 50% of patients who use AVF require a revision within a year [36].

The creation of AVF requires surgical tailoring and reconstruction of blood vessels, and the reconstructed vessels need to adapt to the new hemodynamic environment in a short time. The mechanical stimulation of disturbed flow to the vessel wall, the wound caused by surgery, and the metabolic abnormalities in ESRD patients can accelerate the production of thrombosis, neointima hyperplasia (NIH), etc. These can cause stenosis and prevent the maturity and service life of the fistula [34].

1.6.1 Effects of disturbed flow

After AVF surgery, the blood flow in the fistula increases rapidly. The well-ordered pattern of streamlined flow created by high steady flow produces positive stimulation to the vessel wall, accelerates fistula remodeling, and promotes maturation (fig.1.20). However, due to the complex fistula geometry, when Q_{pa} and Q_{da} converge and flow together into the vein, the disturbed flow will be generated on the vessel wall. Coupled with blood flow pulsation, the inlet section of the vein often produces complex flow patterns (fig.1.20).

Ene-Iordache et al. conducted computer fluid dynamics (CFD) simulations on AVF and found that the disturbed flows exist at the bottom of the artery and the venous inner wall near the anastomosis, which causes the appearance of the low and oscillating wall shear stress (WSS) [37]. They also performed CFD simulations on ideal AVF models from different angles. They found that the anastomosis angle affects the disturbed flow pattern and the WSS distribution on the vessel wall [38].

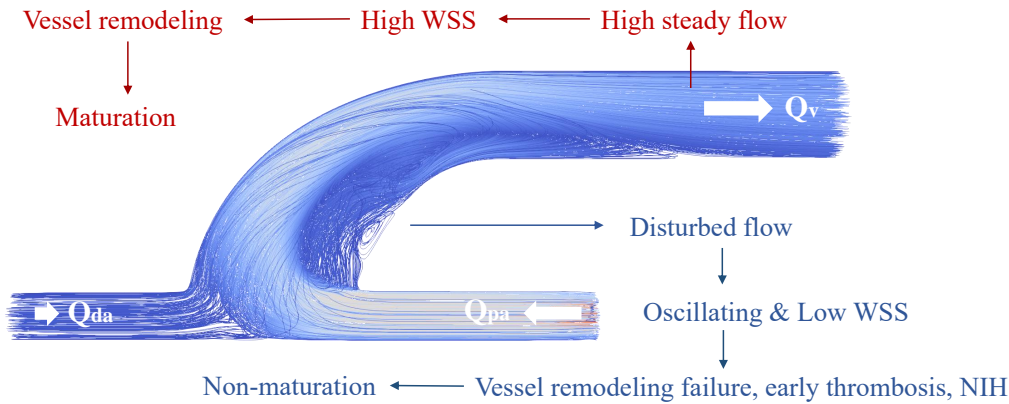


Figure 1.20: Disturbed flow in AVF

These varying and irregular flow patterns include recirculating eddies with reverse streamlines, reciprocating flow whose directions change over time, and flow separation and flow reattachment due to spatial changes [8]. The resulting low WSS and oscillating WSS negatively stimulate the vessel wall. These shear stresses are often not within the normal WSS physiological range on the vessel wall. Therefore their negative impacts will accelerate the development of thrombosis, NIH, etc., and affect the AVF maturation and patency.

ECs perform many essential functions, such as regulating permeability, migration, remodeling, proliferation, apoptosis, biochemical substances production, metabolism, and regulating the contractility of VSMCs [39]. ECs respond and perceive the mechanical factors (such as WSS) to change intracellular signal transduction, gene expression, protein expression, and cell function [34]. In the experiment of ECs exposed to a step-flow channel [39], ECs elongate along the flow direction in a laminar flow with an average WSS higher than the physiological level (fig.1.21B,D). On the contrary, in the area where the average shear stress is lower than the physiological level (fig.1.21A,C), the ECs are polygonal in appearances and have no clear directions.

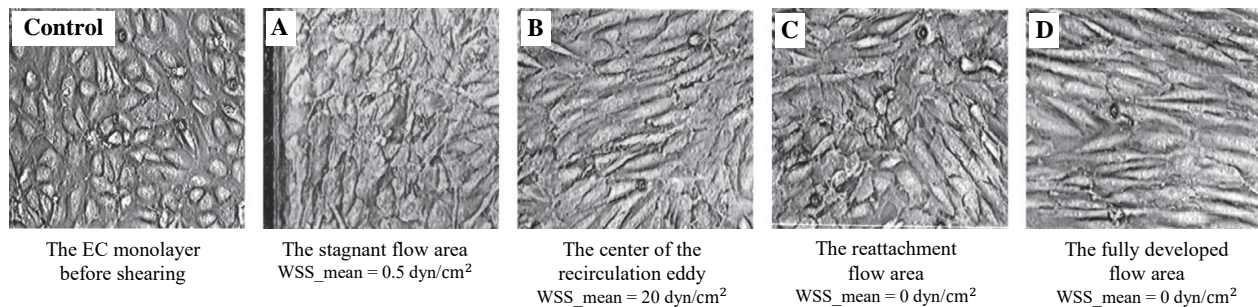


Figure 1.21: Morphological changes induced in a confluent EC mono-layer by exposure to disturbed flow[8]

Shear stress can activate many EC mechanical sensors, such as vascular endothelial growth factor

receptor, integrin, ion channel, intercellular junction protein, etc. The low and oscillating WSSs negatively stimulate ECs to trigger a series of signal transduction pathways, thereby regulating the health and disease functions related to gene and protein expressions [39]. For example, low and oscillating WSSs will up-regulate some genes related to EC proliferation and inflammation, and many genes related to angiogenesis and vascular remodeling will be down-regulated, leaving ECs in proliferation and inflammatory states [8]. Low and oscillating WSSs will cause the activity of eNOS to be impaired, thereby decrease NO secretion to cause activation and proliferation of VSMCs within the vein wall, and lead to failure of vessel outward remodeling [40]. They can also affect the balance of vasodilators and vasoconstrictors, change the VSMCs contractilities, cause endothelial dysfunction, and accelerate the development of thrombosis and atherosclerosis [34]. Experiments have shown that blood flow disorder will degrade intercellular connexins to widen the cell spacing, change the integrity and permeability of the endothelium [8], thereby allowing fibroblasts to migrate from the outer membrane layer to the inner membrane layer to form NIH [34].

1.6.2 Early failure

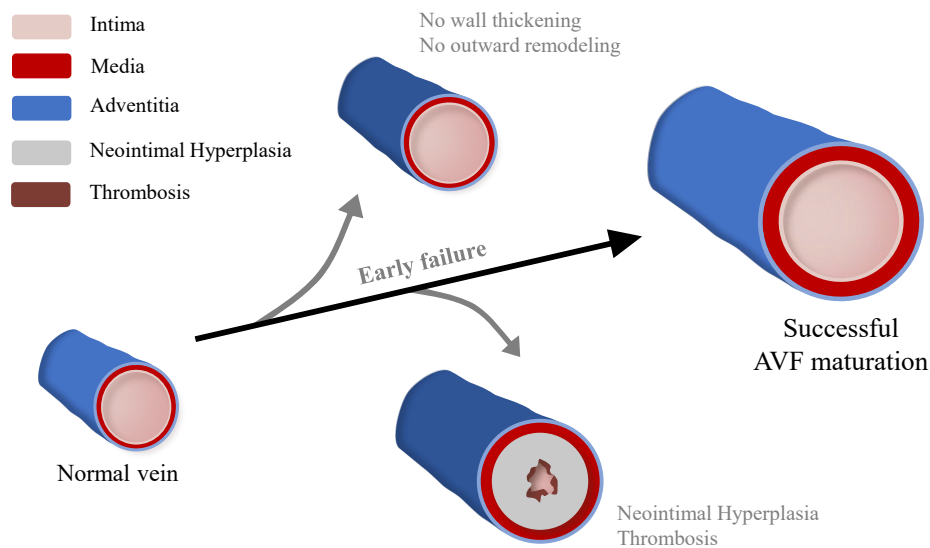


Figure 1.22: AVF early failure

The early failure of AVF means that the fistula cannot mature. Mainly clinical manifestations are the failure of vascular remodeling, early thrombosis, or NIH (fig.1.22). These phenomena are often caused by the wrong choices of vessels or unreasonable anastomosis configuration designs. The systemic inflammatory response in ERSD patients due to metabolic abnormalities and other syndromes will also increase the probability of early failure [34].

1.6.2.1 Vein outward remodeling failure

The occurrence of vein remodeling failure refers to the fact that the intravenous blood flow still cannot reach the ‘6s rule’ dialysis standard within the expected time. This early failure is mainly

caused by the wrong choice of the blood vessels. The 2019 KDOQI clinical practice guideline for vascular access [22] recommends RCAVF (fig.1.4b) use blood vessels with a diameter greater than or equal to 2mm for anastomotic surgery. From a systematic review [41], the author summarized 12 articles (1200 patients in total) and proposed to use the vessel with a diameter greater than or equal to 2 mm, and not recommended to use the vessel with a diameter less than 1.5 mm. In the references [42],[43] and [44], the authors also have different proposals for the recommended vessel diameter ranges. But these are the empirical results, and they still lack theoretical research support.

At the same time, the undesirable anastomosis design will also cause energy loss when the blood passes through the anastomosis, thereby slowing the growth rate of blood flow, increasing the maturity time. The arterial segment below the anastomosis also has the risk of NIH due to the existence of flow stagnation area. If NIH occurs in this area, it will block the blood flow into the vein, leading to the failure of vein remodeling.

1.6.2.2 Neointimal Hyperplasia

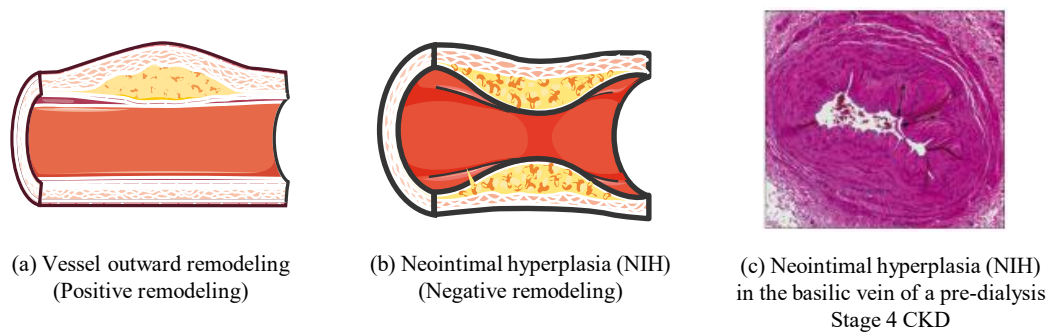


Figure 1.23: Neointimal hyperplasia ((a) and (b) adapted from servier medical art; (c) adapted from [9])

The outward thickening of blood vessels (fig.1.23(a)) is a positive vascular remodeling phenomenon, which can accelerate the maturation of AVF. However, the production of invasive NIH will cause inward vessel remodeling (fig.1.23(b)), which will lead to stenosis and AVF non-mature.

The development of NIH is a complex process that requires activation, phenotype change, and migration of vascular cells. NIH is comprised primarily of smooth muscle alpha-actin-positive, synthetic VSMC phenotype, or vimentin-positive and desmin-negative myofibroblasts that probably migrated from the media or adventitia layers in response to vascular injury [45]. And low and oscillating WSS caused by the disturbed flow change the contractility of VSMCs and accelerate the migration and proliferation of VSMCs to the inner membrane [46].

The damage to blood vessels caused by AVF surgery is unavoidable. In addition, the systemic inflammation inherent in ESRD patients can lead to increased levels of cytokines related to the NIH development (fig.1.23(c)) [9]. One of the most economical and effective ways to prevent NIH

is to optimize the anastomosis geometry to reduce the irritation of the disturbed flow to the vessel wall.

1.6.2.3 Early thrombosis

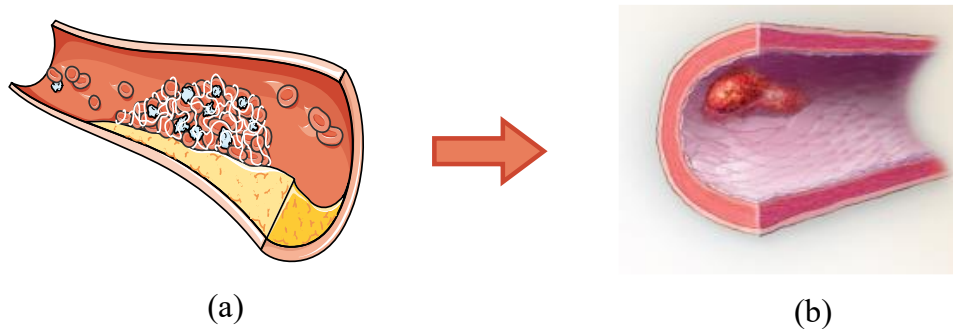


Figure 1.24: Early thrombosis ((a) adapted from servier medical art; (b) adapted from [10])

Virchow's triad [10] clarified the critical components of thrombosis (fig.1.24): hypercoagulable state, endothelial injury, and hemodynamic changes. Due to renal dysfunction in CKD patients, the pro-thrombotic and anti-thrombotic factors in the body are out of balance, resulting in a hypercoagulable state. AVF fistula causes unavoidable endothelial damage to blood vessels. In addition, the systemic concentration of pro-inflammatory and anti-inflammatory cytokines in CKD patients is usually several times higher than that of healthy peoples [47], [48], thereby increasing the ECs inflammation. In the meantime, AVF changes the original shape of blood vessels, increases blood flow, and changes the flow state. The inevitable disturbed flow will be generated near the anastomosis. Therefore, the optimization of AVF configuration is necessary to reduce the development rate of early thrombosis and increase the maturity rate of AVF.

1.6.3 Late failure in the mature AVF

The mature AVF can be used for hemodialysis. However, this VA is not permanent. Recent studied have shown higher failure rates of up to 46%, with one year patencies from 52% to 83% [19]. AVF gradually fails over time and eventually requires interventional treatment or secondary surgery to maintain the normal function. The main reasons for the late failure can be summarized in three points:

- *Local injuries caused by repeated punctures*

The frequency of dialysis three times a week puts a great burden on the blood vessels used for dialysis. The continuous local injuries caused by repeated punctures will aggravate the inflammation, leading to the risk of complications at the puncture site. Careful care of the injured site can extend the using life of the fistula and reduce puncture injuries.

- *Systemic abnormalities in ESRD patients*

ESRD patients have systemic abnormalities, such as uremia, systemic inflammation, endothe-

lial dysfunction, lipid abnormalities, hyperparathyroidism, hyperphosphatemia, and hypercalcemia [49], [50]. These abnormalities can aggravate inflammation and oxidative stress [51] and adversely affect vascular endothelium. At the same time, it will increase the level of some cytokines related to NIH, such as Interleukin-6 (IL-6), and transforming growth factor-beta (TGF- β) [9]. These abnormalities can lead to inward remodeling and narrowing of the blood vessel wall. Timely drug treatment can relieve the damage caused by system abnormalities and improve the patency of the fistula.

- *Pre-existent vascular pathology*

Systemic abnormalities in ESRD patients can lead to atherosclerosis, blood vessel thickening, and blood vessel calcification, etc. These diseases exist in patient vessels before dialysis [52],[53]. Fig.1.23(c) is the NIH existed in the basilic vein of a pre-dialysis patient. These pre-existent vascular pathologies greatly influence the service life of AVF, which need the deliberate choice of blood vessels before surgery.

1.7 Research strategies

Global survey results show that in 2017, the global prevalence of CKD was 9.1%. From 1990 to 2017, the global prevalence of CKD increased by 29.3%. In 2017, CKD resulted in 35.8 million disability-adjusted life-years, and 12 million people died of CKD [54]. From the 2021 report of CKD in the United States, more than 1 in 7, 15% of US adults or 37 million people, are estimated to have CKD [55]. In 2018, about 131,600 people in the United States started treatment for ESRD [55]. Nearly 786,000 people in the United States, or 2 in every 1,000 people, are currently living with ESRD: 71% are on dialysis, and 29% are living with a kidney transplant [55]. In France, 161 ESRD patients who require dialysis for every million population in 2018 [56], which is constantly increasing because of an aging population. The new data shows that there are already more than 5,000 AVF creations in France per year, which is more than aortic surgeries. There are approximately 8,000 deaths and 11,000 new ESRD cases per year, and each year an increase in 3,000 patients. (Data provided by Hospices Civils de Lyon)

VA-related morbidity represents a tremendous burden for patient (pain, anxiety and depression) and healthcare system (hospitalisation, technical procedures and interventions and cost). VA dysfunction is the first reason for hospitalizations in dialysis patients. Each patient has at least one echo-Doppler examination before creation (approximately 50 euros per time) and at least two times per year after VA creation, but most often 3 to 4 per year. Revision surgical procedures are frequent as well as radiological angioplasties, frequently once a year. Each time it is expensive equipment. The French health insurance system estimated the overall cost of care for ESRD at more than 4 billion euros for 61,000 patients treated in 2007, and a steady increase in the number of patients treated has been observed. Fees are highest for hospital-based hemodialysis care, treating around 58% of all dialysis patients [57]. Therefore, how to increase the maturity rate of AVFs and their service lives have been discussed and explored all the time.

1.7.1 Current researches and limitations

Effective treatments to prevent or treat AVF failure require a multidisciplinary approach involving nephrologists, vascular surgeons, and interventional radiologists, allowing careful vessel selections and the use of tailored systemic or localized interventions to improve patient-specific fistulas. In addition to reducing the systemic inflammation and the existing vascular diseases in ESRD patients through medical treatment from a medical perspective. The optimization of AVF anastomosis configurations is also a hot topic in biomechanical research area. Most of the researches on AVF anastomosis configurations have focused on the choices of vessel diameters and the anastomosis angles.

Ene-Iordache et al used the numerical simulations to character the blood flow inside the RCAVF and of patterns of hemodynamic shear stress. They found the low and oscillating WSSs in zones where flow stagnation occurs on the artery floor and on the inner wall of the juxta-anastomotic vein [37]. In their next study [58], they employed image-based CFD in a realistic model of RCAVF (an AVF setting with high blood flow developed at six weeks post-operatively). They found that the inner wall of vein bending segment is a conduit subjected to multidirectional hemodynamic shear stress and simultaneously develops reciprocating disturbed flow in some focal points. Javadzadegan et al present a computational hemodynamic analysis in a model of a mature side-to-side AVF, which is then validated by experimental measurements. Both computational and experimental results confirmed the presence of complex flow patterns within the AVF with vortices initially developing at the center of the venous region and gradually moving downstream [59]. Carroll et al have developed the ideal CFD AVF models to explore flow disturbances and local hemodynamic effects in a standard acute angle (45°) and a smooth vein loop angle (135°). They found a significant reduction in flow disturbance in the smooth vein angle [60]. Jia et al described the hemodynamic condition in a non-uraemic canine model of AVF and found that NIH predisposed to occur in the inner wall of venous segment near the anastomosis. They found that not only the NIH has a strong inverse correlation with WSS levels, but also is related to flow patterns [61]. These numerical hemodynamic researches used mature postoperative AVF models with fixed geometric shapes. Therefore, they can only prove the existence of disturbed fluid in the AVF and the impact of undesirable WSSs on the vessel wall. They can not optimize the anastomosis surgery plan.

Using pulsatile computational fluid dynamics (CFD) simulation with idealized models of RCAVF with different anastomotic angles, Ene-Iordache et al found that the anastomosis angle does impact on the local disturbed flow patterns, the smaller angle (30°) would be the preferred choice that minimizes the development of NIH [38]. This research studied the anastomosis angle of RCAVF, however it changed the distance between blood vessels in the same time. Therefore, the conclusion of this study needs to be further verified.

The research review [41] summarized previous clinical studies and recommended surgeons to choose the arterial and venous diameters equal or greater than 2 mm, and avoid vessels less than or equal to 1.5 mm to ensure the maturity of RCAVF. Vast clinical studies also pointed out that the RCAVF maturity is closely related to the arterial and venous diameters [42], [43], [44], [62], [63]. These are empirical results, and ignored the influence of other blood vessel geometric parameters (such

as anastomosis configuration and vessel distance) when studying the relationship between vessel diameters and RCAVF maturity.

1.7.2 Objectives and outlines

In recent years, with an increase in the capacity of numerical information and analysis systems ('big data'), the medical community is interested in new developments in identifying and treating patients, namely, individualized medicine. Since 2013, individualized medicine has been defined as one of the eight Objectives of Progress by the 'Innovation 2030' Commission. This Ph.D. study aims to provide patient-specific assistance to the RCAVF configuration preoperative planning process to increase the maturation rate of RCAVF and reduce the occurrence of postoperative complications, prolong the service life of the fistula and reduce the patient's pain and their medical cost.

This Ph.D. thesis is divided into five chapters. The first chapter is the general introduction of our research context. Chapters 2 to 4 are the detailed descriptions of our research results during the three-year Ph.D. study. The last chapter is a summary of the entire Ph.D. works and prospects for follow-up researches.

RCAVF is an artificially created vascular access. Therefore, the optimization of its configuration should be carried out from both mechanical and biological perspectives. From a mechanical perspective, the vascular resistance at the artificially designed anastomosis causes an energy loss that affects blood flow rate growth and leads to early failure. We proposed in chapter 2 a theoretical model to optimize the configuration of the RCAVF. This new complete model using the interrelation between the different GPs brings scientific probes about the hemodynamic of RCAVF. Our research was inspired by Murray's law [64]. The geometric structure of human blood vessels has evolved according to natural biological selection. The structure of blood vessels follows the principle of minimum energy loss. AVF is an artificial connection of blood vessels. When the energy loss generated by the designed vascular circuit is small, the blood flow is easier to establish so that venous blood flow can reach the target value more easily and quickly, which facilitates the maturation of the AVF. With the analyses of the theoretical model, we found the relation between the energy loss rate and the geometric parameters of RCAVF, which can explain some empirical results and be used to optimize the RCAVF configuration.

From a biological point of view, due to a sudden change in the shape of blood vessels and a rapid increase in blood flow rate, RCAVF will produce disturbed fluid. Therefore, the low WSS (LWSS), which is smaller than the physiological level, and the oscillating WSS (OWSS) will produce negative mechanical stimulations to the blood vessel wall, which will lead to RCAVF remodel inward and accelerate the occurrence of stenosis. In chapter 3, we numerically analyzed the effect of the anastomotic angle on the disturbed fluid in RCAVF by analyzing the distributions of LWSS and OWSS and the causes of their formations through hemodynamic behaviors. Finally, we concluded the most suitable angle of anastomosis for RCAVF.

In chapter 4, we set two critical values to measure the energy loss rate in RCAVF according to the theoretical model created in 3. In the meanwhile, we designed a Personal Mechano-Bio-faithful

RCAVF preoperative model (PerMeBiO-RCAVF model), which combined the critical energy loss rates and the simulation results in chapter 3. It aims to help surgeons select blood vessels and provide patients with the most suitable anastomosis method. This model has been used to analyze five clinical cases and preliminarily verified its applicability.

A theoretical model to optimize the RCAVF configuration

From a mechanical perspective, the vascular resistance at the artificially designed anastomosis causes an energy loss that affects blood flow rate growth. In this chapter, We theoretically analyze and derive a theoretical model that evaluates the energy loss rate in RCAVF as a function of its blood vessel geometric parameters (GPs) for given flow rates, then verified their accuracies with numerical results. It was found that the diameter of anastomosis (D_a) and the RA diameter (D_{ra}) have much less influence on energy loss than the anastomotic angle (θ) and the CV diameter (D_{cv}), and the distance between blood vessels also has a non-negligible influence on the energy loss. For patients who use RCAVF for dialysis, we suggest surgeons choose the vessels with the larger diameters and a small distance while increasing the angle and diameter of the anastomosis to minimize the energy loss.

Contents

2.1	Introduction	40
2.2	RCAVF geometric parameters	40
2.3	Theoretical analysis	41
2.3.0.1	Energy loss rate in bending cephalic vein (B segment)	42
2.3.0.2	Energy loss rate at anastomosis	43
2.3.0.3	Total energy loss rate in RCAVF	45
2.4	Numerical models for RCAVF energy loss model verification	46
2.4.1	RCAVF 3D virtual model creation	46
2.4.2	Model validation	47
2.5	Results analysis	49
2.5.1	Theoretical model compared to numerical simulation	49
2.5.2	Relationship between energy loss rate and GPs	50
2.6	Discussions and conclusions	58

2.1 Introduction

Patients with end-stage renal disease (ESRD) need to undergo hemodialysis (HD) to survive. The arteriovenous fistula is the gold standard as vascular access for hemodialysis, and it is the access recommended by the NFKDOQI [22] for dialysis treatment. Among all possible AVFs, distal RCAVF is recommended as the first choice of native AVFs. However, due to its small flow capability and thin vessels, the venous outflow after the operation cannot reach the expected blood flow. It will lead to the immaturation of RCAVF and causes a higher early failure rate. Therefore, the choice of radial artery (RA) and cephalic vein (CV) and the design of the anastomosis play an essential role in the postoperative maturity rate of RCAVF.

Analyzing the usability of RA and CV vessels or finding the best configuration of RCAVF through numerical simulations, although more accurate and bio-faithful results can be obtained, the computational effort will consume a lot of time. Therefore, in this chapter, we aim to help surgeons optimize the RCAVF anastomosis plan from the mechanical perspective of minimizing energy loss by analyzing the energy loss in RCAVF. This theoretical approach can provide useful indicators for the surgeons to make the preoperative anastomosis plan.

The research review [41] summarized previous studies and recommended surgeons to choose D_{ra} and D_{cv} equal or greater than 2 mm, and avoid vessels less than or equal to 1.5 mm to ensure the maturity of RCAVF. References [42], [43] and [44] pointed out that the RCAVF maturity was closely related to D_{ra} and D_{cv} . References [65], [66], [67], [38] and [68] are based on numerical simulations of different RCAVF shapes to enforce that θ has an impact on the hemodynamic distribution in a fistula by observing the wall shear stress. It has also been approved in chapter 3. However, these previous works did not offer theoretical explanations, and literatures about the hemodynamic conditions in a recent RCAVF remains poor. Analyses are often carried out to impact variables separately without considering at least their cross-correlated influences or the interaction with other geometric factors such as h and D_a . Actually, surgeons apply some guidelines and have some surgical habits, whereas with very few scientific probes, and the AVF creation varies from center to center. Our research has considered a set of five a prior inter-connected geometric variables in RCAVF through the control of different GPs to improve recommendations for the creation of RCAVF.

2.2 RCAVF geometric parameters

The RCAVF configuration affects the distribution of blood flow in the fistula. After the anastomosis creation, the hemodynamic state significantly influences the maturity rate, primary patency, and service life of the fistula. Before the anastomosis operation, the surgeon needs to evaluate the radial artery (RA) and cephalic vein (CV) performances, measure their diameters, select the most suitable surgical site, and finally design a patient-specific anastomosis plan. In RCAVF creation, there are five geometric parameters (GPs) that can be manually selected and designed by surgeons (as shown in fig.2.1):

- D_{ra} : Radial artery diameter
- D_{cv} : Cephalic vein diameter
- h : blood vessel distance between RA and CV
- D_a : Anastomotic diameter
- θ : Anastomotic angle

D_{ra} and D_{cv} need to be evaluated before the anastomosis to assure maturity of fistula. D_a and θ are designed along with the surgeons' experiences, which have non-negligible influences on the hemodynamic stimulations to vessel walls. The vessel distance h can be modified with the arm's anatomy to help to achieve the ideal anastomotic configuration.

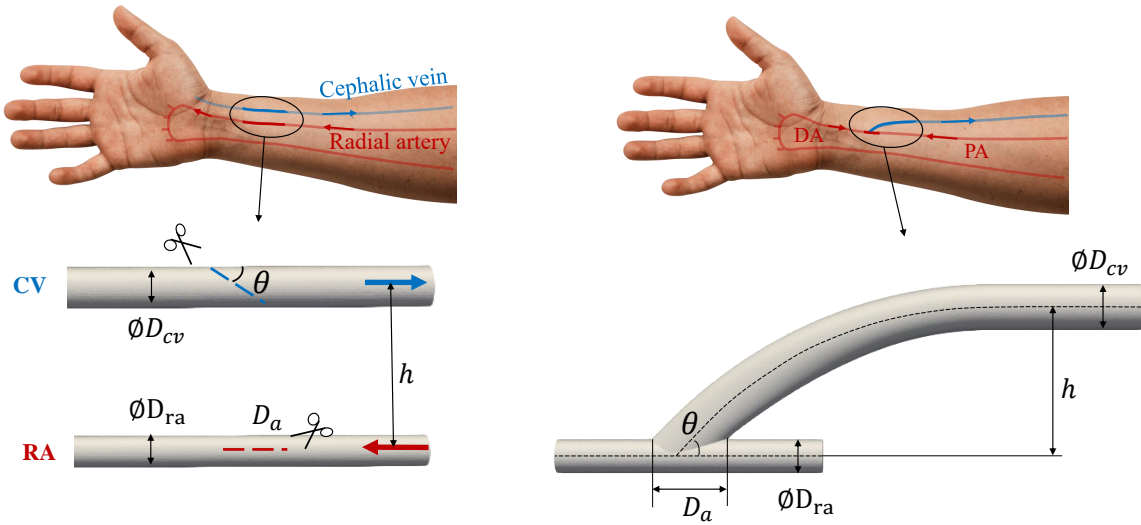


Figure 2.1: RCAVF geometric parameters

2.3 Theoretical analysis

Before the RCAVF creation, surgeons measured and analyzed the quality of the patient vessels through DUS and design a most appropriate RCAVF configuration based on their clinical experiences. During the operation, surgeons release the vein over a certain distance to bring the vein to the artery, then cut the CV obliquely following an angle θ and cut along the axial direction of the RA a length D_a (the details are shown in chapter 1). Then RA and CV will be connected to form the RCAVF vascular access. The blood flow in the proximal artery (PA) enters the fistula through the heel of the anastomosis with a flow rate Q_h equivalent to that of the normal radial artery (22 ml/min). The blood flow in the distal artery (DA) enters the fistula through the toe of the anastomosis at a flow rate Q_t , with the same order of magnitude as that of the wrist (5 ml/min). Q_h and Q_t are calculated by multiplying the average flow velocity in the blood vessel by

the cross-section of the vessel [69], [70] and [71].

The energy loss rate E_{avf} in the RCAVF includes energy lost due to vessel bending (E_b) and friction (E_f) in CV, as well as the dissipation of energy due to change in the direction of blood flow (E_d) at the anastomosis. The blood is laminar flow, and the following assumptions are used:

- Blood is an incompressible Newtonian fluid ($\rho = 1060 \text{ kg/m}^3$, $\mu = 0.0035 \text{ Pa}\cdot\text{s}$) flowing in a rigid horizontal blood vessel;
- The potential energy and the heat transfer are negligible;
- The energy loss due to metabolism is negligible.

2.3.0.1 Energy loss rate in bending cephalic vein (B segment)

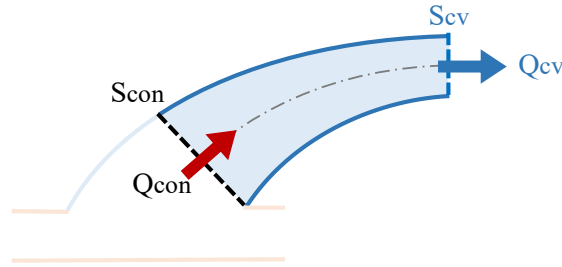


Figure 2.2: Blood flow in bending cephalic vein

The energy loss rate along B segment (fig.2.2) consists of E_b and E_f . We assumed that this segment was a concentric bending vessel with a constant diameter D_{cv} . In [72], E_b is defined as:

$$E_b = \zeta_M \cdot \frac{\rho Q_{cv}^3}{2S_{cv}^2} \quad (2.1)$$

where ζ_M is the minor loss coefficient of the bending vessel, it can be defined as:

$$\zeta_M = A_1 B_1 C_1 \quad (2.2)$$

From reference [72], A_1 , B_1 , and C_1 are defined by:

$$\begin{cases} A_1 = 0.9 \sin \theta & \text{when } \theta \leq 90^\circ \\ B_1 = 0.21 \left[\frac{D_{cv}}{R_0} \right]^i \\ C_1 = 1 \end{cases} \quad (2.3)$$

R_0 is the radius of curvature of the B segment. It can be written as:

$$R_0 = \frac{h - D_{ra}/2}{(1 - \cos \theta)} \quad (2.4)$$

When the ratio of D_{cv} to R_0 is less than 1, i is equal to 2.5; otherwise, i is equal to 0.5. Finally, from equations 2.1, 2.2 and 2.3, E_b can be summarized as:

$$E_b = 0.189 \sin \theta \left[\frac{D_{cv} (1 - \cos \theta)}{h - D_{ra}/2} \right]^i \frac{\rho Q_{cv}^3}{2 S_{cv}^2} \quad (2.5)$$

When blood transports in vessels, the frictional forces will cause pressure loss, thereby consuming energy. The energy loss rate due to friction [64] in this segment can be expressed as:

$$E_f = \frac{128 \mu L_B Q_{cv}^2}{\pi D_{cv}^4} \quad (2.6)$$

where L_B is the length of B segment, which can be calculated by:

$$L_B = \frac{(h - D_{ra}/2)\theta}{1 - \cos \theta} \quad (2.7)$$

2.3.0.2 Energy loss rate at anastomosis

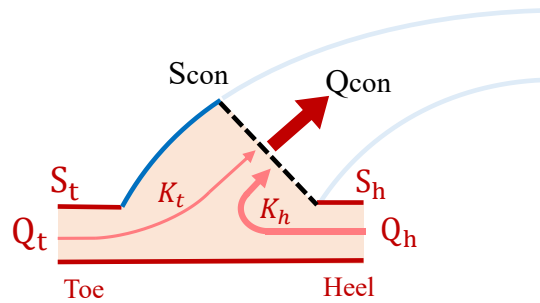


Figure 2.3: Blood flow at anastomosis

Placement of the fistula allows the blood flow in RA to bypass the distal resistance generated by the capillary in the fingers and return to the heart through the anastomosis. For that reason, Q_t flow rate direction of the distal artery changes and flows into the vein together with Q_h (fig.2.3). Q_{con} represents the total blood flow rate at the confluence, which equals Q_{cv} . The resulting energy loss rate at anastomosis can be expressed as:

$$E_a = E_t + E_h = (K_t + K_h) \frac{\rho U_{con}^2}{2} Q_{con} = (K_t + K_h) \frac{\rho Q_{cv}^3}{2 S_{con}^2} \quad (2.8)$$

The minor loss coefficients at toe and heel of anastomosis are K_t and K_h [73] defined by:

$$K_t = 2(1 - q_t)^2 \frac{1}{\varphi_t} \cos\left(\frac{\pi + 3\theta}{4}\right) - 2q_t^2 \frac{1}{\varphi_t} \cos\left(\frac{3\theta}{4}\right) + q_t^2 \frac{1}{\varphi_t} + 1 \quad (2.9)$$

$$K_h = 2q_h^2 \frac{1}{\varphi_h} \cos\left(\frac{\pi + 3\theta}{4}\right) - 2(1 - q_h)^2 \frac{1}{\varphi_h} \cos\left(\frac{3\theta}{4}\right) + q_h^2 \frac{1}{\varphi_h} + 1 \quad (2.10)$$

where q_t and q_h are the ratios of the toe and the heel volume flow rate to the common flow rate. φ_t and φ_h are the ratios of the toe and the heel cross-sectional areas to the common one. They can be expressed as:

$$\begin{cases} q_t = \frac{Q_t}{Q_{con}} \\ q_h = \frac{Q_h}{Q_{con}} \end{cases}, \begin{cases} \varphi_t = \frac{S_t}{S_{con}} \\ \varphi_h = \frac{S_h}{S_{con}} \end{cases} \quad (2.11)$$

Next, we introduce the calculation of the cross-sectional area of the total blood flow at the confluence (S_{con}), as shown in figure 2.4. In the anastomosis operation, surgeons cut CV obliquely to obtain an elliptical cross-section $S_{a_{cv}}$ (the light blue ellipse in figure 2.4), the major axis is $A_{a_{cv}}$, and the minor axis is $B_{a_{cv}}$:

$$A_{a_{cv}} = \frac{D_{cv}}{\sin \theta}, \quad B_{a_{cv}} = D_{cv} \quad (2.12)$$

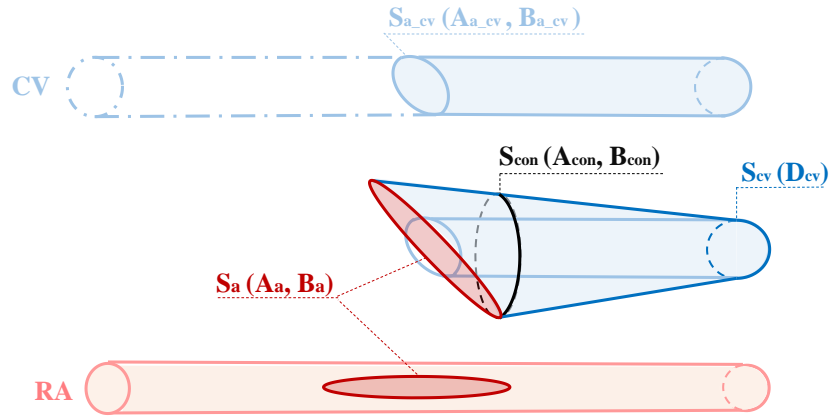


Figure 2.4: 3D simplified diagram of the anastomosis operation (Top is the original CV artery before being stretched (middle) to be linked to the RA (bottom))

Then RA is cut along the axial direction and opened along the radial direction of the blood vessel to obtain an elliptical anastomosis S_a with a major axis A_a and a minor axis B_a (A_a is equal to the anastomotic diameter D_a , and B_a is defined as RA radius R_{ra}). In order to suture CV and RA, $S_{a_{cv}}$ needs to be stretched or compressed along the major axis to give it the same shape as S_a (the red ellipse in figure 2.4). The S_{con} section is perpendicular to the CV axial direction after the CV is stretched or compressed (the black ellipse in figure 2.4 with the major axis A_{con} and the minor axis B_{con}). S_{cv} in figure 2.4 represents the cross-section of CV, a circular cross-section with a diameter of D_{cv} . Figure 2.5 presents the top view and the front view of the blood vessel in the CV stretch segment (the light blue lines in figure 2.5 (a) and (c) represent an undeformed vein). We suppose that B_a and B_{con} evolve linearly from D_{cv} , and A_{con} can be calculated from A_a , D_{cv} , and θ of the imposed deformation. After geometric calculations, the expression of A_{con} and B_{con} are:

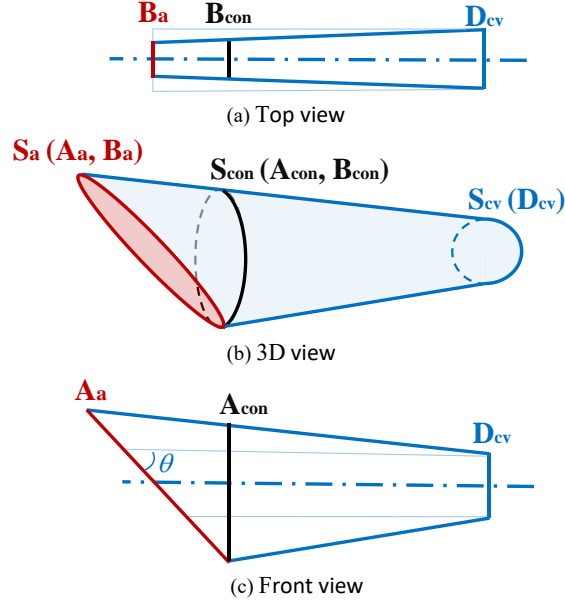


Figure 2.5: Top view, 3D view, and front view of cephalic vein (CV) after stretching

$$\begin{cases} A_{con} = D_a \sin \theta - \frac{(D_a \sin \theta - D_{cv}) D_a \cos \theta}{2h + D_a \sin \theta (1 - \cos \theta)} \\ B_{con} = \frac{D_{ra}}{2} + \frac{(2D_{cv} - D_{ra}) D_a \cos \theta (1 - \cos \theta)}{4h\theta} \end{cases} \quad (2.13)$$

Therefore, the cross-section of the total blood flow at the S_{con} confluence can be obtained from:

$$S_{con} = \frac{\pi A_{con} B_{con}}{4} \quad (2.14)$$

2.3.0.3 Total energy loss rate in RCAVF

From equations 2.5, 2.6, and 2.8, the total energy loss rate in RCAVF (E_{avf}) given by the following equation:

$$\begin{aligned} E_{avf} &= E_b + E_f + E_a \\ &= 0.189 \sin \theta \sqrt{\frac{D_{cv} (1 - \cos \theta)}{h - D_{ra}/2}} \frac{\rho Q_{cv}^3}{2S_{cv}^2} + \frac{128\mu(h - D_{ra}/2)\theta Q_{cv}^2}{\pi D_{cv}^4 (1 - \cos \theta)} + (K_t + K_h) \frac{\rho Q_{cv}^3}{2S_{con}^2} \end{aligned} \quad (2.15)$$

where K_t , K_h , and S_{con} can be obtained by equations 2.9, 2.10 and 2.14.

2.4 Numerical models for RCAVF energy loss model verification

2.4.1 RCAVF 3D virtual model creation

RCAVF can be separated into four segments (fig.2.6). DA, PA and V were defined as straight vessels, and B was the bending vein segment which was regarded as a partial circle with a constant radius of curvature connected with radial artery by anastomosis.

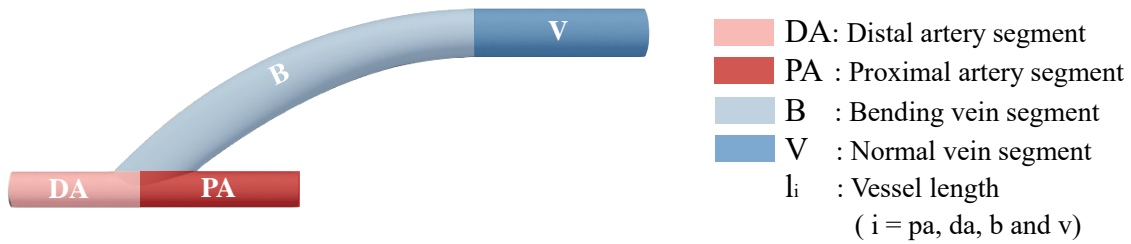


Figure 2.6: RCAVF vascular segments

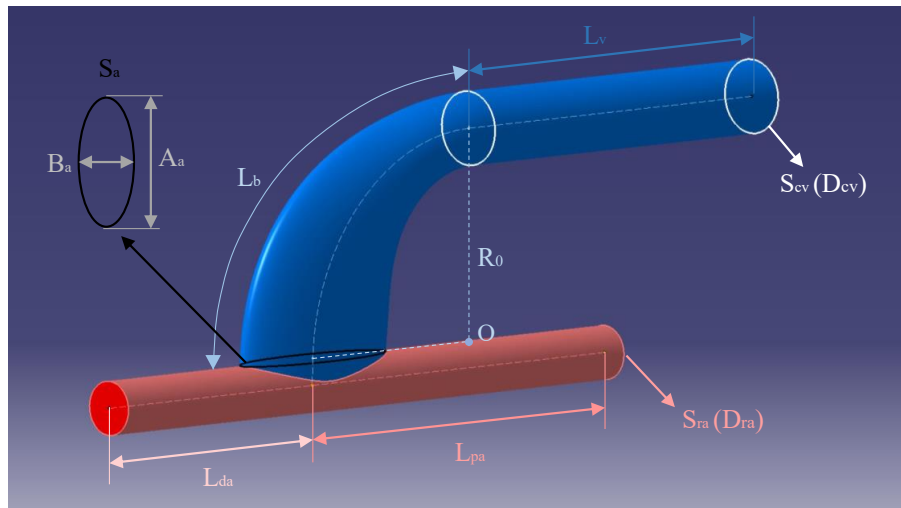


Figure 2.7: RCAVF 3D virtual model creation ($\theta=90^\circ$)

The 3D virtual models of RCAVF were created by CATIA V5, a multi-platform software suite for computer-aided design, computer-aided manufacturing, computer-aided engineering, and 3D, developed by the French company Dassault Systèmes. Fig.2.7 shows a RCAVF vascular model with a 90° anastomosis angle. In the RCAVF models, DA and PA segments were created by straight tubes with the circular cross-sections (S_{ra}). The same way established v segment with a circular cross-section (S_{cv}). The lengths of these three straight segments successively were 15 mm (L_{da}), 25

mm (L_{pa}) and 20 mm (L_v). B segment was a concentric bending tube whose cross-section changed from the anastomotic surface (S_a , black ellipse in fig.2.7) to the cephalic venous surface (S_{cv} , white circle in fig.2.7). Its length (L_b) is equal to the product of the curvature radius of the B segment (R_0) and θ . R_0 was defined as:

$$R_0 = \frac{h - D_{ra}/2}{1 - \cos\theta} \quad (2.16)$$

In the non-mature models, the minor axis of anastomosis (B_a) was defined as the radius of RA. And for mature models, it was equaled to RA diameter. The major axis of anastomosis (A_a) is the anastomotic diameter (D_a), one of the RCAVF GPs.

2.4.2 Model validation

In order to validate the theoretical model, we compare E_{avf} calculated by equation 2.15 and E_{avf_num} obtained with Foam-extend 4.0 numerical simulations. To ensure the relevance of the model, the comparison was made for 25 RCAVFs with different shapes created with Catia V5.

In equation 2.15, there is a total of 5 GPs. We create a standard model (as a reference of fixed values of GPs as shown in table 2.2), then only changed one GP each time. For a given GP, we select five values within its normal range (table 2.1) and keep the remaining GPs consistent with the standard model. Therefore, a total of 25 models were created. The details of the models are shown in table 2.2.

Table 2.1: The research ranges of 5 GPs

GPs	D_{ra} (mm)	D_{cv} (mm)	h (mm)	D_a (mm)	$\theta(^{\circ})$
Research range	[1,4]	[1,4]	[5,50]	[4,12]	[10,90]

In foam-extend 4.0, we use pisoFoam solver to simulate the flow in these geometries with the same initial conditions (flow rate and pressure). The pressure at anastomosis inlets (S_t , S_h) and outlet (S_{cv}) (figure 2.8) are extracted at the third cardiac cycle. They have denoted respectively P_t , P_h , and P_{cv} . According to the law of energy conservation, E_{avf_num} of each model can be calculated by:

$$\frac{\rho}{2} \frac{Q_t^3}{S_t^2} + P_t Q_t + \frac{\rho}{2} \frac{Q_h^3}{S_h^2} + P_h Q_h = \frac{\rho}{2} \frac{Q_{cv}^3}{S_{cv}^2} + P_{cv} Q_{cv} + E_{avf_num} \quad (2.17)$$

Table 2.2: Geometric parameters of 25 RCAVF 3D models

Models	GPs				
	$D_{ra}(\text{mm})$	$D_{cv}(\text{mm})$	$h(\text{mm})$	$D_a(\text{mm})$	$\theta(^{\circ})$
Standard Model	3	3	12	6	30
Models 1-5 (D_{ra} change)	2	3	12	6	30
	2,5				
	3				
	3,5				
	4				
Models 6-10 (D_{cv} change)	3	2	12	6	30
		2,5			
		3			
		3,5			
		4			
Models 11-15 (h change)	3	3	4	6	30
			8		
			12		
			16		
			20		
Models 16-20 (D_a change)	3	3	12	4	30
				6	
				8	
				10	
				12	
Models 21-25 (θ change)	3	3	12	6	30
					45
					60
					75
					90

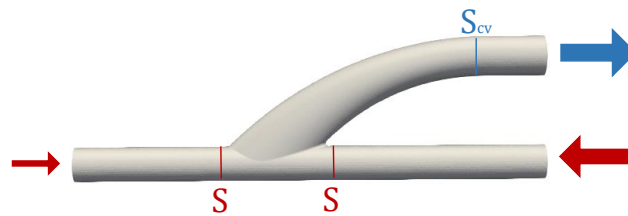


Figure 2.8: RCAVF simulation model

2.5 Results analysis

2.5.1 Theoretical model compared to numerical simulation

We calculated E_{avf} for 25 models using equation 2.15 and compared them with E_{avf_num} obtained by numerical simulations (eq.2.17). The comparisons are shown in figure 2.9. The blue dots in figure 2.9 represent the analytical results (E_{avf}), and the red dots represent the numerical results (E_{avf_num}). We can observe that, for each geometric parameter, E_{avf_num} and E_{avf} have the same profile. The relative difference between the two results defined as $(|E_{avf} - E_{avf_num}|/E_{avf})$ is shown in table 2.3 for each case.

In all cases, the difference between the two approaches is minimal for the standard value of the geometric variables (models 3, 8, 13, 17 and 21). The relative differences between the two approaches are less important when analyzing the impact of the variation of D_{cv} (models 6 to 10) or h (models 11 to 15). It varies between 1 and 7% for D_{cv} . For h , it oscillates between 1 and 9%. In the cases of D_{ra} (models 1 to 5), the relative difference is greater and reaches 11% in model 5 which has the largest D_{ra} . And in the cases of D_a (models 16 to 20), the largest difference appeared in model 20 with the largest D_a and the difference equaled 12.64%. The difference becomes greater when the geometric variables move away from the reference values. Whereas for the θ (models 21 to 25), the difference between the numerical approach and the model tends to increase from 1 to 11% when the angle increases.

Table 2.3: Relative difference between numerical results and analytical results

Models	1	2	3	4	5	6	7	8	9	10
Relative difference (%)	8,99	4,97	0,94	8,86	11,38	6,92	2,41	0,94	1,06	2,5
Models	11	12	13	14	15	16	17	18	19	20
Relative difference (%)	9,03	2,29	0,94	5,71	4,58	8,84	0,94	5,59	8,81	12,64
Models	21	22	23	24	25					
Relative difference (%)	0,94	7,49	9,8	10,82	11,61					

These differences can be explained by the simplifications of the RCAVF geometry made for the theoretical model. When we calculated the energy loss rate in B segment (E_b and E_f), we simplified the bending vein as a concentric bending vessel with a constant diameter D_{cv} . The areas of anastomosis (S_a) and CV (S_{cv}) can be written as:

$$S_a = \frac{\pi A_a B_a}{4}, S_{cv} = \frac{\pi D_{cv}^2}{4} \quad (2.18)$$

Where A_a is the anastomotic diameter, B_a is the minor axis of anastomosis equaled to RA radius. Therefore, the area ratio of the anastomosis to the CV in numerical models is:

$$\frac{S_a}{S_{cv}} = \frac{D_a D_{ra}}{2 D_{cv}^2} \quad (2.19)$$

When the area ratio is closer to 1, the relative difference caused by the geometry simplifications is lower. D_a is defined as 6 mm in the standard numerical model. RA has the same diameter with CV equaled 3 mm, hence the area ratio is 1 which is the smallest in all the numerical models. In the mean time, the standard model has the lowest θ . The area of the cross-section in B segment will closer to the CV area with θ decreasing. Consequently, the relative difference of the energy loss rate between the standard numerical model and theoretical model is the lowest (0.94%). In models 15 to 20, θ augments from 30° to 90° . With θ increasing, the area of the cross-section in B segment is closer to the anastomosis area. Therefore, the relative differences from models 15 to 20 increase. From equation 2.19, the changes of D_a (models 16 to 20), D_{ra} (models 1 to 5) and D_{cv} (models 6 to 10) also lead the area ratio away from 1. Therefore, the relative difference changing tendencies among these sets of models are concave parabolic, and the lowest differences appear in the standard models (models 3, 8 and 17). Another possible explanation of relative difference is linked to the assumptions made initially in reference [73] on which we relied to establish the expression of E_a given by equation 2.8. Nevertheless, we can consider that these differences between E_{avf} and E_{avf_num} remain within an acceptable range. Therefore, equation 2.15 established here can reasonably be exploited to predict the energy loss rate in RCAVF.

2.5.2 Relationship between energy loss rate and GPs

We used Matlab2017 to analyze deeper the relationship between E_{avf} and the different GPs. The curves illustrating this relationship are represented in figures 2.10 to 2.14. For each figure, the evolution of E_{avf} as a function of a GP is illustrated. For each GP, the evolution of the E_{avf} is parameterized by one of the remaining GPs (subfigures (a) to (d)). The three remaining GPs are kept constant and equal to their respective value corresponding to the standard model given in table 2.2 (chapter 2 section 2.4.2).

Thus, figure 2.10 shows the relationship between E_{avf} and D_{ra} . In figure 2.10 (a), we set h , D_a , and θ to the standard constant values and change D_{cv} . From this figure, we observe that for all the values of D_{cv} , the E_{avf} decreased when the D_{ra} increased. For a fixed value of D_{ra} , the energy loss rate was lower when the D_{cv} increased. The decrease in E_{avf} as a function of D_{ra} was more pronounced for the smaller D_{cv} values. This general tendency to have lower losses as the diameter of the artery or vein increases can be explained by lower blood velocities at constant flow and larger diameters. As a result, the friction decreases.

In figure 2.10 (b), we set D_{cv} , D_a , and θ to the constant values and change h . The behavior of E_{avf} versus D_{ra} was the same as in the previous case. The energy loss rate decreased when D_{ra} increased. Here, on the other hand, for a fixed value of D_{ra} , the energy loss was more significant when the distance h increased. This result seems consistent since the friction loss rate is proportional to the distance traveled by the blood. A greater distance h implies a greater length of the bending vein, therefore, a more significant energy loss rate appears.

Figure 2.10 (c) portrays the relationship curve between E_{avf} and D_{ra} when D_{cv} , h , and θ are unchanged and D_a is changed. Here the behavior was the same as for figure 2.10 (a). A larger diameter is the source of a more limited energy loss rate.

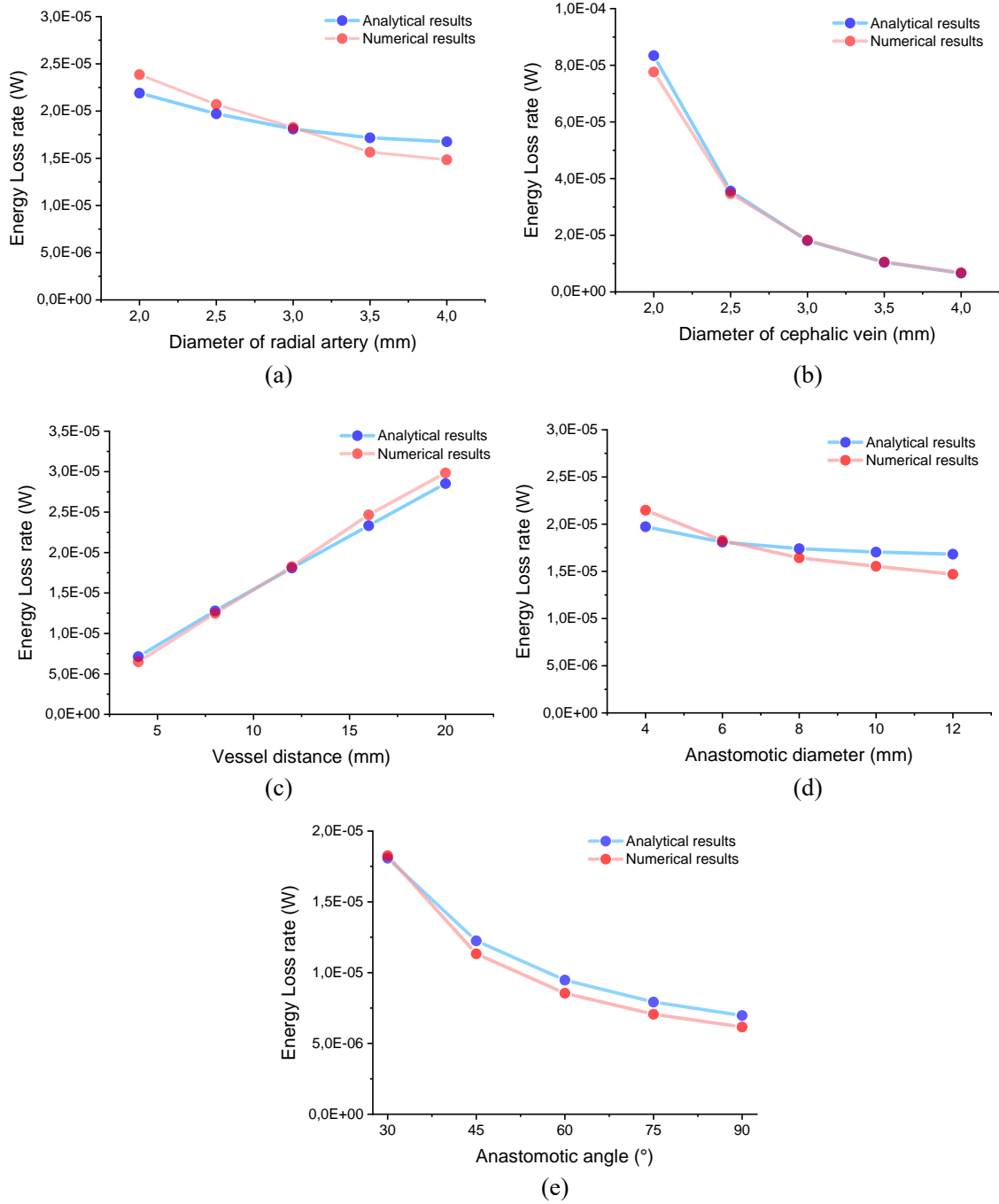


Figure 2.9: Comparison of numerical results and analytical results in 25 models

Figure 2.10 (d) gives the evolution of E_{avf} as a function of D_{ra} and θ when D_{cv} , h , and D_a are unchanged. The decrease in the angle accentuated the decrease in E_{avf} as a function of the diameter.

Without detailing the analysis of all figures 2.10 to 2.14, it is possible to conclude that we have the following general tendencies:

- E_{avf} is inversely proportional to D_{ra} , D_{cv} , D_a , and θ , and proportional to h . In other words, if surgeons want to improve the maturity rate of RCAVF, we suggest them choose RA and CV with larger diameters and closer distance and make an anastomotic plan with a larger anastomotic diameter and anastomosis angle.
- Compared to D_{ra} , D_{cv} has a more significant impact on E_{avf} . Large-diameter CV (D_{cv}) can effectively reduce the energy loss rate in the fistula and increased the maturity rate of RCAVF than large-diameter RA (D_{ra}). Figure 2.10 and figure 2.11 show that when D_{ra} changed, the range of variation of E_{avf} was much smaller than the change caused by changing D_{cv} . We can also see that the curves in figure 2.11 were steeper than figure 2.10. Therefore, we can prove that the maturity rate of RCAVF has a significant correlation with D_{cv} , and the correlation with D_{ra} was relatively weak. This result agreed with the reference [63], which summarized a clinical survey carried out on 96 patients who used RCAVF for dialysis. The author concluded that fistula maturation correlated with D_{cv} , whereas there was no correlation with D_{ra} .
- To increase the maturity rate of RCAVF, the choice of θ was more important than D_a . By comparing figure 2.13 with figure 2.14, we can observe that variation of E_{avf} with θ was more significant than D_a . When θ increased, the energy loss rate can be effectively reduced in RCAVF. It can be seen from figure 2.13 (c) and figure 2.14 (b) that when D_{cv} changed, the effect of D_a on E_{avf} was almost negligible. It can be seen from figure 2.13 (d) and figure 2.14 (d) that only when θ was very small, the D_a have some effect on the energy loss. Therefore, increasing θ was more effective in increasing the maturity of RCAVF than increasing D_a . This was also the main reason why we chose to study the relationship between anastomotic angle and wall shear stress distribution in chapter 3.
- When h was large, it was recommended to choose a larger D_{cv} to reduce E_{avf} . It can be observed from figure 2.12 (b) and Figure 2.12 (d) that the greater the h , the greater the influence of D_{cv} on E_{avf} . Therefore, for some patients with RA and CV on different sides of the arm, the selection of D_{cv} was particularly important. If the patient's CV (D_{cv}) was too small or the anastomosis design cannot be achieved with a large θ due to the limitation of the muscles or other tissues in the arm, in order to guarantee the maturity at this point, we proposed surgeons to decrease the h (for example, releasing part of the CV in the forearm) to reduce the energy loss rate or choose other types of AVF.

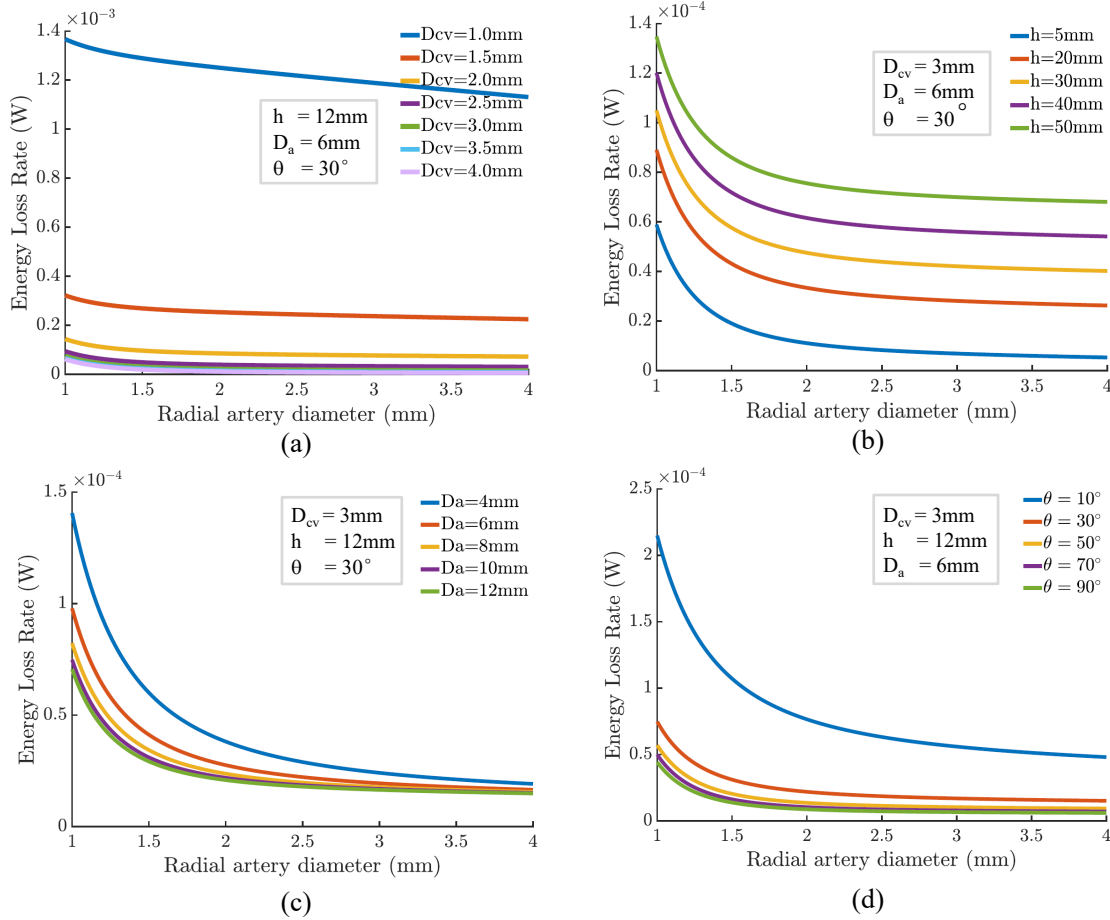


Figure 2.10: The relationship between energy loss rate (E_{avf}) and radial artery diameter (D_{ra})

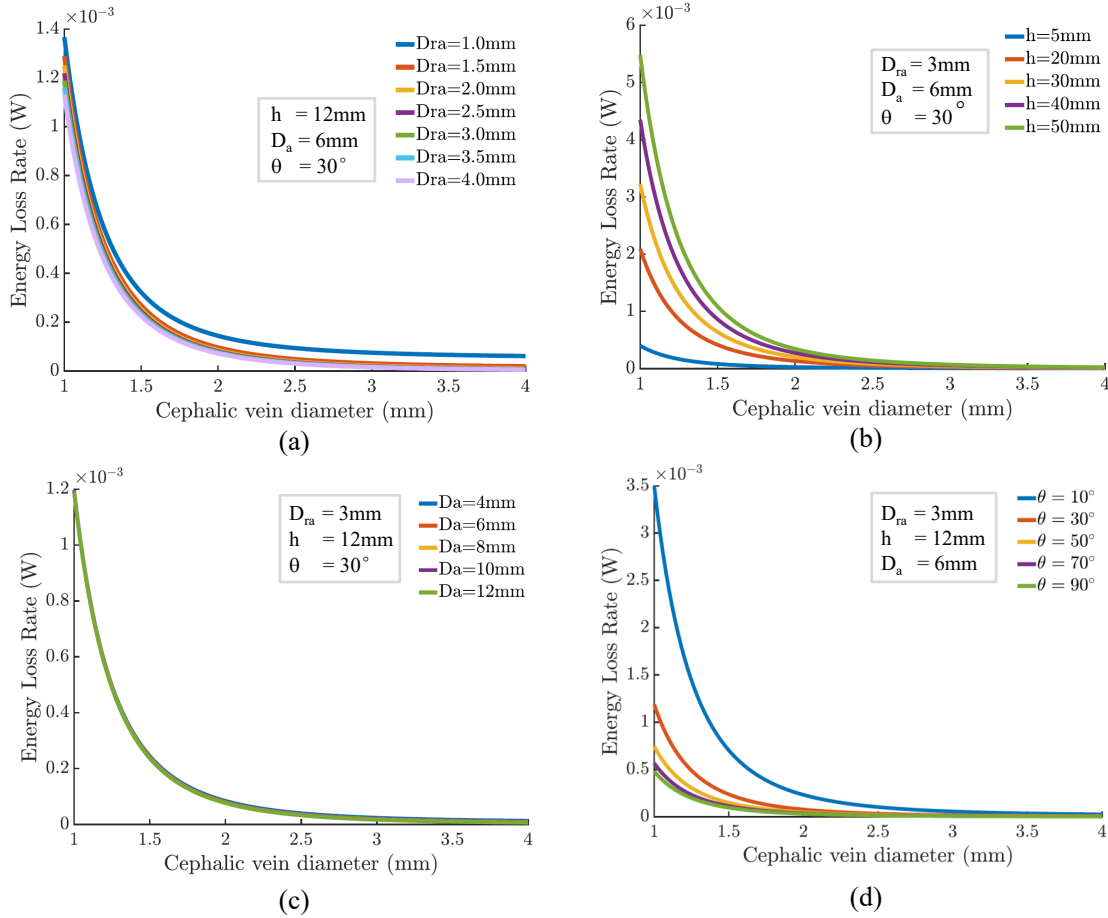
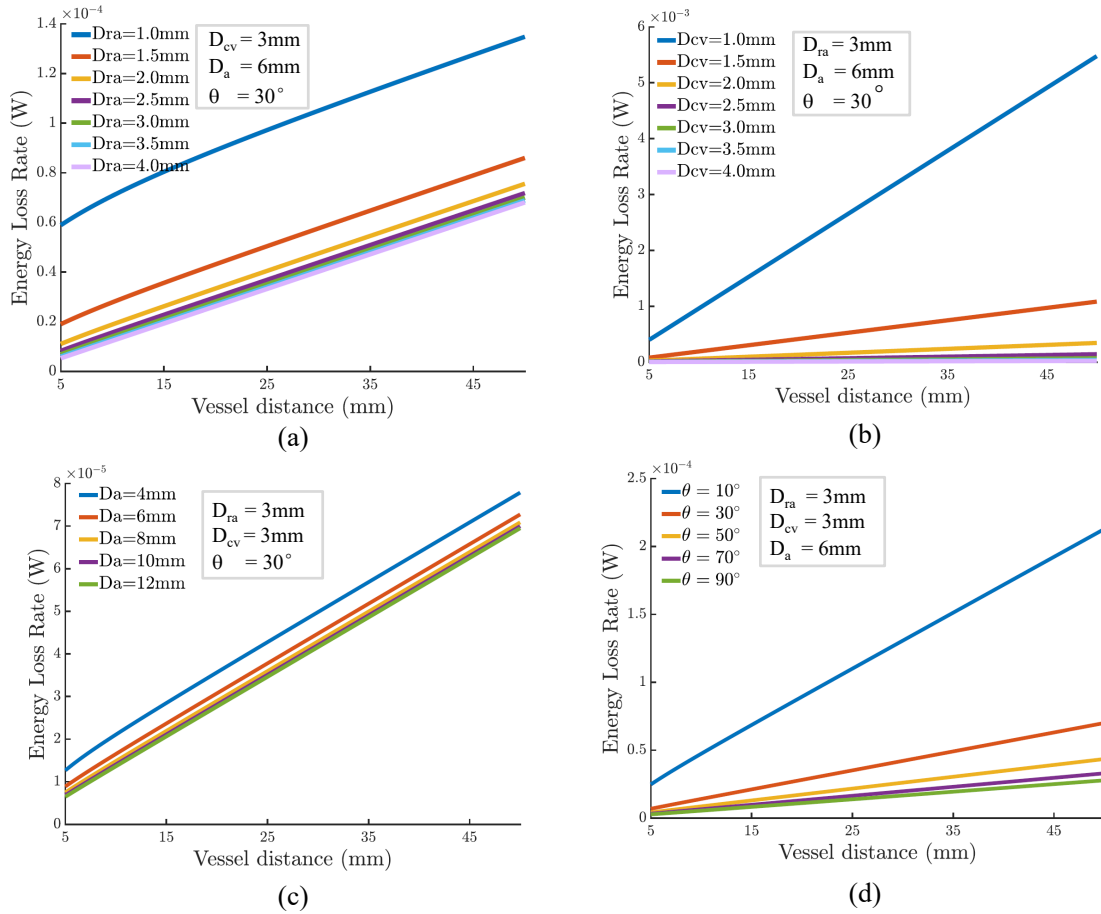
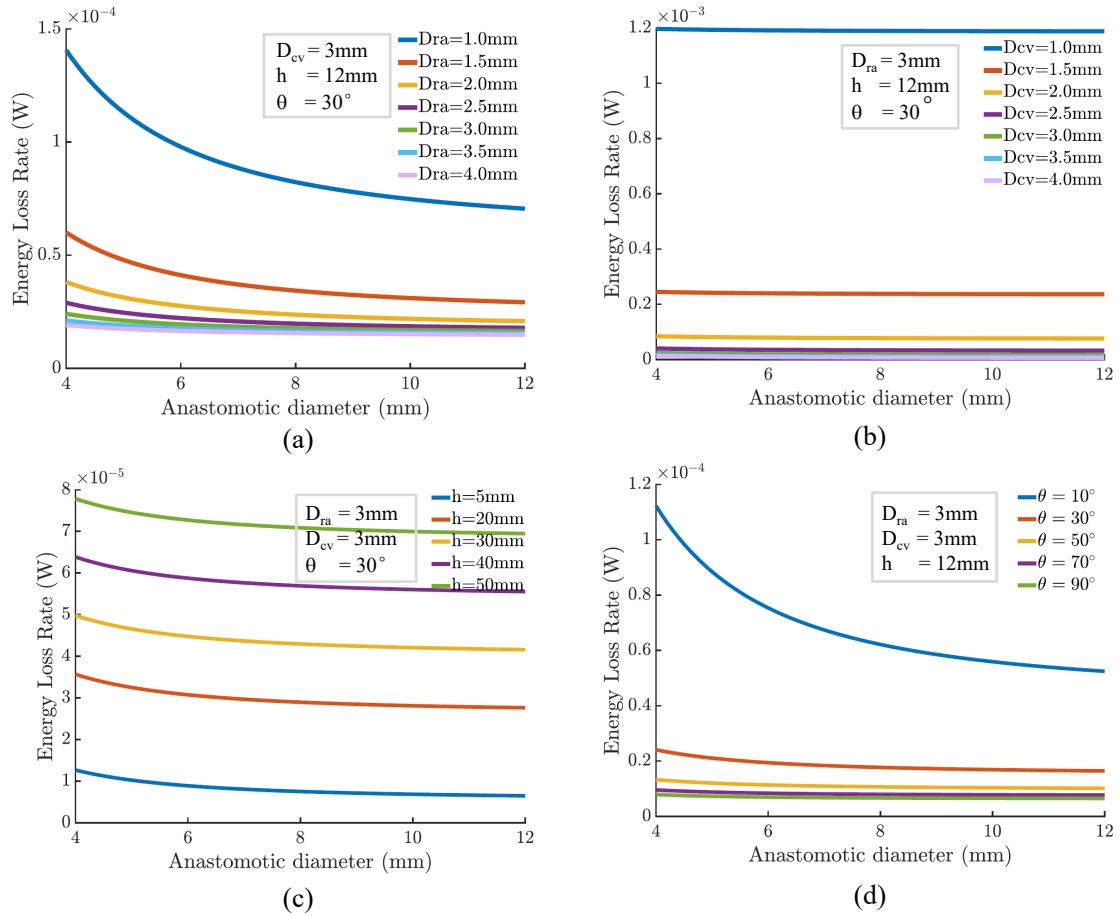


Figure 2.11: The relationship between energy loss rate (E_{avf}) and radial artery diameter (D_{cv})


 Figure 2.12: The relationship between energy loss rate (E_{avf}) and radial artery diameter (h)


 Figure 2.13: The relationship between energy loss rate (E_{avf}) and radial artery diameter (D_a)

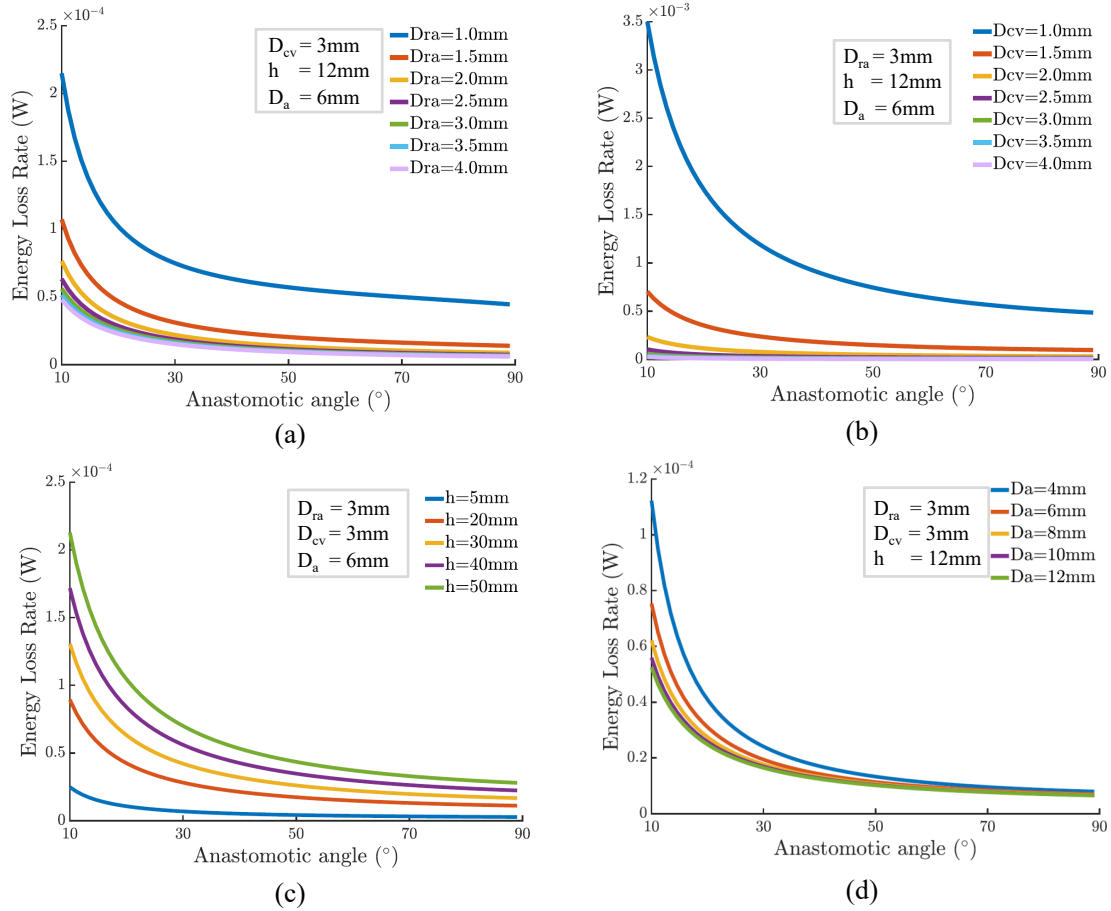


Figure 2.14: The relationship between energy loss (E_{avf}) and anastomotic angle (θ)

2.6 Discussions and conclusions

In this chapter, with evaluations of the energy loss rate E_{avf} in RCAVF, it is found that E_{avf} is inversely proportional to D_{ra} , D_{cv} , D_a , and θ , whereas proportional to h . Therefore, we recommend surgeons choose the vessels with large diameters, close distance, and increase the diameter and angle of the anastomosis to minimize E_{avf} . Simultaneously, we can explain the results of many clinical empiricisms with our formula. For instance, increasing D_{cv} is more effective in guarantee the RCAVF maturity than increasing D_{ra} . We also find that augmenting θ is more significant in reducing E_{avf} than increasing D_{ra} .

It is the first study that proposes to help surgeons design the fistula shapes from the perspective of energy loss. This new complete model studied the different GPs. The θ seems to be an important parameter, more than the anastomotic diameter. This phenomenon can be explained. The energy loss at the RCAVF anastomosis is mainly caused by the friction E_f of the venous bending segment. The loss due to friction is called the major loss because it is much larger than the minor loss (E_a and E_b) due to local shape changes. The change of θ will cause the length of the venous bending segment to change and thus change the major loss, while the change of D_a will only cause a slight change in E_a . Therefore, compared with θ , the influence of D_a on E_{avf} is almost negligible. This result may raise some questions about surgical theories regarding the treatment of AVF complications, such as high flow correction. Depending on the model, reducing D_a to reduce high-flow AVF may not have real meaning. To verify this result, other studies must be conducted on mature AVF using this model.

This model can also be used to design other native AVFs and AVG (arteriove-nous graft) shapes. In use, the inlet flow rate and GPs need to be reset, and the minor loss coefficients K_t and K_h in this model need to be changed according to relevant references when blood flow direction at the anastomosis changes.

Numerical simulation to optimize the RCAFV configuration

In this chapter, we optimize the anastomotic angle of RCAFV through numerical simulation. By observing the hemodynamic behaviors and WSS distributions in the RCAFV, we find that a small anastomosis angle is more conducive to reducing the negative stimulation caused by the disturbed flows on the vessel wall. By comparing the non-mature models and the mature models, we find that the non-mature models can also help the surgeon to optimize the preoperative anastomosis plan of RCAFV. At the same time, we analyze the prone locations of stenoses and their changing trends with θ .

Contents

3.1	Introduction	61
3.2	RCAFV physical modeling	62
3.2.1	Blood mechanical properties	62
3.2.2	Numerical model definitions	63
3.2.2.1	Computational fluid dynamics numerical models	63
3.2.2.2	Fluid-structure coupling numerical model	64
3.2.3	Mechanical properties of RCAFV walls tissue	65
3.3	Computational fluid dynamics simulation	67
3.3.1	The governing equations for fluid dynamics	67
3.3.2	Fluid domain discretization	70
3.3.3	Boundary condition	73
3.3.3.1	Flow rates measured by DUS images	75
3.3.3.2	Inlet velocity profile creations	76
3.3.4	Fluid simulation with Foam-extend	77
3.4	Fluid-structure interaction simulation	79
3.4.1	Fluid-structure coupling equations	79
3.4.1.1	fluid domain	79
3.4.1.2	Solid domain	81
3.4.2	Solid domain discretization	81
3.4.3	Boundary conditions	82
3.4.4	Fluid-structure interaction simulation in Foam-extend	82
3.5	Result analysis	84
3.5.1	Analytical indicators used in the result analysis	84
3.5.1.1	Hemodynamic analysis	84

3.5.1.2	Wall shear stress distributions	85
3.5.2	Comparison between Newtonian and non-Newtonian fluids	86
3.5.3	Comparison between CFD and FSI non-mature RCAVF models	89
3.5.4	RCAVF mature model verified by clinical imaging measurement	94
3.5.5	Analyzing the results of non-mature models	96
3.5.5.1	Hemodynamic flow in non-mature models	96
3.5.5.2	Wall shear stress distributions in non-mature models	99
3.5.6	Analyzing the results of mature models	104
3.5.6.1	Hemodynamic flow in mature models	104
3.5.6.2	Influence of distal artery inlet blood flow on recirculating region in mature models	107
3.5.6.3	Wall shear stress distributions in mature models	111
3.5.7	Discussions and Conclusions	116

3.1 Introduction

From the previous chapter, we find that θ has a much larger impact on energy loss in RCAVF than D_a , it means that the hemodynamic behaviors in RCAVF are much more affected by θ than D_a . For each patient with specific vessel diameters and vessel distance, the way to optimize the RCAVF configuration is to have a more patient-suitable anastomotic design. The favorite way is to improve the anastomotic angle θ . Therefore, the numerical simulations in this chapter aim at seeking for the best θ to ameliorate the hemodynamic behavior in RCAVF.

After AVF creation, the ideal hemodynamic changes in the blood vessel can accelerate the adaptive remodeling of the vessel wall. However, the disturbed flow in the fistula is the critical factor leading to AVF to non-mature and complications. In order to help surgery better understand and visualize natural phenomena in the fistula, the numerical simulation has been taken into consideration. It is used to solve the governing equations of fluid mechanics in the fistula through a numerical method and obtain the discrete quantitative description of the flow field to predict the blood flow in the RCAVF under different anastomosis angles (θ). In this chapter, we will introduce our numerical simulation steps from RCAVF modeling to visualization and help surgery analyze and optimize the RCAVF configuration.

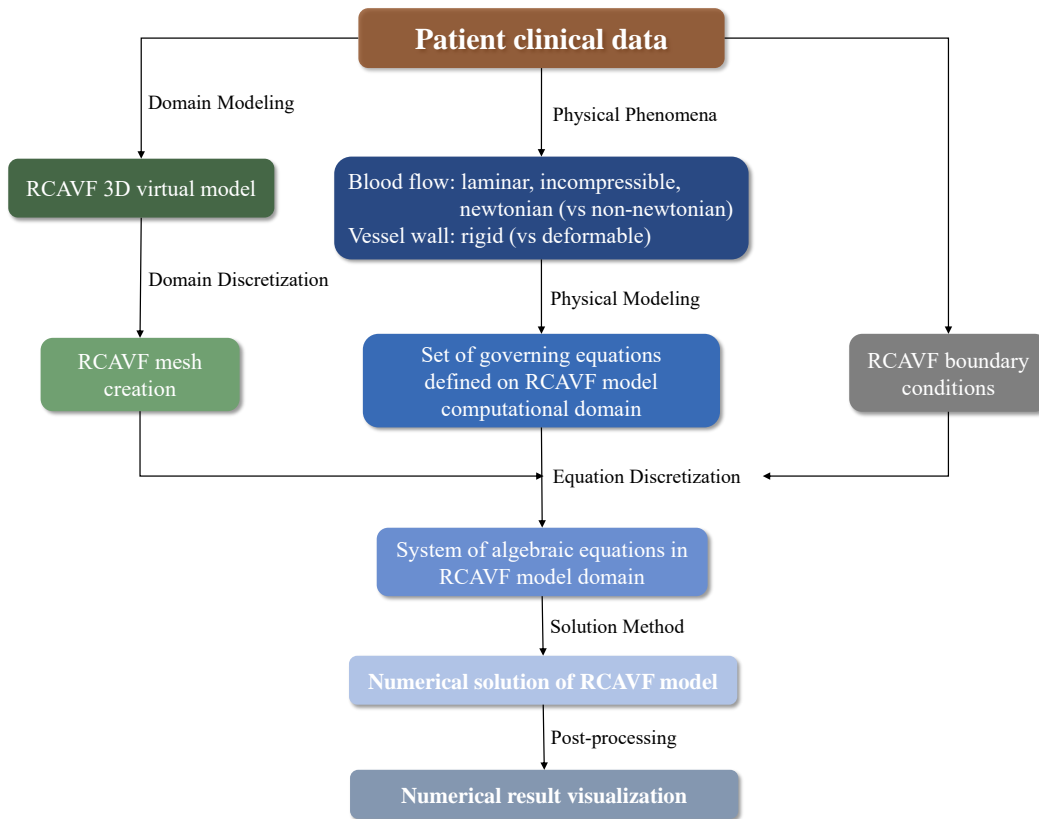


Figure 3.1: RCAVF numerical simulation process

The general numerical simulation processes include [13] [74]: (i) modeling of the geometric domain and the physical phenomena of interest; (ii) discretization of the modeled geometric domain into mesh that forms the computational domain; (iii) equation discretization that transforms the set of conservation partial differential equations governing the physical processes into an equivalent system of algebraic equations defined over each of the elements of the computational domain; (iv) the solution of the resulting set of equations using an iterative solver to yield the final solution field; and (v) Visualize the results through post-processing. RCAVF numerical simulation processes are presented in the fig.3.1. The patient vessel parameters are measured by Doppler ultrasound (DUS). With the clinical data, we created RCAVF 3D virtual models into non-mature and mature models with different anastomotic angles (θ). The RCAVF domain and physical modeling details are described in chapter 2. In this chapter, We compared the simulation results of Newtonian and non-Newtonian fluids, as well as the simulation results of computational fluid dynamics (CFD) and fluid-structure coupling. For CFD simulations, the blood properties in RCAVF models ultimately can be considered as laminar incompressible Newtonian flow and the vessel can be assumed as rigid wall.

All the models are meshed by STAR-CCM+ 12.06.011 [75], which is a commercial computational fluid dynamics (CFD) based simulation software. It allows the modeling and analysis of a range of engineering problems. We use its powerful meshing function to create the mesh for our models. The steps of numerical simulation are realized by open source software: Foam-extend 4.0. Foam-extend is a fork of the OpenFOAM open source C++ library for CFD, which is based on the cell centered finite volume method (FVM). Compared with OpenFOAM, Foam-extend improves the accuracy and stability of FVM discretization and can solve the fluid-structure coupling problems. We used Paraview 5.8.1 to visualize and post-process the simulation results to analyze the mechanical stimulus generated by the disturbing fluid.

3.2 RCAVF physical modeling

3.2.1 Blood mechanical properties

As our research object, blood, its nature and flow state determine the choices of calculation model and calculation method. In our numerical models, blood is considered as :

- *Incompressible fluid*

Blood is composed of blood cells suspended in blood plasma. Plasma, which constitutes 55% of blood fluid, is mostly water (92%) , and contains dissolved proteins, glucose, mineral ions, hormones and blood cells. The blood cells are mainly red blood cells and white blood cells, including leukocytes and platelets. Blood is slightly compressible because of the blood cells. However, in the macroscopic hemodynamic simulation, the compressibility of blood can be ignored. It is usually considered incompressible with constant density of 1060 kg/m^3 in most numerical studies [3].

- *Unsteady fluid*

The important feature of the arterial blood flow is its pulsatile nature. This is its non-ignorable

feature. Therefore, our numerical models used pulsating blood flow.

- *Laminar fluid*

In the tubes, the Reynolds number is defined as [3]:

$$Re = \frac{\text{Inertial forces}}{\text{Viscous forces}} = \frac{\rho v d}{\mu} \quad (3.1)$$

The flow begins to transit to turbulence when the flow exceeds a Re number of approximately 2,300. However, true turbulence will only be found in flows with a Re number of approximately 2,900 [3]. Flows in-between these two values are said to be transitioning and exhibit both laminar and turbulent flow properties.

The flow is laminar in the non-mature models with the Re numbers are lower than 100 (tab.3.1). In the mature models, the flow changes between laminar and transitioning states (tab.3.1). The Re numbers during the systole are greater than 2,300, and during the diastole is less than 2,300. Since the systolic period is relatively short, we assumed that the blood flow is laminar in all the numerical models.

Table 3.1: Re ranges in the numerical models

Models	Blood flowrate range (mL/min)	Re range
Non-mature models	[15,40]	[36,95]
Mature models	[677,1267]	[1450,2714]

- *Newtonian fluid*

Treating blood as a Newtonian fluid is an acceptable assumption in vessels greater than approximately 0.5 mm in diameter[59]. A review study [76] showed that the pattern of wall shear stress in a particular artery for a particular inlet velocity is the same for all non-Newtonian and Newtonian models. The results showed that blood acts as non Newtonian fluid in small arteries [76].The non-Newtonian characteristics happens more evident in the tiny diameters or where the geometry of blood vessels changes [30]. In AVF models, vessel diameters are larger than this critical value, however, the recirculation regions exist in the venous bending segment. Some AVF numerical researches assumed blood as Newtonian fluid [59] [77] and some considered blood as non-Newtonian flow [38] [37]. In mature models, it is acceptable to use the Newtonian fluid due to the large vessel diameters and the high flow rates. To verify the applicability of the Newtonian fluid hypothesis in the non-mature models, we compared these two types of fluids. According to the comparisons of velocity fields and the wall shear stress distributions (shown in section 3.5.2), the Newtonian assumption is acceptable in the non-mature models.

3.2.2 Numerical model definitions

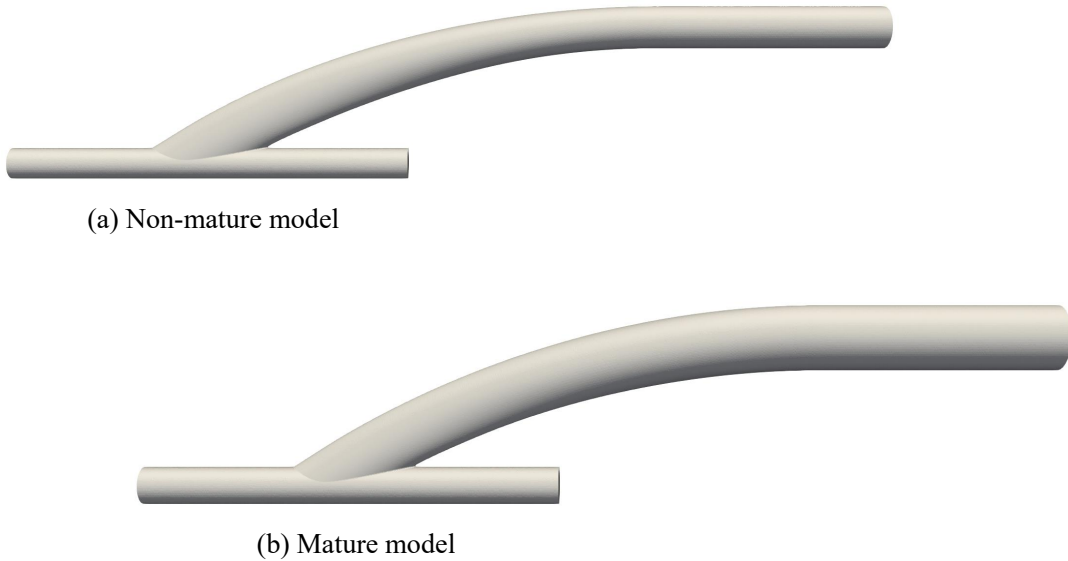
3.2.2.1 Computational fluid dynamics numerical models

In computational fluid dynamics (CFD), the vessel walls are regarded as rigid and zero-thickness layers. The simulations are concentrated on blood rheology. The CFD models are divided into

two groups: non-mature models and mature models. The details of models are shown in table.3.2. Non-mature models are the RCAVFs that have just been anastomosed, and the blood vessels have not yet been dilated. The vessel diameters (D_{ra} , D_{cv}), the vessel distance (h), and the anastomosis diameter (D_a) were measured from an actual patient whose anastomosis was established on March 7th, 2019. Only the anastomotic angle (θ) was changed in five values (30° , 45° , 60° , 75° and 90°). The mature models present the RCAVFs that can be used for dialysis. D_{cv} and D_{ra} were dilated to 6.1 mm and 3 mm (measured on April 26th, 2019). h and D_a remained unchanged, and θ were changed in the same way as non-mature models. (Hospices civils de Lyon provided the patient data.)

Table 3.2: Geometric parameters in CFD models

		Non-mature models	Mature models
GPs	D_{ra}	2.7 mm	3 mm
	D_{cv}	3.7 mm	6.1 mm
	h	12 mm	
	D_a	10 mm	
	θ	$30^\circ, 45^\circ, 60^\circ, 75^\circ, 90^\circ$	

Figure 3.2: Non-mature vs. mature models with θ equals 30°

3.2.2.2 Fluid-structure coupling numerical model

In the reality, vessel tissue is highly-deformable solid media. However CFD models do not take the wall deformation into consideration. In this chapter, we compared the results between CFD and fluid-structure coupling simulations to find if it is essential to consider fluid-structure interaction

(FSI). FSI simulations take many times longer than CFD due to the added complexity of the vessel wall mechanics and in a large part due to the inherent instability in partitioned coupling techniques when dealing with these strongly-coupled problems [78] [76]. Therefore, the FSI simulation was only developed in the non-mature model with θ equal 90° . Because the bending venous length in the 90° model is the smallest, it can speed up the calculation time. In FSI model, we assumed the RCAVF wall with uniform thickness 0.33 mm [79]. The 3D virtual FSI model is shown in fig.3.3.

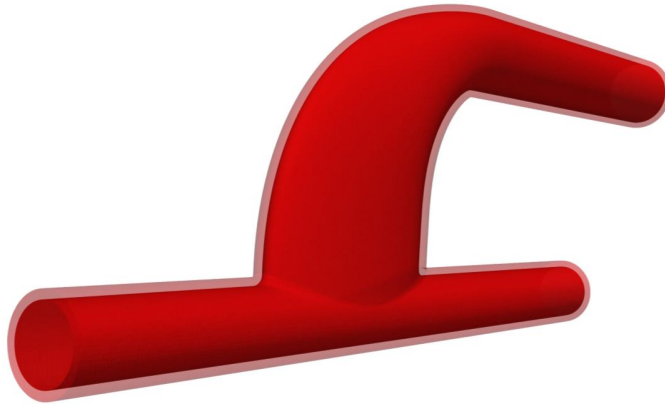


Figure 3.3: RCAVF 3D virtual model with vessel wall ($\theta=90^\circ$)

3.2.3 Mechanical properties of RCAVF walls tissue

Vessel wall mechanics plays an essential role in hemodynamic problems. The mechanical interaction between blood and vessel walls is mainly responsible for propagating pressure waves from the heart to the whole body. This interaction is the main factor that helps regulating blood pressure in the body [78]. Numerical simulations considering fluid-structure interaction (FSI) can make the numerical results more accurate. However, the FSI simulation runs significantly slower than CFD [78]. Therefore, all RCAVF numerical models are simulated by CFD. We only performed FSI simulation on a non-mature model to study the necessity of fluid-structure coupling.

The stress-strain relation is able to give the solid a unique characterization (fig.3.4). σ is the Lagrangian stress which normalize force by the area. The strain, ε , is obtain by normalizing the length change to the starting length. The Hookean or linear elastic material has the linear relation between stress and strain. The straight line in figure 3.4 shows this relation. The constant slope is called the Young modulus of elasticity $E = \sigma/\varepsilon$. It defines a material property and is a measure of the stiffness of the material [11]. Biological materials almost always exhibit a curved stress-strain relationship with convexity towards the strain axis (fig.3.4), which introduce an incremental elastic modulus, E_{inc} , defined as the local slope of the stress-strain relation [11].

From figure 3.5, E_{inc} of the radial artery wall material was significantly elevated in patients with ESRD compared with normotensive subjects or patients with essential hypertension [12]. Such structural changes are not similar to those observed in aging, atherosclerosis, and hypertension. Thus, the role of renal factors may be suggested, such as those related to water logging, the

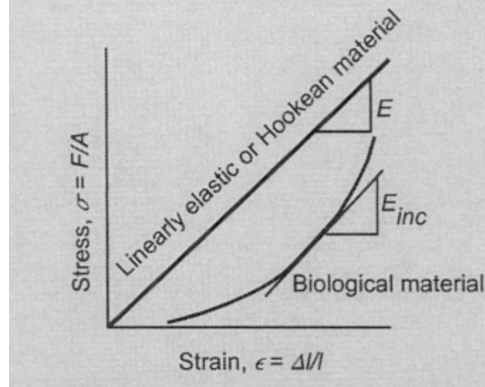


Figure 3.4: The stress-strain relations of biological material and linearly elastic or Hookean material [11]

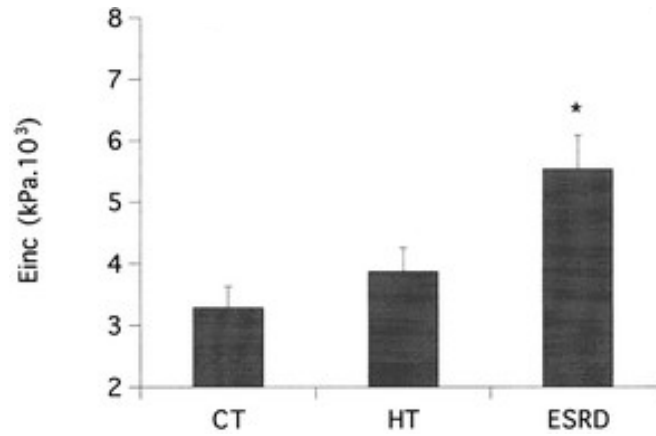


Figure 3.5: Bar graphs showing E_{inc} for the three groups (ESRD: end-stage renal disease; CT: normotensive control subjects; HT: patients with essential hypertension). [12]

accumulation of advanced glycosylation end product, and oxidation damage [80]. This affects not only the arterial wall, but also the venous system. The stiffness of all the vessel walls are increased in patients with ESRD.

Due to the disturbed flow mainly appearing in the bending vein and the slightly differences between the thickness of RA and CV walls, the RA wall was assumed to have the same property as CV wall. In RCAVF FSI simulation, the vessel wall was considered as linear elastic material with the constant thickness of 0.33 mm [81]. Young's modulus was defined by 2 MPa [82] [83] [84]. The density and the poisson's coefficient of vessel wall were defined by 1160 kg/m^3 and 0.454, respectively [83].

3.3 Computational fluid dynamics simulation

3.3.1 The governing equations for fluid dynamics

For the unsteady and three dimensional Newtonian blood flow in RCAVF, its physical phenomena can be described by the Navier-Stokes equations (the continuity and momentum equations), which are highly nonlinear second order partial differential equations in independent variables. The following conservation laws are described under an Eulerian formulation where the focus is on the flow within a specified region in space [13].

- *The continuity equation*

The continuity equation is also called the mass conservation equation. Any flow problem must satisfy the principle of conservation of mass [85], which indicates that in the absence of mass sources and sinks, a region will conserve its mass on a local level. According to this principle, the flux form of the continuity equation can be given by:

$$\frac{\partial \rho}{\partial t} + \nabla \cdot [\rho \vec{v}] = 0 \quad (3.2)$$

With assuming that the blood is incompressible, the pressure changes do not have significant effects on density. It indicates that ρ is constant. Consequently, the continuity equation for incompressible flow can be written as [13]:

$$\nabla \cdot \vec{v} = 0 \quad (3.3)$$

- *The momentum equation*

The principle of conservation of momentum is also a basic principle that any flow system must satisfy. It indicates that in the absence of any external force acting on a body, the body retains its total momentum [13]. Newton's Second Law of motion asserts that the momentum of this specific volume can change only in the presence of a net force acting on it, which could include both surface forces (f_s) and body forces (f_b). By ignoring body forces in RCAVF, conservative form of the momentum equation for incompressible blood flow is obtained as:

$$\rho \frac{\partial \vec{v}}{\partial t} + \rho \nabla \cdot \{ \vec{v} \cdot \vec{v} \} = f_s \quad (3.4)$$

The surface forces are due to pressure and viscous stresses which can be expressed in term

of the Cauchy stress tensor $\vec{\Sigma}$. In the Cartesian coordinate system, the stress tensor can be written as [3]

$$\Sigma = \begin{pmatrix} \sigma_{xx} & \tau_{xy} & \tau_{xz} \\ \tau_{yx} & \sigma_{yy} & \tau_{yz} \\ \tau_{zx} & \tau_{zy} & \sigma_{zz} \end{pmatrix} \quad (3.5)$$

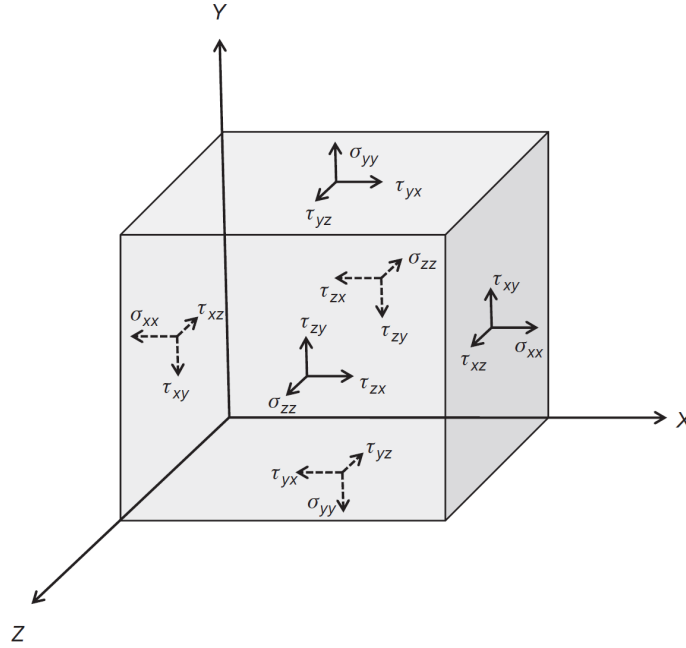


Figure 3.6: The nine components of the stress tensor on a differential fluid volume [3] (for conserve angular momentum, only six tensors are independent)

where σ_{ii} represent normal stresses and τ_{ij} represent shear stress acting on face i in the j direction (fig.3.6). $\vec{\Sigma}$ is usually split into two terms:

$$\vec{\Sigma} = -p\vec{I} + \vec{\tau} \quad (3.6)$$

where \vec{I} is the identity tensor of size (3×3) , p is the pressure, and $\vec{\tau}$ is the viscous stress tensor. p is negative of the mean of the normal stress and is given by eq.3.7. For Newtonian blood flow, $\vec{\tau}$ can be expressed eq.3.8 [13]. where μ is the molecular viscosity coefficient, λ the bulk viscosity coefficient usually set equal to $-(2/3)\mu$, the superscript T refers to the transpose of $\nabla \vec{v}$. These stress tensors play an important role in fistula remodeling and maturation.

$$p = -\frac{1}{3}(\sigma_{xx} + \sigma_{yy} + \sigma_{zz}) \quad (3.7)$$

$$\vec{\tau} = \mu\{\nabla \vec{v} + (\nabla \vec{v})^T\} + \lambda(\nabla \cdot \vec{v})\vec{I} \quad (3.8)$$

The surface force acting on a differential surface element of area dS and orientation \vec{n} (fig.3.7), is $(\vec{\Sigma} \cdot \vec{n})dS$. Applying the divergence theorem, the total surface force acting on the control volume is given by

$$f_s = -\nabla p + [\nabla \cdot \vec{\tau}] \quad (3.9)$$

$$= -\nabla p + \nabla \cdot \{\mu [\nabla \vec{v} + (\nabla \vec{v})^T]\} + \nabla(\lambda \nabla \cdot \vec{v}) \quad (3.10)$$

$$= -\nabla p + \nabla \cdot \{\mu \nabla \vec{v}\} + \vec{Q}^v \quad (3.11)$$

For incompressible blood flows, the divergence of the velocity vector is zero ($\nabla \cdot \vec{v} = 0$) and the viscosity is constant, \vec{Q}^v can be ignored. The momentum equation can be finally written:

$$\rho \frac{\partial \vec{v}}{\partial t} + \rho \nabla \cdot \{\vec{v} \cdot \vec{v}\} = -\nabla p + \nabla \cdot \{\mu \nabla \vec{v}\} \quad (3.12)$$

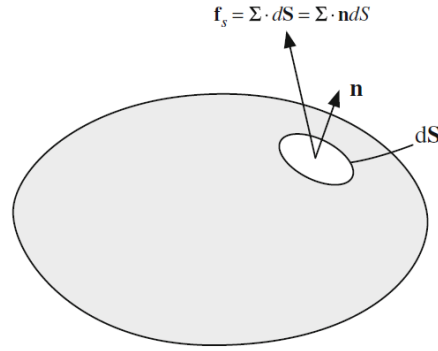


Figure 3.7: The surface forces acting on a differential surface element expressed in terms of the stress tensor[13] (bold font represents vector)

- Conservation of energy

The first law of thermodynamics is one of the basic laws in nature. It states that energy can neither be created nor destroyed during a process; it can only be transformed or transferred from one form (mechanical, kinetic, chemical, et.) to another, while the total energy in an isolated system remains constant. The mathematical description of energy conservation can be written as [13]:

$$\frac{\partial \rho e}{\partial t} + \nabla \cdot [\rho \vec{v} e] = -\nabla \cdot \vec{q}_s - \nabla [p \vec{v}] + \nabla [\vec{\tau} \vec{v}] + \vec{f}_b \cdot \vec{v} + \dot{q}_v \quad (3.13)$$

where e is the total energy per unit mass, \dot{q}_v represents the rate of heat source or sink within the material volume per unit volume, and \vec{q}_s the rate of heat transfer per unit area across the surface area of the material element.

The eq.3.13 can also be written in terms of temperature. For the incompressible RCAVF blood flow, the changes in temperature are not significant, there is no heat source, and the

body force can be ignored, the energy equation becomes:

$$\rho \frac{\partial T}{\partial t} + \rho \nabla \cdot [\vec{v}T] = \nabla \cdot \left[\frac{k}{c_p} \nabla T \right] \quad (3.14)$$

where k is the thermal conductivity and c_p is the isobaric specific heat of the substance.

For the incompressible unsteady blood flow in the RCAVF, the final form of the general governing equations can be described as:

$$\underbrace{\rho \frac{\partial \phi}{\partial t}}_{\text{unsteady term}} + \underbrace{\rho \nabla \cdot (\vec{v}\phi)}_{\text{convection term}} = \underbrace{\nabla \cdot (\Gamma^\phi \nabla \phi)}_{\text{diffusion term}} + \underbrace{Q^\phi}_{\text{source term}} \quad (3.15)$$

ϕ is the transport of a property in flow field. Γ^ϕ and Q^ϕ are various with different equations. Their definitions can be summarized by tab.3.3

Table 3.3: The specific form of each symbol in the general governing equation

Equations	Symbols	ϕ	Γ^ϕ	Q^ϕ
Continuity equation		1	0	0
Momentum equation		\vec{v}	μ	∇p
Conservation of energy		T	$\frac{k}{c_p}$	0

3.3.2 Fluid domain discretization

The most basic consideration of CFD is how to process the continuous fluid in a discrete manner. By discretizing the space area into a sufficient number of calculation areas (a sufficiently small calculation area), and then solving the governing equations in each area, the physical quantity distribution on the overall calculation area will be finally obtained. For 3D simulation, the most important step is the mesh creation.

Mesh includes structured mesh and unstructured mesh (fig.3.8). The two-dimensional (2D) cells of the structured mesh are quadrilaterals, and the three-dimensional (3D) cells are hexahedrons (fig.3.9). Most structured meshes have high quality, require less memory, and lower iteration time during the CFD simulation. Its range of useful geometric objects, however, is relatively narrow. It is more suitable for regular shapes. For solving areas with completely arbitrary geometries, the unstructured meshes have more advantages. Unstructured meshes have no structural restrictions. The nodes and cells are arbitrarily distributed. Its cells include many types (shown in fig.3.9), which allow it has superior geometric flexibility. Nonetheless, there are significant penalties to be paid for this flexibility, both in terms of the connectivity data structures and solution algorithms.

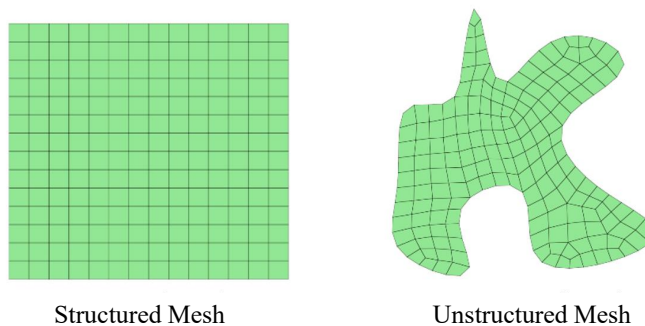
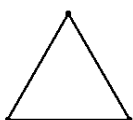


Figure 3.8: Structural mesh and unstructured mesh

2D Cell Types

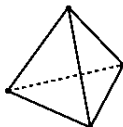


Triangle

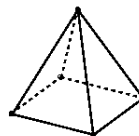


Quadrilateral

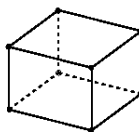
3D Cell Types



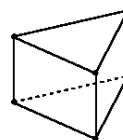
Tetrahedron



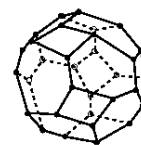
Pyramid



Hexahedron



Prism/Wedge



Polyhedron

Figure 3.9: Mesh cell types

The bending vein segment makes the RCAVF geometry complex. Structured mesh can be used [86], however, it requires a lot of manpower. Since we needed to mesh dozens of RCAVF models, the unstructured meshes were finally taken into consideration. The blood domain was discretised into a polyhedron mesh by STAR-CCM+ 12.06.011 (fig.3.10). The polyhedral mesh is derived directly from the tetrahedral mesh by forming polygons around each node in the tetrahedral mesh. The polyhedral cells hold great promise in producing equivalent accuracy results compared to other unstructured mesh types with the added benefits of faster converge with fewer iterations, robust convergence to lower residual values, and faster solution runtimes [87].

A mesh convergence study is necessary to ensure that the numerical solution is mesh-independent and finds an optimal mesh size to guarantee accuracy. Four meshes were created on the RCAVF non-mature model with $\theta = 90^\circ$ (fig.3.10) of varying cell sizes. The mesh details are shown in the table.3.4. Mesh convergence was studied with a transient analysis, based on the numerical values at systole: blood domain average velocity, blood domain average pressure, and vessel surface average wall shear stress (WSS) in RCAVF. Those average values were post-processed at the third pulse cycle by Paraview 5.8.1, which were the relevant criteria for this sensitivity study. Figure 3.11 shows the WSS distribution in different mesh sizes at systole. It can be found that the WSS distribution in the PA segment and around the anastomosis became stable when the mesh sizes decreased. The average values are compared in the table.3.5. Each result (R) was compared with the result of the densest mesh (Rd), the differences were calculated by equation 3.16. The mesh obtained negligible errors (1%) with 0.25 mm cell size. In conclusion, the mesh size for all the RCAVF models was set as 0.2 mm.

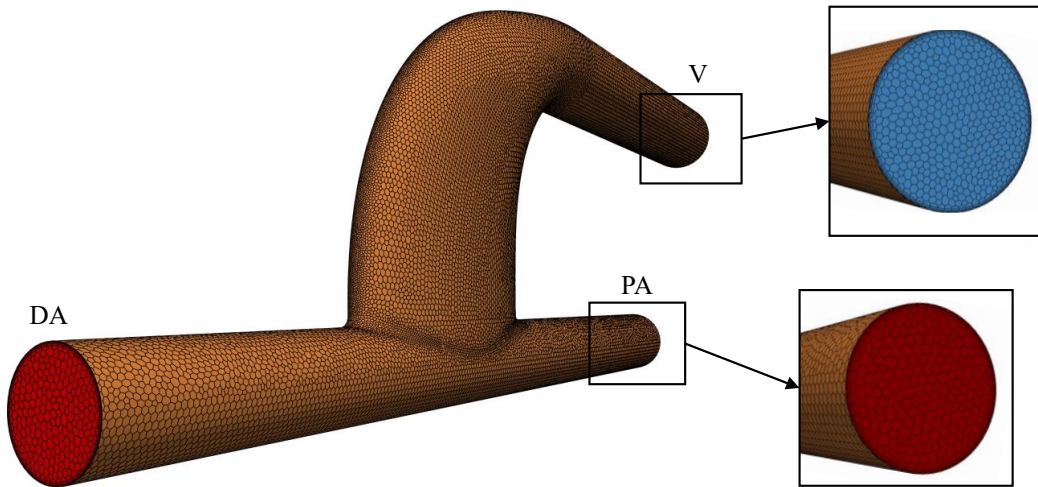


Figure 3.10: RCAVF blood fluid mesh by STAR-CCM+ 12.06.011 with $\theta = 90^\circ$ (250 977 cells)

$$Difference = \frac{|R_d - R|}{R_d} \cdot 100\% \quad (3.16)$$

Table 3.4: Mesh details for mesh convergence analysis

Mesh size	Cells	Vertices
0.2mm	250 977	926 118
0.25mm	177 226	627 541
0.3mm	145 005	500 516
0.35mm	119 400	400 095

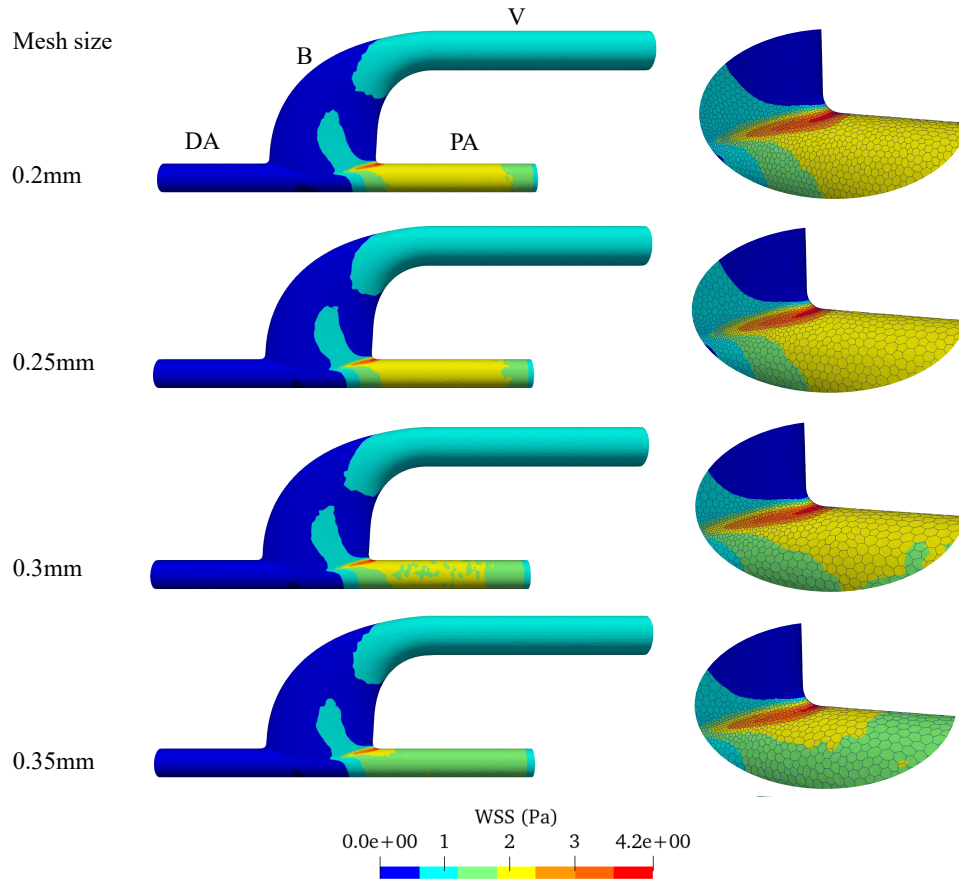


Figure 3.11: Comparison of the WSS distribution of different mesh sizes at systole

3.3.3 Boundary condition

Setting appropriate boundary conditions is vital for a successful simulation. Ill-posed boundary conditions will lead to physically incorrect predictions, and in many cases solver failure. The appropriate boundary conditions will make it possible to impose the uniqueness of the solution during the resolution of the partial derivative equations.

The most common boundary conditions are Dirichlet and Neumann boundary conditions. When using a Dirichlet boundary condition, one prescribes the variable value at the boundary, e.g. $u(x) = \text{constant}$. When using a Neumann boundary condition, one prescribes the gradient normal to the

Table 3.5: Mesh convergence analysis

Mesh size	Domain average velocity (m/s)		Domain average pressure (Pa)		Surface average WSS (dyn/cm ²)	
	Results	Differences	Results	Differences	Results	Differences
0.2mm	0.0205677	-	1186.3	-	1.351	-
0.25mm	0.0206819	0.56%	1184.4	0.16%	1.364	0.56%
0.3mm	0.0208339	1.29%	1183.0	0.28%	1.389	1.29%
0.35mm	0.0208687	1.46%	1181.6	0.4%	1.418	1.46%

boundary of a variable at the boundary, e.g. $\partial_n u(x) = \text{constant}$. In CFD models, there are four boundary conditions that need to be defined which are as follows:

- *DA_inlet*:

The distal radial artery inlet used a constant flow rate Dirichlet boundary, to which a constant flow rate was applied with a flow profile of Poiseuille.

- *PA_inlet*:

The proximal radial artery inlet used a variable flow rate Dirichlet boundary, to which a flow rate was applied which varies according to the cardiac cycle with a flow profile of Poiseuille and flow resulting from in-vivo DUS imaging.

- *V_outlet*:

The cephalic vein outlet used a pressure Dirichlet boundary, to which a constant pressure was applied to all the models. The constant value was set to 8.7mmHg which was defined by the mean pressure of the cephalic vein at rest [88].

- *Blood_wall*:

The vessel wall of RCAVF to which a no-slip Neumann boundary condition was applied to which the velocity gradient normal to the boundary was zero. The fluid velocity near the wall was the same as the velocity of the wall. In the CFD model with rigid walls, this velocity was zero (non-slip at the boundary).

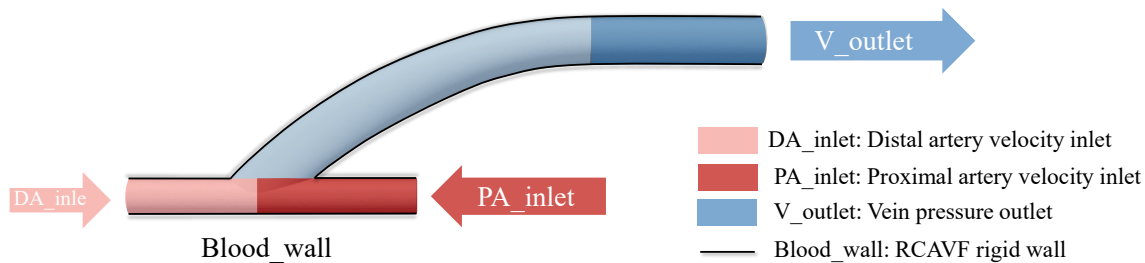


Figure 3.12: RCAVF boundary conditions

3.3.3.1 Flow rates measured by DUS images

- Non-mature models

The mean blood flow in the radial artery at rest is typically less than 25 ml/min [21]. In the non-mature models, we set up a pulse flow with a mean blood flow around 22 ml/min at the proximal RA inlet. The flowrate waveform of PA_inlet (fig.3.13(a)) was adapted from the database established by Willemet et al [89]. They have created a database of 3,325 virtual healthy adult subjects using a validated one-dimensional model of the arterial hemodynamics, with cardiac and arterial parameters varied within physiological healthy ranges. For each simulation, hemodynamic signals (e.g. pressure, flow and distension waveforms) were available at all arterial locations, and allowed the computation of indices of interest. During the anastomosis, the blood flow in RA is stopped by surgical clamps (fig.1.16). When the forceps are released, the blood flow from the distal RA will flow into the fistula along with the blood flow from the proximal RA. The blood flow at DA inlet comes from the blood vessels in the hand, and its pulsation is almost negligible. Therefore we set it to a constant flow with a flow rate of 5 ml/min, calculated by multiplying the average blood velocity at wrist blood vessel (2.87 cm/s) [70] by the smallest cross-section of RA (1.925 mm) [71].

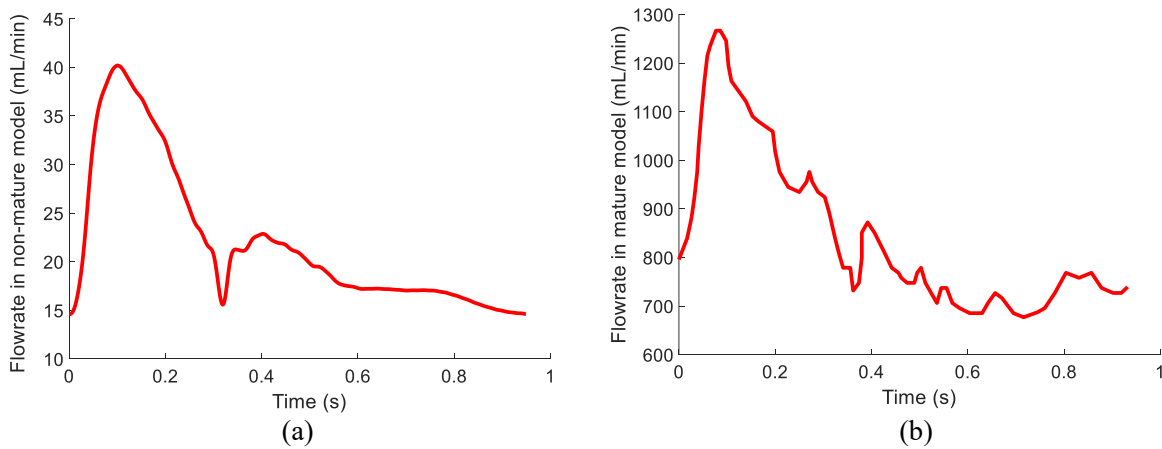
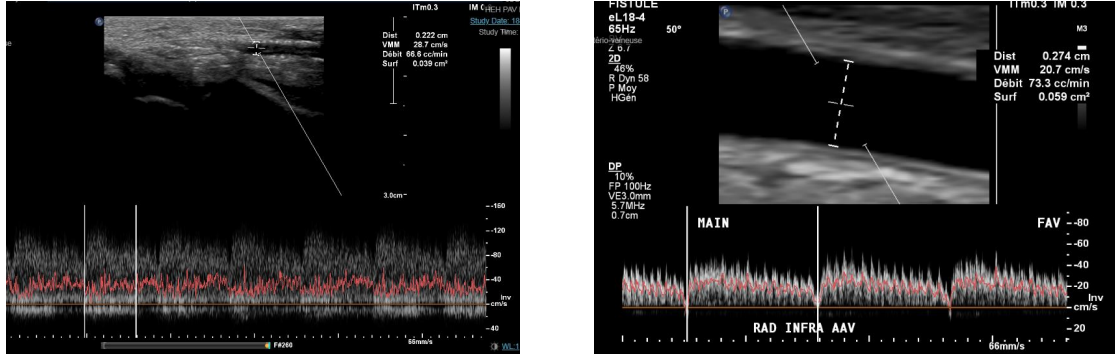


Figure 3.13: (a) The flowrate waveform at the proximal radial artery inlet of non-mature models; (b) The flowrate waveform at the proximal radial artery inlet of mature models

- Mature models

The PA inlet flow rate waveform of mature model was measured by in-vivo DUS imaging (fig.3.13(b)) provided by Hospices Civils de Lyon (HCL). The mean flow rate was 871 ml/min. Due to the resistance of the distal hand capillaries, the DA inlet flow rate is relatively small, and it is normally ignored in fistula DUS imaging measurements. To provide data for our simulations, our clinical partners of HCL measured the DA inlet flow rates of several patients who used RCAVF for dialysis (fig.3.14 shows two of DUS imaging measurements) and found that the pulsation at DA inlet was weak, and the mean flow rates were roughly below 60 to 70 ml/min. In our mature models, the DA inlet flow rate was considered as a constant flow with a flow rate of 60 ml/min.



(a) Flow rate at DA_inlet = 66.6 ml/min

(b) Flow rate at DA_inlet = 73.3 ml/min

Figure 3.14: Flow rates at distal radial artery inlet of two DUS imaging measurements (provided by Hospices civils de Lyon)

3.3.3.2 Inlet velocity profile creations

With the no-slip condition at vessel wall, the blood in the layer in contact with the surface of the vessel comes to a complete stop. This layer also causes the blood in the adjacent layers to slow down gradually as a result of friction. To make up for this velocity reduction, the velocity of the fluid at the midsection of the vessel has to increase to keep the blood flow rate constant. As a result, a velocity gradient develops along the vessel. The velocity profile in fully developed laminar flow in a pipe of radius R is parabolic with a maximum at the centerline and minimum (zero) at the pipe wall [14] (the rightmost velocity profile in fig.3.15). The fully developed velocity profile can be described as a function of the radius r :

$$V(r) = 2V_{avg}(1 - \frac{r^2}{R^2}) \quad (3.17)$$

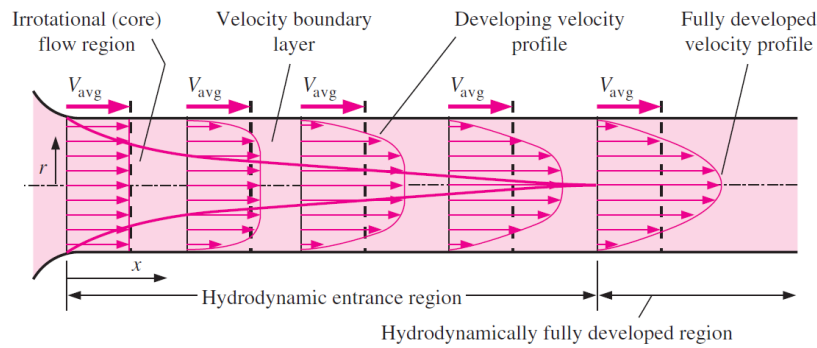


Figure 3.15: Hydrodynamic entry length in a circular pipe [14]

If we set the boundary condition of the inlet to blood flow rate, then we will get a uniformly distributed velocity field (V_{avg}) at the inlet (the leftmost velocity profile in fig.3.15). Blood flow needs to be fully developed before entering the anastomosis. Therefore, the hydrodynamic entry

length has to be considered into our models. Long blood vessels will increase the computation burden and augment the calculation time (especially in fluid-structure interaction simulations). To solve this problem, we used Matlab to construct velocity parabolic profiles at arterial inlets after mesh creations.

First, the inlet mesh points needed to be extracted, and the boundary points (red crosses in fig.3.16) were separated from the inner points (blue points in fig.3.16) to set their velocities to zero. The velocity of each inner point were defined by eq.3.17. All the velocity fields during the pulses were written in the files of Foam-extend form. The complete program is available in appendix A. The PA inlet diastolic and systolic velocity profiles of non-mature and mature models are shown in fig.3.17.

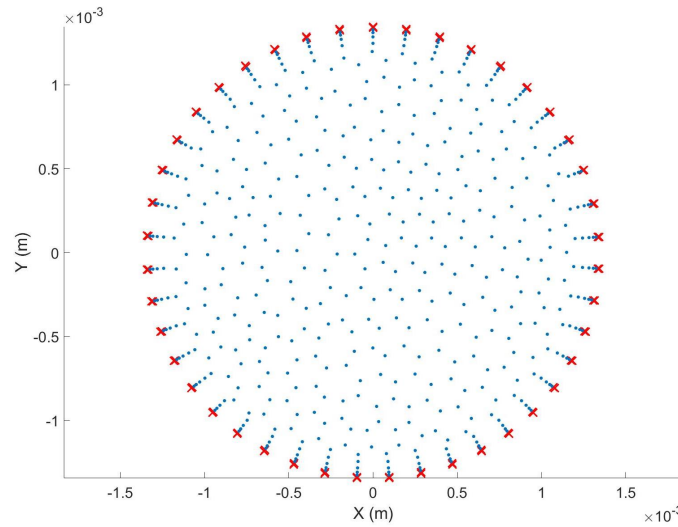


Figure 3.16: Separate the boundary points and inner points

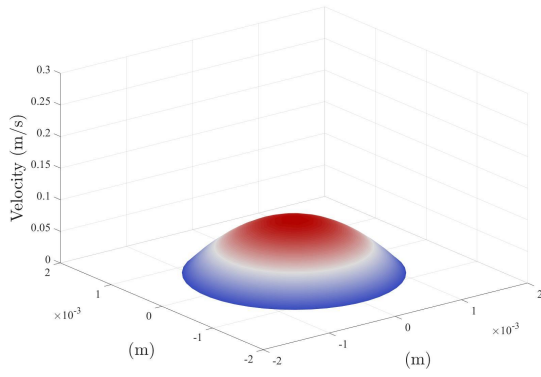
3.3.4 Fluid simulation with Foam-extend

All the numerical fiches of CFD definition details in Foam-extend 4.0 are available in appendix B. The boundary conditions were described in **U** and **P**. The blood properties were defined by **RASproperties**, **transportProperties** and **turbulenceProperties**. The time step for the Newtonian models was set to $\Delta t = 1e-3$ s. For the Non-newtonian case, the time step was set to $\Delta t = 1e-5$ s to guarantee the convergence of the results. The time step parameters, calculation time and the results writing are indicated in the **controlDict**.

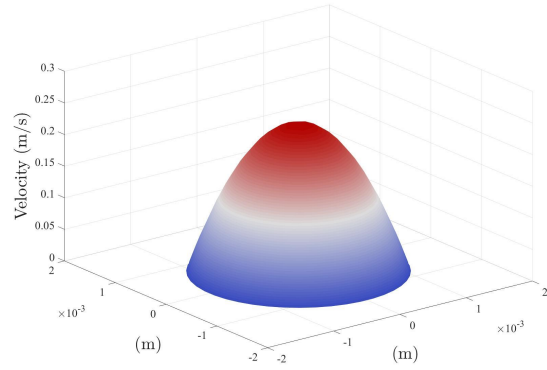
In CFD, there are two basic algorithms to solve the governing equations:

- Pressure Implicit Splitting of Operators (PISO)
- Semi-Implicit Method for Pressure Linked Equations (SIMPLE)

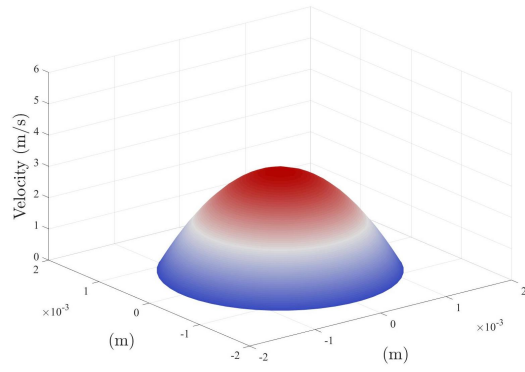
PISO algorithm was proposed by Issa in 1986 without iterations and with large time steps and a lesser computing effort [90]. It is an extension of the SIMPLE algorithm used in CFD to solve



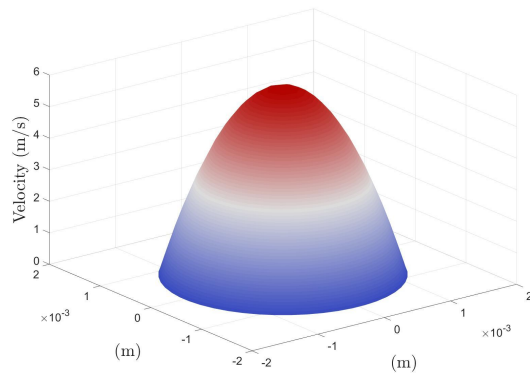
(a) Diastolic velocity profile in non-mature models



(b) Systolic velocity profile in non-mature models



(c) Diastolic velocity profile in mature models



(d) Systolic velocity profile in mature models

Figure 3.17: Velocity profiles at proximal radial artery inlet

the Navier-Stokes equations. PISO is a pressure-velocity calculation procedure for unsteady flow, however, SIMPLE is used for steady state problems. In a comparison study [91], the PISO scheme was found to predict accurate results and was robust. In RCAVF with time-varying `PA_inlet` boundary condition, the PISO algorithm was chosen to solve the equations of fluid fields. The solvers used to solve the equations on the whole fluid domain are precised in `fvSchemes` and `fvSolutions`.

3.4 Fluid-structure interaction simulation

Fluid-structure coupling problems play an important role in many scientific and technical fields, but the in-depth numerical study of these problems remains a challenge due to their strong non-linearity and multidisciplinary characters. For most FSI problems, analytical solutions are impossible to obtain, and the experiments have a limited scope. Numerical simulations are the most common method to study the physics involved in the complex interaction between the fluid and the solid.

A fluid-structure coupling problem is defined by the fluid equations, the solid equations, and the transmission conditions at the fluid-structure interface. The governing equations of fluid usually use the Eulerian approach, however, the solid mechanics is normally described by the Lagrangian approach. The Eulerian algorithms describe that kinematic variables of the fluid flow are related to a spatial fixed system. The computational mesh is fixed and the continuum moves with respect to the grid (fig.3.18). In the Eulerian description, large distortions in the continuum motion can be handled with relative ease, but generally at the expense of precise interface definition and the resolution of flow details. The Lagrangian approach describe that the solid variables are related to a coordinate system fixed on the material in which each individual node of the computational mesh follows the associated material particle during motion (fig.3.18). Whereas its inability to follow large distortions of the computational domain without recourse to frequent remeshing operations [13].

To combine the advantages of these two descriptions, a hybrid description, Lagrangian-Eulerian formulations (ALE) [15], has been developed in FSI algorithms allowing a clear delineation of fluid-structure interfaces. In the ALE description, the nodes of the computational mesh may be moved with the continuum in normal Lagrangian manner, be held fixed in Eulerian manner or be moved in some arbitrarily specified way to give a continuous rezoning capability (fig.3.18). In the ALE description of motion, neither the Lagrangian coordinates X nor the Eulerian coordinates x is taken as the reference. Thus, a new coordinate frame, the referential coordinates χ , is introduced to identify the mesh points.

3.4.1 Fluid-structure coupling equations

3.4.1.1 fluid domain

In order to express the governing equation in an ALE framework, a new variable, convective velocity \vec{c} , is brought to the equations. It is the relative velocity between the fluid flow velocity field (\vec{v}^f)

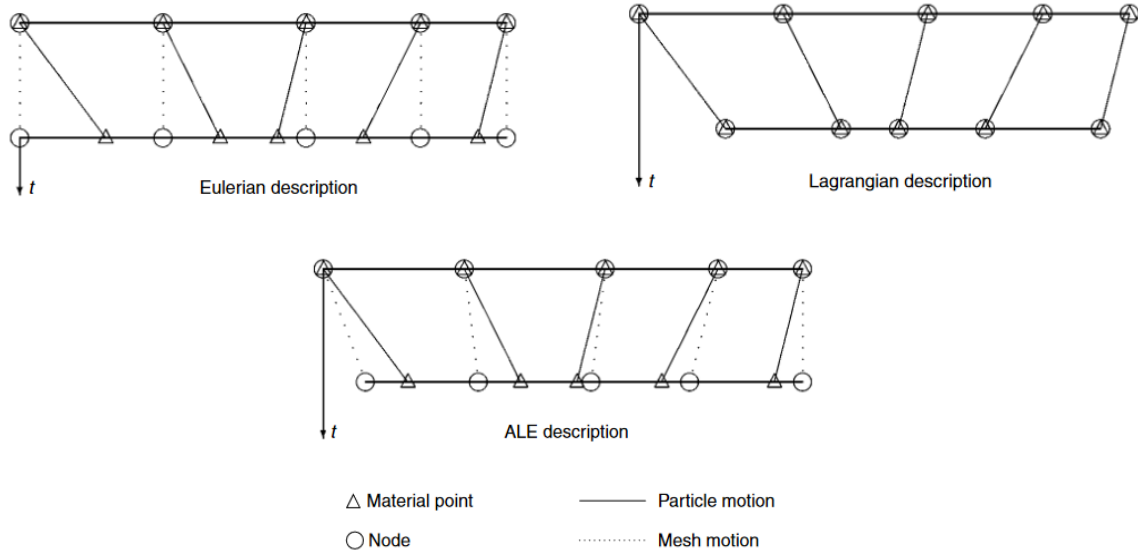


Figure 3.18: One-dimensional example of Lagrangian, Eulerian and ALE mesh and particle motion [15]

and the mesh velocity ($\vec{\omega}$), defined as:

$$\vec{c} = \vec{v}^f - \vec{\omega} \quad (3.18)$$

The ALE form of the governing equations are:

- *The continuity equation for incompressible flows:*

$$\nabla \cdot \vec{v}^f = 0 \quad (3.19)$$

- *The momentum equation for incompressible Newtonian flows:*

$$\rho^f \left. \frac{\partial \vec{v}^f}{\partial t} \right|_{\chi} + \rho^f \nabla \cdot \{ \vec{c} \cdot \vec{v}^f \} = -\nabla p + \nabla \cdot \{ \mu^f \nabla \vec{v}^f \} \quad (3.20)$$

the bar with χ on the temporal term means that the derivative is calculated with the referential coordinates χ fixed;

- *Conservation of energy in terms of temperature for incompressible flows:*

$$\rho^f \left. \frac{\partial T^f}{\partial t} \right|_{\chi} + \rho^f \nabla \cdot [\vec{c} T^f] = \nabla \cdot \left[\frac{k^f}{c_p^f} \nabla T^f \right] \quad (3.21)$$

3.4.1.2 Solid domain

The total Lagrangian formulation of the solid governing equation which is written in equation 3.22, derived from Newton's Second Law, is one of the most used principles in solid mechanics [92]. The subscript 0 is for differential operators calculated at the initial solid configuration.

$$\underbrace{\rho_0^s \frac{\partial^2 \vec{u}^s}{\partial t^2}}_{\text{Inertial forces}} = \underbrace{\rho_0^s \vec{g}}_{\text{Body forces}} + \underbrace{\nabla_0 \cdot \vec{P}}_{\text{Surface forces}} \quad (3.22)$$

\vec{u} is the solid displacement. The stress and deformation are represented by the normal stress tensor \vec{P} . We used the elastic linear model to analyze the deformations of RCAVF wall. Therefore, the equation 3.22 can be written as a function of the Lamé's constant μ^s and λ^s which are related to Young's modulus and Poisson's ratio of the solid [92]:

$$\rho_0^s \frac{\partial^2 \vec{u}^s}{\partial t^2}(\vec{X}, t) = \nabla_0 \cdot [(2\mu^s + \lambda^s) \nabla_0 \vec{u}^s] + \nabla_0 \cdot [-(\mu^s + \lambda^s) \nabla_0 \vec{u}^s + \mu^s \nabla_0^T \vec{u}^s + \lambda^s \text{tr}(\nabla_0 \vec{u}^s) \vec{I}] \quad (3.23)$$

3.4.2 Solid domain discretization

The vessel wall mesh was created by the extruder mesher in STAR-CCM+ 12.06.011. The extruder meshing model can be activated for any of the core mesh types and enabled for any boundary. It can extrude from the specified boundary in the normal or specified direction to produce orthogonal extruded cells, which can result in a lower cell count or better cell quality.

The vessel wall mesh was extruded from the RCAVF non-mature model when θ equal 90° (fig.3.19). The wall mesh was extruded in the normal direction of the fluid-structure interface with 4 constant thickness layers. The total thickness was equal to the vessel wall thickness 0.33 mm.

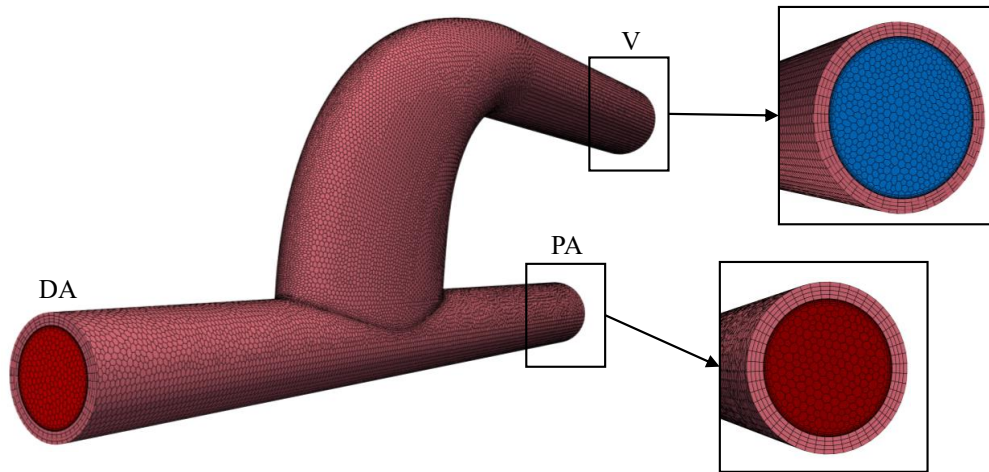


Figure 3.19: RCAVF FSI mesh by STAR-CCM+ 12.06.011 with $\theta = 90^\circ$ (144 504 cells in vessel wall)

3.4.3 Boundary conditions

In the fluid field, the blood fluid inlets and outlet conditions (DA_inlet, PA_inlet, and V_outlet) were set as the same as CFD non-model. In the solid field (fig.3.20), the inlets and outlet conditions of RCAVF walls (PA_inlet_solid, DA_inlet_solid and V_outlet_solid) were applied as fixed displacement Dirichlet boundary conditions.

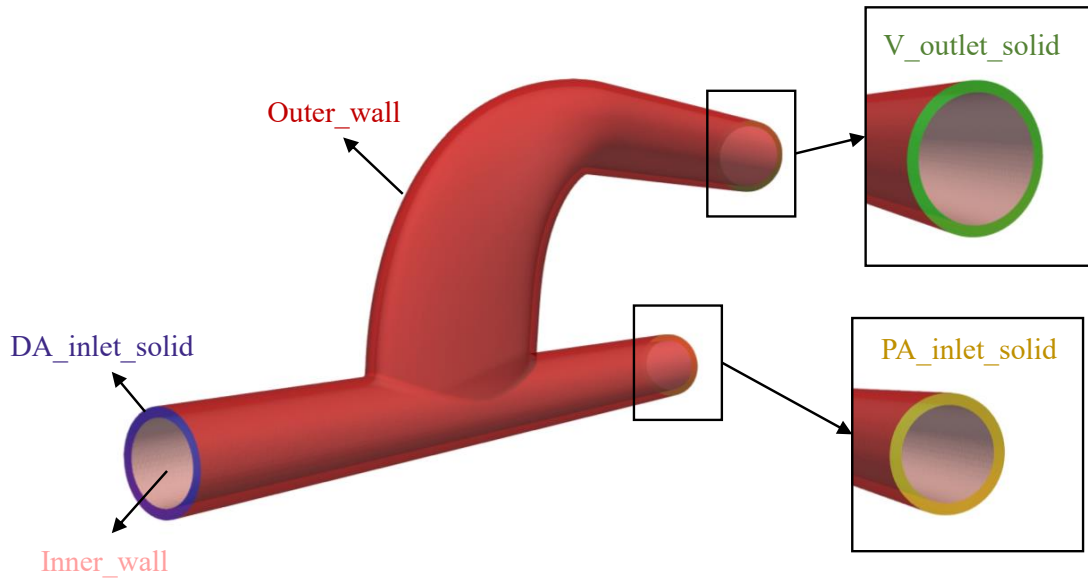


Figure 3.20: FSI boundary conditions

To close the problem of the solid governing equations in the FSI simulations, the displacements of inner and outer surfaces of RCAVF walls (Inner_wall, Outer_wall) have to be provided and used as initial conditions. The Neumann boundary condition was applied to them. On the Outer_wall, the initial surface traction is due to the extravascular pressure in the forearm, which was set to 0 mmHg [93]. Inner_wall and Blood_wall are the FSI interfaces. Their boundary conditions are evaluated by the transmission condition at the fluid-structure interface:

$$v^f = v^s \quad (3.24)$$

$$(\sigma^f \cdot n^f) + (\sigma^s \cdot n^s) = 0 \quad (3.25)$$

The continuity of velocity at the interface is guaranteed by the dynamic condition which is calculated from the flow governing equations, whereas the solid equation is solved with an imposed pressure due to the dynamic condition of stress continuity at the interface.

3.4.4 Fluid-structure interaction simulation in Foam-extend

FSI problems are usually solved by two major methods: monolithic and partitioned methods [94]. In monolithic method, the fluid and structure domains will be solve in a single system (fig.3.21).

Because of its built-in coupling mechanism, it is more powerful. Without coupling approximation, the final solution has less numerical errors. Nonetheless a monolithic approach is much more difficult to be implement for each specific problem. When physical geometries or properties of the problem become complex, this type of method is less flexible and no longer possible. Since each case requires specific numerical computation procedures which needs more expertise and knowledge of programming.

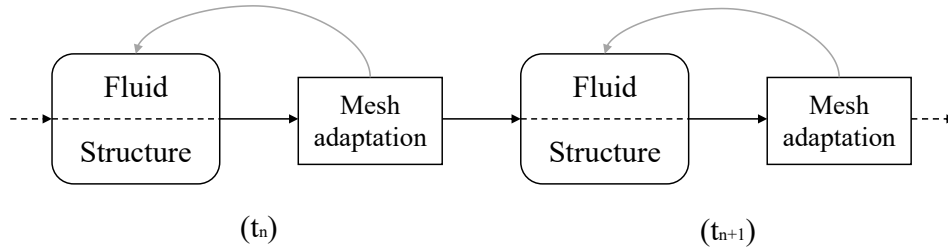


Figure 3.21: Monolithic method

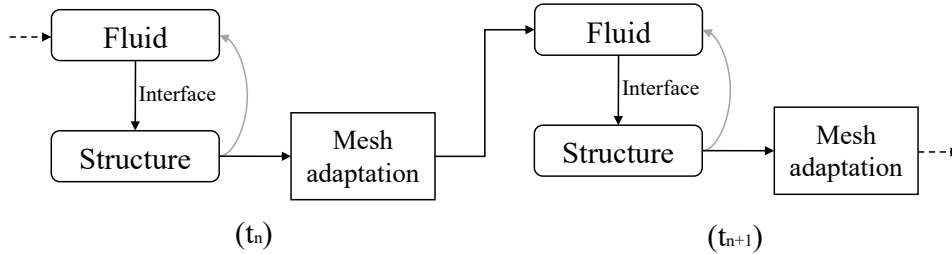


Figure 3.22: Partitioned method

In partitioned method, the fluid and the solid are considered as two distinct regions. They are solved separately and have their own discretization and numerical schemes (fig.3.22). Compared to the monolithic method, it can be better adapted for each specific problem and requires less effort and computational time. As shown in figure 3.22, the fluid domain is solved in the first step, and the solution is transferred to the solid by the interface. Afterwards, the mesh will be adapted with the new condition. According to the different data exchanging times between the fluid and solid, partitioned method can be separated into two groups: weak coupling and strong coupling (fig.3.23). The weak coupling scheme (explicit scheme) only have one change of data. For the large displacements, it requires very small time-steps and the simulation is easy to diverge. The strong coupling scheme (implicit scheme) has an additional loop in its resolution algorithm, which guarantees the cohesion between the mesh deformation and the dynamic conditions at the interface after each time-step. With numerous iterations between the two domains, the partitioned method makes the calculation time longer and needs more effort. Therefore, this method often uses an under-relaxation technique to stabilize the coupling process.

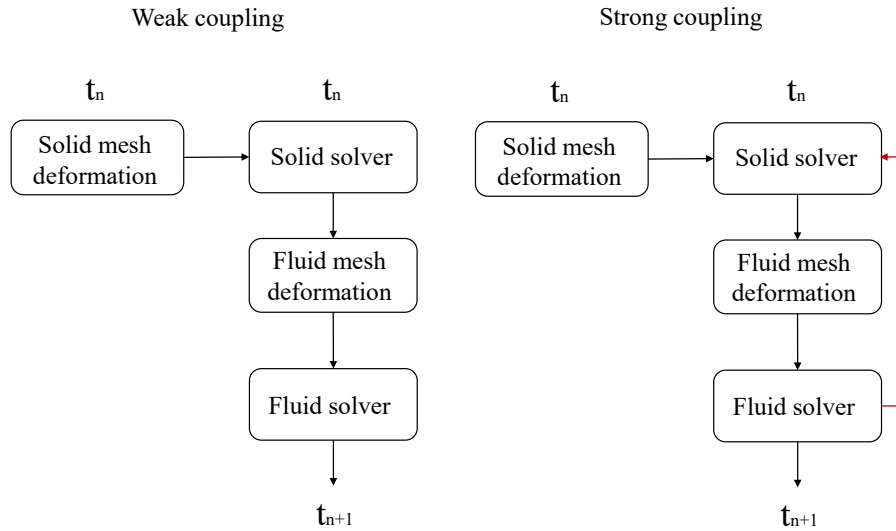


Figure 3.23: Resolution process for a fluid-structure interaction problem with weak coupling and strong coupling using the partitioned method

The FSI model of RCAVF was solved by the solver `fsiFoam` in `Foam-extend 4.0`, which uses the partitioned method with the strong coupling scheme. We chose Aiken relaxation [95] to accelerate the coupling process. All the numerical fiches in `Foam-extend` are available in appendix C.

3.5 Result analysis

3.5.1 Analytical indicators used in the result analysis

3.5.1.1 Hemodynamic analysis

Hemodynamic analysis plays an important role in CFD result analysis. It helps the surgeons better understand and intuitively observe the flow patterns in the artificial fistulas. From the RCAVF cross-sections, the disturbed flow fields can be easily observed. With the comparisons of flow patterns at different pulsatile times or with different anastomotic angles, the developments of the reversed flows and the disturbed flow locations will be found. Knowledge of the streamlines can be also useful in fluid dynamics which are the field lines in a fluid flow. They differ when the flow changes with time. They show the direction in which a massless fluid element will travel at any point in time. They can clearly present where recirculating eddies exist in RCAVFs and how they change with different θ . At the meantime, by tracing the streamlines at different inlets, we can explore the main cause of the disturbed flow in RCAVF. In our researches, the numbers of streamlines in different inlets were the same as their flow rate values.

3.5.1.2 Wall shear stress distributions

Wall shear stress (WSS) is an essential factor in the early failure of the fistula. The low wall shear stress (LWSS) and the oscillating wall shear stress (OWSS), mainly caused by the disturbed flow, are the undesirable mechanical stimulations leading to fistula dysfunction. The details has been discussed in chapter 1 section 1.6. A variety of hemodynamic wall parameters has been proposed to quantify the WSS distributions as potential indicators of vascular wall dysfunction [96], which can be divided by magnitude-based indicators, gradient-based indicators, and harmonic-based indicators. Magnitude-based indicators are significantly correlated with vascular wall dysfunction and are used most commonly as indicators of disturbed flow. They include:

- *Time-Averaged Wall Shear Stress (TAWSS)*

TAWSS calculated the average WSS magnitude over the cardiac cycle. It is defined as:

$$TAWSS = \frac{1}{T} \int_0^T |\vec{\tau}_w| dt \quad (3.26)$$

where $\vec{\tau}_w$ is the wall shear stress. TWASS can be used to observe the WSS distribution on the vessel wall to find the low WSS regions [97]. Normally, the magnitude of WSS in the venous system is from 1 to 6 dyn/cm^2 , and it is between 10 and 70 dyn/cm^2 in the arterial system [8]. In the non-mature models, since the vein has not been successfully remodeled and the vessel wall still retains its original properties, the LWSS region in the venous segment is the area where TAWSS is less than 1 dyn/cm^2 . In the arterial segment, the LWSS exists where TAWSS is less than 10 dyn/cm^2 . For the mature models, the vein is considered to have the same properties as the artery due to the vein remodeling. Therefore, the LWSS appears in the region where TAWSS is lower than 10 dyn/cm^2 .

- *Oscillatory Shear Index (OSI)*

OSI was formulated to account for the cyclic departure of the WSS vector from its predominant axial alignment. It can be written as:

$$OSI = \frac{1}{2} \left(1 - \frac{\left| \int_0^T \vec{\tau}_w dt \right|}{\int_0^T |\vec{\tau}_w| dt} \right) \quad (3.27)$$

where T is the period of the cardiac cycle. It is a dimensionless parameter to estimate the OWSS region. Its value change between 0 to 0.5. Higher OSI indicating larger WSS direction variations. It provides an index which describes the shear stress acting in directions other than the direction of the temporal mean shear stress vector [98]. In order to better determine the location of the higher OWSS, this study focused on the observation of the OSI region greater than 0.001.

- *Relative Residence Time (RRT)*

RRT is the the relative residence time of non-adherent particles in the blood flow moving

adjacent to the vascular wall. It is proportional to a combination of TAWSS and OSI:

$$RRT \sim [(1 - 2 \cdot OSI) \cdot TAWSS]^{-1} \quad (3.28)$$

The RRT have to be normalized by a reference value which calculated by the fully developed, time-averaged, blood volume flow in the straight part of the normal cephalic vein in the lower forearm, where the inlet averaged flow rate was set to 28 ml/min [99]. With this transformation, the RRT value near 1 indicates a condition of shear environment similar to the normal level, while RRT below 1 indicates high WSS zones and RRT higher than 1 locates the areas with both LWSS and OWSS or areas with only LWSS. It has been recommended as a robust single metric which incorporates information on both low and oscillating WSS [96].

3.5.2 Comparison between Newtonian and non-Newtonian fluids

We use the non-mature model with θ equals 90° to analyze the Newtonian and non-Newtonian fluid behaviors. The viscosity of Newtonian fluid is set to $0.0035 \text{ Pa} \cdot \text{s}$. The non-Newtonian behavior is presented by Carreau model [100], the fluid viscosity is defined as:

$$\eta = \eta_\infty + \frac{\eta_0 - \eta_\infty}{(1 + (\lambda\dot{\gamma})^2)^{2/(n-1)}} \quad (3.29)$$

Table 3.6: Parameters of Carreau model [18]

Parameters	Definitions	Values
η_0	Dynamic viscosity of blood at high shear rate	$0.0035 \text{ Pa} \cdot \text{s}$
η_∞	Dynamic viscosity of blood at low shear rate	$0.056 \text{ Pa} \cdot \text{s}$
λ	Relaxation time constant	3.313 s
n	Power low index in Carreau model	0.3568
ρ	Blood density	$1060 \text{ kg} \cdot \text{m}^{-3}$

the definitions of Carreau model parameters are shown in table 3.6. Figure 3.24 shows the relation curves of two models between viscosity and the shear rate. In Foam-extend, they are specified in the **transportProperties** (shown in fig.3.25). The numerical viscosity values are divided by the blood density in figure 3.25, and k is the relaxation time constant (λ). The results are analyzed at the third cardiac cycle.

The results are visualized and post-processed by ParaView 5.8.1. We extract five different cross-sections in RCAVF (shown in fig.3.26) to compare the velocity profiles between Newtonian and non-Newtonian models at systole. The velocity ranges of the two models are almost the same. According to the comparisons from cross-sections A to E, there is almost no difference in the velocity fields. The maximal velocities (U_{max}) in Newtonian and non-Newtonian fluid domains, shown in table 3.7, are basically identical. The figure 3.27 represents the streamlines in two models. The red curves trace the blood flow trajectories entering from PA, and the blood flow trajectories are traced by blue cures entering from DA. A recirculation site is found at the heel of anastomosis in both models. This disturbed flow is slightly denser in the Newtonian model than

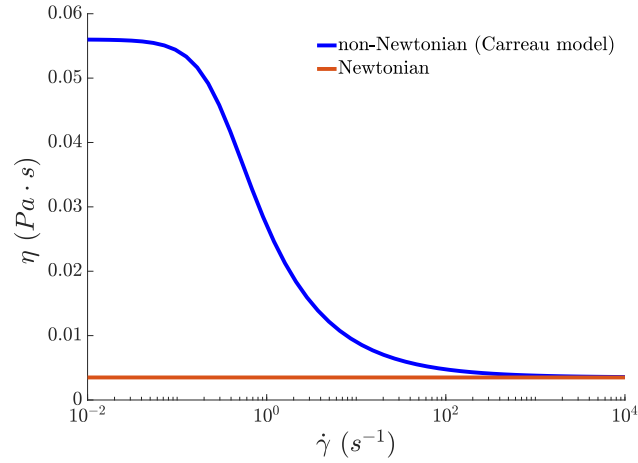


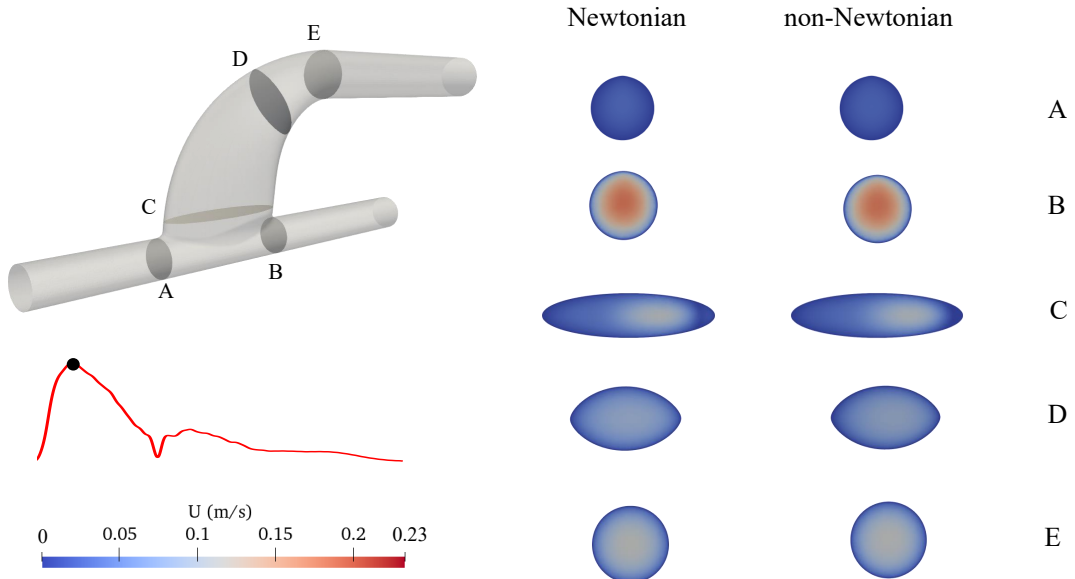
Figure 3.24: Viscosity curves of Newtonian and non-Newtonian (Carreau model)

```

BirdCarreauCoeffs
{
    nu0      nu0      [ 0 2 -1 0 0 0 0 ] 5.283e-5;
    nuInf     nuInf    [ 0 2 -1 0 0 0 0 ] 3.30189e-6;
    k         k        [ 0 0 1 0 0 0 0 ] 3.313;
    n         n        [ 0 0 0 0 0 0 0 ] 0.3568;
}

```

Figure 3.25: Definition of Carreau model parameters in Foam-extend

Figure 3.26: Comparison of velocity fields in different cross-sections of RCAVF during systole between Newtonian model and non-Newtonian model ($\theta = 90^\circ$)

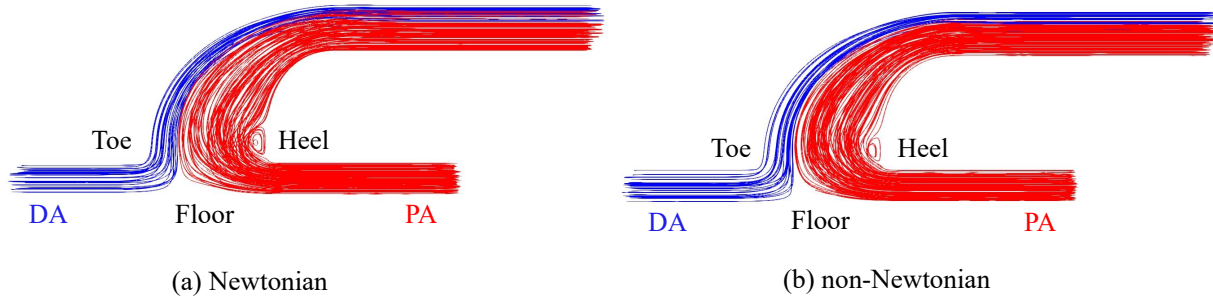


Figure 3.27: The streamlines during systole in Newtonian and non-Newtonian models

in the non-Newtonian model.

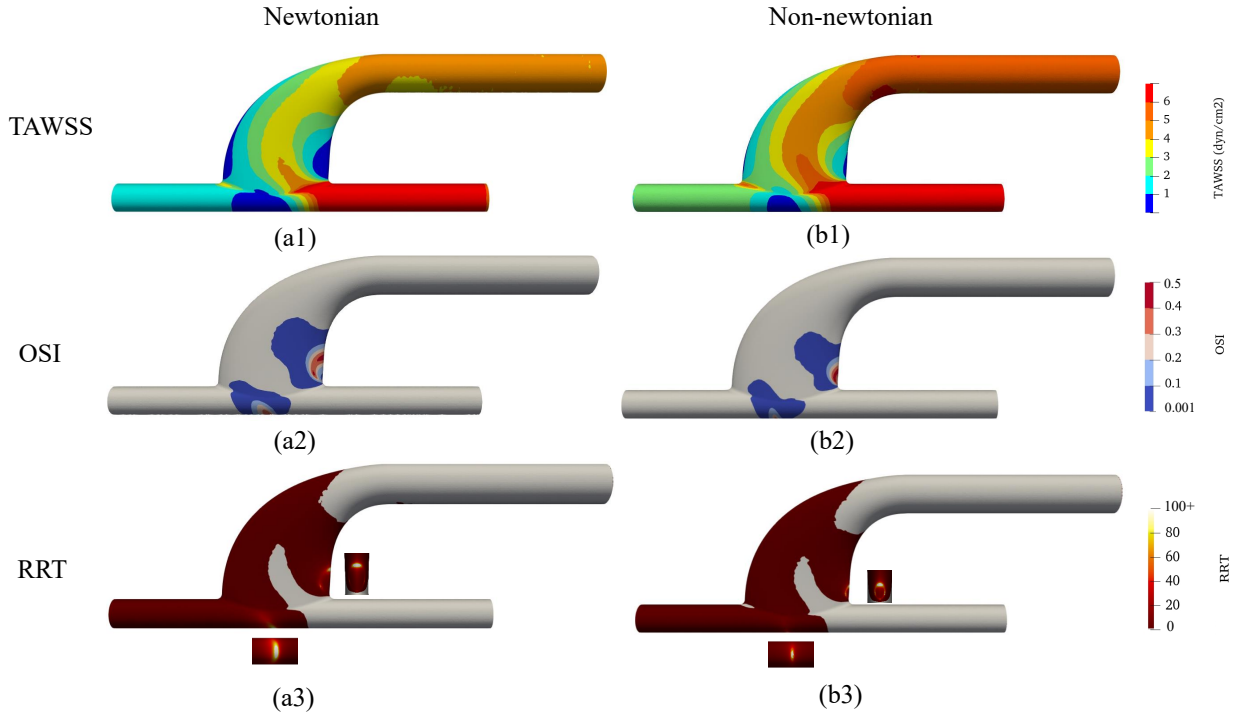


Figure 3.28: Comparisons of WSS indicators between Newtonian model and non-Newtonian model ($\theta = 90^\circ$)

The figure 3.28 shows the WSS distribution comparisons between two models. TAWSS can observe the LWSS locations. The figure 3.28 (a1) and (b1) are the TAWSS patterns, the dark blue presents the LWSS regions where TAWSS was less than 1 dyn/cm^2 . The minimal TAWSS ($TAWSS_{min}$) on the RCAVF surface is 0.2 dyn/cm^2 in Newtonian model and 0.269 dyn/cm^2 in non-Newtonian model (tab.3.7). The surface maps of OSI are shown in figure 3.28 (a2) and (b2). The values below 0.001 are represented by gray to emphasize the area with high OSI. The highest OSI (OSI_{max}) of

Table 3.7: Flow properties comparisons between Newtonian and non-Newtonian models

	U_{max} (m/s)	$TAWSS_{min}$ (dyn/cm ²)	OSI_{max}	RRT_{max}
Newtonian	0.2328	0.200	0.497	1511.1
non-Newtonian	0.2326	0.269	0.495	855.0

the two models are quite closed (shown in table 3.7), whereas the high OSI areas of the Newtonian model are larger than non-Newtonian. The RRT patterns are almost the same in two conditions (shown in figure 3.28 (a3) and (b3)). RRT values lower than 1 are scaled with the gray. The higher the RRT, the brighter the color. The brightest surface indicates that the RRT is greater than 100. By careful comparison, the bright areas in figure 3.28 (a3) are larger than figure 3.28 (b3), and the peak RRT (RRT_{max}) in the Newtonian model, represented in table 3.7, is higher than non-Newtonian.

The above comparisons demonstrate that the Newtonian property underestimate the WSS. It is related to the difference between Newtonian and non-Newtonian fluid properties at low shear rates (fig.3.24). The low shear rates typically produce by the irregular flows. In RCAVF, the PA flow and DA flow reattached at the anastomosis floor, and a recirculating eddy appeared around the anastomosis heel (fig.3.27). The reversed streamlines and the reciprocating flow generate the low shear rates, resulting in the different WSS levels and areas around the anastomosis between the two models. However, these differences do not lead to an estimate of the risk location of RCAVF. Therefore, it will not affect our research for the best anastomotic angle by comparing the risk areas. In the meantime, due to the relaxation time of the non-Newtonian blood. The viscoelastic properties of the fluid require a relatively small time step to capture the desired effects, which cause it expensive to compute. Consequently, we assumed that the blood flow in all the models had Newtonian property.

3.5.3 Comparison between CFD and FSI non-mature RCAVF models

We compared the results of CFD and FSI simulations through the non-mature RCAVF model with $\theta = 90^\circ$. The purpose of this work is to explore the influence of fluid-structure coupling simulation on the hemodynamic behaviors and WSS distributions in RCAVF and discuss the necessity of using this numerical method.

The hemodynamics in RCAVF will change due to the change of blood vessel geometry. Meanwhile, the blood flows merge at the anastomosis, and the flow rate in the vein increases rapidly, which will cause the deformation of the blood vessel wall. In the FSI simulation, we can observe the displacement of the blood vessel wall. The figure 3.29 shows the displacement of the outer wall of RCAVF. The deformation of RCAVF vessel wall is minimal, and the maximum deformation position is located in the bending vein near the anastomosis. We extract one point in the area whose displacement fluctuates between 1.44 mm and 1.51 mm during one cardiac cycle (shown in fig.3.30). In order to observe the deformation of the blood vessel wall more clearly, we magnify the displacement five times, as shown in figure 3.29. The gray transparent blood vessels represent the

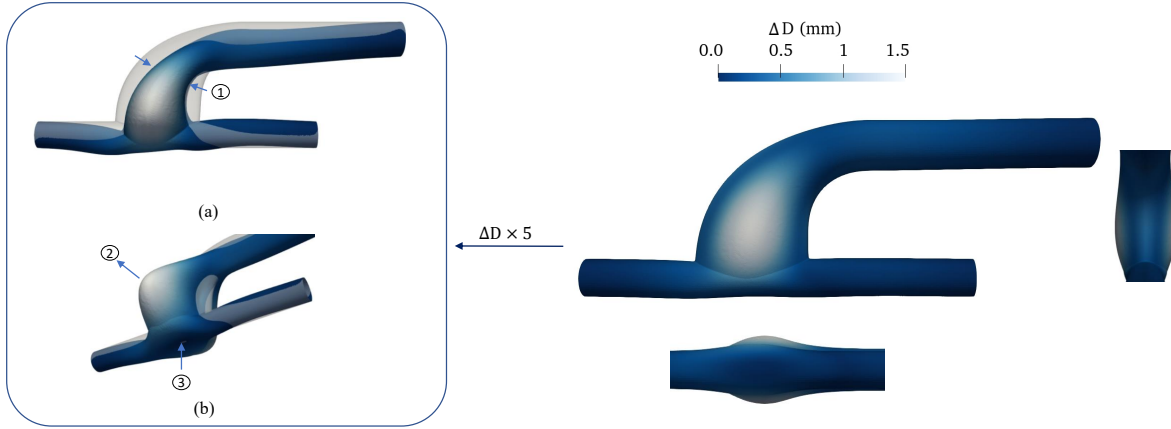


Figure 3.29: Displacement of the outer wall in non-mature model with $\theta = 90^\circ$ (Gray transparent blood vessels represent the blood vessel wall without deformation)

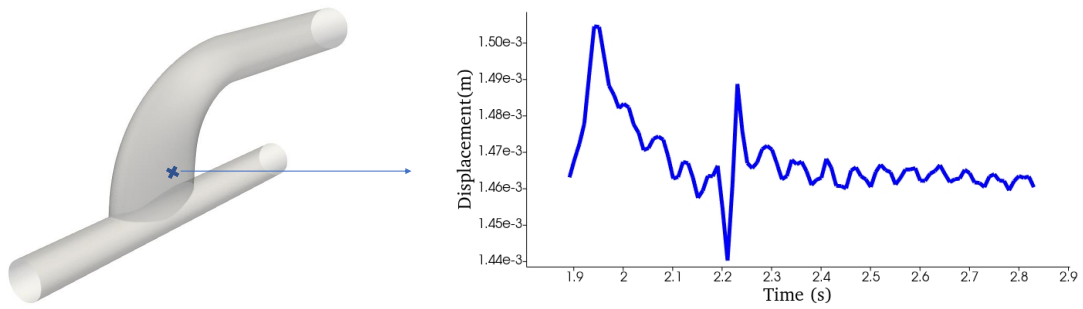


Figure 3.30: Displacement of a point at the bending venous segment during the third cardiac cycle

blood vessel wall without deformation. Figure 3.29 (a) illustrates the main view of RCAVF and figure 3.29 (b) presents the view below the artery. The significant displacement in RCAVF can be divided into three types, displacements 1 and 2 are the displacements that occur on the CV blood vessel wall, and displacement 3 occurs on the RA blood vessel wall. Due to the merge of blood flows at the anastomosis, the venous blood flow rate is greatly increased. The blood vessel wall has to expand outwards to reduce the high pressure caused by the high flow rate to maintain the stability of the vascular environment, which results in a dilatative displacement 2. However, in the B segment, the appearance of the curved section leads to the generation of the reverse pressure gradient ($dp/dx > 0$), which leads to the occurrence of the reflux region (the details will be explained in subsection 3.5.5.1). Therefore, it causes constrictive displacement 1. Due to the concentration of blood flows and the rapid changes of blood directions, a low pressure area is generated in the arterial blood vessel below the anastomosis. It results in constrictive displacement 3 of the blood vessel wall.

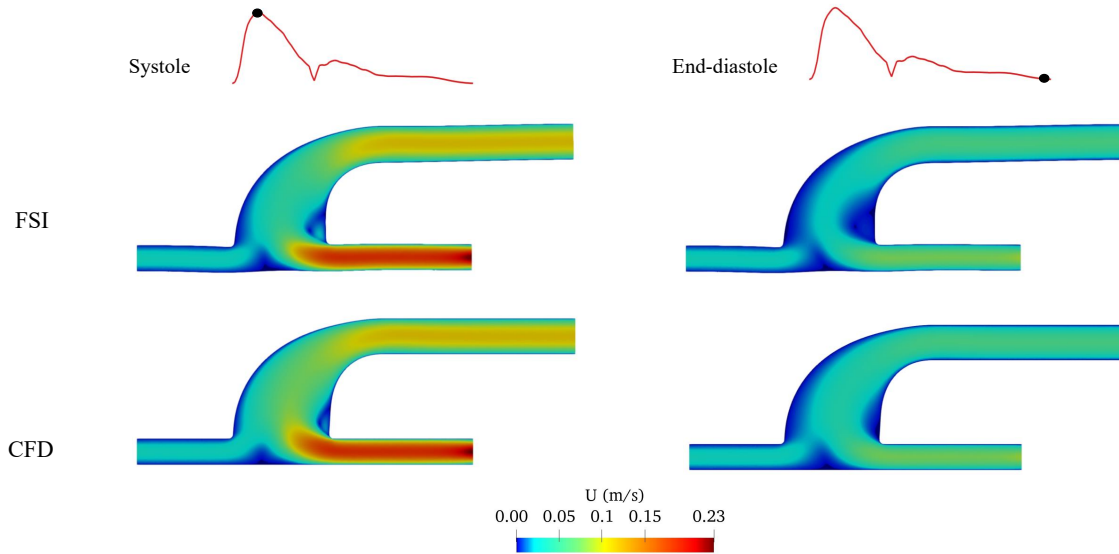


Figure 3.31: Comparison of velocity fields at systole and end-diastole between FSI and CFD models ($\theta = 90^\circ$)

Figure 3.31 illustrates the velocity fields at systole and end-diastole between FSI and CFD numerical simulation methods. It can be seen from this comparison that the two simulation results have the same velocity field range. The area of the low speed region in the FSI model is slightly larger than that in the CFD model. The area of the reflux region generated near the heel of anastomosis in the FSI velocity field is also slightly larger than that in the CFD model.

We establish the identical five cross-sections as subsection 3.5.2, and the velocity profile comparisons at systole are shown in the figure 3.32. There is almost no difference in the velocity profiles within the straight blood vessels (cross-sections A, B, and E). The blood velocities in the B segment of the FSI model are lower than the result of the CFD model (cross-sections C and D). In order to compare the velocities in FSI and CFD models more clearly, we calculated the mean velocities on the four cross-sections. Since the DA inlet flow rate is minimal and constant, the

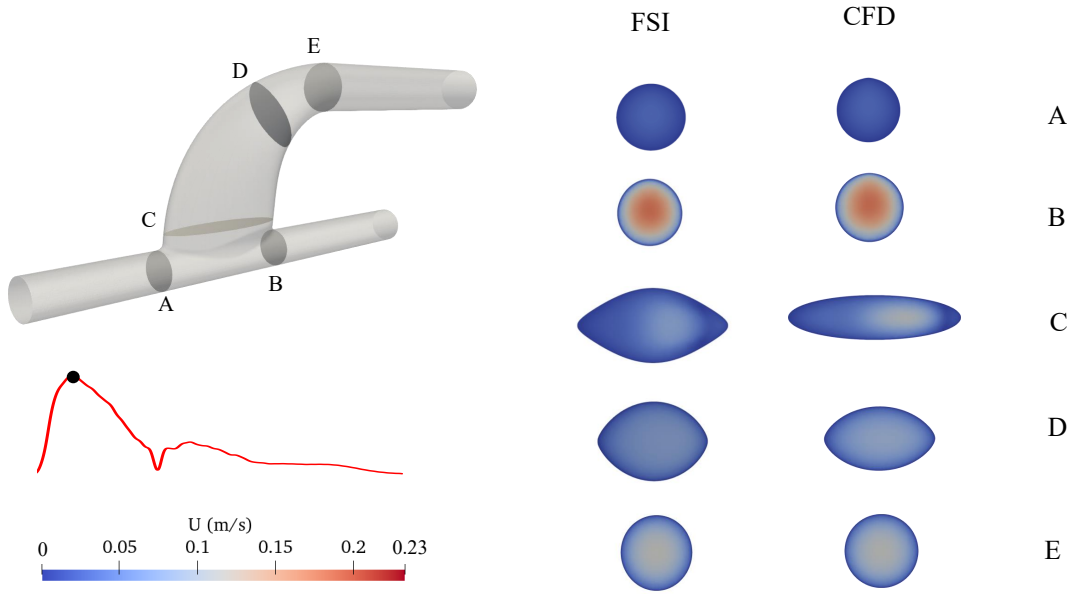


Figure 3.32: Velocity profiles during systole in FSI and CFD models ($\theta = 90^\circ$)

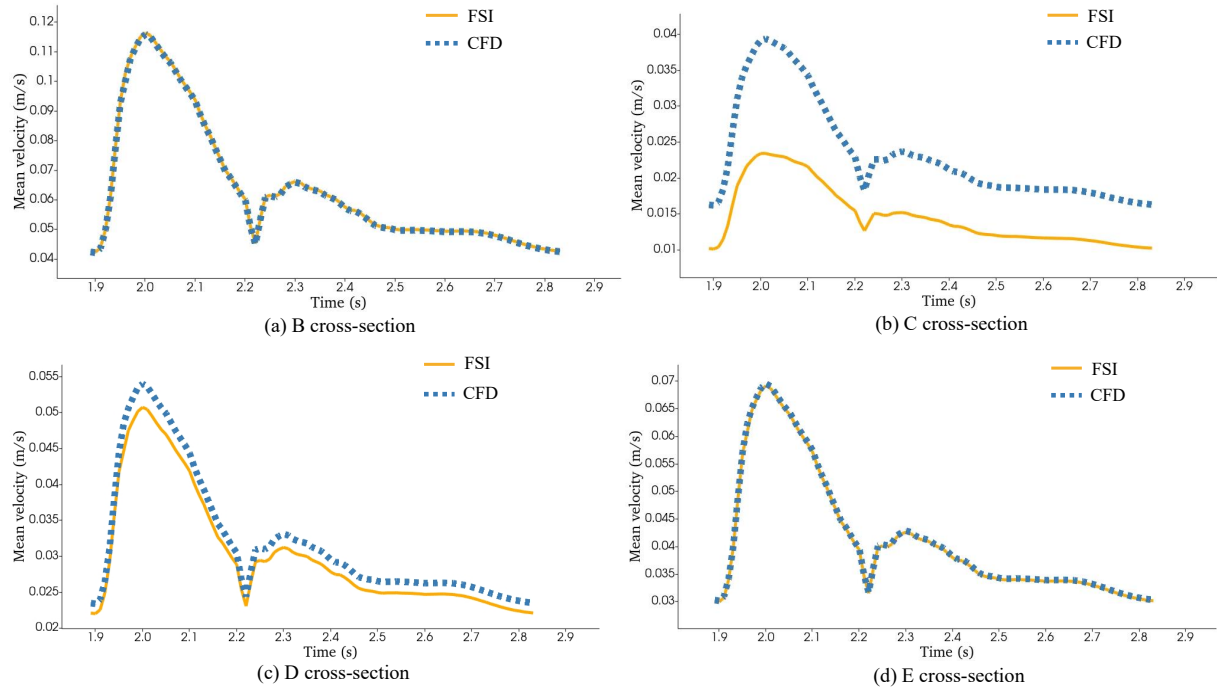


Figure 3.33: The comparison of the mean velocity over the cross sections between FSI and CFD models ($\theta = 90^\circ$)

mean velocity curves within one pulse are only extracted at cross-sections B to E. The comparisons are shown in figure 3.33. The blue dotted curves represent the CFD result, and the yellow curves represent the FSI result. We can intuitively observe that the mean velocity curves at B and E cross-sections coincide. The mean velocities of the FSI model at C and D cross-sections are smaller than the CFD model. The velocity differences in the bending vein segment are due to the changes in the lumen areas. As shown in table 3.8, The A, B, and E cross-sections in the straight vessels almost have the same areas between the FSI and CFD models. However, the C and D cross-section areas of the FSI model are much larger than that of the CFD model, decreasing the blood velocities.

Table 3.8: Comparison of cross-section areas at systole between FSI and CFD models ($\theta = 90^\circ$)

Cross-sections	A	B	C	D	E
FSI	5.72	5.73	33.97	14.80	10.79
CFD	5.70	5.70	20.47	13.97	10.72

As the velocity field changes, the WSS on the blood vessel wall also changes. As shown in table 3.9, the minimal TAWSS in the FSI model is lower than that in the CFD model, and the total low TAWSS (less than 1 dyn/cm^2) areas in the FSI model is higher than that in the CFD model. The maximal OSI values between the two models are similar. The total area of high OSI (from 0.001 to 0.5) in the FSI model is higher than that in the CFD model. As for RRT, the maximal RRT value in the FSI model is much lower than that in the CFD model, whereas the total area of high RRT (greater than 1) in the FSI model is more significant than that in the CFD model. However, as shown in figure 3.34, the locations of low TAWSS, high OSI, and high RRT in the FSI model are appeared at the same sites compared with CFD model (WSS indicator distributions are shown in subsection 3.5.2 figures 3.28 (a1) to (a3)).

Table 3.9: Comparison of WSS indicators between FSI and CFD models ($\theta = 90^\circ$)

WSS indicators	TAWSS		OSI		RRT	
	$\min(\text{dyn/cm}^2)$	$\text{area}(\text{mm}^2)$	max	$\text{area}(\text{mm}^2)$	max	$\text{area}(\text{mm}^2)$
FSI	0.12	88.18	0.49	151.12	591.02	364.25
CFD	0.20	47.17	0.50	118.37	1511.11	330.15

From the above comparisons, the CFD simulation generally overestimates velocities and WSS values. However, its predictions of LWSS and OWSS locations are similar to the FSI simulation results. Since we aim to study the trend of WSS with different θ , the CFD model will not affect the results. Although the FSI simulation is closer to reality, running a coupled fluid and structure simulation highly increases the computational work. We need to simulate and compare ten different models to find the relationship between the anastomotic angle and the WSS distribution. CFD simulation can significantly improve our simulation efficiency. In summary, in the following simulation analyses, we choose the CFD simulation method.

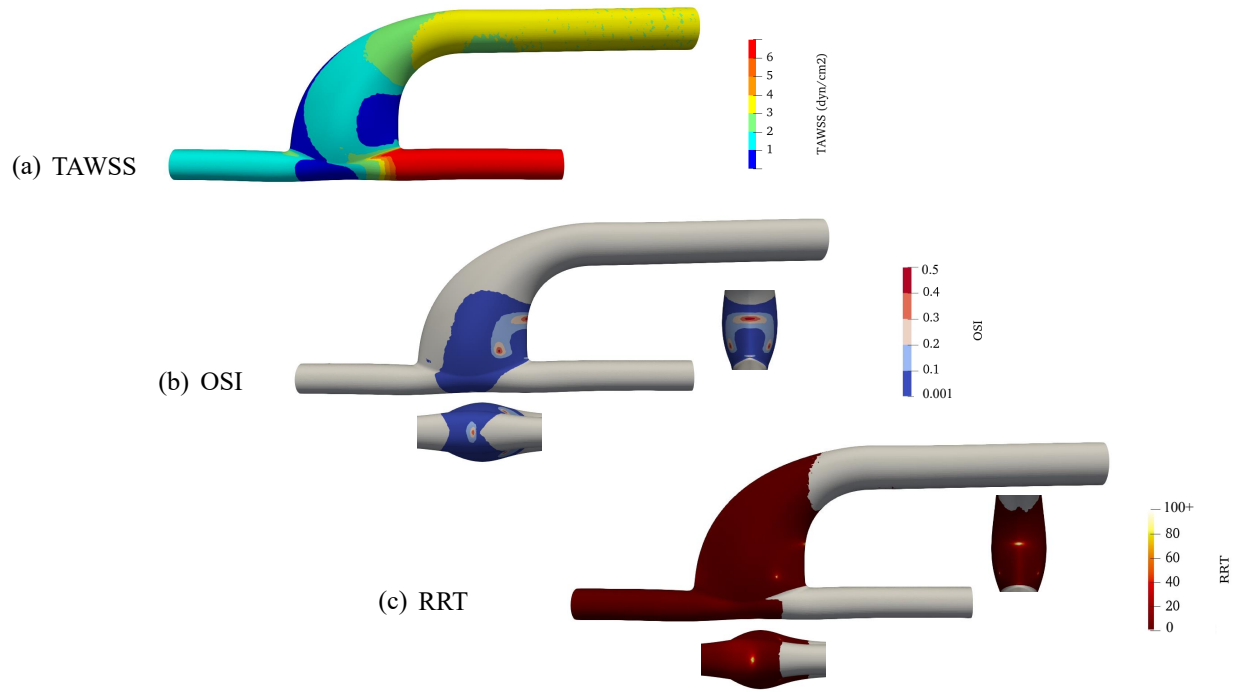


Figure 3.34: WSS indicators in FSI model

3.5.4 RCAVF mature model verified by clinical imaging measurement

A patient-specific RCAVF model is created based on the clinical data to verify our simulation results with DUS measurement.

The clinical information is provided by Hospices Civils de Lyon (HCL). The RCAVF was established on March 11th, 2021, by using a 1.4 mm D_{ra} and 2.8 mm D_{cv} . The vessel distance h equals to 14 mm. An anastomosis connected RA and CV with 10 mm D_a and $40^\circ \theta$. The RCAVF was measured by DUS (Philips Affiniti 70 G) on April 16th, 2021. After one month of remodeling, D_{ra} and D_{cv} expended to 4.2 mm and 4.4 mm. The average flow rate during a cardiac cycle of the brachial artery (BA), located at the upper arm (shown in fig.1.7), increased to 860 ml/min. In clinical measurement, BA flow rate is considered as same as the flow rate in CV, which is defined as the flow rate of RCAVF. To verify the numerical results, an additional DUS measurement was created at the bending vein near anastomosis (the vein segment in the gray bow shown in fig.3.35 (c)) shown in fig.3.35 (a). DUS measured the velocity field and the average velocity waveform near the cross-section A, which can be used to confirm the numerical simulation.

With the clinical measurements, the definitions of GPs are shown in table 3.10. The DA_inlet boundary condition is set to the constant value of 60 ml/min, as same as all the mature models. The PA_inlet boundary condition uses a time-varying flow rate, to which the average value equals to 800 ml/min (the sum of the flow rate of DA_inlet and PA_inlet is equal to the flow rate measured at BA) and the flow waveform is the same as BA measured by DUS.

The V_outlet is applied to a constant pressure 8.7 mmHg (the normal pressure of the cephalic vein).

Table 3.10: The GPs in a patient-specific RCAVF mature model

GPs	D_{ra} (mm)	D_{cv} (mm)	h (mm)	D_a (mm)	θ ($^\circ$)
Values	4.2	4.4	14	10	40

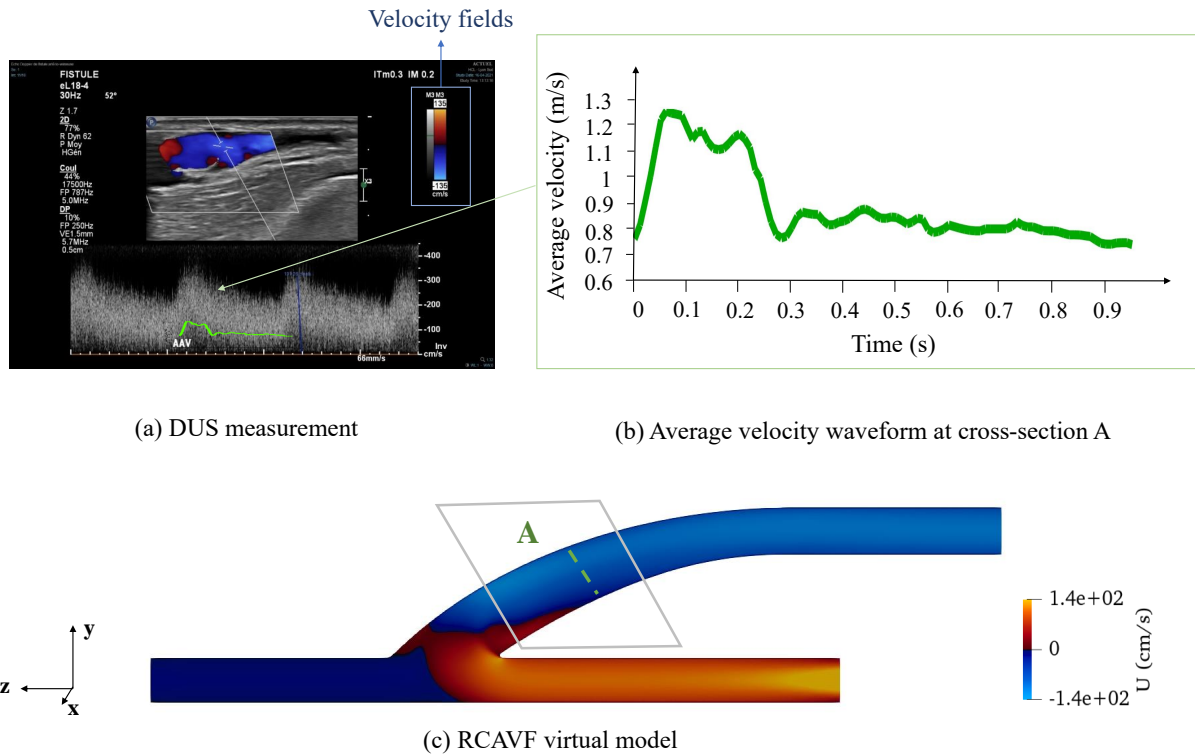


Figure 3.35: Comparison between the numerical result of RCAVF virtual model and DUS measurement

Due to the limit of DUS imaging, only the hemodynamic behaviors can be observed. With the Color Doppler image, the blood speed and the moving direction are represented by different colors. The flow moving towards the detector is red (i.e., blood flows to the left in fig.3.35 (a)) with positive velocity values. In contrast, blood far away from the detector is blue with negative velocity values. The lighter the colors, the higher the speeds. In the simulation results, the velocity component in the z-direction is closest to the way the blood flowing in the DUS measurement. Therefore, figure 3.35 (c) represents the velocity field in z direction, which is changing from -140 cm/s to 140 cm/s in the numerical model and well corresponded with DUS measurement (the velocity field was between -135 cm/s and 135 cm/s). The average velocity waveform measured by DUS had a lot of noises (shown in the lower part of fig.3.35 (a)) due to the appearance of disturbed flows in this area. We calculate the average velocity waveform of cross-section A in the numerical model, shown in figure 3.35 (b), the maximal speed is 125.13 cm/s. We scale down the average velocity waveform obtaining from the simulation results and put it into the DUS image

(the green curve in figure 3.35 (a)). It can be observed that the simulation results are located in the average velocity range measured by DUS, which is slightly lower than the DUS result. This is because we only calculate the velocity component in the z direction, hence the values are slightly less than the magnitude average velocity waveform.

Through the comparisons of hemodynamic behaviors, it is found that there is a difference in the velocity field. A reflux site (red area) appeared near the outer wall of the bending vein in the DUS image (fig.3.35 (a)), which is found near the toe of anastomosis in the numerical model (fig.3.35 (c)). The difference may come from the assumption that blood vessels were concentric straight tubes set in the simulation. In reality, the human body's blood vessels are tortuous, especially for ESRD patients, the metabolic abnormalities will lead to blood vessel lesions. Sudden changes in local blood vessel walls will lead to local blood flow changes. This difference may also be caused by the choosing size of the color box (the slanted gray box in fig.3.35 (a)) during the DUS measurement [101]. Larger the color box size, the lower the image resolution and quality, which will lead to aliasing.

Through the above comparisons, our simulation results of hemodynamic behaviors are in a good agreement with the DUS measurement, which indicates that our numerical models can well describe the hemodynamic behaviors in RCAVF.

3.5.5 Analyzing the results of non-mature models

3.5.5.1 Hemodynamic flow in non-mature models

Figure 3.36 represents the velocity fields of non-mature models changing with θ at systole and end-diastole. By comparison, it is found that the low velocity zones (LVZs) normally appear around the anastomosis. At systole, LVZs are more local, which are near the heel (hLVZ), toe (tLVZ), and floor (fLVZ) of anastomosis. At end-diastole, fLVZs become slightly larger. As for hLVZs and tLVZs, they increase more obviously at end-diastole, and develop along the bending vein wall to the V segments. Whereas they only exist in the B segments. By comparing the velocity fields of different θ , it can be found that hLVZs increase with θ increase. However, they decrease slightly at 90° compared to 75° . The tLVZs, at systole, are more larger in small θ models.

By observing the streamlines in RCAVF (fig.3.37), we find that hLVZs exist disturbed flows. Figure 3.37 represents the streamlines in 2 non-mature models ($\theta = 30^\circ$ and $\theta = 90^\circ$) at systole and end-diastole. The red curves show the streamline entered from PA, and the pink curves are the streamlines of DA inlet. The partial streamlines at the local anastomotic site are enlarged and the arrows are added to indicate the flow direction.

By observing the streamlines in figure 3.37, a recirculating flow is found at hLVZ. The flow near the boundary is determined by the relative balance among inertial force, pressure gradient and viscous force. Viscous forces always block and slow down the flow. The direction of the pressure gradient in the boundary layer is determined by the outflow situation (fig.3.38). When the pressure gradient decreases ($dp/dx < 0$), it can accelerate the flow in the boundary layer to ensure fluid particles have

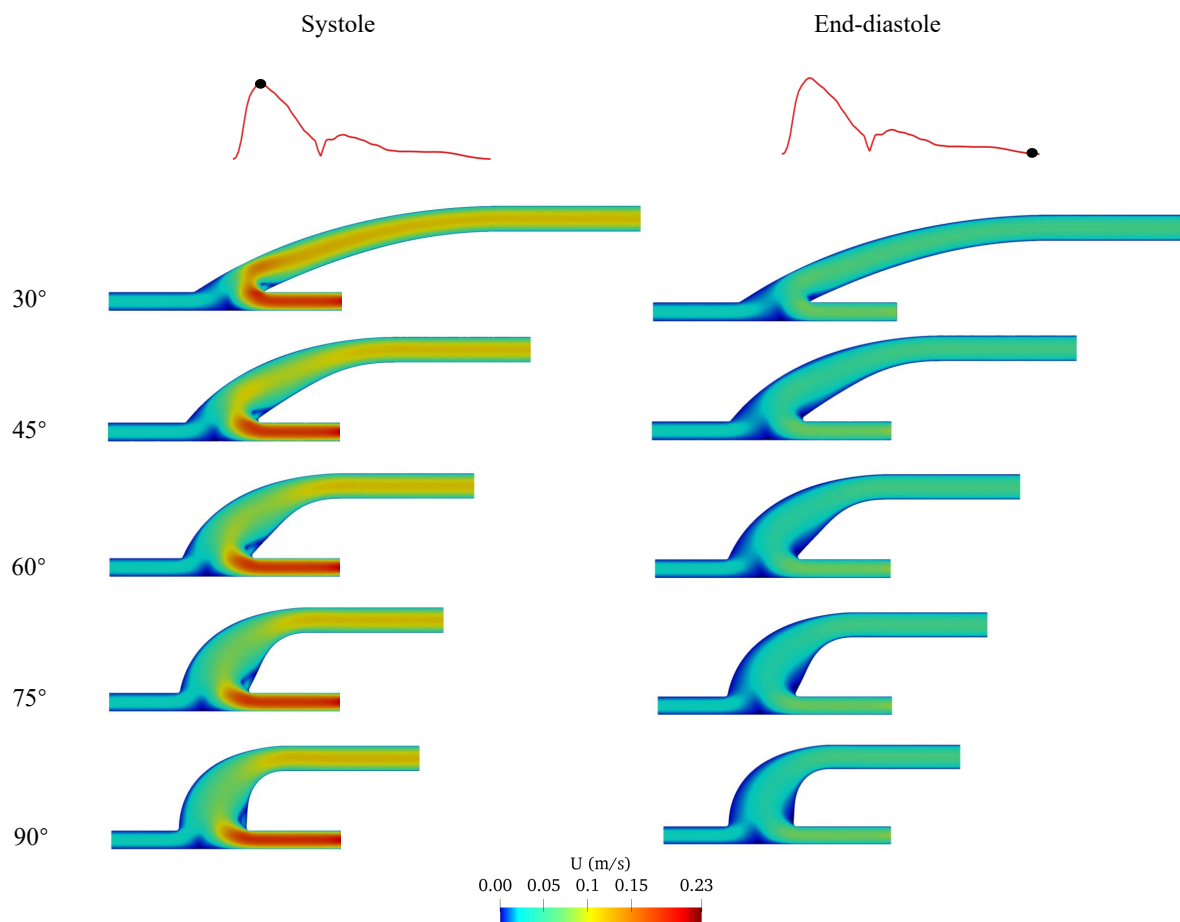


Figure 3.36: Velocity fields in non-mature models

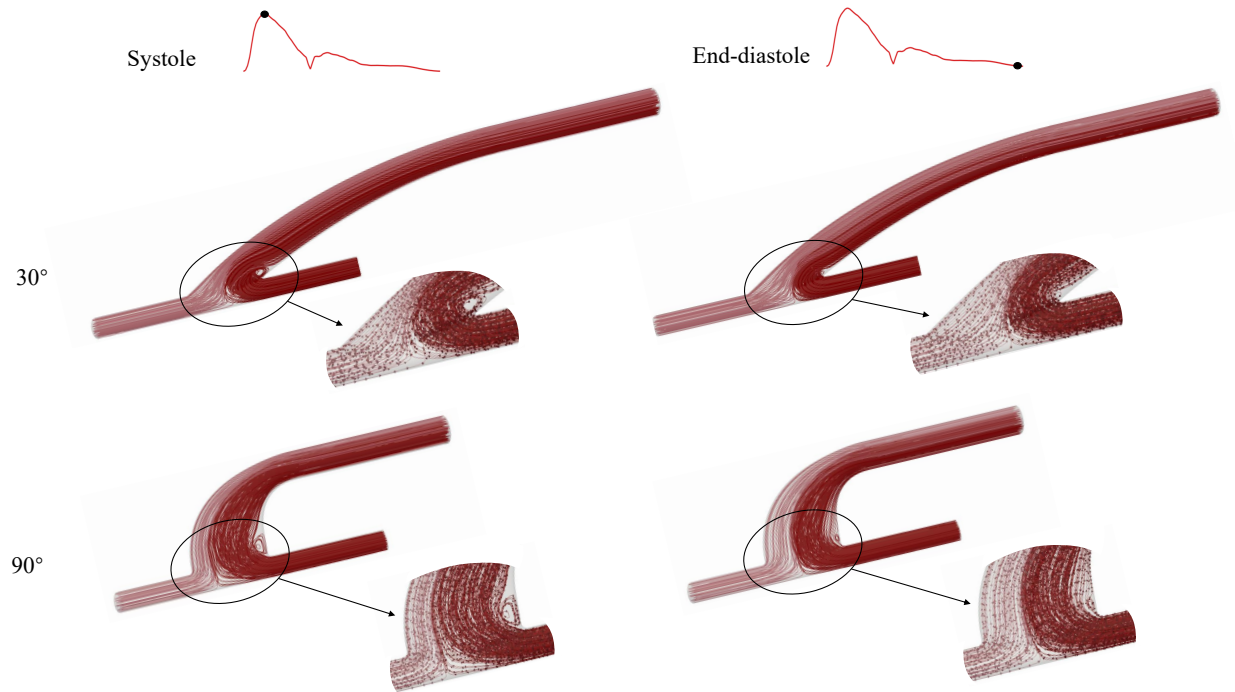


Figure 3.37: Streamlines in non-mature models ($\theta = 30^\circ$ and $\theta = 90^\circ$)

enough kinetic energy to overcome viscous friction and flow downstream smoothly. Conversely, under the action of the reverse pressure gradient ($dp/dx > 0$), the fluid particles in the layer are blocked by both reverse pressure and viscous force, causing rapid loss of kinetic energy, which will exhaust all kinetic energy at a certain place. With no-slip boundary conditions, this situation always occurs firstly near the object surface. Once this happens, according to the continuity requirement, the downstream fluid will flow backward under the action of the reverse pressure gradient causing the recirculating eddies (fig.3.38). Figure 3.37 are the streamlines in non-mature models with θ equals 30° and 90° . The recirculating eddies exist at the heel of anastomosis in all the non-mature models. At the heel of anastomosis, due to the rapid change of the boundary, the blood velocities decrease, resulting in an increase in the blood flow downstream pressure, causing a reverse pressure gradient, which result in boundary layer separation. At systole, the eddy scales are significantly larger than end-diastole (fig. 3.37). In the meanwhile, they are increased with θ from 30° to 60° and slightly decrease from 75° to 90° .

The boundary at the toe of anastomosis is also changed, whereas its curvature is more gentle than that at the heel of anastomosis. Although the curvature will cause the velocity to decrease, which will lead to the reverse pressure gradient, the confluence with the high-speed systolic blood flow at the PA inlet will cause the DA blood flow to have the same high flow rate after anastomosis, thereby decreasing the downstream blood pressure of DA. Therefore, the reverse pressure gradient only exists at the toe before the blood flows merge. Due to the rapid confluence of blood flows at the anastomosis, the reverse pressure gradient is not able to generate a recirculating flow, which only reduces the flow rate. Therefore, the LVZs exist at the toe

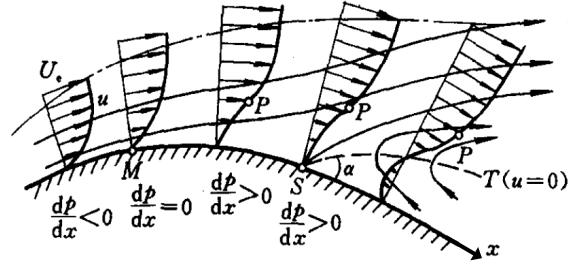


Figure 3.38: The cause of recirculating eddy [16]

of anastomosis before the flows merging site at systole. When θ increases, the merging site of the two blood is closer to the toe, which leads to the tLVZ area investment proportional to θ . At end-diastole, as θ increase, tLVZ gradually develops to the V segment. The increase of θ augments the cross-sectional of the anastomosis. In the meantime, the flow rate of PA decreases at end-diastole (compared to systole), which reduces the blood flow velocity at the merging point. Therefore, the blood pressure after the toe is higher than that of the systolic. The ideal pressure gradient ($dp/dx|_0$) produced at this time is not as obvious as systole, which leads to a more significant tLVZ appearance. As the blood flow continues to flow to the V segment, the cross-section of the blood vessel gradually decreases, and the flow velocity will gradually increase. Therefore, the ideal pressure gradient gradually increases, and the tLVZ area decreases accordingly.

The LVZ at the floor of anastomosis is caused by the convergence of fluids that come from the DA inlet and PA inlet (fig.3.37). Due to the resistance between the fluids, the blood flows are forced to change the directions and flow together to the anastomosis. Therefore, a triangular low-velocity area is formed at this area.

3.5.5.2 Wall shear stress distributions in non-mature models

The wall shear stress distributions in RCAVF are closely related to the blood hemodynamic behaviors near the vessel wall. The high-speed, smooth streamlines near the vascular boundary can accelerate the outward remodeling of vessels and promote the maturation of RCAVF. On the contrary, the disturbed streamlines will bring low shear stress and oscillating shear stress, which will accelerate the generation of stenosis and finally lead to RCAVF dysfunction (the details were discussed in chapter 1). This section will study the relation between WSS distributions and θ by observing the WSS at systole and end-diastole, TAWSS, OSI, and RRT.

WSS & TAWSS

Hemodynamic situation in the RCAVFs just after anastomosis suturing was investigated by non-mature models, which means the venous diameter has not been remodeled. Therefore, the WSS should still be measured by the normal range of WSS in vivo. In the human body, the magnitude of the shear force in the venous system is from 1 to 6 dyn/cm², and it is between 10 and 70 dyn/cm² in the arterial system [8]. In figure 3.39 and figure 3.40, the navy blue

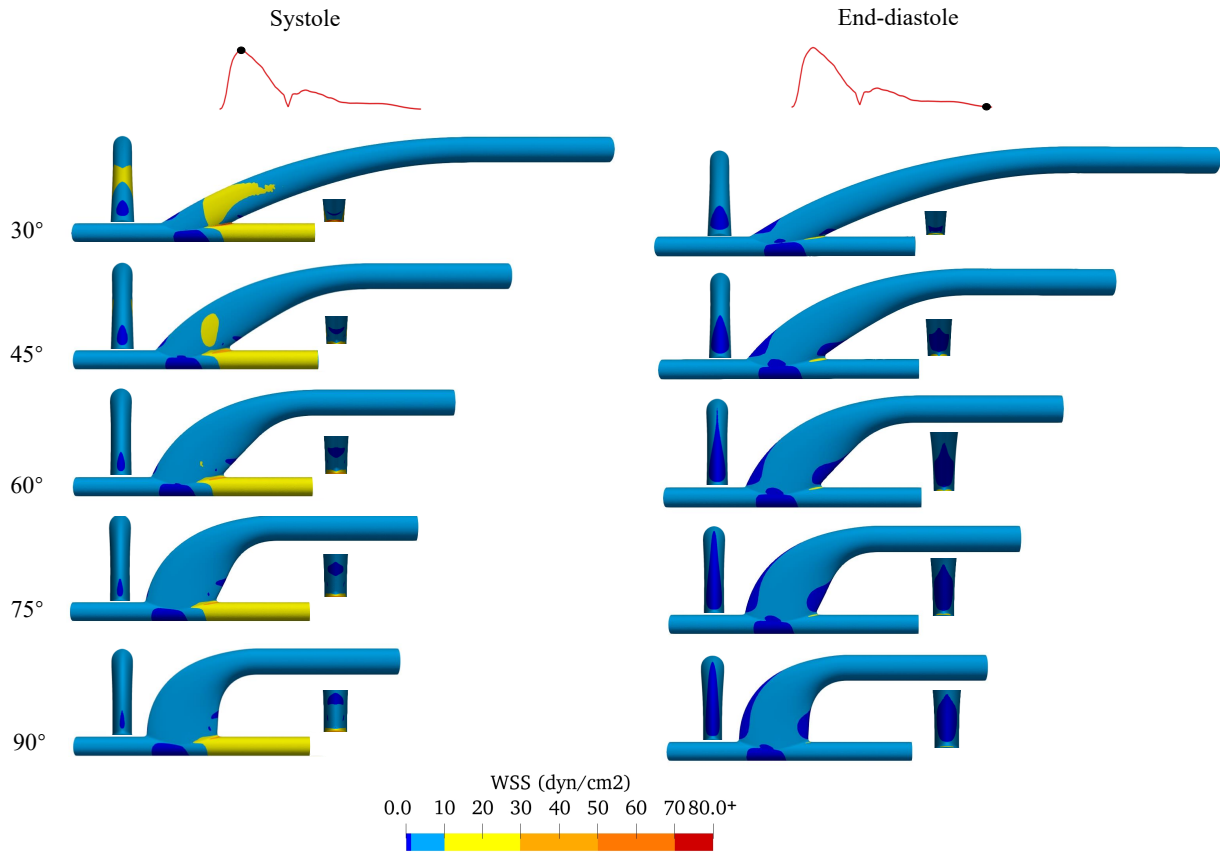


Figure 3.39: WSS distributions in non-mature models at systole and end-diastole (each set of figures shows respectively the left, main and right views of RCAVF)

represents the shear stress value inferior to 1 dyn/cm^2 . In the vein (B segment and V segment), this color indicates that the area is affected by a subnormal level of WSS. We refer to the WSS and TAWSS in the navy blue region as LWSS and LTAWSS, respectively. The blue region represents the shear stress value between 1 and 10 dyn/cm^2 , which is the WSS normal range in vein and subnormal range in the artery. The rest of the colors represent the paranormal values of WSS in the vein, and only the red region represents the paranormal WSS values in the artery. By observing figure 3.39 and figure 3.40, it can be found that RA is almost in blue region except in the systolic stage. This occurs because the blood flow entering from the DA inlet, the anastomosis, and the venous bending section produce resistance to the blood flow entering from the PA inlet. Hence the WSS levels are slightly lower than the normal values in the normal arterial system.

Figure 3.39 illustrates the WSS distributions of different θ at systolic and end-diastolic moments. At systole, it can be distinctly observed that the WSS decreases with the increase of θ . The LWSS regions (navy blue regions) are located at the LVZs (toe, heel, and floor of anastomosis). From the left views of RCAFV, the changing of LWSS regions near the toe of the anastomosis can be clearly followed. LWSS areas are slightly increased from 30° to 45° , then decrease with θ augmenting. By comparing the right view of RCAFV, the LWSS region near the heel of anastomosis is continually increasing with θ increasing and moves away from the heel. At end-diastole, the LWSS region obviously increases with θ before 60° and changes slightly among the larger anastomotic angles. As for the LWSS regions in the RA, they appear at the floor of anastomosis, whose sizes do not change a lot among different θ at systole or end-diastole.

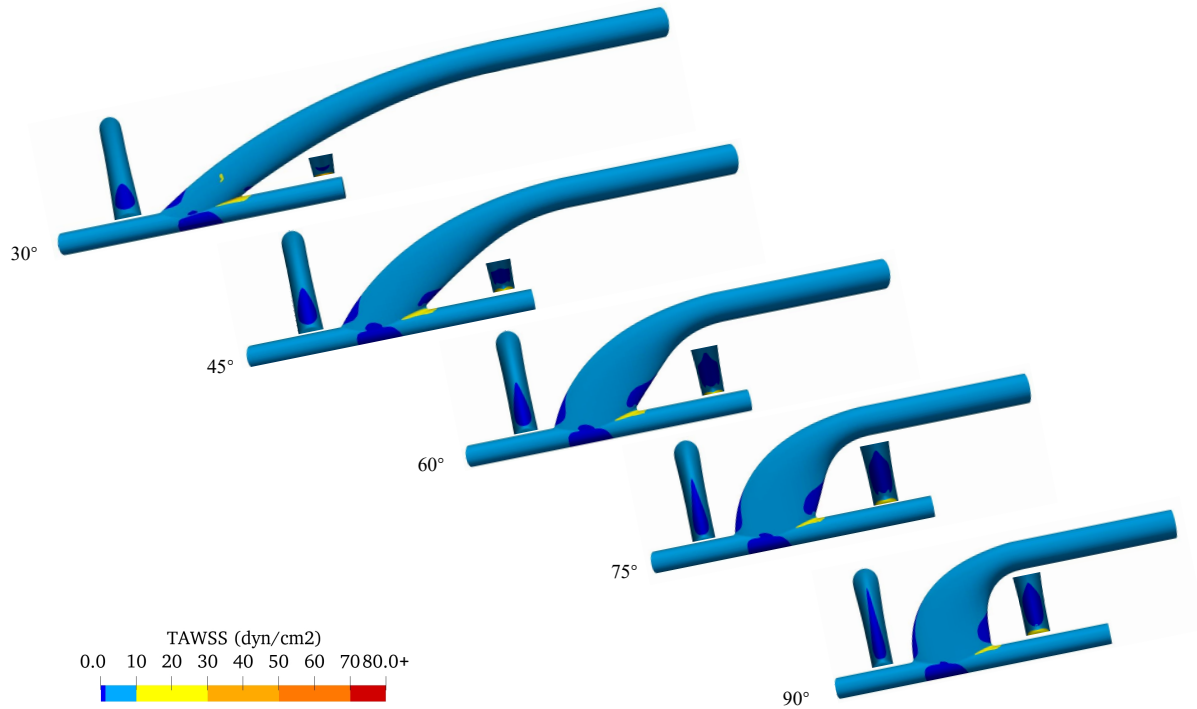


Figure 3.40: TAWSS distributions in non-mature models

Table 3.11: LTAWSS in non-mature models

	$\theta(^{\circ})$	30	45	60	75	90
CV	Toe_min (dyn/cm^2)	0.55	0.37	0.32	0.30	0.32
	Heel_min (dyn/cm^2)	0.64	0.46	0.39	0.36	0.41
	CV_area (mm^2)	11.00	19.36	23.33	23.61	21.61
RA	Floor_min (dyn/cm^2)	0.23	0.20	0.20	0.19	0.20
	Floor_area (mm^2)	25.17	25.85	25.37	25.32	25.56

TAWSS distributions in figure 3.40 are similar to the WSS distributions at end-diastole. Since TAWSS gives the average value of WSS over a pulse period, the low TAWSS regions are relatively smaller than the end-diastolic moment. However, the evolution of LTAWSS regions with θ is the same as the end-diastolic moment. We calculate the minimal TAWSS values near toe (Toe_min), heel (Heel_min), and floor (Floor_min) of anastomosis (shown in table 3.11). In the meanwhile, we also determine the total areas of LTAWSS in the vein (CV_area) and artery (Floor_area). The evolution of CV_area is basically proportional to θ . It increases rapidly from 30° to 60° , peaks at 75° , and is a slight pullback at 90° . The changing trends of minimal TAWSS are opposite to that of LTAWSS areas in CV. The minimal TAWSS values near the toe and heel reduce rapidly until 60° , reach the lowest value at 75° , then rose slightly at 90° . As for the change of the minimal TAWSS values near the floor, it is identical with the change of its total LTAWSS areas, which can be considered as constant.

OSI

Figure 3.41 represents the OSI distributions in non-mature models. The OSI values lower than 0.001 are illustrated with gray. The warmer the color in figure 3.41, the greater the value of OSI, and the more intense the WSS oscillation. According to the figure 3.41, the high OWSS values locate mainly near the heel and floor of anastomosis, where the disturbed flows exist. The total area when OSI is higher than 0.001 (OSI_area) is represented in table 3.12, which changes in the same way as LWSS regions in CV. The maximal OSI values appear in the models with larger θ (tab.3.12). These data indicates that the OWSS has a greater impact on the RCAVF with the larger anastomotic angles.

Table 3.12: OSI in non-mature models

$\theta(^{\circ})$	30	45	60	75	90
OSI_area (mm^2)	54.49	89.14	120.36	123.69	118.37
OSI_max	0.47	0.49	0.49	0.50	0.50

RRT

The RRT is a robust indicator which takes the both LWSS and OWSS into consideration. In figure 3.42, the RRT values lower than 1, representing the region without the dangers caused by LWSS

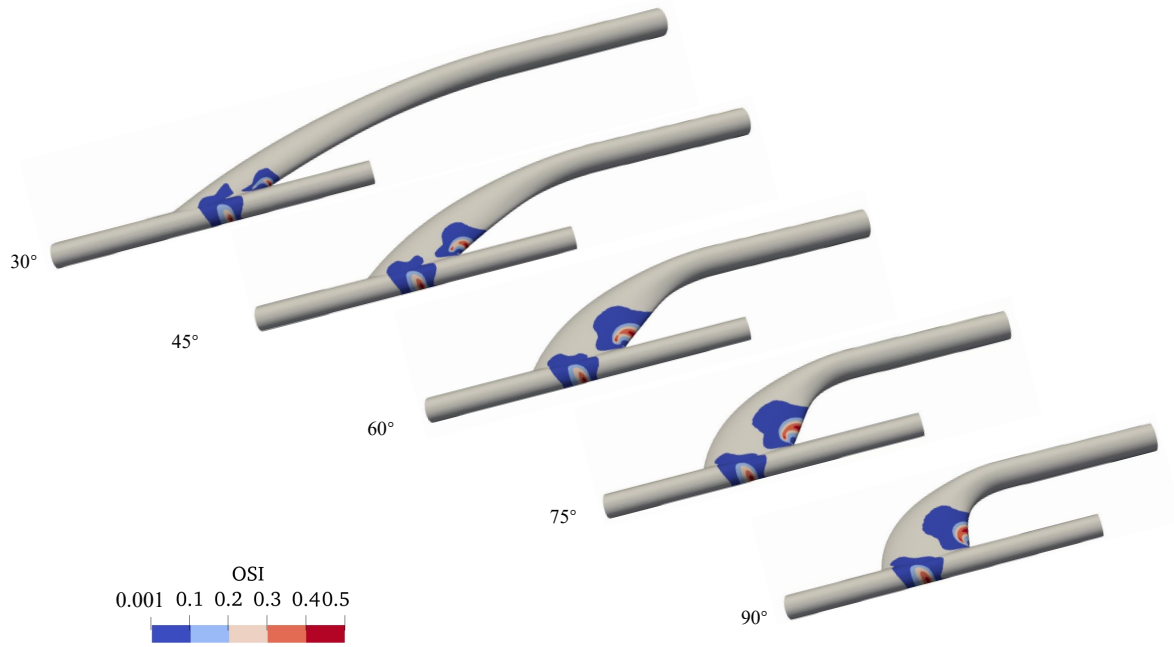


Figure 3.41: OSI distributions in non-mature models

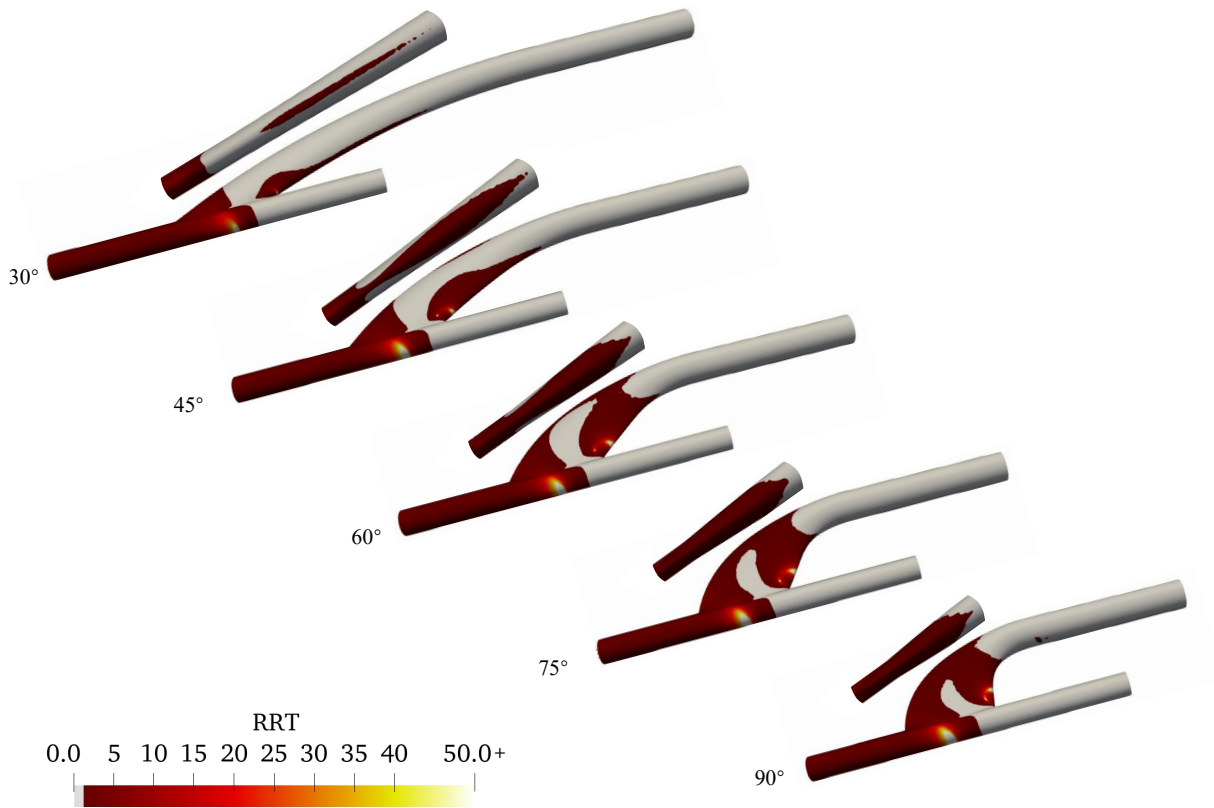


Figure 3.42: RRT distributions in non-mature models

or OWSS, were shown by gray. The larger the RRT value, the brighter the color of the area shown in figure 3.42. The figure 3.42 shows the views of RCAVF from right below and from the top left. From the view of top left, the RRT developed from toe to the V segment along the B segment with θ increasing. The total area of RRT larger than 1 (RRT_area) was continually increasing from 30° to 75°, and the maximal RRT value (RRT_max) is found in the 75° model (shown in table 3.13). In the 90° model, RRT_area and RRT_max slightly decrease. After 60°, red region of RRT has almost completely occupied the blood vessel wall of B segment at the toe side. When the θ increases, the area of B segment decreases. Therefore, the RRT_area in 90° model, shown in table 3.13, is smaller than 75° model.

Table 3.13: RRT in non-mature models

$\theta(^{\circ})$	30	45	60	75	90
RRT_area (mm ²)	237.43	299.65	331.38	343.64	330.15
RRT_max	186.11	570.14	708.18	1559.98	1511.11

3.5.6 Analyzing the results of mature models

3.5.6.1 Hemodynamic flow in mature models

The mature models simulate the mature RCAVFs that can be used for dialysis. In this set of models, the fluid fields are changed due to the high flow rate and vasodilation. Figure 3.43 represents the velocity fields at systole and end-diastole in mature models. It is obvious to observe that the dimensions of recirculating zones are significantly expanded comparing to the non-mature models. The reflux region begins at the heel of anastomosis and ends at the forepart of the V segment. The width of the reflux region along the vascular radial direction increases with θ increasing when θ is smaller than 60°, and remains similarly at 75° and 90°. An LVZ appears in the recirculating region near the heel of anastomosis when θ is larger than 60°. The tLVZs in mature models exist in both systole and end-diastole, which do not develop along the bending vein. With θ increasing, the tLVZ decreases and almost disappears at 90°. The fLVZs exist in the same regions comparing to the non-mature models, and their differences between systole and end-diastole are not obvious. The larger the θ , the closer fLVZ is to the toe of anastomosis.

The figures 3.44 and 3.45 illustrate the streamlines in mature models at systole and end-diastole, which could help us better understand the blood flow in mature RCAVF. The streamlines entering from the PA inlet are represented in red lines, and the pink lines are the streamlines entering from the DA inlet. From these figures, the recirculating region takes up nearly half area of B segment. The reflux dimension at systole is larger than that at end-diastole. At systole, the streamlines in the recirculating region are denser than that at end-diastolic moment. By observation, it can be found that most of the streamlines entering from the DA inlet flowed into the recirculating region. In the meanwhile, with θ augmenting, the hydraulic area of B segment increases. A second small reflux region in B segment near the heel of anastomosis is produced in the largest recirculating region when θ is larger than 60° (fig.3.45). In the following analyzes, the models with θ larger or equal 60° are called large- θ models, and the models with θ lower than 60° are called small- θ models.

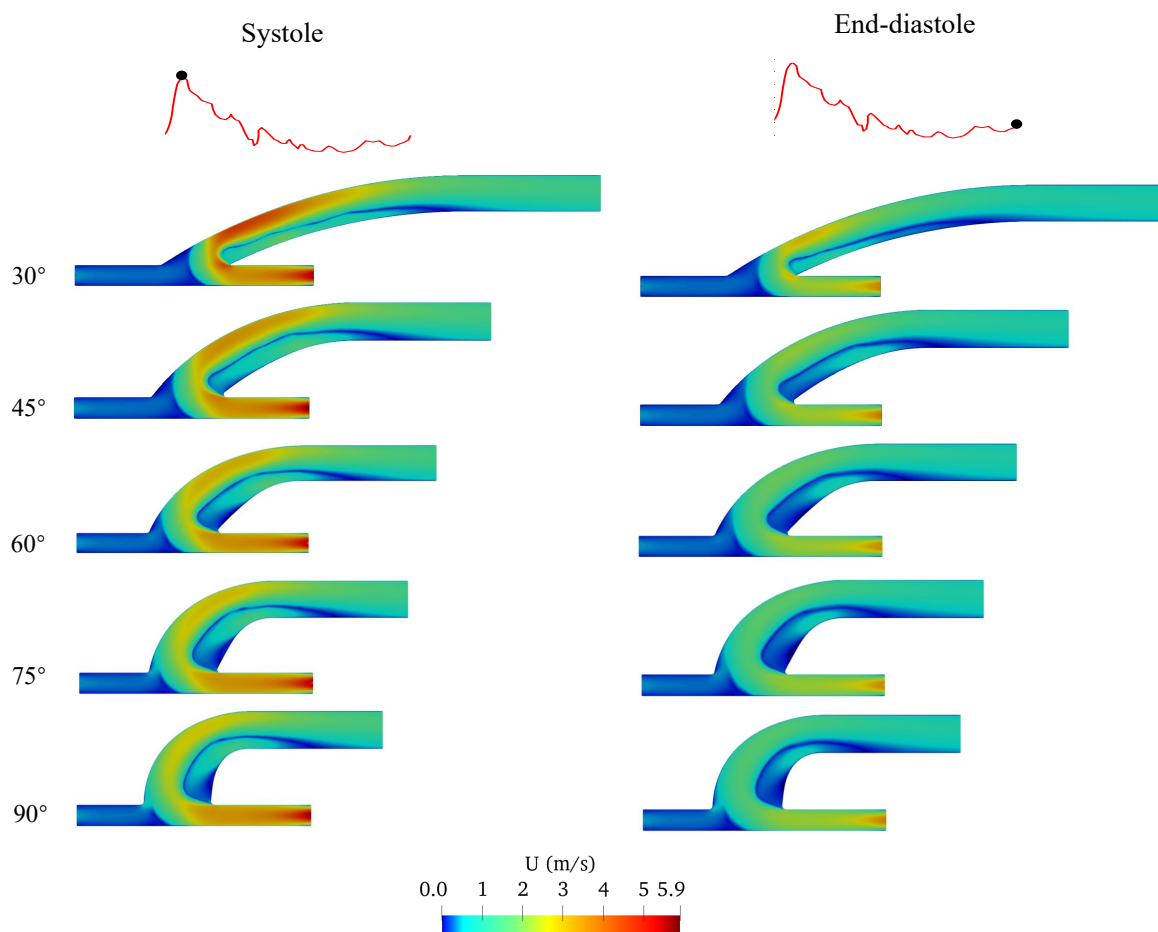


Figure 3.43: Velocity fields in mature models

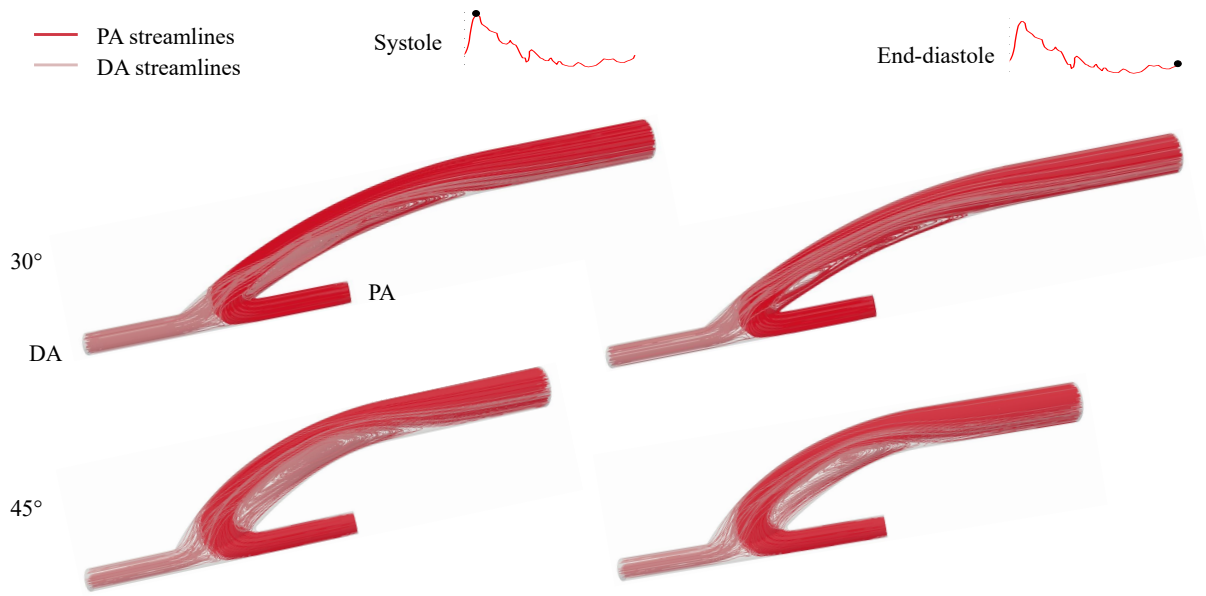


Figure 3.44: Streamlines in mature models with small anastomotic angles ($\theta = 30^\circ, 45^\circ$)

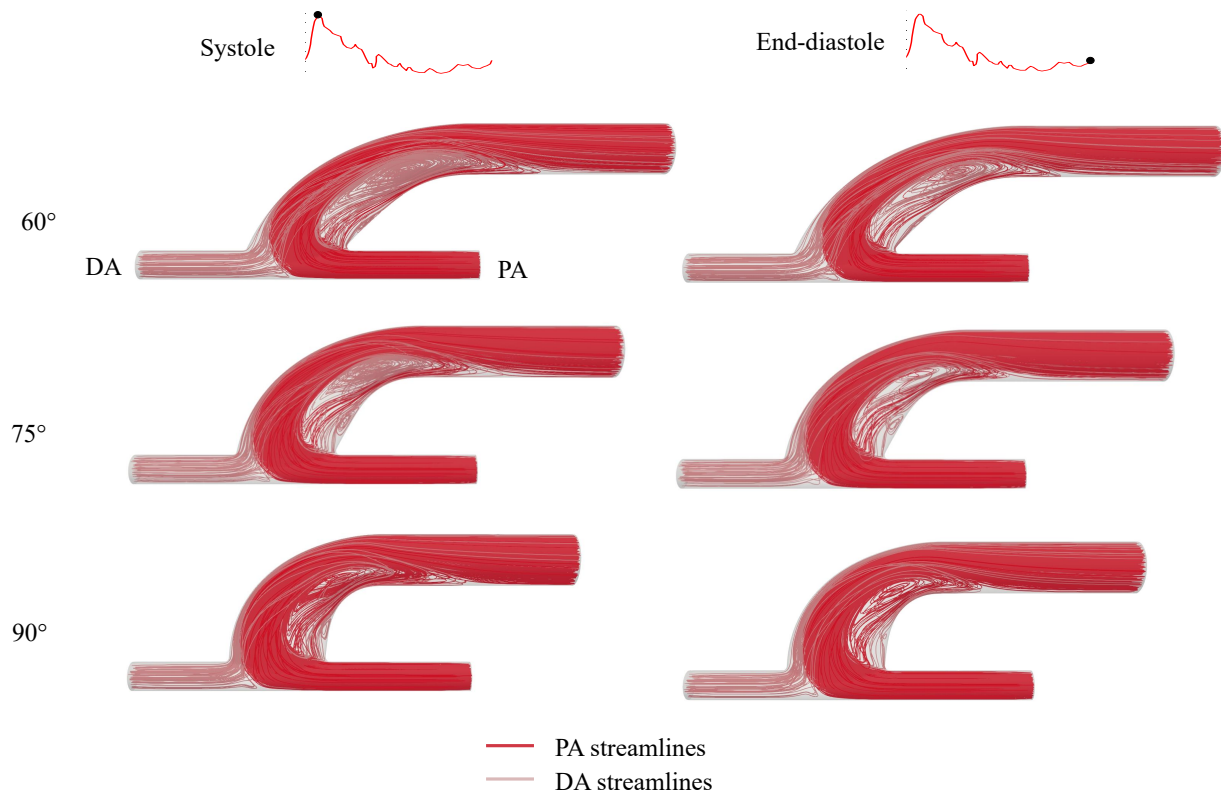
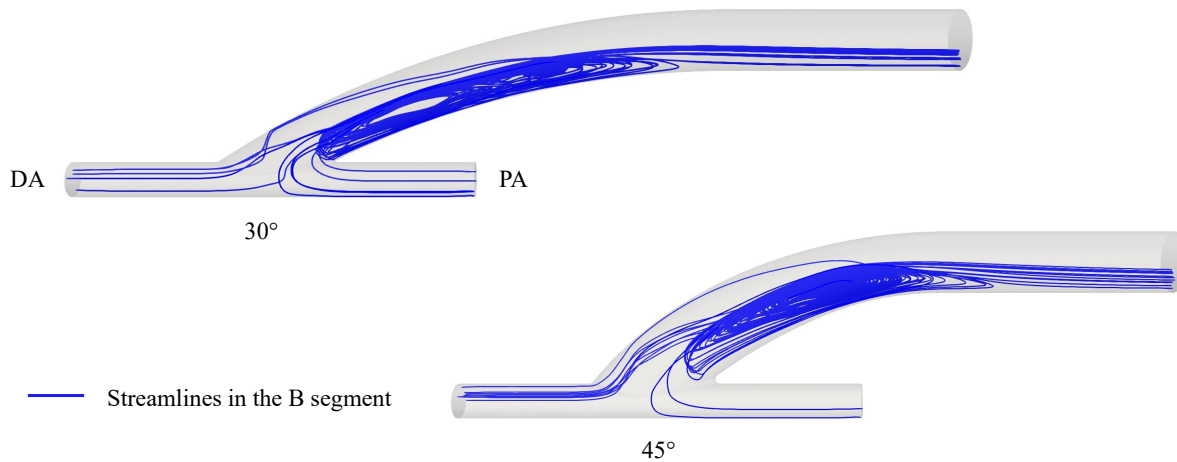


Figure 3.45: Streamlines in mature models with larger anastomotic angles ($\theta = 60^\circ, 75^\circ, 90^\circ$)

Figure 3.46: Streamlines of eddies in small- θ models

To better analyze the source of recirculating flow, the streamlines at systole in the disturbed area are extracted separately shown in figures 3.46 and 3.47. Ten streamlines are randomly selected in the largest reflux region, along with the B segment, represent in blue. Four streamlines are extracted in the smaller reflux region generated in the large- θ models (shown in fig.3.47), which are represented by red lines. With θ increasing from 30° to 60° , the streamlines entering from PA inlets flowing into the reflux region decrease and increase with θ when θ larger than 60° . By observing the red streamlines in figure 3.47, the small reflux region is mainly caused by the blood flow at the DA inlet.

3.5.6.2 Influence of distal artery inlet blood flow on recirculating region in mature models

In order to explore the influence of the blood flow entering from DA inlet on the disturbed fluid, we reduce the blood flow at the DA inlet to 20 ml/min in 60° mature model and re-simulate. The streamlines at systole and diastole in the new model are represented in figure 3.48. The dimension of recirculating region in B segment is similar to the 60° mature model with 60 ml/min flow rate at DA inlet (fig.3.45). However, most of the DA blood flow flow into the cephalic vein through the recirculating region from both sides of the blood flow entering from PA. In addition, a third reflux region is appeared at the toe of anastomosis. In figure 3.49, we extract the streamlines of recirculating regions at systole with the same way. The reflux streamlines in B segment, near the heel of anastomosis and at the toe of anastomosis are represented by blue, red and green lines, respectively. And the number of streamlines are ten for blue, and four for red and green. It can be found that the blue and red streamlines mainly come from the PA inlet flow, and half of the green lines come from PA inlet and half come from DA inlet.

In the 60° mature RCAVF model, by changing the blood flow at the DA inlet, it can be found that the DA inlet blood flow is not the leading cause of the disturbed fluid in the B segment. Most parts of the DA inlet blood flow enter the cephalic vein through the disturbed area. Therefore, when the DA inlet flow is less, there will be less DA flow appearing in the disturbed region. At

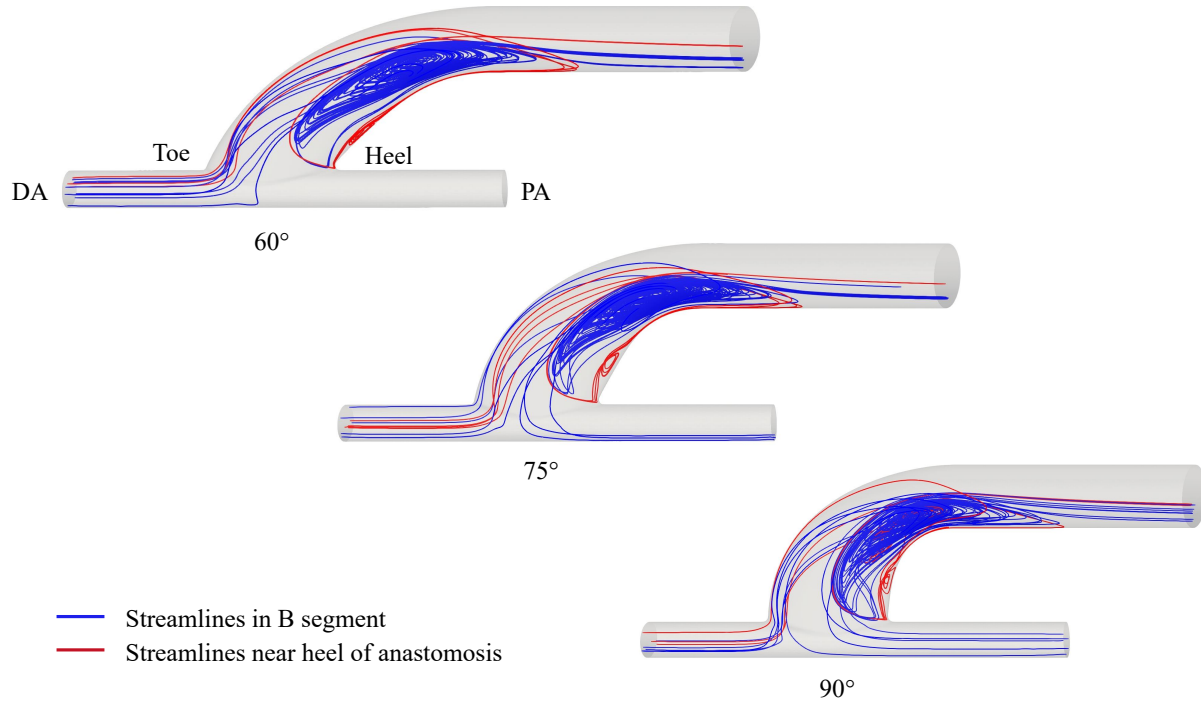


Figure 3.47: Streamlines of eddies in large- θ models

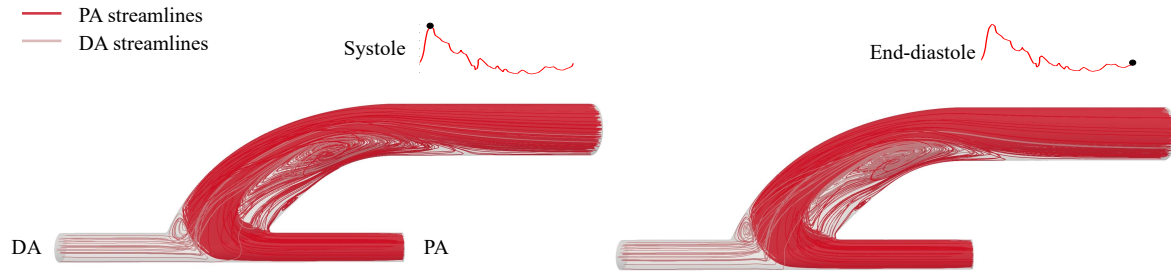


Figure 3.48: Streamlines in mature model with low flow rate from DA inlet ($\theta = 60^\circ$)

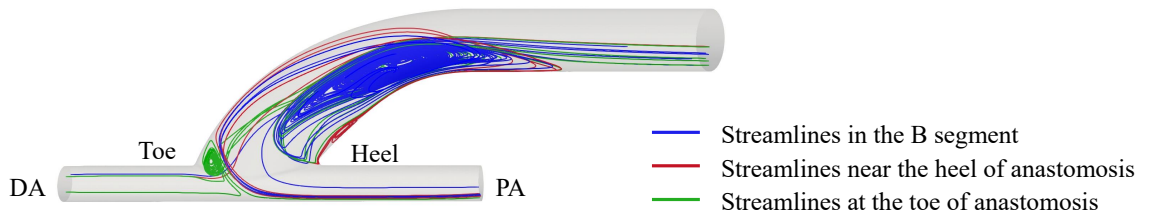


Figure 3.49: Streamlines of eddies in mature model with low flow rate from DA inlet ($\theta = 60^\circ$)

the same time, when the DA inlet flow rate decreases, a new recirculating region will be generated at the toe of anastomosis, which is caused by the increasing difference in energy produced by the inlet blood flow of PA and DA inlets.

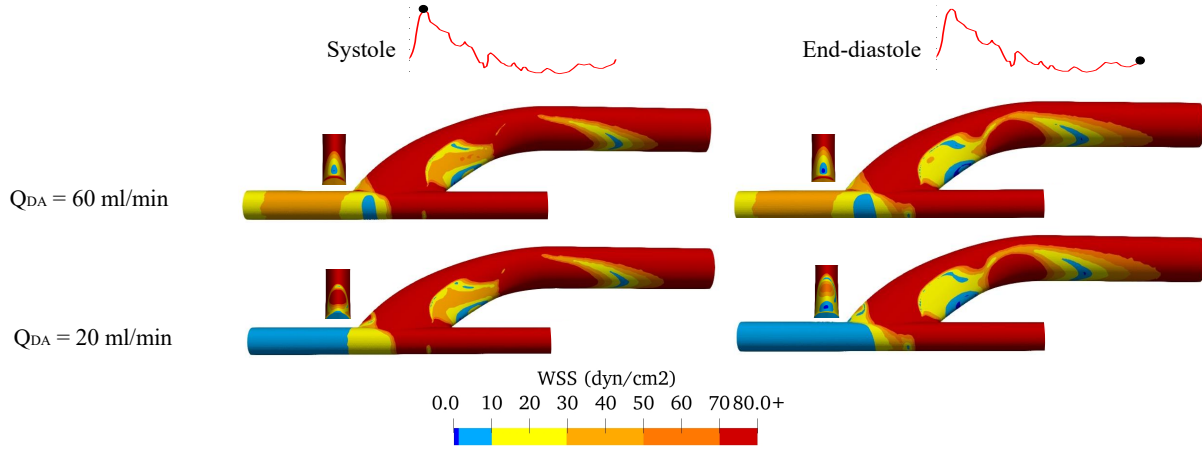


Figure 3.50: WSS distributions in mature models with different flow rates at DA inlet ($\theta = 60^\circ$)

In order to better analyze the influence of DA inlet blood flow on disturbed regions, we compare their WSS distributions. Figure 3.50 shows the WSS distributions at systole and end-diastole with different DA inlet flow rates (Q_{DA}). The WSS distributions in PA, B, and V segments are similar between these two models. The minimal WSS (WSS_{min}) appears in the blue region near the heel of anastomosis. At systole, the WSS_{min} is 0.15 dyn/cm^2 with Q_{DA} equals to 60 ml/min, and is 0.2 dyn/cm^2 with lower Q_{DA} . At end-diastole, the WSS_{min} is 0.05 dyn/cm^2 with Q_{DA} equal to 60 ml/min, and is 0.03 dyn/cm^2 in another model. By observing figure 3.50, the differences of WSS distributions exist in DA segment and the toe of anastomosis. The WSS values are reduced in the DA segment in the model with lower Q_{DA} due to the DA inlet velocity gradient decreasing. And the appearance of a new reflux region results in the different WSS distributions at the toe of anastomosis between the two models.

Figure 3.51 represents the comparisons of three WSS indicators. The differences of TAWSS distributions in the two models are the same as the WSS distributions. The minimal TAWSS near the heel of anastomosis equals to 3.17 dyn/cm^2 with higher Q_{DA} and equals to 3.05 dyn/cm^2 with lower Q_{DA} . The minimal TAWSS at the toe of anastomosis is 1.25 dyn/cm^2 with Q_{DA} equals to 60 ml/min, which is a little bit lower than the minimum value in the lower Q_{DA} model (equals to 2.56 dyn/cm^2). The area with TAWSS values lower than 10 dyn/cm^2 (blue region) are much the same (9.29 mm^2 for higher Q_{DA} and 9.17 mm^2 for lower Q_{DA}). Comparing the OSI distributions, their differences are found at the toe of anastomosis due to the recirculating flow. However, the total area of OSI greater than 0.001 do not show much difference in the two models (220 mm^2 for higher Q_{DA} and 230 mm^2 for lower Q_{DA}). By observing the RRT, the highest value (RRT_{max}) exists near the heel of anastomosis in both models. The RRT_{max} in model with lower Q_{DA} (88.48) is greater than the maximal value in model with higher Q_{DA} (79.55). And the average value of

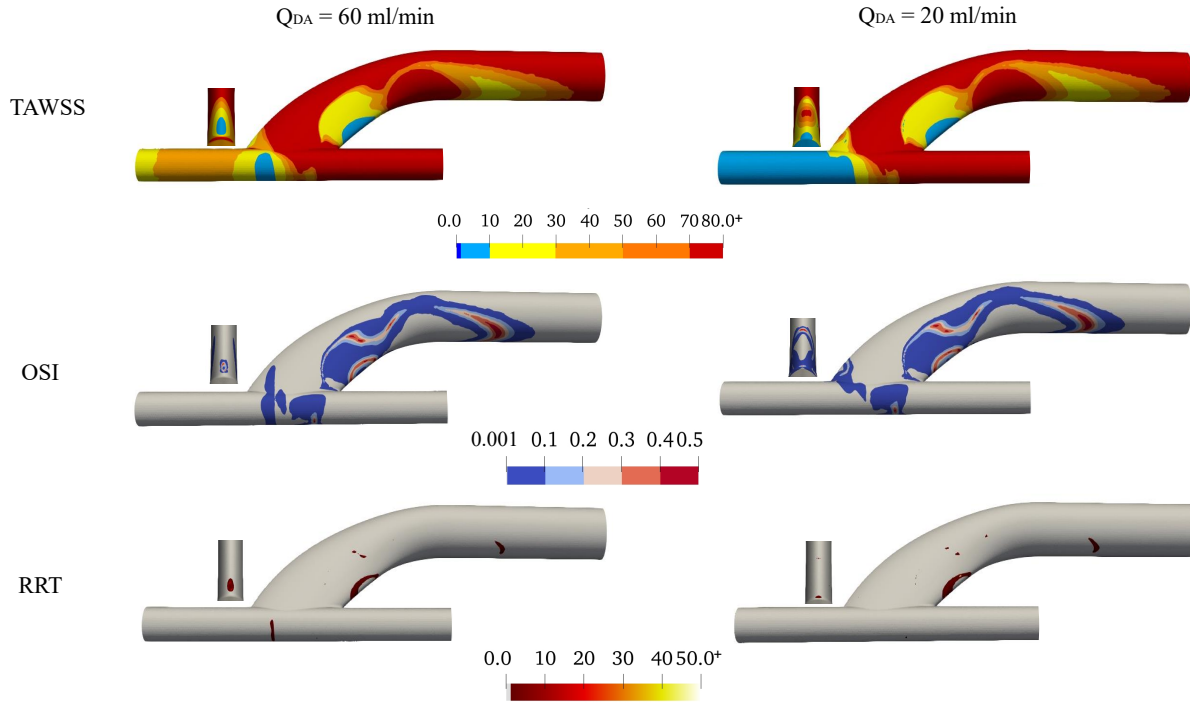


Figure 3.51: TAWSS, OSI and RRT distributions in mature models with different flow rates at DA inlet ($\theta = 60^\circ$)

RRT in model with lower Q_{DA} (3.02) is also slightly larger than the model with higher Q_{DA} (2.57). The total areas of RRT larger than 1 in the lower Q_{DA} model (5.35 mm^2) is less than the larger Q_{DA} model (6.17 mm^2).

The change in WSS distributions caused by the change in DA inlet flow rates was not significant through the above comparisons. With Q_{DA} decreasing, the kinetic energy of the blood flow entering from the DA inlet decreases. Therefore, when encountering the high-energy blood flow entering from the PA inlet, a large reverse pressure gradient is generated near the toe of anastomosis, resulting in the appearance of disturbed fluid. However, by comparing the distributions of WSS, the reflux area at the toe of anastomosis reduces the generation of local LWSS, thereby reducing the value of RRT. Although changing Q_{DA} can bring some changes to the WSS distribution in RCAVF, the negative mechanical stimulations caused by LWSSs and OWSSs received at the toe of anastomosis are pretty small compared with the LWSS and OWSS located near the heel of anastomosis. Hence, the blood flow entering from the DA inlet has no significant effect on optimizing WSS distribution in RCAVF. According to the previous analyses of the streamlines in mature models, it can be found that there is a strong correlation between θ and the disturbed fluid in the B segment. In the following subsection 3.5.6.3, we will analyze the WSS distributions in mature RCAVF models under different anastomotic angles.

3.5.6.3 Wall shear stress distributions in mature models

WSS & TAWSS

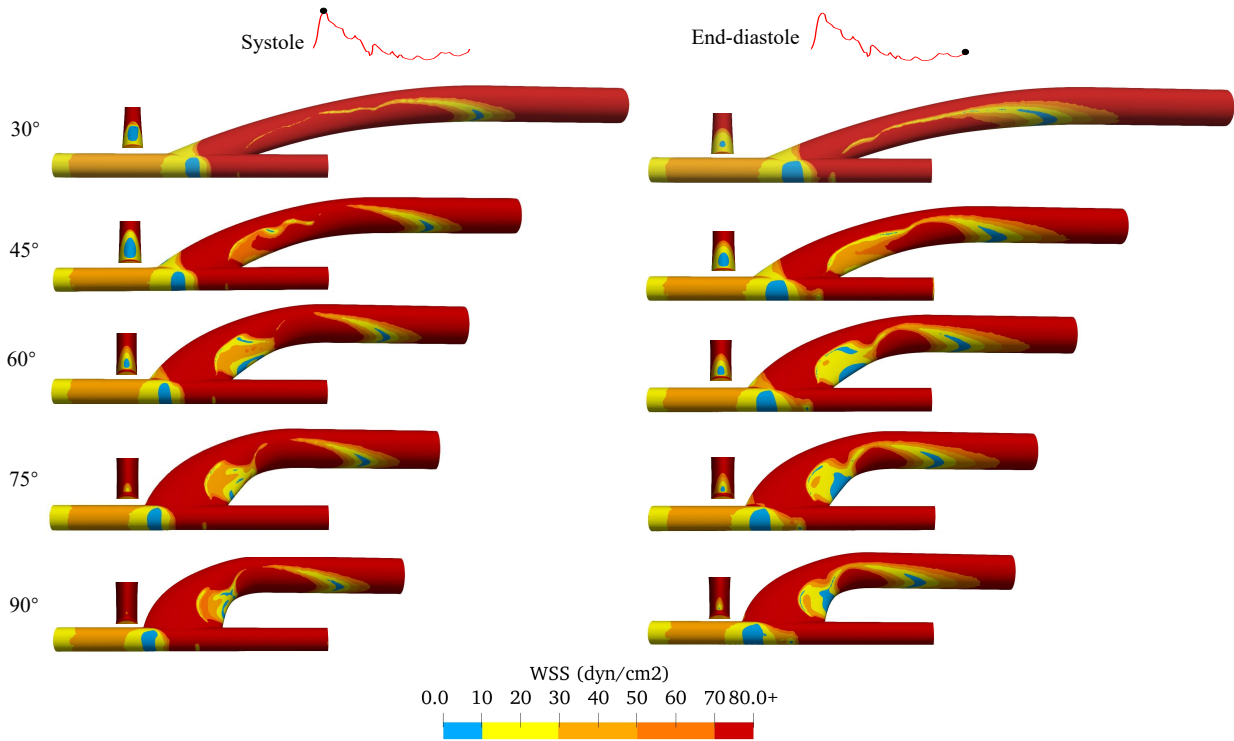


Figure 3.52: WSS distributions in mature models

Figure 3.52 shows the WSS distributions at systole and end-diastole and their changes with θ . In the mature RCAVF, the CV vessel wall has been successfully remodeled and has similar properties to the RA vessel wall. Therefore, the WSS needs to be measured by the normal range of WSS in arterial system, which is between 10 and 70 dyn/cm^2 [8]). The blue regions in figure 3.52 and figure 3.53 represent the areas suffered by the LWSS (WSS lower than 10 dyn/cm^2). In general, the blue areas appear mainly in four regions: the region at the toe of anastomosis (t region), the region in the B segment near the heel of anastomosis (h region), the region appeared in the forepart of the V segment (v region), and the region at the floor of anastomosis located in radial artery (f region).

By observing the figure 3.52, the area of f region at end-diastole is larger than that of the systolic moment, whereas it do not have the significant changes between different θ . At both systolic and end-diastolic moments, the t region has the same changing tends. The maximal area of t region locates in 45° model, decreases from 45° to 75° models, and disappears in 90° model. As for h region, it only exists in the large- θ models. The location of v region is the end position of the largest recirculating flow in the B segment. At systole, the distance between the v region and anastomosis is larger than that at end-diastole, which indicates that the scale of the largest disturbed flow changed with PA inlet flow in the mature model. And with θ increasing, more part of the disturbed flow will enter the straight vein segment.

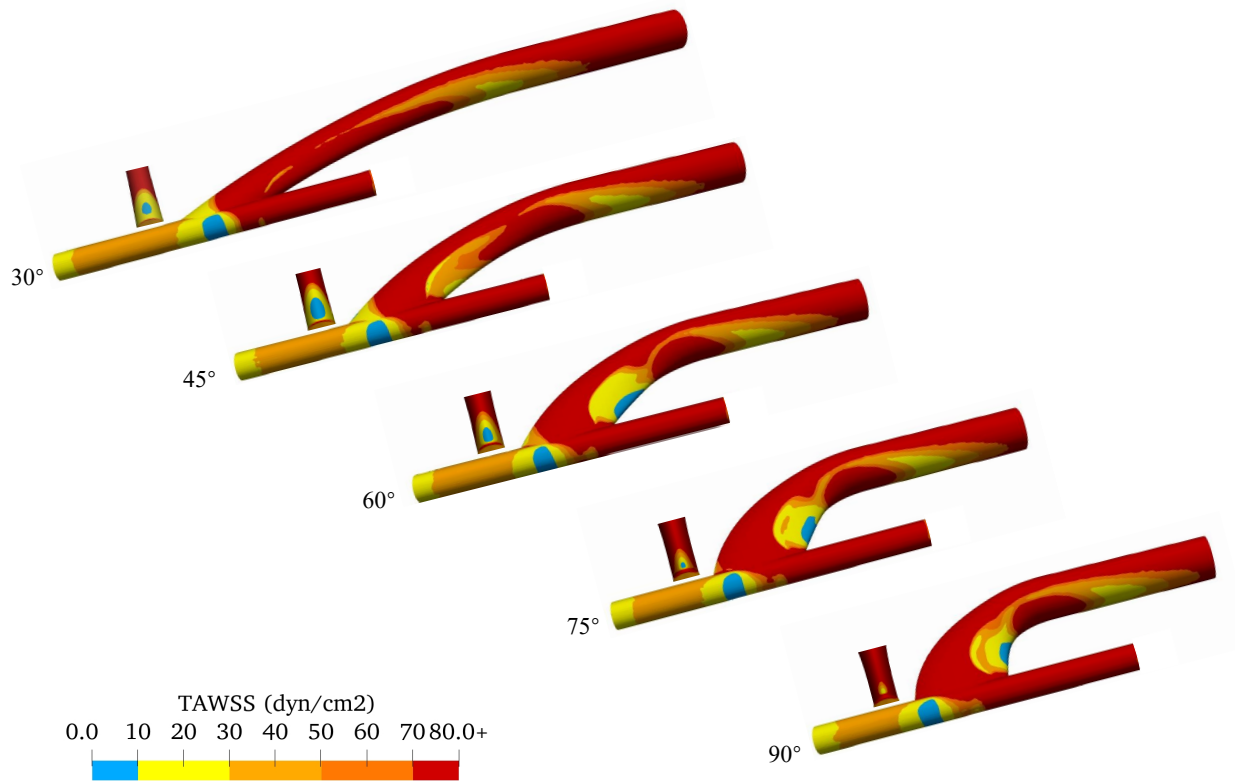


Figure 3.53: TAWSS distributions in mature models

Figure 3.53 represents the TAWSS distributions in mature models. The v region disappeared when we calculated the average WSS during one cardiac cycle. This is because the position of v region is constantly changing, and because of the high blood flow in the mature RACVF, the WSSs near the v region are large. Hence with the TAWSS post-processing, the v region disappears. On the contrary, the t , h and f regions exist and their changing trends are the same as that of WSS. In table 3.14, we calculate the minimal TAWSS values in t (Toe_min), h (Heel_min) and f (Floor_min) regions, and the total area of LTAWSS in CV (CV_area) and RA (RA_area). Under these comparisons, the minimal TAWSS value of t region decreases from 30° to 45° , increases with θ augmenting after 45° , and higher than 10 dyn/cm^2 in 90° model. The h region only appears in large- θ models. Therefore, the CV_area is rapidly augmented in 60° models. The minimal TAWSS values and total LTAWSS areas of f region do not change much with different θ .

Table 3.14: The LTAWSS in mature models

	$\theta(^{\circ})$	30	45	60	75	90
CV	Toe_min (dyn/cm^2)	6.94	0.55	1.25	4.80	-
	Heel_min (dyn/cm^2)	-	-	3.17	4.80	2.80
	CV_area (mm^2)	1.25	2.78	9.29	7.47	5.67
RA	Floor_min (dyn/cm^2)	2.59	2.35	2.27	1.75	1.91
	Floor_area (mm^2)	8.56	8.90	8.02	8.15	8.31

OSI

In the mature models, as the dimension of the disturbed fluid increases, the range of OWSS increases accordingly in the meantime. As shown in figure 3.54, the colored areas represent the OWSSs greater than 0.001, which are mainly located along the B segment at the boundaries of reflux flows. Since the length of the B segment decreases as θ increasing, the colored area is reduced. When θ is larger than 60° , a new recirculating region will be generated near the heel of anastomosis, which leads to this area being affected by OWSSs. The floor of anastomosis also has the impact of OWSS due to the confluence of blood flows. At the toe of anastomosis, the influence of OWSS is inversely proportional to the θ . As can be seen from the figure 3.44 and figure 3.45, with the increase of θ , the hydraulic area of the B segment increases simultaneously. More DA inlet blood fluid flows with PA inlet blood fluid in parallel into the vein along the passing area near DA in the B segment. However, in the small- θ models, due to the limitation of the vascular lumen area of the B segment, most of the DA inlet blood flow needs to flow into the vein through both sides of the PA inlet flow. Therefore, their interference ranges of OWSS at the toe of anastomosis are greater than that of the large- θ models.

RRT

The figure 3.55 shows the distributions of RRT greater than 1 in mature models. Compared to the non-mature models (fig.3.42), the range of RRT is significantly reduced in mature models due

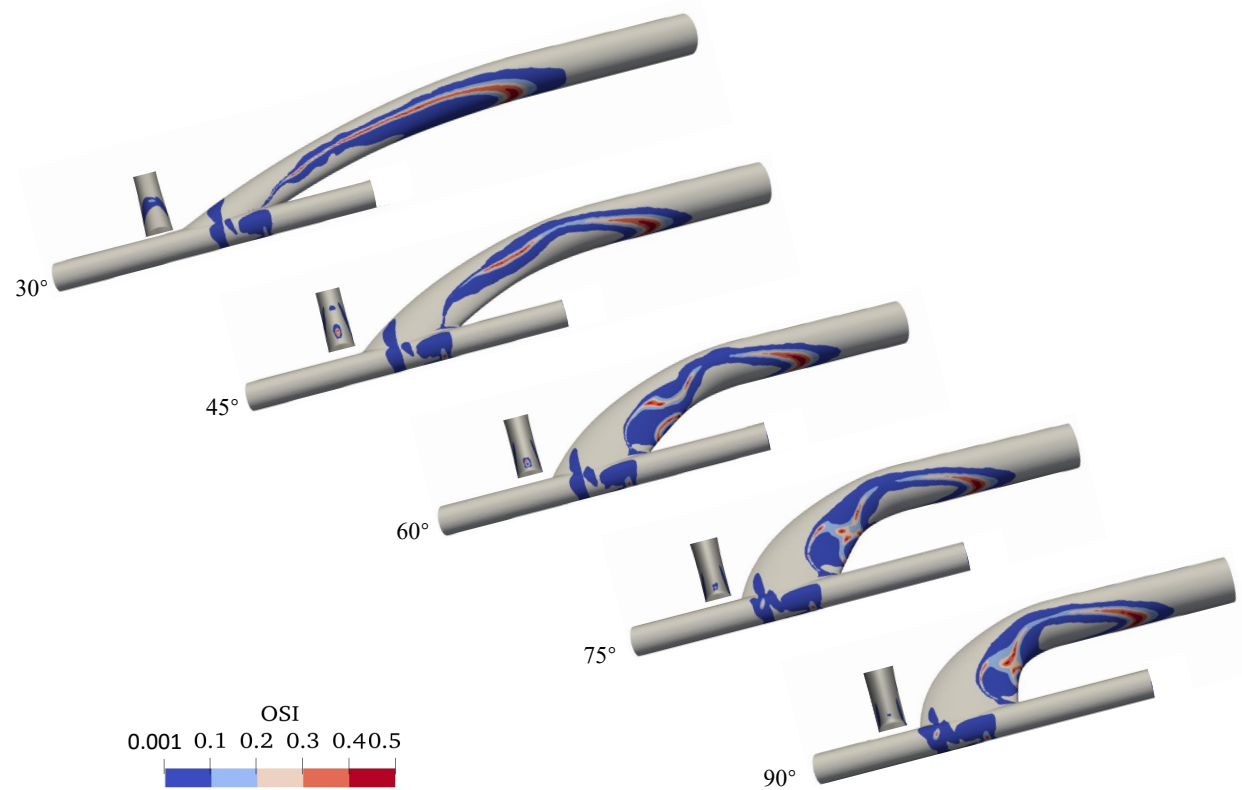


Figure 3.54: OSI distributions in mature models

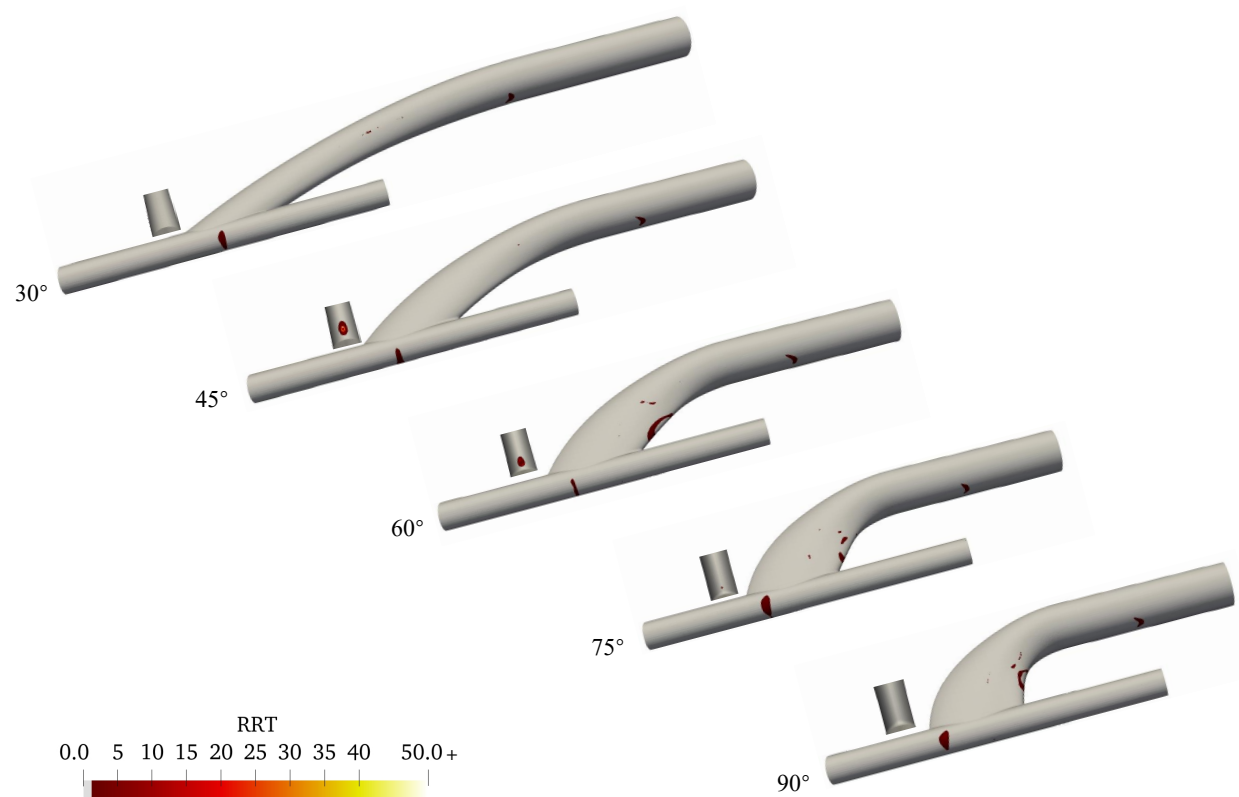


Figure 3.55: The distributions of RRT higher than 1 in mature models

to the vessel remodeling. The total colored area (RRT_area shown in table 3.55) increases with θ until 60° model, and reduces from 60° to 90° models due to the augmentation of RRT at f region. However, the maximum value of RRT (RRT_max) appears at the toe of anastomosis in the 45° model. The maximal RRTs in large-angle models, located near the heel of anastomosis, are also significant comparing to the maximal RRT in the 30° model.

Table 3.15: RRT in mature models

$\theta(^{\circ})$	30	45	60	75	90
RRT_area (mm ²)	2.39	4.23	6.17	5.07	4.58
RRT_max	9.59	143.44	79.55	73.46	54.03

3.5.7 Discussions and Conclusions

By observing the relationship between the hemodynamic behaviors, LWSS and OWSS distributions and the anastomotic angle in non-mature and mature models, the stenosis-prone locations in RCAVF can be described by figure 3.56. The sites of early stenoses in non-mature RCAVFs can be divided into two types: type a and type b (fig.3.56(a)). The sites of stenoses in mature RCAVFs can be divided into four types: type 1 to type 4 (fig.3.56(b)-(d)), which change with different θ .

The locations of recirculating flows and the three indicators (TAWSS, OSI, and RRT) in non-mature models indicate that the early stenoses tend to occur around the anastomosis shown in figure 3.56(a). The type a represents the early stenosis located in the radial artery at the floor of anastomosis. This type of early stenosis is caused by the attachment of two inlet flows, leading to the vanished velocity gradient and shear stress in this area. As the energy difference between the two inlets changes, the position will shift slightly. When the energy difference increases, the early stenosis-prone location of type a will be closer to the toe of anastomosis. The early stenosis type b is produced by the recirculation eddy appeared at the heel of anastomosis. At the anastomosis, the reverse pressure gradient ($dp/dx > 0$) caused by the rapid change of the local geometry of the blood vessel leads to the formation of the early stenosis type b. Since the blood flow at the PA inlet and the diameters of blood vessels have not increased in the initial stage of RCAVF, the recirculation eddy scale is small and close to the heel of anastomosis.

With the gradual maturity of RCAVF, the blood flows in RCAVF increase exponentially, and the blood vessels will remodel outward to adapt to the new hemodynamic environment. With the increase of blood flow rates and lumen areas, disturbed flows will be generated accordingly. These undesirable fluids will produce negative mechanical stimulations to the blood vessel walls, leading to stenoses. It will finally lead to RCAVF dysfunction. By analyzing the streamlines and the distributions of WSS, we find that the stenosis-prone locations can be divided into four types (fig.3.56(b)-(d)), which change with different θ . Stenosis type 1 appears in the radial artery at the floor of anastomosis. Its cause is the same as that of the stenosis type a in the non-mature model. The stenosis type 1 is closer to the toe of anastomosis due to the energy difference between the two inlets, which is larger than that in the non-mature model. Stenosis type 3 is located at the

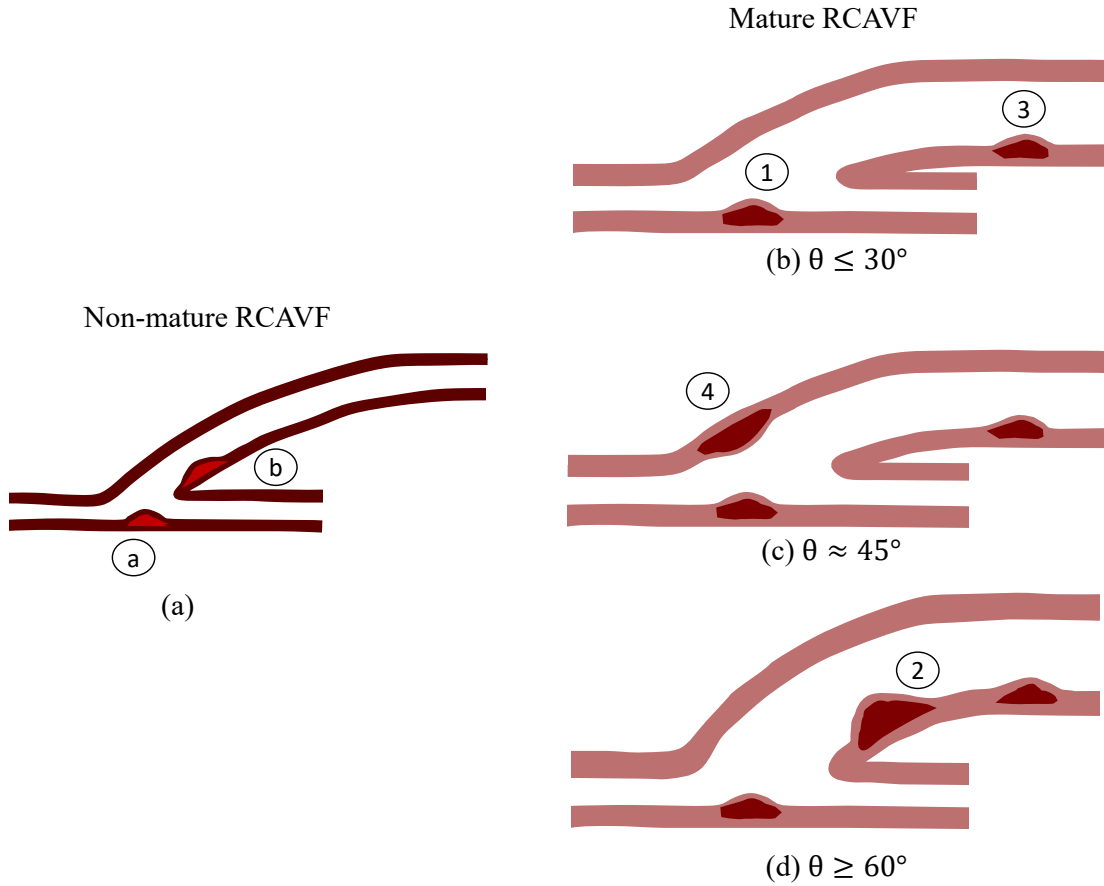


Figure 3.56: The classifications of stenosis-prone locations in RCAVF (a) The stenosis-prone locations in non-mature RCAVF (b) The stenosis-prone locations in non-mature RCAVF when θ is less than or equals 30° (c) The stenosis-prone locations in mature RCAVF when θ is around 45° (d) The stenosis-prone locations in mature RCAVF when θ is larger than or equals 60°

end of the most significant recirculation eddy in the B segment. The boundary layers of blood flows separate at the surface of the vessel wall to form a recirculation eddy. At the separation point, under the combined actions of the vanished velocity gradient and shear stress and the pulsatile PA inlet flow, the undesirable LWSS and OWSS are produced in this area, thus leading to stenosis type 3. The lumen area of the B segment increases with θ augmenting, causing the stenosis type 2 produced in the B segment near the heel of anastomosis. With the comparisons of three WSS indicators, the risk of stenosis type 2 is more significant than type 3 in large-angle RCAVF ($\theta \geq 60^\circ$). The stenosis type 4 is mainly produced when θ is around 45° . In this middle range of anastomosis angle, the vessel diameters gradually increase with θ , whereas the DA inlet blood flow is still limited by the lumen area of the B segment, resulting in negative mechanical stimulations caused LWSSs and OWSSs to the blood vessel wall near the toe of anastomosis.

Our predictions of stenosis-prone locations in RCAVF based on the simulation results can be verified by a clinical study[17]. Figure 3.57 represents the three specific sites of stenosis in mature RCAVF identified by this clinical research. Sharmila et al. followed 24 ESRD patients undergoing RCAVF dialysis with anastomotic angles around 49° . All 24 patients were found to have at least one localized stenosis. The detected locations of stenoses were divided into three types shown in figure 3.57. The risk locations of stenosis type 1 and type 2 are the same as our estimations of numerical results. The difference of stenosis type 3 is caused by the dorsal branch, which is not considered in our RCAVF models. The stenosis type 4 predicts in our 45° RCAVF mature model does not appear in their results. The measuring way of anastomotic angle may cause this difference. In the clinical study, the θ was measured by the internal angle of the anastomosis (fig.3.57), which is smaller than the θ defined in our numerical model. Therefore, the clinical results were more inclined to the results predicted by the 60° RCAVF mature model. For RCAVF using θ smaller than 60° , it has the risk of stenosis at the toe of the anastomosis with our predictions, whereas this risk is less than the risk in the bending venous segment. This clinical study only recorded the stenoses representing a reduction in luminal cross-sectional areas larger than 40%. Therefore, the difference may come from the fact that the stenosis generated at the toe of anastomosis was not obvious and was not recorded.

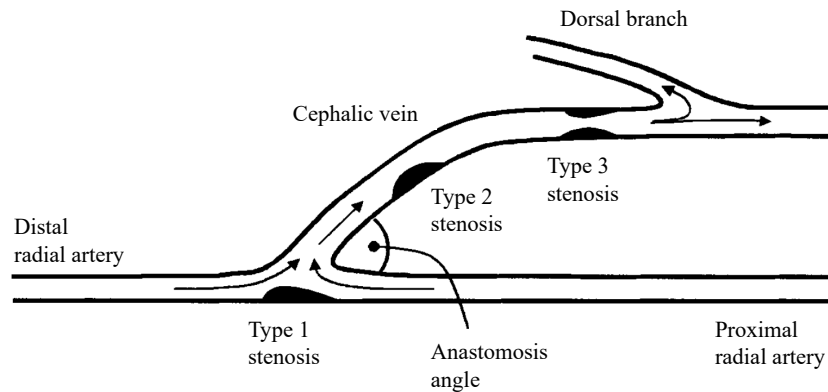


Figure 3.57: The three specific sites of stenosis in mature RCAVF identified by a clinical study [17]

By analyzing and comparing the hemodynamic behaviors and the distributions of three WSS indicators, the best range of anastomotic angles in non-mature RCAVF is under 30° , which can minimize the risk of early stenoses. To prolong the service life of mature RCAVF, using the anastomotic angle under 30° is also an efficient method. By comparing the relationship between the θ and risk of stenosis, it can be seen that their changing trends in the non-mature and mature models are almost the same. The risk of stenosis increases with the increase of θ . The non-mature models reach a peak at 75° , and the peak of the mature model is at 60° . After that, the stenosis risk slightly decreases as θ increasing. Therefore, the non-mature model can help surgeons choose the optimal anastomotic angle when they want to create tailor-made RCAVF anastomosis for different patients, such as considering the vessel wall thickness, the different blood flow rates, the different distance between the vessels, etc.

Personalized mechano-bio-faithful RCAVF preoperative model

In this chapter, we define two critical energy loss rates (CEL) in RCAVF according to the theoretical analyses in chapter 2. Combining CEL and numerical results, we created a new RCAVF model: personalized mechano-bio-faithful (PerMeBio) RCAVF preoperative model. This model aims to help surgeons from the mechanical and biological point of view to choose blood vessels and provide suggestions on the anastomosis preoperative plan, thereby increasing the maturity rate of RCAVF, reducing the risk of stenosis and prolonging the service life of RCAVF. With this model, we analyzed five cases and initially verified its applicability.

Contents

4.1	Introduction	121
4.2	Critical energy loss rate (CEL)	121
4.2.1	CEL definition	121
4.2.2	CEL to help for RCAVF anastomosis design	122
4.3	Personalized mechano-bio-faithful RCAVF preoperative model (PerMeBio-RCAVF model)	124
4.4	Clinical cases analyses	127
4.4.1	Clinical data acquisition	127
4.4.2	Clinical cases analyzed by PerMeBio-RCAVF model	129
4.5	Discussions and conclusions	132

4.1 Introduction

In chapter 4, we analyzed the RCAVF configuration from a mechanical point of view. By following the principle of minimum energy loss, It was found that D_a and D_{ra} have less influence on energy loss than θ and D_{cv} , and the distance between blood vessels h also has a non-negligible influence on E_{avf} . We suggested surgeons choose the vessels with larger diameters and a small distance while increasing the anastomotic angle for patients who use RCAVF for dialysis. This chapter will define two critical energy loss rates (CEL_a , CEL_b) based on the energy loss rate model to help surgeons evaluate the blood vessels and choose the ideal range of θ . However, blood vessels in the human body are different from mechanical pipes. The diameter of blood vessels and the thickness of blood vessel walls will change under the mechanical stimulations. Ideal mechanical stimulations accelerate the maturation of RCAVF, whereas the negative stimulus produced by LWSS and OWSS will make RCAVF unable to mature or even cause dysfunction. Although increasing the anastomotic angle can reduce the energy loss in RCAVF, our numerical research in chapter 3 found that the RCAVFs with θ lower than 30° can be less affected by LWSSs and OWSSs, which is more conducive to the vessel remodeling and can prolong the service life. In this chapter, we will combine the results of the numerical model (chapter 3) and theoretical model (chapter 4) to create a personalized mechano-bio-faithful RCAVF preoperative model (PerMeBio-RCAVF model) to assist the surgeons in RCAVF vascular selections and anastomosis plan formulation.

4.2 Critical energy loss rate (CEL)

To ensure the maturity and primary patency of RCAVF, the Kidney Disease Out-comes Quality Initiative (KDOQI) [22] and the European Society for Vascular Surgery (ESVS) [19] pointed out in the 2019 vascular access clinical guidelines that it is recommended to use an artery and vein with a diameter greater or equal to 2mm. From a systematic review [102], the author summarized 12 articles (1200 patients in total) and proposed to use CV and RA with a diameter greater than or equal to 2 mm, and not recommended to use CV and RA with a diameter less than 1.5 mm. In the references [42], [43] and [44], the authors also have different proposals for the recommended D_{cv} and D_{ra} ranges. All these suggested critical D_{cv} and D_{ra} values can ensure a high RCAVF maturity rate range from 1.5 mm to 2 mm. However, no research has high-lighted a precise critical value of D_{cv} and D_{ra} that can guarantee the maturity of RCAVF. Our analyses found that the reason for this phenomenon was that they ignore the impacts of θ . It can be observed from figure 2.14 (a) that when D_{cv} equals 3 mm, D_a equals 6mm, and h equals 12 mm, the E_{avf} generated when D_{ra} equals 1 mm and θ equals 70° is less than and the case when D_{ra} equals 2 mm and θ equals 10° . Therefore, to minimize the energy loss in RCAVF, the choice of θ is also essential while considering the vessel diameters. We proposed a Critical Energy Loss rate (CEL) concept to help surgeons choose the range of θ reasonably to minimize E_{avf} while considering patient' s specific D_{cv} and D_{ra} .

4.2.1 CEL definition

Critical energy loss rate (CEL) refers to the maximum allowable energy loss rate in the RCAVF. To define the CEL, h was set according to the distribution of blood vessels on the forearm of each

patient. From the results of theoretical model, since D_a has a relatively lesser impact on energy loss compared to θ , we fixed it to a constant value: 6.41mm [44]. CEL was defined as the smallest E_{avf} (when θ equals 90°) obtained from the critical D_{ra} and D_{cv} .

This value of CEL was calculated from the critical values of D_{ra} and D_{cv} as reported by references [102], [42], [43] and [44]. Thus, for this analysis, the critical D_{ra} and D_{cv} evolved in the range of 1.5 mm to 2 mm. We were able to deduce an interval $[CEL_a, CEL_b]$ that can be used to find the best geometry guaranteeing the maturity of the fistula. These conditions are summarized in table 4.1.

Table 4.1: Definition of CEL

	GPs				
	$D_{ra}(\text{mm})$	$D_{cv}(\text{mm})$	$h(\text{mm})$	$D_a(\text{mm})$	$\theta(^{\circ})$
CEL_a	2	2	Clinic data of the patient	6,41	90
CEL_b	1,5	1,5			

4.2.2 CEL to help for RCAVF anastomosis design

The purpose of the definition of CEL is to help surgeons assess, from a mechanical point of view, the usability of patients' blood vessels. In the case of usable blood vessels, the concept of critical energy loss rate could help design a better shape of anastomosis.

In reality, D_{ra} , D_{cv} are fixed values for each patient which can be measured by DUS. h can also be measured by surgeons. D_a does not have a lot influence on the energy loss analysis. Therefore, in this analysis, we maintained D_a at a constant value of 10 mm, which corresponded to the value practiced by our hospital partners. With the definitions of 4 GPs, we got the relation between E_{avf} and θ ($E_{avf}(\theta)$). The approximate relationship curves of $E_{avf}(\theta)$ are shown in the figure 4.1. The black curves in figure 4.1 represent the evolution of the energy loss rate in RCAVF with θ which calculated by using the reel D_{ra} , D_{cv} , and h of each patient. The red and blue lines present CEL_a and CEL_b , respectively. With CEL_a and CEL_b , we can calculate two critical anastomotic angle θ_a and θ_b through the $E_{avf}(\theta)$ curve, which provides a range of critical θ .

Table 4.2: Recommended level for anastomosis design

Recommend levels	Definition	Comments
C	$CEL_b \leq E_{avf}$	Not recommend
B	$CEL_a < E_{avf} < CEL_b$	Must combine surgeons' clinical experiences
A	$E_{avf} \leq CEL_a$	Recommend

By comparing E_{avf} with CEL_a and CEL_b , we divided the anastomosis design into three possible levels, as shown in table 4.2. When θ is greater than or equals to θ_a , E_{avf} is less than or equals to CEL_a (the red area in figure 4.1), this θ range is the most recommended range, and we define it as

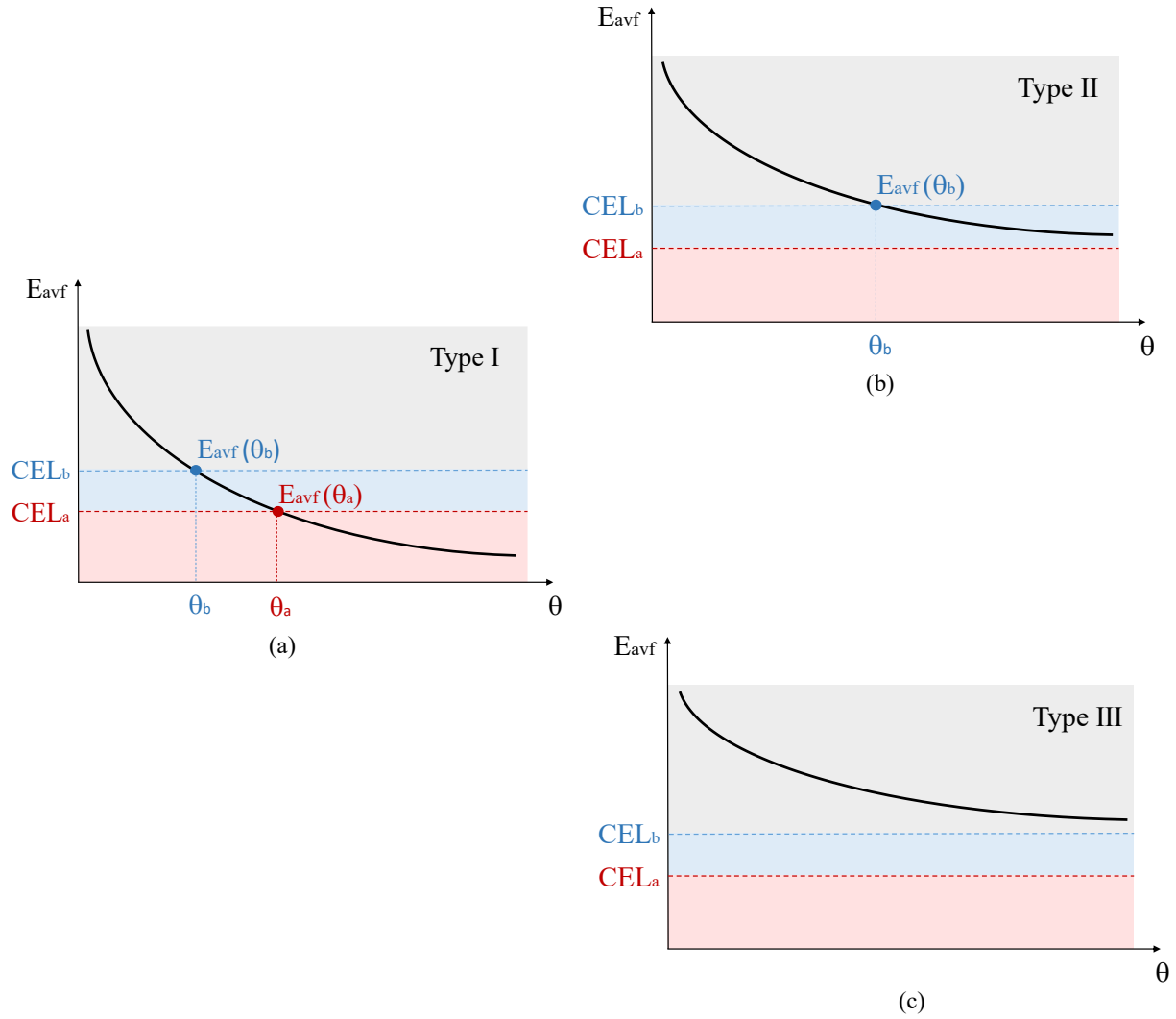


Figure 4.1: The relationship between E_{avf} and θ regarding the critical energy loss

the A-level anastomosis design. When θ is between θ_a and θ_b , E_{avf} is between CEL_a and CEL_b (the blue area in figure 4.1). At this time, θ is classified as B-level. If surgeons choose θ within this range, the performance of the patient's blood vessel wall properties should be evaluated. For patients with low vascular wall elasticity and tortuous blood vessels, surgeons must combine their own clinical experiences to use θ within this range before surgery. For an anastomosis design with θ smaller than θ_b , E_{avf} will be greater than CEL_b (the grey area in figure 4.1). This type of anastomosis design is not recommended. The anastomosis with this configuration causes the blood flow to consume a lot of energy, affects the increase of blood flow rate and affects the maturation of RCAFV.

Not all the blood vessels can get θ_a and θ_b . For the patient with small vascular diameters, the $E_{avf}(\theta)$ curves may show as figures 4.1 (b) and (c). Therefore, the blood vessels used for RCAFV can be divided into three types:

- *Type I*: θ_a and θ_b can be calculated,
- *Type II*: Only θ_b can be calculated,
- *Type III*: Neither of θ_a or θ_b can be calculated.

We recommend that surgeons choose the blood vessel Type I with an A-level anastomosis configuration to minimize the energy loss in RCFAV. For the blood vessel of Type I and Type II with B-level anastomosis design, the surgeons need to evaluate the patient's vascular performance in advance. For RCAFV with C-level anastomosis, all three types of blood vessels are not recommended.

4.3 Personalized mechano-bio-faithful RCAFV preoperative model (PerMeBio-RCAFV model)

It is not enough to use the above methods to select RA and CV and to design an anastomosis since the blood vessel wall will be remodeled under the influence of WSS. The negative stimulations of LWSS and OWSS on the blood vessel wall will hinder the expansion of the blood vessel and increase the probability of stenosis. Therefore, to create a personalized mechano-bio-faithful RCAFV preoperative model, the results of the numerical model (chapter 3) must combine with CEL to help for RCAFV blood vessel evaluations and the anastomotic angle recommendations.

Under analyzing the relation between θ and WSS distributions (chapter 3), we found that the LWSS and OWSS in RCAFV have the most negligible impact when using a small anastomotic angle ($\theta \leq 30^\circ$). However, in the analysis of RCAFV energy loss rate (chapter 4), it was found that the smaller the θ , the greater the E_{avf} when the distance between blood vessels remained constant. Because the smaller the θ , the longer the length of the venous bending segment (B segment), which will consume more energy. At this time, the E_{avf} needs to be reduced by changing the blood vessel distance between RA and CV. Therefore, we built a preoperative model to help surgeons pre-design the RCAFV and minimize the risk of stenoses.

The definition of our model is shown in figure 4.2. This model aims to help surgeons tailor RCAFVs for patients from the mechanical (energy loss) and biological (the influences of WSS on vascular remodeling) perspectives of vascular. Hence the model was named personalized mechano-bio-faithful

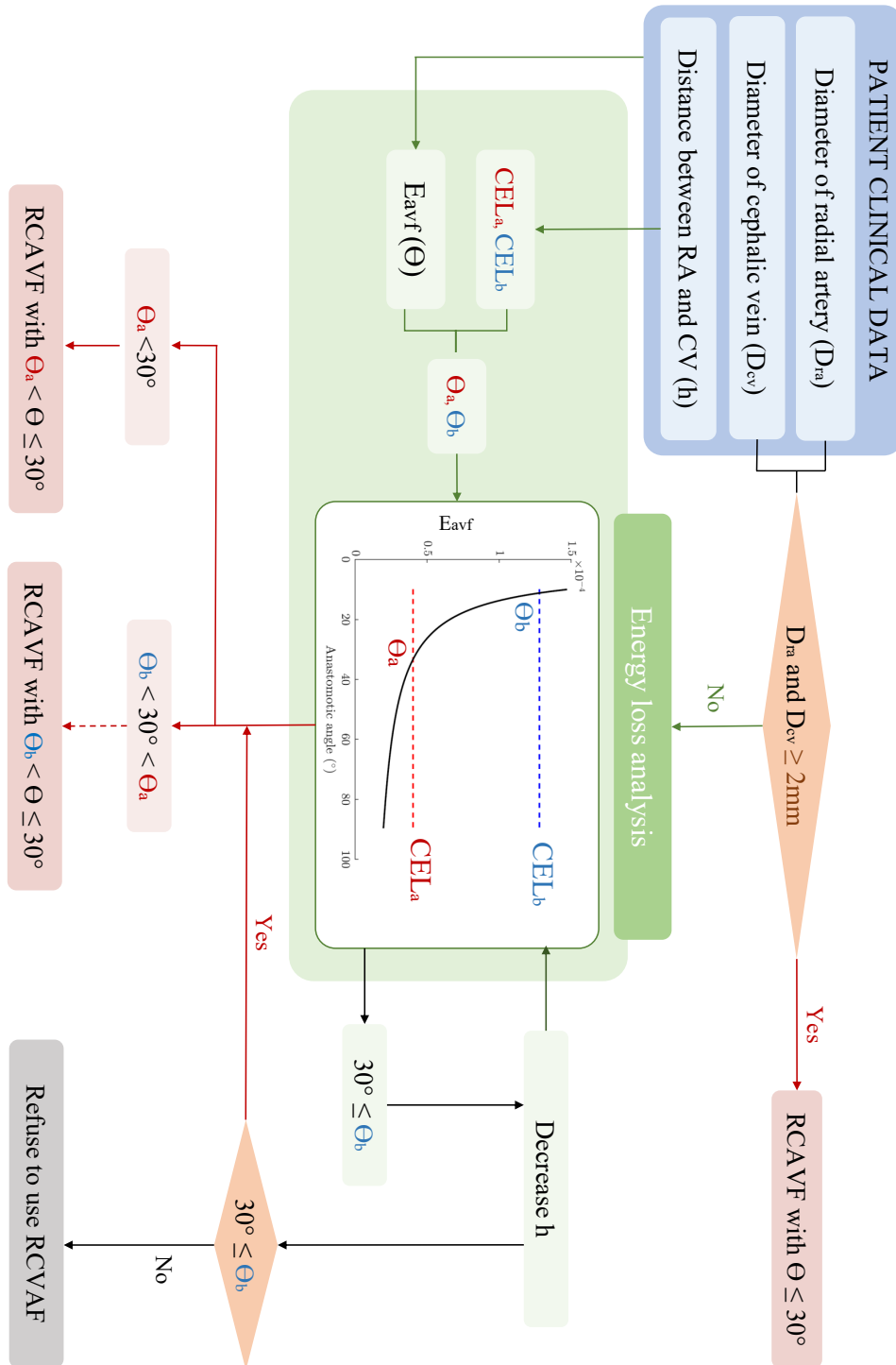


Figure 4.2: Personalized mechano-bio-faithful RCAVF preoperative model (PerMeBio-RCAVF model)

RCAVF preoperative model (PerMeBio-RCAVF model). The DUS examination is available to surgeons to measure the vessel diameters (D_{ra} , D_{cv}) of the patient. Surgeons, in the meantime, can measure the distance between RA and CV (h). These three measurable personalized GPs are marked in the blue box in figure 4.2. The anastomotic diameter D_a can be designed according to the clinical experiences of different surgeons. Therefore, the comprehensive analyses of anastomotic angle θ , the last and most crucial GP, can be summarized as following steps:

- First, we need to compare the diameters of RA and CV with the 2mm proposed in the fistula guidelines of RCAVF (KDOQI [22], and ESVS [19]). If the diameters of both vessels are greater than or equal to 2mm, we suggest that surgeons directly use the anastomotic angle lower or equal to 30° for the patient. As showing in figure 2.11 and figure 2.10. When the vessel diameters are larger than 2 mm, the fluctuations of energy loss caused by changing h and θ are relatively smaller than that caused by the vessel diameters lower than 2 mm. Therefore, for this type of blood vessels, we should pay more attention to the influences of WSS on blood vessel remodeling and focus on the choices of θ . As for patients undergoing dialysis with RCAVF with at least one blood vessel diameter less than 2mm, we recommend that the surgeon perform an energy loss analysis of the vascular structure in this patient.
- With the theoretical model and critical energy loss rate definition, CEL_a and CEL_b can be calculated with the patient's specific vessel distance h . Considering patient's real D_{ra} and D_{cv} , we can get the relationship curve between E_{avf} and θ . Therefore, the critical anastomotic angles θ_a and θ_b can be calculated. These steps are shown in the green box in figure 4.2.
- After the energy loss analysis, we need to compare the critical θ with 30° . This step aims to reduce energy loss while reducing the negative stimulation of LWSS and OWSS on the vessel wall, thereby increasing the maturity rate of RCAVF while reducing the risk of stenosis and increasing the service life of RCAVF.
 - We compare θ_a with 30° . If θ_a is less than 30° , we recommend that the patient use an anastomotic angle between θ_a and 30° . At this time, the anastomosis design uses blood vessel Type I with an A-level anastomosis configuration.
 - If 30° is between θ_b and θ_a , then the recommending range of the anastomotic angle is between θ_b and 30° . However, the anastomosis design uses blood vessel Type I with a B-level anastomosis configuration. In this condition, the performance of the patient's blood vessel wall properties should be evaluated.
 - If 30° is less than θ_b , it means that if the patient uses RCAVF with an anastomosis angle lower or equals 30° , however, the risk of stenosis in the fistula is reduced, a large amount of energy loss will be caused due to the small dimensions of blood vessels or larger vessel distance. It will affect the maturation of RCAVF. At this point, if we want to reduce the energy loss in the RCAVF, we can achieve it by reducing h . The reduced value of h needs to be calculated by the energy loss rate model. If the patient's blood vessels can obtain θ_a or θ_b which is less than 30° by reducing h , this patient can use RCAVF for hemodialysis. If the vessels are blocked by muscles or other tissues in the forearm, h cannot be reduced to the ideal range. In this case, we recommend that the patient use other types of fistulas.

4.4 Clinical cases analyses

4.4.1 Clinical data acquisition

PerMeBio-RCAVF model is a new virtual model to help surgeons design a personal RCAVF. Its operability needs to be verified by clinical cases. With the help of Dr. Nellie Della Schiava, a vascular surgeon of Hospices civils de Lyon (HCL), we followed five ESRD patients using RCAVF for dialysis. We recorded the GPs (D_{ra} , D_{cv} , h , D_a and θ) of these patients before the operations, and measured the dilating CV diameters ($D_{cv.1m}$) and the cephalic venous blood flow rates ($Q_{cv.1m}$) after one month of RCAVF creations. At the same time, examining the RCAVFs to analyze their maturations and the stenosis risks. All the measurements were achieved by DUS generated by Philips Affiniti 70 G. The clinical information was listed in the table shown in figure 4.3. The details of each clinical case are as follows:

- *PATIENT No.1:*

Case No.1 is a male patient. His RA diameter is 1.4 mm, and CV diameter is 2.8 mm. The distance between his RA and CV is 14 mm. The surgeon designed an RCAVF anastomosis with a 10 mm diameter and a 40° angle for him. The RCAVF was created on 11 March 2021. The patient acted on a DUS examination on 16 April 2021. The flow rate of fistula ($Q_{cv.1m}$) augmented to 800 ml/min and met the dialysis standards. The RCAVF did not have the stenosis risks. However, the CV diameter only dilated to 4.4 mm. Therefore, the RCAVF of patient No.1 did not mature at one month. The CV diameter was still too small for dialysis puncture.

- *PATIENT No.2:*

The RA diameter of male patient No.2 is 1.7 mm, and his CV diameter is 2.5 mm. This patient has a large distance between the RA and CV, which equals 43 mm. The surgeon liberated part of the CV vessel in his forearm, approached the CV and RA to 10 mm, and an RCAVF anastomosis was designed with a 10 mm diameter and a 10° angle. The RCAVF was achieved on 11 March 2021. The patient followed a DUS examination on 15 April 2021. After one month remodeling, his RCAVF had an excellent vascular performance. The flow rate of the fistula augmented to 1300 ml/min, and the CV diameter dilated to 7.3 mm, which met the dialysis requirements. The RCAVF of patient No.2 successfully matured at one month and has already under dialysis treatment.

- *PATIENT No.3:*

Case No.3 is the third male patient. His RA diameter is 2.6 mm, and CV diameter is 2.1 mm. The distance between the RA and CV is 11 mm. The surgeon designed an RCAVF anastomosis with a 10 mm diameter and a 70° angle for him. The RCAVF was established on 12 March 2021. With the DUS examination created on 16 April 2021, it was found that the $Q_{cv.1m}$ merely augmented to 440 ml/min and the CV diameter only dilated to 3.0 mm. The vascular conditions were quite tricky. The RCAVF was pre-thrombotic, where two stenoses were exited at the floor of anastomosis in RA and near the heel of anastomosis in CV. It caused the RA diameter to decrease to 1.1 mm. The surgeon decided to dilate the artery and the vein urgently.

PATIENTS	SEX	CREATION DATES	GPs					DUS MEASUREMENTS	MATURATION AFTER 1 MONTH (YES/NO)
			D _{ra} (mm)	D _{ev} (mm)	h (mm)	D _a (mm)	θ (°)		
No.1	Male	11 March 2021	1.4	2.8	14	10	40	DATE	16 April 2021
								Q _{ev_lm}	800 ml/min
								Dev_lm	4.4 mm
No.2	Male	11 March 2021	1.7	2.5	43	10	10	DATE	15 April 2021
								Q _{ev_lm}	1300 ml/min
								Dev_lm	7.3 mm
No.3	Male	12 March 2021	2.6	2.1	11	10	70	DATE	16 April 2021
								Q _{ev_lm}	440 ml/min
								Dev_lm	3.0 mm
No.4	Female	25 March 2021	1.7	3.2	25	10	60	DATE	30 April 2021
								Q _{ev_lm}	400 ml/min
								Dev_lm	4.3 mm
No.5	Female	31 March 2021	2.5	3.5	45	10	75	DATE	4 May 2021
								Q _{ev_lm}	700 ml/min
								Dev_lm	4.4 mm

Figure 4.3: Clinical information for 5 ESRD patients using RCAVF for dialysis (data provided by Hospices civils de Lyon)

- *PATIENT No.4:*

Case No.4 is a female patient. Her RA diameter is 1.7 mm, and CV diameter is 3.2 mm. The distance between his RA and CV is 25 mm. The RCAVF configuration was designed by an anastomosis with a 10 mm diameter and a 60° angle. The RCAVF was operated on 25 March 2021, and a DUS examination followed on 30 April 2021. According to observations, the situation of this patient was not optimistic. Stenosis was found near the heel of anastomosis in CV. Therefore, the $Q_{cv,1m}$ was just 400 ml/min and the $D_{cv,1m}$ only dilated to 4.3 mm. She also underwent a dilative treatment within 15 days.

- *PATIENT No.5:*

The female patient No.5 has a 2.5 mm RA diameter and 3.5 mm CV diameter. The distance between the RA and CV is 45 mm. The surgeon created an RCAVF anastomosis with a 10 mm diameter and a 75° angle on 31 March 2021. The patient went by a DUS examination on 4 May 2021. The Q_{cv} met the dialysis standards, which augmented to 700 ml/min. However, the CV diameter only dilated to 4.4 mm. Therefore, the RCAVF of this patient did not mature at one month due to the undesirable CV diameter. Dialysis treatment still had to wait for further expansion of CV.

4.4.2 Clinical cases analyzed by PerMeBio-RCAVF model

PATIENT No.3 & No.5

Patient No.3 and patient No.5 had the similar vascular conditions. Their D_{cv} and D_{ra} were all larger than 2 mm. With the proposition of PerMeBio-RCAVF model (fig.4.2), the best θ for them is under 30°. However, the actual anastomotic angles used by these two patients are both greater than 60°, which belonged to the dangerous angle range (analyzed in chapter 3).

For patient No.3, although the anastomosis with 70° θ can reduce the energy loss in the blood vessels, the energy consumption between the 70° and 30° anastomotic angles did not change significantly due to the close the blood vessels distance of this patient (11 mm) as shown in figure 2.12 (d). However, through the analysis of relation between θ and the distribution WSS in RCAVF (chapter 3) in non-mature models, the negative mechanical stimulations of LWSS and OWSS received at the floor and heel of anastomosis in large- θ non-mature RCAVF model were much greater than the 30°. Therefore, although this patient has the blood vessels larger than 2 mm which are in the suggesting range of the fistula guidelines ([22] [19]) and other clinical researches ([102], [42], [43] [44]), it still cannot mature. And the locations of the pre-stenoses were consistent with the prediction of our non-mature model, which were located at the confluence of blood flows in artery (stenosis type a) and the region where the disturbed fluid was generated (stenosis type b) as shown in figure 3.56 (a)).

The D_{cv} of patient No.5 is much larger than that of patient No.3. Although the distance between the blood vessels of patient No.5 is very large, it will not cause excessive energy loss because D_{cv} has the most significant impact on energy loss. In figure 2.11 (b), when D_{cv} is equal to 3.5mm, the energy losses produced by 5 mm h and 50 mm h were almost the same. Therefore, for this patient, the impact of WSS on the vessel wall should be considered more in the anastomosis design. In the analyses of chapter 3, the general WSS level in the large-angle RCAVF models was lower than

that of the 30° model. And the total area of LTAWs in the 75° non-mature RCAVF model was about twice that of 30° (tab.3.11), and it was about seven times in the mature model (tab.3.14). The presence of high wall shear stress that stimulates the outward expansion of the vessel wall [34], hence an anastomosis with θ less than 30° is more conducive to the maturation of RCAVF. Although there was no stenosis in the fistula of this patient, the lower overall WSS level in the 75° RCAVF slowed down the maturation speed. His venous blood vessels only expanded by 0.9mm in one month, which was the slowest growth speed among all the observed patients. Consequently, after one month, the patient could not undergo a dialysis treatment because the vein diameter did not reach the ideal value.

PATIENT No.1 & No.2 & No.4

The initial conditions of the blood vessels in these three patients are very similar. The diameters of their radial artery are lower than 2 mm. According to the PerMeBio-RCAVF model, we recommend to add the studies of energy loss rate for these three cases.

PATIENT No.1

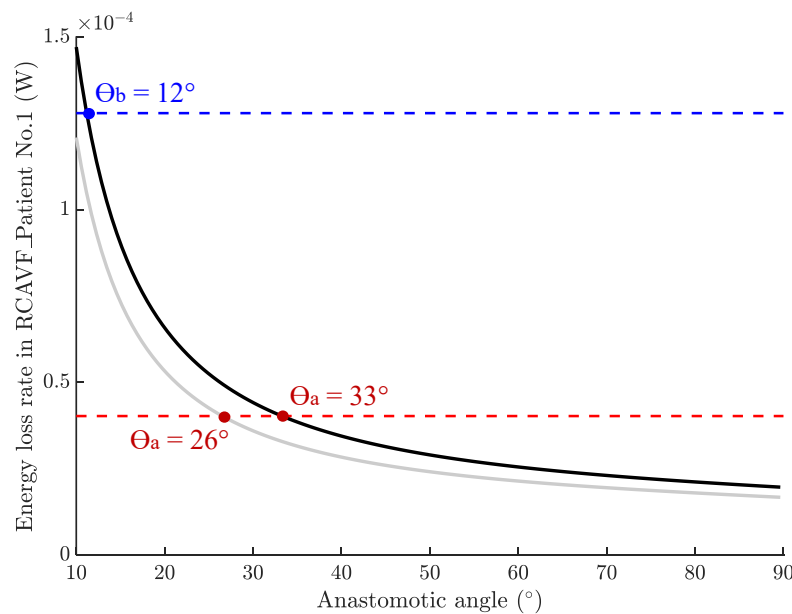


Figure 4.4: The analysis of energy loss rate for patient No.1

For case No.1, with D_{ra} equals 1.4 mm, D_{cv} equals 2.8 mm, and h equals 14 mm, we can obtain the relation curve of $E_{avf}(\theta)$ (the black curve in figure 4.4). By assuming that the vessel diameters are 2 mm and 1.5 mm, separately, we can get CEL_a (the red dot line in figure 4.4) and CEL_b (the blue dot line in figure 4.4). Therefore, the critical anastomotic angles can be calculated. θ_a equals 33° and θ_b equals 12° . We recommend the surgeon to choose a θ between 12° and 30° . If the patient's initial vascular condition is not ideal, we suggest that the surgeon can appropriately reduce h according to the tissue structure of the patient's forearm. When h is decreased from 14 mm to 10 mm, the $E_{avf}(\theta)$ will change to the gray curve shown in figure 4.4. In this condition,

θ_a equals 33° , and θ_b is lower than 10° . The best choice of θ is between 26° and 30° . In reality, the anastomosis of this patient was designed by a 40° angle. With the DUS examination after one month, the flow rate of the fistula met the dialysis standards. However, the CV diameter only dilated to 4.4 mm. Although the 40° model has less risk of stenosis than the large- θ RCAVF models, the total level of WSS in 40° RCAVF is still lower than that in RCAVF with small θ ($\theta \leq 30^\circ$). Therefore, although the surgeon did not find the stenosis sites in his fistula, his RCAVF could not be used for dialysis one month after the anastomosis due to the insufficient dilatation of D_{cv} .

PATIENT No.2

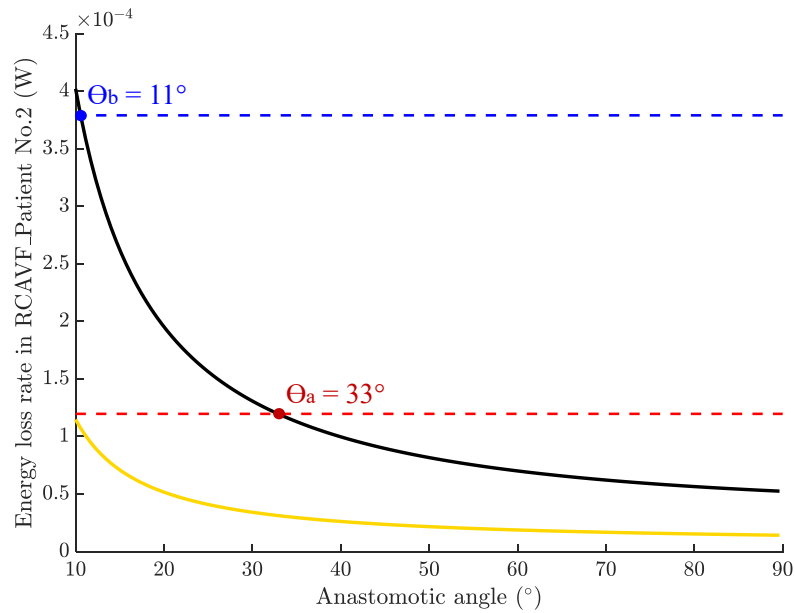


Figure 4.5: The analysis of energy loss rate for patient No.2

Case No.2 is the only case in which RCAVF has successfully matured within one month. Due to the large distance of the patient's blood vessels (h equals 43 mm), the surgeon liberated part of the CV vessel in his forearm, approached the CV and RA to 10 mm, and designed an RCAVF anastomosis with a 10° angle. The relation curve of $E_{avf}(\theta)$ can be traced by the black curve in figure 4.5 with the original GPs of this patient. When h was decreased to 10 mm, the E_{avf} was reduced. The new relation curve of $E_{avf}(\theta)$ is described by the yellow curve in figure 4.5. With the new closer vessel distance, the critical anastomotic angle θ_a was smaller than 10° . Therefore, the angle of the anastomosis used by this patient was within our recommended range. The DUS examination presented that the patient's RCAVF had an excellent RCAVF performance after one month. The flow rate of the fistula and the CV diameter all met the dialysis requirements. Due to the correct choice of θ , this patient No.2 has already under dialysis treatment.

PATIENT No.4

Patient No.4 has a larger vein compared to the two previous patients. And the vessel distance is smaller than case No.2. However, this patient's RCAVF not only did not mature after one month,

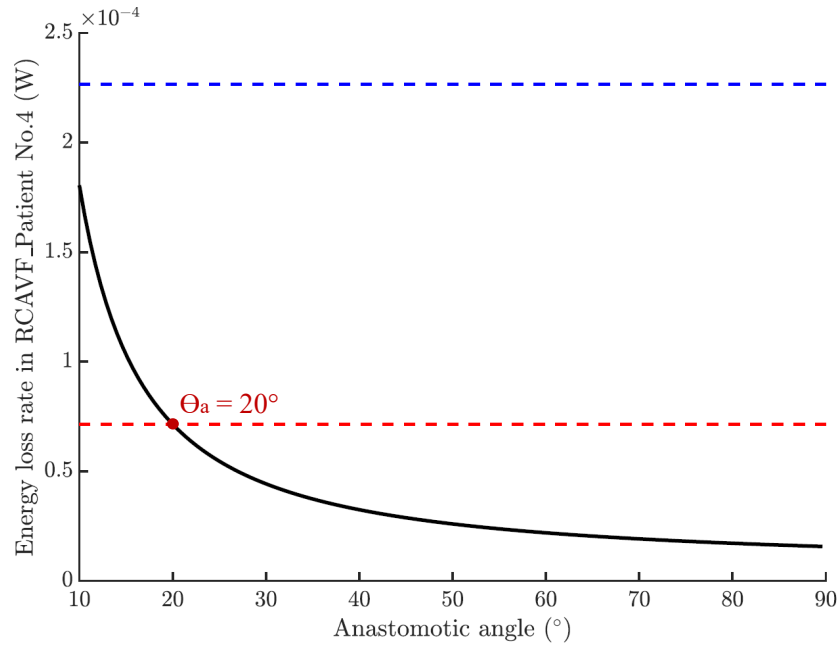


Figure 4.6: The analysis of energy loss rate for patient No.4

but also developed stenosis near the heel of anastomosis in CV. With her original vascular GPs ($D_{ra} = 1.7$ mm, $D_{cv} = 3.2$ mm, and $D_{ra} = 25$ mm), the $E_{avf}(\theta)$ can be illustrated by the black curve in figure 4.6. With calculating critical values, the θ_a equaled 20° , and θ_b was lower than 10° . Therefore, the best recommended range of θ of this patient was between 20° and 30° . However, the patient's anastomosis was created with a 60° angle, which is the most dangerous θ analyzed by our mature models. The influences of the negative mechanical stimulations caused by disturbed flow near the heel of anastomosis in 60° RCAVF are more serious than that in the RCAVF with a small θ . Therefore, under the undesirable WSS environment, the $Q_{cv,1m}$ was just increased to 400 ml/min, and the $D_{cv,1m}$ only dilated to 4.3 mm after one month. A vascular dilative treatment had been taken into consideration to figure out the pre-stenosis.

4.5 Discussions and conclusions

In this chapter, we use the energy loss rate equation derived in chapter 2 and set two energy loss rate thresholds based on clinical data and fistula guidelines. The RA and CV used for RCAVF anastomosis can be evaluated mechanically through these two CELs. Due to the remoldability of blood vessels, we need to consider the mechanical stimulations of WSSs on the blood vessel wall while optimizing its internal energy loss. Therefore, we combined the numerical simulation results in chapter 3 with CELs to create the PerMeBio-RCAVF model, which can more comprehensively optimize the RCAVF configuration from the perspective of mechanics and biology.

We used this model to analyze five clinical cases with aides of our cooperate hospital (HCL). The preoperative anastomotic plans provided by the PerMeBio-RCAVF model were compared with the actual plans, and the stenoses locations were compared with the areas we predicted. All these five

cases have substantial agreements with the analyses of the PerMeBio-RCAVF model. Therefore, the applicability of this model can be preliminarily judged.

Conclusions and perspectives

5.1 Conclusions

With the development of science and the advancement of medical technology, the average life expectancy has been extended. At the same time, as more women receive education and work, the fertility rate is also decreasing year by year. Therefore, population aging is an inevitable trend in the world. With the increase in the number of older people, in addition to affecting the labor force, it will also bring a heavy financial burden on the government and enterprises in terms of medical insurance. It is particularly prominent in terms of medical and nursing expenditures for chronic diseases. As one of the well-known chronic diseases, chronic kidney disease (CKD), its treatment is facing severe tests. From the overall situation of the world, this challenge is mainly manifested in the CKD prevention and treatment with the "three highs" of high prevalence, high combined cardiovascular disease rate, and high mortality, as well as low awareness, low prevention and treatment rates, and low cognition of combined cardiovascular disease, the "three lows" characteristics. In view of the current increasing incidence of CKD worldwide and the general lack of knowledge about the prevention and treatment of this disease, the International Society of Nephrology (ISN) and the International Federation of Kidney Foundation (IFKF) jointly proposed that the second Thursday in March is designated as World Kidney Day from 2006 onwards to raise people's awareness of CKD and related cardiovascular, and pay attention to the urgent global needs for early detection and prevention of CKD.

According to estimates by ISN and IFKF, CKD patients account for one-tenth of the world's population, that is, more than 500 million people, and most of them have not received timely diagnosis and treatments. The consequence of undetected CKD patients is loss of renal function leading to renal failure and the need for dialysis or transplantation. Although dialysis and transplantation can save patients' lives and improve their life qualities, their families and society have to bear huge medical expenses regardless of dialysis or kidney transplantation. In the United States, the annual cost of each dialysis patient is 65,000 dollars, and the annual cost of kidney transplantation is 40,000 dollars. Expensive dialysis costs mainly come from maintaining the fistula function and the secondary repair of the dysfunctional fistula. The research purpose of this Ph.D. project is to help patients increase the postoperative maturity rate of RCAVF (the preferred vascular access in fistula) and prolong its service life to reduce the physical and mental pains and economic burdens caused by the fistula dysfunction.

In chapter 1, we gave a detailed introduction to the background of the subject. We explained the standard treatment methods for ESRD patients, introduced the types of vascular access commonly

used in dialysis, and compared their advantages and disadvantages. Then we introduced the clinical methods commonly used in fistula examination. At the same time, we briefly introduced the blood and the vascular wall structure of the arteries and veins used for fistula. The maturity standard of AVF and the mechanical stimulation required for maturity were analyzed. Finally, we summarized the reasons for the immature and dysfunction of RCAFV.

In chapter 2, we first introduced the five geometric parameters (GPs) in RCAFV and the creation methods of RCAFV models used in our research. Inspired by Murry's law, we optimized the RCAFV configurations by reducing the energy loss in RCAFV, thereby increasing the maturity rate. We created a theoretical model for calculating the energy loss rate in RCAFV. The simulation results were used to verify the theoretical results. Through this theoretical model, we analyzed the relationship between the energy loss in RCAFV and its five GPs. The study found that RA and CV with a large diameter and a short distance should be selected, and a large anastomosis angle should be used for anastomosis design to reduce the energy loss in RCAFV. At the same time, through the separate analysis of each geometric parameter, D_{cv} has the most significant impact on the energy loss in the RCAFV, followed by θ and h , and the most negligible impact is D_{ra} and D_a .

In chapter 3, we studied the relationship between the WSS distributions and the anastomotic angle in RCAFV. In the RCAFV anastomosis operation, the surgeons need to design the diameter and the angle of the anastomosis. In the research on the energy loss of RCAFV, it was found that the influence of θ on energy loss was much more significant than D_a . Therefore, it can be inferred that the angle of anastomosis greatly influences the hemodynamic distribution in the RCAFV. Therefore, we created five different θ (30° , 45° , 60° , 75° , and 90°) within the range of 0° to 90° . By performing CFD simulations on these models, we selected the optimal θ by comparing the WSS distributions in the RCAFV models with different θ . Our analyses of θ were carried out in two sets of models. The non-mature model simulated the RCAFV just after the anastomosis, which presented the vessels with normal blood flows and original forms (the blood vessels have not been remodeled). The mature model simulated the blood flow state in the mature RCAFV, which illustrated the RCAFV that meets the dialysis requirement. We analyzed the distributions of WSS, TAWSS, OSI, and RRT to determine the locations of LWSS and OWSS, as well as their minimum values and distribution areas at different angles. And by observing the hemodynamic behaviors (velocity fields, streamlines), the causes of LWSS and OWSS were analyzed. Through the above research, we have reached the following conclusions:

- No matter the non-mature models or the mature models, the 30° model receives the least LWSS and OWSS stimulations, and the large-angle models suffer the greater LWSS and OWSS stimulations. Therefore, we recommend surgeons choose an anastomotic angle less than or equal to 30° for RCAFV.
- Although the hemodynamic distributions in the non-mature and mature models are different, the changing trend between WSS distributions and θ is the same. Therefore, the non-mature model can pre-simulate the RCAFV to help the surgeon make a more reasonable preoperative fistula design.
- Through the comparison of the two groups of models, we analyzed the prone locations of

stenosis in RCAFV and the development trend of stenosis during RCAFV maturation under different θ .

In chapter 4, we merged the results of the previous two chapters to create a PerMeBio RCAFV model. The purpose of this model is to optimize RCAFV from a mechanical and biological perspective to help the surgeon to judge whether the patient's blood vessels can be used for RCAFV and create RCAFV tailored for different patients according to their blood vessel parameters. We used this model to analyze five clinical cases and initially verified its operability.

5.2 Perspectives

In the future, we hope to expand the model to all types of autologous AVF. The general model will be named as PerMeBio-AVF model. To achieve this thought, we will use the same methods to analyze the fistula on the upper arm.

Preoperative examination of AVF can be performed by Magnetic resonance imaging (MRI) and Doppler ultrasound (DUS). With different examining methods, our model can be separated into two types (shown in figure 5.1). PerMeBio-AVF model can be used to analyze the DUS examination. PerMeBio-AVF FSI model will be applied to treat the MRI results.

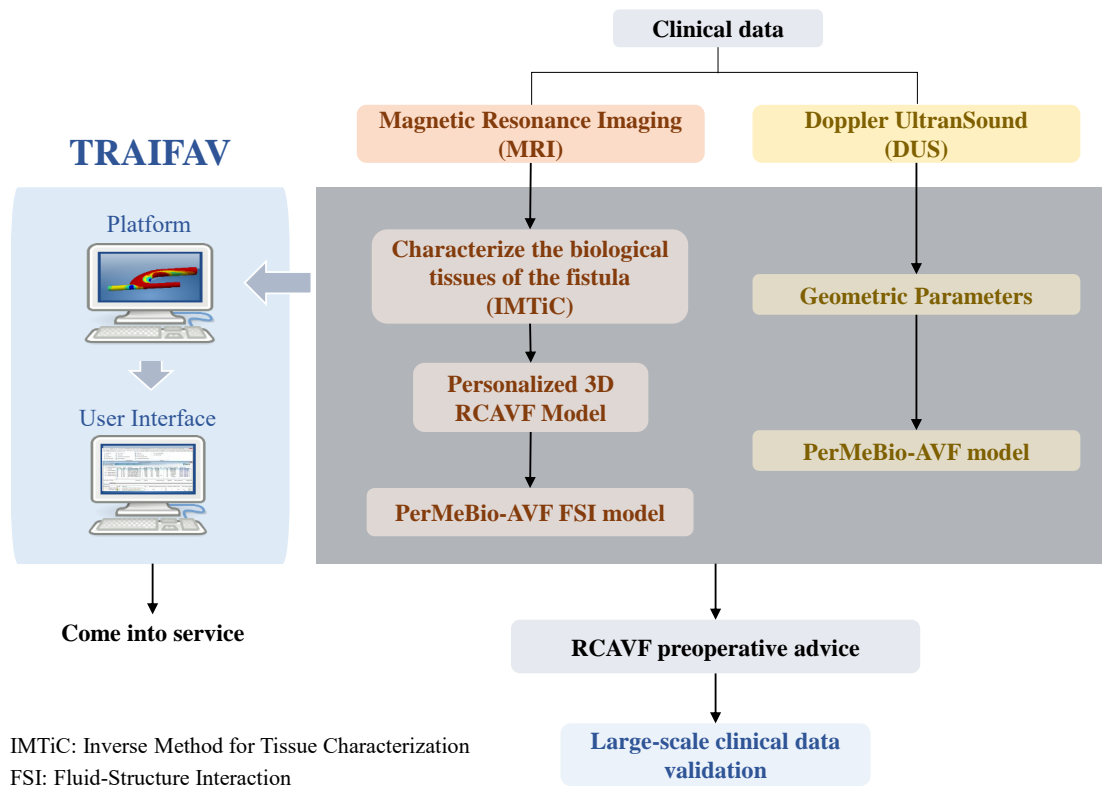


Figure 5.1: TRAIFAV (Traitement des fistule artério-veineuses) project

Due to its economy and efficiency, DUS examination is used most commonly. Through DUS measurement, we can obtain the geometric parameters of blood vessels. Therefore, we can pre-model patient's AVF configuration through the PerMeBio-AVF model. However, some patients will also use MRI for preoperative examinations. Using this examining method, we can perform a 3D reconstruction of the patient's blood vessels through a series of DICOM images. At the same time, IMTiC software (a new software created by LaMCoS and CREATIS, which can obtain mechanical characteristics (resistance, elasticity) of vessels from patient's MRI data) can be applied to analyze the natural properties of the patient's blood vessel wall. Therefore, we can perform an FSI simulation to simulate the actual hemodynamic behaviors in patients' vessels and find the best personal angle of anastomosis. This individual numerical result of best θ can replace the numerical result of ideal models in the PerMeBio-AVF model. The new model is named as PerMeBio-AVF FSI model (shown in figure 5.1).

At present, the PerMeBio-RCAVF model only analyzed five clinical cases. To assure the operability of the model, a large amount of clinical data must be studied. Our ultimate goal is to use this model to aid the surgeons in the creation of fistulas. Therefore, a digital platform can help surgeons efficiently, conveniently, and safely use this model to make a preoperative anastomosis plan. We have successfully applied for the TRAIFAV (traitement des fistule artério-veineuses) project funded by the French National Centre for Scientific Research (CNRS) in July 2021. The objective of this project is to develop new free software, which allows multiphysics numerical simulations to provide the support for surgeons to design the AVF (shown in figure 5.1).

In the future, we will complete our model and verify it through a large number of clinical cases. Finally, we will develop a digital and user-friendly platform that can automatically process patient data to help surgeons design the autologous AVF configuration.

Matlab code of the Poiseuille flow adapted to a circular face

The Matlab below allows to adapt a Poiseuille profile to a circular surface, and create the time-various inlet velocity files for Foam-extend.

```

1  % Import the geometric data of PA inlet face
2  points = importdata('donnees\faceCentres_PA_inlet');
3  cycle = load('donnees\3_cycles_flowrate.txt');
4  Vc = 2.*cycle(:,2)./(pi.*0.00135.^2);          %PA inlet maximal velocity (m/s)
5  t = cycle(:,1);                                %Pulse time (s)
6
7
8  % Switching to polar coordinates
9  [theta, R, Z] = cart2pol(points(:,1), points(:,2), points(:,3));
10
11 % Separate the boundary points and inner points
12 Rmax = max(R);
13 IDXext = find(abs(R-Rmax)<1e-5);
14 Pext = points(IDXext, :);
15 Pint = points;
16 Pint(IDXext, :) = [];
17
18 % Calculate the velocity of each point
19 Rm = mean(R(IDXext));
20 V = Vc * (1-(R.^2/Rm^2));
21 V(:, IDXext) = 0; % Set the boundary velocity to 0
22
23 % Write source files for Foam-extend
24 new_path = 'PA_inlet';
25 if exist(new_path, 'dir')
26     rmdir(new_path, 's');
27 end
28 mkdir(new_path);
29 cd(new_path);

```


30
31
32
33
34
35
36
37
38
39
40
41
42
43
44
45
46
47
48
49
50
51
52
53
54
55
56
57
58
59
60
61
62
63

```
for i=1:length(Vc)
```

$$\mathbf{v} = \mathbf{V}(\mathbf{i}, :)' ;$$

```
%%% Write the velocity into file
```

```
if i==1
```

```
mkdir(sprintf('%i', t(i)));
```

```
else
```

```
mkdir(sprintf('%1.3f', t(i)));
```

end

```
if i==1
```

```
cd(sprintf('%i', t(i)));
```

```
else
```

```
cd(sprintf('%1.3f', t(i)));
```

end

```
fid = fopen('U', 'w');
```

```
fprintf(fid, 'FoamFile\n{\n version    2.0;\n format      ascii;\n');
```

```
fprintf(fid, '    class    vectorAverageField;\n object    values;\n}\n');
```

```
fprintf(fid, '// * * * * * * * * * * * * * * * * * * * * * * * * * * * * //
```

```
fprintf(fid, '\n// Average\n\n(0 0 0) \n\n // Data on points\n');
```

```
fprintf(fid, '1916\n');
```

```
fprintf(fid, '\n');
```

```
fprintf(fid, '(%1.8f %1.8f %1.8f)\n', [zeros(length(v), 1), zeros(length(v), 1), v]);
```

```
fprintf(fid, ')\n');
```

```
fclose(fid);
```

```
cd ../
```

end

```
cd ../
```

Setting up the numerical models with rigid walls in Foam-extend

U

```

1  /*-----* C++ *-----*/
2  | ===== |
3  | \ \      / F i e l d      | foam-extend: Open Source CFD |
4  | \ \      / O p e r a t i o n | Version: 4.0 |
5  | \ \      / A n d           | Web: http://www.foam-extend.org |
6  | \ \      / M a n i p u l a t i o n | |
7  \*-----*/
8  FoamFile
9  {
10     version      2.0;
11     format        ascii;
12     class         volVectorField;
13     object        U;
14 }
15 // *****
16
17 dimensions      [0 1 -1 0 0 0 0];
18
19 internalField uniform (0 0 0);
20
21
22 boundaryField
23 {
24     PA_inlet
25     {
26         type              timeVaryingMappedFixedValue;
27         dataDir             "$FOAM_CASE/constant/boundaryData/PA_inlet/"
28         offset              (0 0 0);
29         setAverage          off;
30     }

```

```

31     DA_inlet
32     {
33         type            timeVaryingMappedFixedValue;
34         dataDir          "$FOAM_CASE/constant/boundaryData/DA_inlet/"
35         offset           (0 0 0);
36         setAverage       off;
37
38     }
39     V_outlet
40     {
41         type            pressureInletOutletVelocity;
42         value           uniform (0 0 0);
43     }
44     Blood_wall
45     {
46         type            fixedValue;
47         value           uniform (0 0 0);
48     }
49 }
50
51 // *****

```

p

```

1  /*-----* C++ -*-----*\
2  | ===== | |
3  | \\      / F ield      | foam-extend: Open Source CFD |
4  | \\      / O peration  | Version: 4.0 |
5  | \\      / A nd        | Web: http://www.foam-extend.org |
6  |  \\/      M anipulation | |
7  \*-----*/
8  FoamFile
9  {
10     version    2.0;
11     format      ascii;
12     class      volScalarField;
13     object      p;
14 }
15 // *****
16
17 dimensions    [0 2 -2 0 0 0 0];
18
19 internalField uniform 0;
20

```

```

21 boundaryField
22 {
23     PA_inlet
24     {
25         type            zeroGradient;
26     }
27     DA_inlet
28     {
29         type            zeroGradient;
30     }
31     V_outlet
32     {
33         type            fixedValue;
34         value            uniform 1.09168;
35     }
36     Blood_wall
37     {
38         type            zeroGradient;
39     }
40 }
41 }
42
43 // *****

```

RASProperties

```

1  /*-----*- C++ -*-----*\
2  | ===== |
3  | \ \      / F i e l d      | foam-extend: Open Source CFD |
4  | \ \      / O p e r a t i o n | Version: 4.0 |
5  |  \ \ /   A n d              | Web: http://www.foam-extend.org |
6  |   \ \ /   M a n i p u l a t i o n |
7  \*-----*-
8  FoamFile
9  {
10     version    2.0;
11     format      ascii;
12     class       dictionary;
13     location    "constant";
14     object      RASProperties;
15 }
16 // *****
17
18 RASModel      laminar;

```

```

19
20 turbulence      off;
21
22 printCoeffs     off;
23
24 // *****

transportProperties

1  /*-----*- C++ -*-----*\
2  | ===== |
3  | \ \ / F i e l d | foam-extend: Open Source CFD |
4  | \ \ / O p e r a t i o n | Version: 4.0 |
5  | \ \ / A n d | Web: http://www.foam-extend.org |
6  | \ \ / M a n i p u l a t i o n | |
7  /*-----*-
8  FoamFile
9  {
10     version 2.0;
11     format  ascii;
12     class  dictionary;
13     location "constant";
14     object  transportProperties;
15 }
16 // * * * * *
17
18 transportModel Newtonian;
19
20 nu          nu [0 2 -1 0 0 0 0] 3.30189e-6;
21
22 // *****

turbulenceProperties

1  /*-----*- C++ -*-----*\
2  | ===== |
3  | \ \ / F i e l d | foam-extend: Open Source CFD |
4  | \ \ / O p e r a t i o n | Version: 4.0 |
5  | \ \ / A n d | Web: http://www.foam-extend.org |
6  | \ \ / M a n i p u l a t i o n | |
7  /*-----*-
8  FoamFile
9  {
10     version 2.0;

```

```

11     format      ascii;
12     class       dictionary;
13     location     "constant";
14     object       turbulenceProperties;
15 }
16 // * * * * *
17
18 simulationType    RASModel;
19
20 // *****

controlDict

1 /*-----*- C++ -*-----*\
2 | ===== |
3 | \ \      / F i e l d      | foam-extend: Open Source CFD |
4 | \ \      / O p e r a t i o n | Version: 4.0 |
5 |  \ \ /   A n d              | Web: http://www.foam-extend.org |
6 |  \ \ /   M a n i p u l a t i o n | |
7 \*-----*-*/
8 FoamFile
9 {
10     version      2.0;
11     format        ascii;
12     class         dictionary;
13     location      "system";
14     object        controlDict;
15 }
16 // * * * * *
17
18 application      pisoFoam;
19
20 startFrom        latestTime;
21
22 startTime        0;
23
24 stopAt           endTime;
25
26 endTime          3;
27
28 deltaT           1e-03;
29
30 writeControl      timeStep;
31

```

```

32 writeInterval    1000;
33
34 purgeWrite       0;
35
36 writeFormat       ascii;
37
38 writePrecision    15;
39
40 writeCompression  uncompressed;
41
42 timeFormat        general;
43
44 timePrecision     6;
45
46 runTimeModifiable yes;
47
48
49 // ***** //

fvSchemes

1 /*-----*- C++ -*-----*\
2 | ===== |
3 | \\      / F ield      | foam-extend: Open Source CFD |
4 | \\      / O peration  | Version:    4.0              |
5 |  \\    /  A nd        | Web:        http://www.foam-extend.org |
6 |   \\   /  M anipulation | |
7 \*-----*/
8 FoamFile
9 {
10     version    2.0;
11     format      ascii;
12     class       dictionary;
13     location    "system";
14     object      fvSchemes;
15 }
16 // ***** //
17
18 ddtSchemes
19 {
20     default     Euler;
21 }
22
23 gradSchemes

```

```

24 {
25     default          Gauss linear;
26     grad(p)          Gauss linear;
27     grad(U)          cellLimited Gauss linear 0.333;
28 }
29
30 divSchemes
31 {
32
33     default          none;
34     div(phi,U)       Gauss upwind;
35     div(phi,nuTilda) Gauss limitedLinear 1;
36     div((nuEff*dev(T(grad(U)))) Gauss linear;
37 }
38
39 laplacianSchemes
40 {
41     default          Gauss linear corrected;
42 }
43
44 interpolationSchemes
45 {
46     default          linear;
47 }
48
49 snGradSchemes
50 {
51     default          corrected;
52 }
53
54 fluxRequired
55 {
56     default          no;
57     p;
58 }
59
60 // ***** //

fvSolution

1 /*-----* C++ -*-----*\
2 | ===== |
3 | \ \      / F ield      | foam-extend: Open Source CFD |
4 | \ \      / O peration  | Version: 4.0 |

```



```

5 |  \ \ /   A nd           | Web:      http://www.foam-extend.org   |
6 |  \ \ /   M anipulation |                                     |
7 | *-----* /
8 FoamFile
9 {
10     version      2.0;
11     format        ascii;
12     class         dictionary;
13     location      "system";
14     object        fvSolution;
15 }
16 // * * * * *
17
18 solvers
19 {
20     p
21     {
22         solver      GAMG;
23         tolerance    1e-10;
24         relTol       0;
25         minIter      1;
26         maxIter      1000;
27         smoother     GaussSeidel;
28         nPreSweeps    0;
29         nPostSweeps   2;
30         nFinestSweeps 2;
31         scaleCorrection true;
32         directSolveCoarsest false;
33         cacheAgglomeration true;
34         nCellsInCoarsestLevel 20;
35         agglomerator  faceAreaPair;
36         mergeLevels   1;
37     }
38
39     pFinal
40     {
41         solver      GAMG;
42         tolerance    1e-10;
43         relTol       0;
44         minIter      1;
45         maxIter      1000;
46         smoother     GaussSeidel;
47         nPreSweeps    0;

```

```

48     nPostSweeps    2;
49     nFinestSweeps  2;
50     scaleCorrection true;
51     directSolveCoarsest false;
52     cacheAgglomeration true;
53     nCellsInCoarsestLevel 20;
54     agglomerator    faceAreaPair;
55     mergeLevels     1;
56 }
57
58 cellMotionU
59 {
60     solver          GAMG;
61     tolerance        1e-10;
62     relTol           0;
63     minIter          1;
64     maxIter          100;
65     smoother         GaussSeidel;
66     nPreSweeps        0;
67     nPostSweeps       2;
68     nFinestSweeps     2;
69     scaleCorrection   true;
70     directSolveCoarsest false;
71     cacheAgglomeration true;
72     nCellsInCoarsestLevel 20;
73     agglomerator      faceAreaPair;
74     mergeLevels       1;
75 }
76
77 U
78 {
79     solver          PBiCG;
80     preconditioner   DILU;
81     tolerance        1e-10;
82     relTol           0;
83     minIter          1;
84 }
85
86 UFinal
87 {
88     solver          PBiCG;
89     preconditioner   DILU;
90     tolerance        1e-10;

```

```
91         relTol         0;
92         minIter         1;
93     }
94
95 }
96
97 PISO
98 {
99     nCorrectors         5;
100    nNonOrthogonalCorrectors 4;
101 }
102
103 // ***** //
```

Setting up the numerical models with fluid-structure coupling in Foam-extend

C.1 Fluid

The principle files of fluid are the same as in Annex ???. The following files are the definitions of fluid-structure interaction.

setBatch

```
1 faceSet Blood_wall-zone new patchToFace Blood_wall
2 quit
```

dynamicMeshDict

```
1  /*-----*- C++ -*-----*\
2  | ===== |
3  | \ \ / F i e l d | foam-extend: Open Source CFD |
4  | \ \ / O p e r a t i o n | Version: 4.0 |
5  | \ \ / A n d | Web: http://www.foam-extend.org |
6  | \ \ / M a n i p u l a t i o n | |
7  \*-----*\
8  FoamFile
9  {
10     version 2.0;
11     format ascii;
12     class dictionary;
13     object dynamicMeshDict;
14 }
15 // ***** //
16
17 dynamicFvMesh dynamicMotionSolverFvMesh;
18
19 solver velocityLaplacian;
20 diffusivity quadratic inverseDistance 1(Blood_wall);
21
```

```

22 nNonOrthogonalCorrectors 2;
23 leastSquaresVolPoint yes;
24
25 // *****

fluidProperties

1 /*-----*- C++ -*-----*\
2 | ===== |
3 | \ \ / F i e l d | foam-extend: Open Source CFD |
4 | \ \ / O p e r a t i o n | Version: 4.0 |
5 | \ \ / A n d | Web: http://www.extend-project.de |
6 | \ \ / M a n i p u l a t i o n | |
7 /*-----*-
8 FoamFile
9 {
10     version 2.0;
11     format ascii;
12     class dictionary;
13     object fluidProperties;
14 }
15 // *****

17 fluidSolver pisoFluid;
18
19 pisoFluidCoeffs
20 {
21     nCorrectors 5;
22     nNonOrthogonalCorrectors 4;
23 }
24
25 // *****

fsiProperties

1 /*-----*- C++ -*-----*\
2 | ===== |
3 | \ \ / F i e l d | foam-extend: Open Source CFD |
4 | \ \ / O p e r a t i o n | Version: 4.0 |
5 | \ \ / A n d | Web: http://www.foam-extend.org |
6 | \ \ / M a n i p u l a t i o n | |
7 /*-----*-
8 FoamFile
9 {
10     version 2.0;

```

```

11     format      ascii;
12     class       dictionary;
13     object      fsiProperties;
14 }
15 // *****
16
17 solidPatch Inner_wall;
18 solidZone Inner_wall-zone;
19
20 fluidPatch Blood_wall;
21 fluidZone Blood_wall-zone;
22
23 relaxationFactor 0.02;
24
25 interfaceDeformationLimit 0;
26
27 outerCorrTolerance 1e-6;
28 nOuterCorr 500;
29
30 interpolatorUpdateFrequency 0;
31
32 couplingScheme Aitken;
33
34 couplingReuse 0;
35
36 coupled yes;
37 predictor yes;
38
39 // *****

```

C.2 Solid

D

```

1  /*-----*- C++ -*-----*/
2  | ===== |
3  | \ \      / F ield      | foam-extend: Open Source CFD |
4  | \ \      / O peration  | Version:      4.0             |
5  | \ \      / A nd         | Web:          http://www.foam-extend.org |
6  |  \ \     / M anipulation | |
7  /*-----*/
8  FoamFile
9  {
10     version      2.0;

```

```

11     format      ascii;
12     class       volVectorField;
13     object      D;
14 }
15 // * * * * *
16
17
18 dimensions      [0 1 0 0 0 0 0];
19
20
21 internalField uniform (0 0 0);
22
23 boundaryField
24 {
25
26     PA_inlet_solid
27     {
28         type          fixedValue;
29         value          uniform (0 0 0);
30     }
31     DA_inlet_solid
32     {
33         type          fixedValue;
34         value          uniform (0 0 0);
35     }
36     V_outlet_solid
37     {
38         type          fixedValue;
39         value          uniform (0 0 0);
40     }
41     Inner_wall
42     {
43         type          tractionDisplacement;
44         traction       uniform ( 0 0 0 );
45         pressure       uniform 0;
46         value          uniform (0 0 0);
47     }
48     Outer_wall
49     {
50         type          tractionDisplacement;
51         traction       uniform ( 0 0 0 );
52         pressure       uniform 0;
53         value          uniform (0 0 0);

```

```

54     }
55
56 }
57
58 // *****

```

DD

```

1  /*-----*- C++ -*-----*\
2  | ===== |
3  | \ \      / F i e l d      | foam-extend: Open Source CFD |
4  | \ \      / O p e r a t i o n | Version: 4.0 |
5  |  \ \ /   A n d              | Web: http://www.foam-extend.org |
6  |   \ \ /   M a n i p u l a t i o n |
7  \*-----*-
8  FoamFile
9  {
10     version    2.0;
11     format      ascii;
12     class       volVectorField;
13     object      DD;
14 }
15 // * * * * *
16
17 dimensions      [0 1 0 0 0 0 0];
18
19 internalField uniform (0 0 0);
20
21 boundaryField
22 {
23
24     PA_inlet_solid
25     {
26         type      fixedValue;
27         value      uniform (0 0 0);
28     }
29     DA_inlet_solid
30     {
31         type      fixedValue;
32         value      uniform (0 0 0);
33     }
34     V_outlet_solid
35     {
36         type      fixedValue;

```



```

37         value            uniform (0 0 0);
38     }
39     Inner_wall
40     {
41         type              tractionDisplacementIncrement;
42         traction          uniform ( 0 0 0 );
43         pressure          uniform 0;
44         value            uniform (0 0 0);
45     }
46     Outer_wall
47     {
48         type              tractionDisplacementIncrement;
49         traction          uniform ( 0 0 0 );
50         pressure          uniform 0;
51         value            uniform (0 0 0);
52     }
53 }
54 }
55
56 // ***** //
pointD
1  /*-----*-- C++ -*-----*\
2  | ===== |
3  | \ \      / F ield      | foam-extend: Open Source CFD |
4  | \ \      / O peration  | Version: 4.0 |
5  | \ \      / A nd        | Web: http://www.foam-extend.org |
6  |  \ \     M anipulation | |
7  \*-----*--*/
8  FoamFile
9  {
10     version    2.0;
11     format     ascii;
12     class      pointVectorField;
13     object     pointD;
14 }
15 // * * * * * //
16
17 dimensions    [0 1 0 0 0 0 0];
18
19 internalField uniform (0 0 0);
20
21 boundaryField

```

```

22 {
23     PA_inlet_solid
24     {
25         type            fixedValue;
26         value            uniform (0 0 0);
27     }
28     DA_inlet_solid
29     {
30         type            fixedValue;
31         value            uniform (0 0 0);
32     }
33     V_outlet_solid
34     {
35         type            fixedValue;
36         value            uniform (0 0 0);
37     }
38     Inner_wall
39     {
40         type            calculated;;
41         value            uniform (0 0 0);
42     }
43     Outer_wall
44     {
45         type            calculated;;
46         value            uniform (0 0 0);
47     }
48 }
49 }
50
51 // ***** //

setBatch

1 faceSet Inner_wall-zone new patchToFace Inner_wall
2 quit

rheologyProperties

1 /*-----*-- C++ -*-----*\
2 | ===== | |
3 | \\ / F ield | foam-extend: Open Source CFD |
4 | \\ / O peration | Version: 4.0 |
5 | \\ / A nd | Web: http://www.foam-extend.org |
6 | \\ M anipulation | |
7 /*-----*/

```

```

8 FoamFile
9 {
10     version    2.0;
11     format      ascii;
12     class       dictionary;
13     object      rheologyProperties;
14 }
15 // * * * * *
16
17 planeStress no;
18
19 rheology
20 {
21     type          linearElastic;
22     rho           rho [1 -3 0 0 0 0 0] 1160;
23     E             E [1 -1 -2 0 0 0 0] 2e6;
24     nu           nu [0 0 0 0 0 0 0] 0.454;
25 }
26
27 // *****
28
29 solidProperties
30
31 /*-----*- C++ -*-----*\
32 | ===== |
33 | \ \      / F ield      | foam-extend: Open Source CFD |
34 | \ \      / O peration  | Version: 4.0 |
35 | \ \      / A nd        | Web: http://www.foam-extend.org |
36 | \ \      / M anipulation | |
37 \*-----*/
38
39 FoamFile
40 {
41     version    2.0;
42     format      ascii;
43     class       dictionary;
44     object      solidProperties;
45 }
46 // * * * * *
47
48 solidSolver unsTotalLagrangianSolid;
49
50 unsTotalLagrangianSolidCoeffs
51 {
52     nCorrectors 500;

```

```

22     convergenceTolerance 1e-10;
23     relConvergenceTolerance 1e-7;
24     nonLinear off;
25     debug no;
26 }
27
28 unsIncrTotalLagrangianSolidCoeffs
29 {
30     nCorrectors 500;
31     convergenceTolerance 1e-10;
32     relConvergenceTolerance 1e-7;
33     nonLinear off;
34     debug no;
35 }
36
37 // ***** //
controlDict

1 /*-----*- C++ -*-----*\
2 | ===== |
3 | \ \ / F i e l d | foam-extend: Open Source CFD |
4 | \ \ / O p e r a t i o n | Version: 4.0 |
5 | \ \ / A n d | Web: http://www.foam-extend.org |
6 | \ \ / M a n i p u l a t i o n | |
7 /*-----*/
8 FoamFile
9 {
10     version 2.0;
11     format ascii;
12     class dictionary;
13     location "system";
14     object controlDict;
15 }
16 // ***** //
17
18 application stressFoam;
19
20 startFrom latestTime;
21
22 startTime 0;
23
24 stopAt endTime;
25

```

```

26 endTime          3;
27
28 deltaT            1e-5;
29
30 writeControl      timeStep;
31
32 writeInterval     1000;
33
34 purgeWrite        0;
35
36 writeFormat        ascii;
37
38 writePrecision     6;
39
40 writeCompression  uncompressed;
41
42 timeFormat         general;
43
44 timePrecision      6;
45
46 runTimeModifiable yes;
47
48 adjustTimeStep     no;
49
50 maxCo              0.2;
51
52 // ***** //

fvSchemes

1  /*-----* C++ *-----*\
2  | ===== |
3  | \ \      / F ield      | foam-extend: Open Source CFD |
4  | \ \      / O peration  | Version: 4.0 |
5  |  \ \ /   A nd          | Web: http://www.foam-extend.org |
6  |   \ \ /   M anipulation | |
7  \*-----*/

8 FoamFile
9 {
10     version      2.0;
11     format        ascii;
12     class         dictionary;
13     object        fvSchemes;
14 }

```

```

15 // ****
16
17 d2dt2Schemes
18 {
19     default none;
20     d2dt2(D) Euler;
21     d2dt2(DD) Euler;
22 }
23
24 ddtSchemes
25 {
26     default none;
27     ddt(D) Euler;
28     ddt(DD) Euler;
29
30 }
31
32 gradSchemes
33 {
34     default leastSquares;
35 }
36
37 divSchemes
38 {
39     default Gauss linear;
40 }
41
42 laplacianSchemes
43 {
44     default none;
45     laplacian(DD,D) Gauss linear skewCorrected 1;
46     laplacian(DDD,DD) Gauss linear skewCorrected 1;
47 }
48
49 snGradSchemes
50 {
51     default none;
52     snGrad(D) skewCorrected 1;
53     snGrad(DD) skewCorrected 1;
54 }
55
56 interpolationSchemes
57 {

```

```

58     default          none;
59     interpolate(mu)   linear;
60     interpolate(lambda) linear;
61 }
62
63 // *****
64
65 fvSolution
66
67 /*-----*- C++ -*-----*\
68 | ===== |
69 | \ \      / F ield      | foam-extend: Open Source CFD |
70 | \ \      / O peration  | Version:      4.0             |
71 | \ \      / A nd        | Web:          http://www.foam-extend.org |
72 | \ \      / M anipulation | |
73 \*-----*-
74
75 FoamFile
76 {
77     version      2.0;
78     format       ascii;
79     class        dictionary;
80     object       fvSolution;
81 }
82 // *****
83
84 solvers
85 {
86     D
87     {
88         solver      GAMG;
89         tolerance   1e-11;
90         relTol      0;
91         minIter     1;
92         maxIter     1000;
93         smoother    GaussSeidel;
94         nPreSweeps  0;
95         nPostSweeps 2;
96         nFinestSweeps 2;
97         scaleCorrection true;
98         directSolveCoarsest false;
99         cacheAgglomeration true;
100        nCellsInCoarsestLevel 20;
101        agglomerator  faceAreaPair;
102        mergeLevels  1;

```

```
36     };
37
38     DD
39     {
40         solver          PCG;
41         preconditioner  DIC;
42         tolerance       1e-11;
43         relTol          0;
44     }
45 }
46
47 // ***** //
```


Bibliography

- [1] Olivier Geoffroy, Marc Tassart, Alain-Ferdinand Le Blanche, Antoine Khalil, Viviane Duédal, Jérôme Rossert, Jean-Michel Bigot, and Frank P Boudghène. Upper extremity digital subtraction venography with gadoterate meglumine before fistula creation for hemodialysis. *Kidney international*, 59(4):1491–1497, 2001. 10, 20
- [2] Anthony L Mescher. *Junqueira’s basic histology: text and atlas*, volume 12. McGraw-Hill Medical 13th ed. New York, 2013. 10, 21, 22, 23
- [3] Jagannath Mazumdar. *Biofluid mechanics*. World Scientific, 2015. 10, 11, 22, 23, 62, 63, 68
- [4] Marine Menut. *Chirurgie endovasculaire virtuelle pour patient-spécifique: Application au traitement de l’anévrisme de l’aorte thoracique*. PhD thesis, Université de Lyon, 2017. 10, 24
- [5] CARL F Rothe. Mean circulatory filling pressure: its meaning and measurement. *Journal of Applied Physiology*, 74(2):499–509, 1993. 10, 24
- [6] Mary Hammes. Hemodynamic and biologic determinates of arteriovenous fistula outcomes in renal failure patients. *BioMed research international*, 2015, 2015. 10, 25
- [7] AR Pries and TW Secomb. Control of blood vessel structure: insights from theoretical models. *American journal of physiology-Heart and circulatory physiology*, 288(3):H1010–H1015, 2005. 10, 29
- [8] Jeng-Jiann Chiu and Shu Chien. Effects of disturbed flow on vascular endothelium: pathophysiological basis and clinical perspectives. *Physiological reviews*, 91(1):327–387, 2011. 10, 28, 31, 32, 85, 99, 111
- [9] Haimanot Wasse, Rong Huang, Nawazish Naqvi, Eileen Smith, Dezhi Wang, and Ahsan Husain. Inflammation, oxidation and venous neointimal hyperplasia precede vascular injury from avf creation in ckd patients. *The journal of vascular access*, 13(2):168–174, 2012. 10, 33, 35
- [10] Bruce Furie and Barbara C Furie. Mechanisms of thrombus formation. *New England Journal of Medicine*, 359(9):938–949, 2008. 10, 34
- [11] Nicolaas Westerhof, Nikolaos Stergiopoulos, Mark IM Noble, and Berend E Westerhof. *Snapshots of hemodynamics: an aid for clinical research and graduate education*. Springer, 2018. 11, 65, 66
- [12] Jean-Jacques Mourad, Xavier Girerd, Pierre Boutouyrie, Stéphane Laurent, Michel Safar, and Gérard London. Increased stiffness of radial artery wall material in end-stage renal disease. *Hypertension*, 30(6):1425–1430, 1997. 11, 65, 66
- [13] Fadl Moukalled, L Mangani, Marwan Darwish, et al. *The finite volume method in computational fluid dynamics*, volume 113. Springer, 2016. 11, 62, 67, 68, 69, 79

- [14] A Cengel Yunus. *Fluid Mechanics: Fundamentals And Applications (Si Units)*. Tata McGraw Hill Education Private Limited, 2010. 11, 76
- [15] J Donea, A Huerta, JP Ponthot, and A Rodríguez-Ferran. Arbitrary lagrangian-eulerian methods. in: *Encyclopedia of computational mechanics second edition*. 2017. 11, 79, 80
- [16] MKP Make. Predicting scale effects on floating offshore wind turbines. 2014. 12, 99
- [17] Sharmila Sivanesan, Thien V How, and Ali Bakran. Sites of stenosis in av fistulae for haemodialysis access. *Nephrology, dialysis, transplantation: official publication of the European Dialysis and Transplant Association-European Renal Association*, 14(1):118–120, 1999. 13, 118
- [18] Shewaferaw S Shibeshi and William E Collins. The rheology of blood flow in a branched arterial system. *Applied rheology*, 15(6):398–405, 2005. 14, 86
- [19] Jürg Schmidli, Matthias K Widmer, Carlo Basile, Gianmarco de Donato, Maurizio Gallieni, Christopher P Gibbons, Patrick Haage, George Hamilton, Ulf Hedin, Lars Kamper, et al. Editor’s choice—vascular access: 2018 clinical practice guidelines of the european society for vascular surgery (esvs). *European Journal of Vascular and Endovascular Surgery*, 55(6):757–818, 2018. 16, 19, 20, 34, 121, 126, 129
- [20] Bernard Canaud, Pedro Ponce, M Teresa Parisotto, et al. Vascular access management for haemodialysis: A value-based approach from nephrocare experience. *Vascular Access Surgery-Tips and Tricks*, 2019. 17, 19, 28
- [21] BS Dixon. Why don’t fistulas mature? *Kidney international*, 70(8):1413–1422, 2006. 17, 26, 75
- [22] Charmaine E Lok, Thomas S Huber, Timmy Lee, Surendra Shenoy, Alexander S Yevzlin, Kenneth Abreo, Michael Allon, Arif Asif, Brad C Astor, Marc H Glickman, et al. Kdoqi clinical practice guideline for vascular access: 2019 update. *American Journal of Kidney Diseases*, 75(4):S1–S164, 2020. 18, 28, 30, 33, 40, 121, 126, 129
- [23] Pietro Ravani, Suetonia C Palmer, Matthew J Oliver, Robert R Quinn, Jennifer M MacRae, Davina J Tai, Neesh I Pannu, Chandra Thomas, Brenda R Hemmelgarn, Jonathan C Craig, et al. Associations between hemodialysis access type and clinical outcomes: a systematic review. *Journal of the American Society of Nephrology*, 24(3):465–473, 2013. 19
- [24] Maria G Marques and Pedro Ponce. Pre-operative assessment for arteriovenous fistula placement for dialysis. In *Seminars in dialysis*, volume 30, pages 58–62. Wiley Online Library, 2017. 20
- [25] Nils R Planken, Jan H Tordoir, Lucien E Duijm, Harrie C van den Bosch, Frank M van der Sande, Jeroen P Kooman, Michiel W de Haan, and Tim Leiner. Magnetic resonance angiographic assessment of upper extremity vessels prior to vascular access surgery: feasibility and accuracy. *European radiology*, 18(1):158–167, 2008. 20

- [26] Tyler J Fraum, Daniel R Ludwig, Mustafa R Bashir, and Kathryn J Fowler. Gadolinium-based contrast agents: A comprehensive risk assessment. *Journal of Magnetic Resonance Imaging*, 46(2):338–353, 2017. 20
- [27] Ismail Mihmanli, Kazim Besirli, Sebu Kurugoglu, Kadir Atakir, Seemab Haider, Gunduz Ogut, Furuzan Numan, Emir Canturk, and Ayla Gurel Sayin. Cephalic vein and hemodialysis fistula: surgeon’s observation versus color doppler ultrasonographic findings. *Journal of ultrasound in medicine*, 20(3):217–222, 2001. 21
- [28] Jonathan D Jansen. *Knowledge in the blood*. Stanford University Press, 2020. 21
- [29] Devajyoti Biswas. *Blood flow models: a comparative study*. Mittal Publications, 2002. 22
- [30] Nikolay Bessonov, Adélia Sequeira, Sergey Simakov, Yu Vassilevskii, and Vitaly Volpert. Methods of blood flow modelling. *Mathematical modelling of natural phenomena*, 11(1):1–25, 2016. 23, 63
- [31] H Schmid-Schönbein and RE Wells. Rheological properties of human erythrocytes and their influence upon the “anomalous” viscosity of blood. *Ergebnisse der Physiologie Reviews of Physiology, Volume 63*, pages 146–219, 1971. 23
- [32] Seymour Glagov, Ray Vito, Don P Giddens, and Christopher K Zarins. Micro-architecture and composition of artery walls: relationship to location, diameter and. *J Hypertens*, 10(6):S101–S104, 1992. 24
- [33] Patrick B Snowhill, David J Foran, and Frederick H Silver. A mechanical model of porcine vascular tissues-part i: determination of macromolecular component arrangement and volume fractions. *Cardiovascular Engineering*, 4(4):281–294, 2004. 24
- [34] Haidi Hu, Sandeep Patel, Jesse J Hanisch, Jeans M Santana, Takuya Hashimoto, Hualong Bai, Tambudzai Kudze, Trenton R Foster, Jianming Guo, Bogdan Yatsula, et al. Future research directions to improve fistula maturation and reduce access failure. In *Seminars in vascular surgery*, volume 29, pages 153–171. Elsevier, 2016. 28, 30, 31, 32, 130
- [35] Kozaburo Hayashi and Takeru Naiki. Adaptation and remodeling of vascular wall; biomechanical response to hypertension. *Journal of the mechanical behavior of biomedical materials*, 2(1):3–19, 2009. 30
- [36] Nirvana Sadaghianloo, Julie Contenti, Alan Dardik, and Nathalie M Mazure. Role of hypoxia and metabolism in the development of neointimal hyperplasia in arteriovenous fistulas. *International journal of molecular sciences*, 20(21):5387, 2019. 30
- [37] Bogdan Ene-Iordache and Andrea Remuzzi. Disturbed flow in radial-cephalic arteriovenous fistulae for haemodialysis: low and oscillating shear stress locates the sites of stenosis. *Nephrology Dialysis Transplantation*, 27(1):358–368, 2012. 30, 36, 63
- [38] Bogdan Ene-Iordache, Luca Cattaneo, Gabriele Dubini, and Andrea Remuzzi. Effect of anastomosis angle on the localization of disturbed flow in ‘side-to-end’ fistulae for haemodialysis access. *Nephrology Dialysis Transplantation*, 28(4):997–1005, 2013. 30, 36, 40, 63

- [39] Shu Chien. Effects of disturbed flow on endothelial cells. *Annals of biomedical engineering*, 36(4):554–562, 2008. 31, 32
- [40] Yutaka Matsubara, Gathe Kiwan, Arash Fereydooni, John Langford, and Alan Dardik. Distinct subsets of t cells and macrophages impact venous remodeling during arteriovenous fistula maturation. *JVS: Vascular Science*, 1:207–218, 2020. 32
- [41] Ali Kordzadeh, Jameson Chung, and Yiannis P Panayiotopoulos. Cephalic vein and radial artery diameter in formation of radiocephalic arteriovenous fistula: a systematic review. *The journal of vascular access*, 16(6):506–511, 2015. 33, 36, 40
- [42] J Parmar, M Aslam, and N Standfield. Pre-operative radial arterial diameter predicts early failure of arteriovenous fistula (avf) for haemodialysis. *European journal of vascular and endovascular surgery*, 33(1):113–115, 2007. 33, 36, 40, 121, 122, 129
- [43] K Bashar, M Clarke-Moloney, PE Burke, EG Kavanagh, and SR Walsh. The role of venous diameter in predicting arteriovenous fistula maturation: when not to expect an avf to mature according to pre-operative vein diameter measurements? a best evidence topic. *International Journal of Surgery*, 15:95–99, 2015. 33, 36, 40, 121, 122, 129
- [44] Nikola Gjorgjievski, Pavlina Dzekova-Vidimliski, Lada Trajcheska, Ana Stojanoska, Gjushen Selim, Irena Rambabova-Bushljetik, Igor Nikolov, Juija Gjorgievska, Zoran Janevski, Shkle-qim Muharremi, et al. Impact of preoperative arterial and venous diameter on achievement of the adequate blood flow in arteriovenous fistula for hemodialysis. *Therapeutic apheresis and dialysis: official peer-reviewed journal of the International Society for Apheresis, the Japanese Society for Apheresis, the Japanese Society for Dialysis Therapy*, 2020. 33, 36, 40, 121, 122, 129
- [45] Prabir Roy-Chaudhury, Yang Wang, Mahesh Krishnamoorthy, Jianhua Zhang, Rupak Banerjee, Rino Munda, Sue Heffelfinger, and Lois Arend. Cellular phenotypes in human stenotic lesions from haemodialysis vascular access. *Nephrology Dialysis Transplantation*, 24(9):2786–2791, 2009. 33
- [46] Lijie Fan and Takeshi Karino. Effect of a disturbed flow on proliferation of the cells of a hybrid vascular graft. *Biorheology*, 47(1):31–38, 2010. 33
- [47] Siren Sezer, F Nurhan Özdemir, Zübeyde Arat, Münire Turan, and Mehmet Haberal. Triad of malnutrition, inflammation, and atherosclerosis in hemodialysis patients. *Nephron*, 91(3):456–462, 2002. 34
- [48] Bi-cheng Liu, LI Li, GAO Min, Yan-li Wang, and Ji-rong Yu. Microinflammation is involved in the dysfunction of arteriovenous fistula in patients with maintenance hemodialysis. *Chinese medical journal*, 121(21):2157–2161, 2008. 34
- [49] Prabir Roy-Chaudhury, Lawrence M Spergel, Anatole Besarab, Arif Asif, and Pietro Ravani. Biology of arteriovenous fistula failure. *Journal of nephrology*, 20(B):150, 2007. 35
- [50] Patrick Steven Tucker, Vincent James Dalbo, Thin Han, and Michael Ian Kingsley. Clinical and research markers of oxidative stress in chronic kidney disease. *Biomarkers*, 18(2):103–115, 2013. 35

- [51] Anna Machowska, Juan Jesus Carrero, Bengt Lindholm, and Peter Stenvinkel. Therapeutics targeting persistent inflammation in chronic kidney disease. *Translational Research*, 167(1):204–213, 2016. 35
- [52] Philippe Brunet, Bertrand Gondouin, Ariane Duval-Sabatier, Laetitia Dou, Claire Cerini, Françoise Dignat-George, Noemie Jourde-Chiche, Angel Argiles, and Stéphane Burtey. Does uremia cause vascular dysfunction. *Kidney and blood pressure research*, 34(4):284–290, 2011. 35
- [53] Jacques Blacher, Alain P Guerin, Bruno Pannier, Sylvain J Marchais, and Gérard M London. Arterial calcifications, arterial stiffness, and cardiovascular risk in end-stage renal disease. *Hypertension*, 38(4):938–942, 2001. 35
- [54] Boris Bikbov, Caroline A Purcell, Andrew S Levey, Mari Smith, Amir Abdoli, Molla Abebe, Oladimeji M Adebayo, Mohsen Afarideh, Sanjay Kumar Agarwal, Marcela Agudelo-Botero, et al. Global, regional, and national burden of chronic kidney disease, 1990–2017: a systematic analysis for the global burden of disease study 2017. *The Lancet*, 395(10225):709–733, 2020. 35
- [55] Centers for Disease Control, Prevention, et al. Chronic kidney disease in the united states, 2019. *Atlanta, GA: US Department of Health and Human Services, Centers for Disease Control and Prevention*, 2019. 35
- [56] Cécile Couchoud, Mathilde Lassalle, B Stengel, and C Jacquelinet. Réseau épidémiologie information néphrologie. *Rapport annuel*, 2018. 35
- [57] Isabelle Bongiovanni, Anne-Line Couillerot-Peyronnet, Cléa Sambuc, Emmanuelle Dantony, Mad-Hélénie Elsensohn, Yoël Sainsaulieu, René Ecohard, and Cécile Couchoud. Cost-effectiveness analysis of various strategies of end-stage renal disease patients’ care in france. *Néphrologie & thérapeutique*, 12(2):104–115, 2016. 35
- [58] Bogdan Ene-Iordache, Cristina Semperboni, Gabriele Dubini, and Andrea Remuzzi. Disturbed flow in a patient-specific arteriovenous fistula for hemodialysis: multidirectional and reciprocating near-wall flow patterns. *Journal of biomechanics*, 48(10):2195–2200, 2015. 36
- [59] Ashkan Javadzadegan, Nay Myo Lwin, Muhammad Asyraf, Anne Simmons, and Tracie Barber. Analysis of blood flow characteristics in a model of a mature side-to-side arteriovenous fistula. *Artificial organs*, 41(11):E251–E262, 2017. 36, 63
- [60] John Carroll, Ramon L Varcoe, Tracie Barber, and Anne Simmons. Reduction in anastomotic flow disturbance within a modified end-to-side arteriovenous fistula configuration: Results of a computational flow dynamic model. *Nephrology*, 24(2):245–251, 2019. 36
- [61] Lan Jia, Lihua Wang, Fang Wei, Haibo Yu, Hongye Dong, Bo Wang, Zhi Lu, Guijiang Sun, Haiyan Chen, Jia Meng, et al. Effects of wall shear stress in venous neointimal hyperplasia of arteriovenous fistulae. *Nephrology*, 20(5):335–342, 2015. 36

- [62] Leigh Anne Dageforde, Kelly A Harms, Irene D Feurer, and David Shaffer. Increased minimum vein diameter on preoperative mapping with duplex ultrasound is associated with arteriovenous fistula maturation and secondary patency. *Journal of vascular surgery*, 61(1):170–176, 2015. 36
- [63] M Khavanin Zadeh, F Gholipour, Zeinab Naderpour, and M Porfakharan. Relationship between vessel diameter and time to maturation of arteriovenous fistula for hemodialysis access. *International journal of nephrology*, 2012, 2012. 36, 52
- [64] Yuan-cheng Fung. *Biomechanics: circulation*. Springer Science & Business Media, 2013. 37, 43
- [65] Zane S Jackson, Hiroyuki Ishibashi, Avrum I Gotlieb, and B Lowell Langille. Effects of anastomotic angle on vascular tissue responses at end-to-side arterial grafts. *Journal of vascular surgery*, 34(2):300–307, 2001. 40
- [66] Yves Pousset, Patrick Lermusiaux, Gaëlle Berton, Jean-Marie Le Gouez, and René Leroy. Numerical model study of flow dynamics through an end-to-side anastomosis: choice of anastomosis angle and prosthesis diameter. *Annals of vascular surgery*, 20(6):773–779, 2006. 40
- [67] IJ Freshwater, YS Morsi, and T Lai. The effect of angle on wall shear stresses in a lima to lad anastomosis: numerical modelling of pulsatile flow. *Proceedings of the Institution of Mechanical Engineers, Part H: Journal of Engineering in Medicine*, 220(7):743–757, 2006. 40
- [68] G Prouse, S Stella, C Vergara, S Engelberger, R Trunfio, R Canevascini, L Giovannacci, et al. Computational analysis of turbulent haemodynamics in radiocephalic arteriovenous fistulas with different anastomotic angles, 2019. 40
- [69] Tomáš Juza and Daniel Vlk. Immediate effect of physical exercise on blood flow velocity in radial artery in young adults. *Lékař a technika-Clinician and Technology*, 48(4):118–122, 2018. 42
- [70] Katherine E Wilson, Jimmy Tat, and Peter J Keir. Effects of wrist posture and fingertip force on median nerve blood flow velocity. *BioMed research international*, 2017, 2017. 42, 75
- [71] Sunil Beniwal, Kapil Bhargava, and Satish K Kausik. Size of distal radial and distal ulnar arteries in adults of southern rajasthan and their implications for percutaneous coronary interventions. *Indian heart journal*, 66(5):506–509, 2014. 42, 75
- [72] Isaak E Idelchik. Handbook of hydraulic resistance. *Washington*, 1986. 42
- [73] MD Bassett, DE Winterbone, and RJ Pearson. Calculation of steady flow pressure loss coefficients for pipe junctions. *Proceedings of the institution of mechanical engineers, part C: Journal of Mechanical Engineering Science*, 215(8):861–881, 2001. 43, 50
- [74] Jiyuan Tu, Guan Heng Yeoh, and Chaoqun Liu. *Computational fluid dynamics: a practical approach*. Butterworth-Heinemann, 2018. 62
- [75] S CD-adapco. Star ccm+ user guide version 12.04. *CD-Adapco: New York, NY, USA*, 2017. 62

- [76] Blessy Thomas and KS Sumam. Blood flow in human arterial system-a review. *Procedia Technology*, 24:339–346, 2016. 63, 65
- [77] Thomas O Brien, Michael Walsh, and Tim McGloughlin. On reducing abnormal hemodynamics in the femoral end-to-side anastomosis: the influence of mechanical factors. *Annals of Biomedical Engineering*, 33(3):310–322, 2005. 63
- [78] Iolanda Decorato, Zaher Kharboutly, Tommaso Vassallo, Justin Penrose, Cécile Legallais, and Anne-Virginie Salsac. Numerical simulation of the fluid structure interactions in a compliant patient-specific arteriovenous fistula. *International journal for numerical methods in biomedical engineering*, 30(2):143–159, 2014. 65
- [79] Dereje Getachew, Ayalew Astatkie, and Kinfe Lemma. Diameter, vessel thickness and angle of bifurcation of the radial artery in ethiopian cadavers. *Journal of Morphological Sciences*, 35(02):129–135, 2018. 65
- [80] Zenji Makita, Richard Bucala, Elliot J Rayfield, H Fuh, KR Manogue, A Cerami, H Viassara, EA Friedman, AM Kaufman, SM Korbet, et al. Reactive glycosylation endproducts in diabetic uraemia and treatment of renal failure. *The Lancet*, 343(8912):1519–1522, 1994. 67
- [81] Amac Kiray, Ipek Ergür, Hamid Tayefi, HA Bağriyanik, and AK Bacakoğlu. Anatomical evaluation of the superficial veins of the upper extremity as graft donor source in microvascular reconstructions: a cadaveric study. *Acta Orthopaedica et Traumatologica Turcica*, 47(6):405, 2013. 67
- [82] Stephane Laurent, Xavier Girerd, Jean-Jacques Mourad, Patrick Lacolley, Lionel Beck, Pierre Boutouyrie, Jean-Pierre Mignot, and Michel Safar. Elastic modulus of the radial artery wall material is not increased in patients with essential hypertension. *Arteriosclerosis and thrombosis: a journal of vascular biology*, 14(7):1223–1231, 1994. 67
- [83] Sun Cheol Park, Ryungeun Song, Sunho Kim, Hyun Kyu Kim, Seung-Hyun Kim, and Jinkee Lee. Fabrication of artificial arteriovenous fistula and analysis of flow field and shear stress by using μ -piv technology. *Journal of Mechanical Science and Technology*, 30(12):5503–5511, 2016. 67
- [84] F Pukacki, T Jankowski, M Gabriel, G Oszkinis, Z Krasinski, and S Zapalski. The mechanical properties of fresh and cryopreserved arterial homografts. *European Journal of Vascular and Endovascular Surgery*, 20(1):21–24, 2000. 67
- [85] R Byron Bird. Transport phenomena. *Appl. Mech. Rev.*, 55(1):R1–R4, 2002. 67
- [86] Winston Guess. Fluid-structure interaction modelling of a patient-specific arteriovenous access fistula. Master’s thesis, University of Cape Town, 2016. 72
- [87] Wei Wang, Yong Cao, and Tsubasa Okaze. Comparison of hexahedral, tetrahedral and polyhedral cells for reproducing the wind field around an isolated building by les. *Building and Environment*, 195:107717, 2021. 72

- [88] ALTON OCHSNER JR, RALPH COLP JR, and GE Burch. Normal blood pressure in the superficial venous system of man at rest in the supine position. *Circulation*, 3(5):674–680, 1951. 74
- [89] Marie Willemet, Phil Chowienzyk, and Jordi Alastruey. A database of virtual healthy subjects to assess the accuracy of foot-to-foot pulse wave velocities for estimation of aortic stiffness. *American Journal of Physiology-Heart and Circulatory Physiology*, 309(4):H663–H675, 2015. 75
- [90] Raad I Issa, AD Gosman, and AP Watkins. The computation of compressible and incompressible recirculating flows by a non-iterative implicit scheme. *Journal of Computational Physics*, 62(1):66–82, 1986. 77
- [91] Iain Edward Barton. Comparison of simple-and piso-type algorithms for transient flows. *International Journal for numerical methods in fluids*, 26(4):459–483, 1998. 79
- [92] Ted Belytschko, Wing Kam Liu, Brian Moran, and Khalil Elkhodary. *Nonlinear finite elements for continua and structures*. John wiley & sons, 2013. 81
- [93] DO Bates, JR Levick, and PS Mortimer. Subcutaneous interstitial fluid pressure and arm volume in lymphoedema. *International journal of microcirculation, clinical and experimental*, 11(4):359–373, 1992. 82
- [94] C Michler, SJ Hulshoff, EH Van Brummelen, and René De Borst. A monolithic approach to fluid–structure interaction. *Computers & fluids*, 33(5-6):839–848, 2004. 82
- [95] Ulrich Küttler and Wolfgang A Wall. Fixed-point fluid–structure interaction solvers with dynamic relaxation. *Computational mechanics*, 43(1):61–72, 2008. 84
- [96] Sang-Wook Lee, Luca Antiga, and David A Steinman. Correlations among indicators of disturbed flow at the normal carotid bifurcation. *Journal of biomechanical engineering*, 131(6), 2009. 85, 86
- [97] Xiaoyi He and David N Ku. Pulsatile flow in the human left coronary artery bifurcation: average conditions. *Journal of biomechanical engineering*, 118(1):74–82, 1996. 85
- [98] David N Ku, Don P Giddens, Christopher K Zarins, and Seymour Glagov. Pulsatile flow and atherosclerosis in the human carotid bifurcation. positive correlation between plaque location and low oscillating shear stress. *Arteriosclerosis: An Official Journal of the American Heart Association, Inc.*, 5(3):293–302, 1985. 85
- [99] Ramazan Albayrak, Seref Yuksel, Mehmet Colbay, Bumin Degirmenci, Gursel Acarturk, Alpay Haktanır, and Ozcan Karaman. Hemodynamic changes in the cephalic vein of patients with hemodialysis arteriovenous fistula. *Journal of Clinical Ultrasound*, 35(3):133–137, 2007. 86
- [100] Sonia Tabakova, E Nikolova, and St Radev. Carreau model for oscillatory blood flow in a tube. In *AIP conference proceedings*, volume 1629, pages 336–343. American Institute of Physics, 2014. 86

- [101] Matthias Hofer. Teaching manual of color duplex tomography, 2004. 96
- [102] Ali Kordzadeh, Jameson Chung, and Yiannis P Panayiotopoulos. Cephalic vein and radial artery diameter in formation of radiocephalic arteriovenous fistula: a systematic review. *The journal of vascular access*, 16(6):506–511, 2015. 121, 122, 129



FOLIO ADMINISTRATIF

THÈSE DE L'UNIVERSITÉ DE LYON OPÉRÉE AU SEIN DE L'INSA LYON

NOM : YANG

Date de soutenance : 19 10 2021

Prénom : Yang

Titre : Analysis of Personalized Mechano-Bio-faithful Radio-Cephalic Arteriovenous Fistula

Nature : Doctorat

Numéro d'ordre :
2021LYSEI067

École doctorale : Mécanique, Énergétique, Génie Civil et Acoustique (MEGA)

Spécialité : Biomécanique

Résumé : End-stage renal disease (ESRD) is one of the leading chronic diseases in the world, with a high incidence and extensive damage. For patients with ESRD, timely and effective dialysis treatment is the most well-discussed way to sustain their lives. Dialysis Vascular Access (VA) should be reliable and simple access that allows blood to be introduced and returned quickly and correctly. It is necessary to connect the artery and the superficial vein to build a VA that meets the demands of dialysis called arteriovenous fistula (AVF). The AVF uses native vessels and is developed to adapt to the anatomical and physiological characteristics of the patient. Due to the change in vascular geometry, the hemodynamics of AVF changes. The arterial flow will continue to increase. To accommodate the high flow and high blood pressure, the vein must reshape and increase the wall thickness to protect the vein. This process of change is called fistula maturation and usually lasts about a month. Typically, surgeons rely on their clinical experiences to design RCAVF configurations. Due to the lack of understanding of hemodynamics in AVF, unreasonable anastomosis design will lead to variable and irregular flow patterns. The resulting low-wall shear stress (WSS) and oscillating WSS negatively stimulate the vessel wall, affecting the maturation and permeability of the AVF. In this Ph.D., we focused on radio-cephalic arteriovenous fistula (RCAVF), the first and most common choice of AVF. The RCAVF setup has been optimized both mechanically (reduce energy loss in RCAVF) and biologically (minimize low, oscillating WSS on the vessel wall to slow the development of strictures). Finally, we designed a mechano-bio-faithful personal preoperative RCAVF model (PerMeBiO-RCAVF model) to provide patient-specific assistance to the preoperative planning process of the RCAVF setup to increase the rate of RCAVF maturation and reduce complications.

Mots-clés : Dialysis, radio-cephalic arteriovenous fistula (RCAVF), energy loss, computational fluid dynamics (CFD), fluid-structure interaction (FSI), wall shear stress

Laboratoire de recherche : Laboratoire de Mécanique des Contacts et des Structures (LaMCoS)

Directeur de thèse: Benyebka BOU-SAÏD

Président de jury : Patrick LERMUSIAUX

Composition du jury : Philippe VEZIN, Shengzhang WANG, Pascale KULISA, Hassan ZAHOUANI